University of Naples Federico II

Department of Structures for Engineering and Architecture

34st cycle Ph.D. program in Structural and Geotechnical Engineering and Seismic Risk

and

National Technical University of Athens

School of Civil Engineering

Ph.D. program in Civil Engineering

SEISMIC FRAGILITY ASSESSMENT VIA NON-LINEAR ANALYSIS: PRACTICAL ISSUES AND TOOLS FOR ENGINEERING APPLICATIONS

ΑΠΟΤΊΜΗΣΗ ΣΕΙΣΜΙΚΉΣ ΤΡΩΤΌΤΗΤΑΣ ΜΈΣΩ ΜΗ ΓΡΑΜΜΙΚΉΣ ΑΝΆΛΥΣΗΣ: ΠΡΑΚΤΙΚΆ ΘΈΜΑΤΑ ΚΑΙ ΥΠΟΛΟΓΙΣΤΙΚΆ ΕΡΓΑΛΕΊΑ ΕΦΑΡΜΟΓΉΣ

Jointly-supervised Ph.D. thesis

by

Roberto Baraschino

ADVISORS: Prof. Iunio Iervolino

Prof. Dimitrios Vamvatsikos

CO-ADVISOR: Dr. Georgios Baltzopoulos

YEAR 2022

"Los de afuera son de palo"
Obdulio Varela

"Penso che un uomo senza utopia, senza sogno, senza ideali, vale a dire senza passione, senza slanci, beh, sarebbe un mostruoso animale fatto semplicemente di istinto e di raziocinio, una specie di cinghiale laureato in matematica pura"
Fabrizio De Andrè

"There is no true understanding without a certain range of comparison"
Marc Bloch

ACKNOWLEDGEMENTS

Mi si perdoni la scelta, forse un po' provinciale, di scrivere queste righe in italiano ma sono fermamente convinto del fatto di non essere in grado di esprimere i miei sentimenti in maniera profonda, naturale e sincera se non nella lingua nella quale penso.

Ringrazio innanzitutto il Prof. Iunio Iervolino per avermi dato in questi anni la possibilità di affrontare sfide tanto complicate quanto stimolanti. La sua guida, spesso severa, ha contribuito in maniera preponderante alla mia crescita professionale.

Ringrazio il Prof. Dimitrios Vamvatsikos per avermi dato l'opportunità di svolgere questo dottorato in cotutela. Purtroppo, il piccolo inconveniente che da due anni ci perseguita mi ha negato la possibilità di trascorrere qualche mese ad Atene e questo rimarrà il rimpianto più grande di questa esperienza. La sua capacità di unire alla qualità della ricerca un approccio quasi ludico è per me fonte di forte ispirazione.

Ringrazio il Dr. Georgios Baltzopoulos per avermi praticamente iniziato a questo mondo (è un bene o un male? ai posteri l'ardua sentenza). La sua capacità di avere sempre risposte ai miei mille quesiti, la sensazione che dà di sapere sempre di cosa sta parlando, mi ha sempre sorpreso ed anche un po' inquietato.

Ringrazio il Dr. Pasquale Cito, probabilmente la persona con la quale condivido più cose: età, luogo di nascita, laurea triennale, laurea magistrale, dottorato, ufficio (le cui mura sono fortunatamente mute) e, ahimè, perdita esponenziale di capelli. Il quotidiano confronto, rigorosamente scientifico, ha contribuito al raggiungimento di questo risultato. Il mio augurio è che tutto l'impegno che ci mette verrà ricompensato da una brillante e meritata carriera. Ma, mi raccomando con lui, di non trascurare la forma fisica se vuole provare a starmi dietro ancora per un po'.

Ringrazio Adriana, collega e amica, il cui aiuto morale e materiale è stato fondamentale per la stesura di questa tesi. La sua pignoleria, talvolta leggermente fastidiosa (...), ha evitato la mia deriva folle davanti al misterioso mondo Office. Di lei apprezzo, più di ogni altra cosa, il modo assolutamente disinteressato con il quale presta il proprio aiuto agli altri. Dote rara.

Ringrazio tutti gli altri componenti del nostro gruppo di ricerca, il Dr. Eugenio Chioccarelli ed i ragazzi dottorandi o quasi dottorati: Francesco,

Mabel ed Antonio (x2). Il costante confronto umano e professionale ha indirettamente contribuito alla mia crescita.

Ringrazio il Dr. Mariano Di Domenico, lui non lo sa, ma la passione che ci mette in quello che fa, il come lo fa, e l'entusiasmo che trasmette sono fonte di ispirazione quotidiana: è nato per fare questo, nessun dubbio che prima o poi raccoglierà tutto ciò che merita. "Dai, Dai, Dai!".

Ringrazio tutti quelli che, farei sicuramente torto a qualcuno elencandone i nomi, hanno contribuito ad alleggerire le giornate con un caffè, una battuta, uno sclero ed un sano confronto intellettuale. A tal riguardo, le pause pranzo pre-pandemia rimarranno i momenti più belli e spensierati qui vissuti, tra zoofilia, rap impovvisati, e tutti i discorsi aventi come incipit "per 100 mila euro faresti". Li ricordo con un misto di nostalgia e rimpianto.

Ringrazio la mia famiglia ed i miei genitori nello specifico per ciò che sono e per i valori che hanno sempre testimoniato ai miei occhi: laborosità, dignità, umiltà ed amore incondizionato. Senza radici saremmo poco più che robot, ed io sono fiero delle mie che non baratterei per nulla al mondo. Senza loro niente di tutto questo sarebbe accaduto.

Il meglio si tiene per la fine, no? Ringrazio quindi mia moglie, Adelaide. L'anno scorso mi ha reso l'uomo più felice del mondo, ma è da un'infinità di anni che mi ricorda quotidianamente le meraviglia di persona che è. L'abnegazione, la fiducia, l'amore puro, la capacità di perdono, gli occhi rassicuranti forieri di dolcezza sono stati e saranno per sempre la mia benzina, la mia linfa, il mio porto sicuro. Senza lei semplicemente non esisto io, ma una mia copia consunta e sbiadita. Ti amo.

Napoli, 3 marzo 2022

Roberto

ΕΚΤΕΤΑΜΈΝΗ ΠΕΡΊΛΗΨΗ

1 ΕΙΣΑΓΩΓΗ

Στο πλαίσιο της σεισμικής μηχανικής με βάση την επιτελεστικότητα (*performance-based earthquake engineering* - PBEE, [1]) ένα αξιοσημείωτο πρόβλημα που τίθεται συχνά είναι αυτό της αξιολόγησης της συχνότητας των σεισμών που οδηγεί μια κατασκευή σε αστοχία επίτευξης ενός στόχου επιτελεστικότητας (μια κατάσταση που συχνά αναφέρεται, στο πλαίσιο των κατασκευαστικών κωδίκων, ως υπέρβαση μιας οριακής κατάστασης). Αυτός ο υπολογισμός, σε μια από τις απλούστερες μορφές του, μπορεί να πραγματοποιηθεί με την υλοποίηση του θεωρήματος της συνολικής πιθανότητας:

$$\lambda_f = \int_{im} P\left[EDP > edp_f \left| IM = im \right. \right] \cdot \left| d\lambda_{im} \right| . \quad (1)$$

Η εξίσωση (1) εισάγει δύο τυχαίες μεταβλητές διεπαφής, τη λεγόμενη παράμετρο μηχανικής απαίτησης (EDP) και το μέτρο σεισμικής έντασης (IM) που σε αυτό το πλαίσιο θα θεωρηθούν και οι δύο βαθμωτές, για λόγους απλότητας. Οι άλλοι όροι που εμφανίζονται στην εξίσωση είναι: η ετήσια συχνότητα σεισμών που μπορούν να προκαλέσουν δομική αστοχία, ο ρυθμός υπέρβασης μιας ορισμένης τιμής ενός IM εδαφικής κίνησης, δηλαδή η δεσμευμένη πιθανότητα ότι η δομική απόκριση δεδομένου συγκεκριμένου επιπέδου σεισμικής έντασης, υπερβαίνει το όριο του στόχου επιτελεστικότητας, edp_f και $P\left[EDP > edp_f \left| IM = im \right. \right]$ είναι η *σεισμική τρωτότητα*. Το EDP είναι ένας γενικός όρος που χρησιμοποιείται για οποιοδήποτε μέτρο δομικής απόκρισης που μπορεί να χρησιμοποιηθεί για να ελεγχθεί ή να προσδιοριστεί εάν η κατασκευή δεν έχει επιτύχει έναν δεδομένο στόχο επιτελεστικότητας λόγω, για παράδειγμα, υπερβολικής τάσης ή παραμόρφωσης. Παραδείγματα EDP που χρησιμοποιούνται συχνά για κτιριακές κατασκευές είναι ο ανηγμένος λόγος μετατόπισης μεταξύ ορόφων ή στο ύψος της οροφής. Σε αυτό το πλαίσιο, η αστοχία μπορεί να εκφραστεί ως η υπέρβαση μιας προκαθορισμένης τιμής EDP κατωφλίου. Από την άλλη πλευρά, ένα IM μπορεί να είναι κάποια ενόργανη μέτρηση του πλάτους της εδαφικής κίνησης, όπως η μέγιστη επιτάχυνση εδάφους (PGA), ή μια ποσότητα

ελαστικής απόκρισης, όπως η φασματική ψευδο-επιτάχυνση σε διάφορες περιόδους, . Ο όρος λ_{im} είναι ένα μέτρο της σεισμικής επικινδυνότητας σε μια συγκεκριμένη τοποθεσία και μπορεί να εκτιμηθεί μέσω πιθανολογικής ανάλυσης σεισμικής επικινδυνότητας και είναι η απόλυτη τιμή του διαφορικού του

Σύμφωνα με τη σύγχρονη προσέγγιση, η τρωτότητα μπορεί να αξιολογηθεί αναλυτικά μέσω διαφόρων διαδικασιών που όλες απαιτούν μη γραμμική δυναμική ανάλυση ενός δομικού αριθμητικού μοντέλου που υπόκειται σε ένα σύνολο εδαφικών κινήσεων, επιλεγμένο σύμφωνα με την σεισμική επικινδυνότητα της τοποθεσίας [2]. Η ανάλυση στοχεύει στη δημιουργία ενός επαρκούς δείγματος δομικής απόκρισης που ανταποκρίνεται στο δείγμα των εδαφικών κινήσεων.

Τα κύρια μειονεκτήματα του υπολογισμού της σεισμικής τρωτότητας με βάση τη δυναμική ανάλυση είναι η υπολογιστική επιβάρυνση και η προσπάθεια που πρέπει να καταβληθεί για την προσομοίωση της έντονα μη γραμμικής δομικής συμπεριφοράς. Ο συνδυασμός της πολυπλοκότητας του αριθμητικού μοντέλου, του απαιτούμενου αριθμού αναλύσεων και της ανάγκης για περίπλοκη εκ των υστέρων επεξεργασία αποτελεσμάτων μπορεί να σημαίνει τέτοιες απαιτήσεις σε ανθρώπινους και υπολογιστικούς πόρους που οι μηχανικοί έχουν ισχυρά κίνητρα να αναζητήσουν απλούστερες, προσεγγιστικές εναλλακτικές λύσεις. Η πιο αξιοσημείωτη εναλλακτική απλούστευση, η οποία χρησιμοποιείται στα πλαίσια του PBEE με διάφορες μορφές σχεδόν εξ αρχής, περιλαμβάνει την προσφυγή σε ένα ισοδύναμο μη γραμμικό σύστημα ενός βαθμού ελευθερίας (*single degree of freedom* - SDOF). Ένα βασικό σημείο σε αυτήν την προσέγγιση είναι η αντιστοίχιση ενός καταστατικού νόμου δύναμης-παραμόρφωσης που διέπει την απόκριση του SDOF συστήματος υπό μονοτονική πλευρική φόρτιση, που συνήθως αναφέρεται ως καμπύλη-σκελετός ή ραχοκοκαλιά. Ο ορισμός αυτής της ραχοκοκαλιάς βασίζεται συνήθως στην (αριθμητικά-αξιολογημένη) απόκριση της αρχικής κατασκευής πολλαπλών βαθμών ελευθερίας (MDOF) σε ένα προοδευτικά αυξανόμενο προφίλ πλευρικής δύναμης, γνωστό ως καμπύλη υπερωθητικής ανάλυσης (*static pushover curve* - SPO). Λόγω της προσεγγιστικής φύσης τους, οι μέθοδοι που βασίζονται σε SPO έχουν περιορισμούς που έχουν τεκμηριωθεί και συζητηθεί εκτενώς στη βιβλιογραφία (π.χ., [3,4]). Το άλλο βασικό σημείο που είναι κοινό μεταξύ των μεθόδων που βασίζονται σε SPO είναι ο υπολογισμός της σεισμικής ζήτησης του

ισοδύναμου συστήματος SDOF και η επακόλουθη εκτίμηση της σεισμικής ζήτησης της αρχικής κατασκευής MDOF (π.χ. [5]).

Όπως αναφέρθηκε προηγουμένως, η αξιολόγηση της σεισμική τρωτότητας βασίζεται συχνά στα αποτελέσματα της μη γραμμικής δυναμικής ανάλυσης ενός σύνθετου ή απλοποιημένου αριθμητικού προσομοιώματος, το οποίο υποβάλλεται σε ένα σύνολο εδαφικών κινήσεων, προκειμένου να καταγραφεί η μεταξύ καταγραφών μεταβλητότητα της δομικής απόκρισης (π.χ., [6,7]). Έτσι, όταν η πιθανότητα αστοχίας μιας κατασκευής, για δεδομένη σεισμική ένταση, συνάγεται από ένα σύνολο (δείγμα) δομικών αποκρίσεων από δυναμική ανάλυση, αυτό αποτελεί μόνο μια βάσει δείγματος εκτίμηση της σεισμική τρωτότητας.

Κατά συνέπεια, οποιοσδήποτε υπολογισμός σεισμικής διακινδύνευσης που υπολογίζεται με βάση αυτήν την τρωτότητα, όπως η ετήσια συχνότητα αστοχίας, είναι επίσης μια εκτίμηση, η οποία θα αναφέρεται εφεξής ως $\hat{\lambda}_f$, της άγνωστης πραγματικής τιμής λ_f. Με άλλα λόγια, οποιοδήποτε πιθανολογικό μοντέλο για τη σεισμική τρωτότητα που βασίζεται σε ένα πεπερασμένο δείγμα δομικών αποκρίσεων, θα επηρεαστεί από την αβεβαιότητα εκτίμησης και αυτή η αβεβαιότητα θα μεταδοθεί στον εκτιμητή του ποσοστού αστοχίας $\hat{\lambda}_f$ (π.χ., [8]).

Προηγούμενη έρευνα προσανατολισμένη στο PBEE σχετικά με το θέμα έχει συζητηθεί σχετικά με τον αριθμό των εγγραφών που θα έπρεπε να χρησιμοποιηθούν για την εκτίμηση της κατανομής των EDP σε ένα μόνο επίπεδο (ή λωρίδα) έντασης [2,6].

Η επίδραση της αβεβαιότητας εκτίμησης στην παραμετρική τρωτότητα διερευνήθηκε και σε ορισμένες από αυτές τις προηγούμενες μελέτες που εξέτασαν την αβεβαιότητα εκτίμησης για τις παραμέτρους τρωτότητας (e.g., [9,10]) Αναγνωρίστηκε ότι χρειαζόταν περαιτέρω έρευνα για τη διερεύνηση της επίδρασης αυτής της αβεβαιότητας στο πραγματικό τελικό αποτέλεσμα. δηλαδή η εκτίμηση του ποσοστού αστοχίας.

Στο πλαίσιο αυτό, η παρούσα διπλωματική εργασία επικεντρώνεται στην επίτευξη των παρακάτω διακριτών στόχων:

- παροχή εργαλείων και μεθοδολογιών για την αξιολόγηση της λειτουργίας σεισμική τρωτότητα μέσω απλοποιημένων μέσων προσεγγίσεων που βασίζονται σε pushover;

- να παρέχει επιχειρησιακά εργαλεία για την ποσοτικοποίηση της αβεβαιότητας εκτίμησης πίσω από εκτιμήσεις σεισμική διακινδύνευση λόγω της μεταβλητότητας της δομικής απόκρισης από αρχείο σε αρχείο;
- να διερευνήσει την επιλογή του αριθμού των εγγραφών που θα χρησιμοποιηθούν για δυναμική ανάλυση για την επίτευξη μετρήσιμων επιπέδων μέσου σχετικού σφάλματος εκτίμησης στις μετρήσεις σεισμικής επικινδυνότητας;
- να διερευνήσει τη χρήση των παραμετρικών σεισμική τρωτότητα στο πλαίσιο ενός ιταλικού ερευνητικού έργου (RINTC, [11]) που εξέτασε κτίρια σχεδιασμένα με κώδικα που ανήκουν σε διαφορετικές δομικές τυπολογίες.

2 ΕΚΤΙΜΗΣΗ ΣΕΙΣΜΙΚΗΣ ΤΡΩΤΟΤΗΤΑΣ ΜΕΣΩ ΣΤΑΤΙΚΗΣ ΚΑΙ ΔΥΝΑΜΙΚΗΣ ΜΗ-ΓΡΑΜΜΙΚΗΣ ΑΝΑΛΥΣΗΣ: ΕΦΑΡΜΟΓΗ ΣΤΑ ΛΟΓΙΣΜΙΚΑ SPO2FRAG ΚΑΙ DYANAS

Οι μέθοδοι που χρησιμοποιούνται για την εξαγωγή συναρτήσεων τρωτότητας μπορούν να ταξινομηθούν ως εμπειρικές, αναλυτικές ή υβριδικές. Τα τελευταία χρόνια έχει δοθεί έμφαση στην αναλυτική προσέγγιση, η οποία βασίζεται σε αριθμητικά μοντέλα, ειδικά για συναρτήσεις τρωτότητας για κτίρια. Οι σύγχρονες αναλυτικές μέθοδοι βασίζονται σε προηγμένα αριθμητικά μοντέλα της κατασκευής που υποβάλλονται σε μη γραμμικές δυναμικές αναλύσεις. Ένα κλασικό παράδειγμα τέτοιας ανάλυσης είναι η αυξητική δυναμική ανάλυση (IDA, [12]), που συνεπάγεται πολλαπλασιασμό των καταγραφών επιτάχυνσης σε αυξανόμενα επίπεδα έντασης (όπως μετράται από το επιλεγμένο IM) και εκτίμηση της δομικής απόκρισης σε κάθε τέτοιο επίπεδο. Στην πραγματικότητα, επειδή κανένα μονόβαθμο IM δεν διαθέτει τυπικά πλήρη επεξηγηματική ισχύ σε σχέση με τη δομική απόκριση, εμφανίζεται μεταβλητότητα της απόκρισης για δεδομένη σεισμική ένταση, που πρέπει να αποτυπωθεί. Έτσι, η IDA επιδιώκει να χαρτογραφήσει στατιστικά τη σεισμική δομική απόκριση, από τα πρώτα σημάδια μη γραμμικής ανελαστικής συμπεριφοράς μέχρι την τελική κατάρρευση. Οι προτεινόμενες επεκτάσεις αυτής της μεθοδολογίας δυναμικής ανάλυσης επιφυλάσσουν τη δυνατότητα να ληφθεί υπόψη η αβεβαιότητα στο ίδιο το αριθμητικό μοντέλο ([13–15]). Οι εναλλακτικές της IDA στρατηγικές δυναμικής ανάλυσης που

χρησιμοποιούνται για την εκτίμηση της δομικής τρωτότητας είναι η ανάλυση νέφους και η ανάλυση πολλαπλών λωρίδων (MSA) ([16–19]). Ως επέκταση της IDA, έχει προταθεί ένας άλλος τύπος δυναμικής ανάλυσης που ονομάζεται back-to-back IDA (B2B-IDA) [20] για την αξιολόγηση της δομικής απόκρισης για μια κατασκευή που είχε προηγουμένως υποστεί ζημίες και εξακολουθεί να μην έχει επισκευαστεί.

Όπως αναφέρθηκε προηγουμένως, τα κύρια μειονεκτήματα της εξαγωγής συναρτήσεων τρωτότητας με βάση τη δυναμική ανάλυση είναι ο χρόνος που καταναλώνεται για την εκτέλεση ανάλυσης και ο χρόνος και δεξιότητες που απαιτούνται από τον χρήστη για να προσομοιώσει τη μη-γραμμική δομική συμπεριφορά. Για αυτούς τους λόγους, η χρήση απλουστευμένων μεθόδων που καταφεύγουν σε μια καμπύλη ραχοκοκαλιάς ενός συστήματος SDOF που υπόκειται σε δυναμική ή στατική διέγερση έχει θεωρηθεί ως εναλλακτική προσέγγιση, με όλους τους σχετικούς περιορισμούς.

Κατά τη διάρκεια των ετών, οι ημι-εμπειρικές μέθοδοι που είναι διαθέσιμες για αυτόν τον υπολογισμό έχουν εξελιχθεί από τον κανόνα ίσης μετατόπισης σε εξισώσεις που σχετίζονται με τον λόγο αντοχής προς την πλαστιμότητα ανά περίοδο ταλαντωτή (συχνά συντομογραφούνται ως σχέσεις $R-\mu-T$, [21]) και τελικά στον αλγόριθμο στατικής προώθησης στο IDA (SPO2IDA) του [22]. Ενώ προηγούμενες προσεγγίσεις που βασίζονται σε ανελαστικά φάσματα επικεντρώνονταν στη μέση απόκριση ταλαντωτών SDOF με ελαστοπλαστικές ή διγραμμικές περιβάλλουσες μονότονης φόρτισης, το πιο πρόσφατο εργαλείο SPO2IDA έχει τη δυνατότητα να αντιμετωπίζει πιο περίπλοκες καμπύλες SPO και, το πιο σημαντικό, προσφέρει άμεσες εκτιμήσεις της διασποράς της δομικής απόκρισης. Αυτά τα δύο στοιχεία καθιστούν το SPO2IDA ιδιαίτερα κατάλληλο για εφαρμογή εντός του πλαισίου PBEE, καθώς διευκολύνει την αντιμετώπιση της αβεβαιότητας στη σεισμική δομική απόκριση για οριακές καταστάσεις που πλησιάζουν την κατάρρευση.

Μετά από μια επισκόπηση σχετικά με τις μεθόδους δυναμικής ανάλυσης και τις τελευταίες εξελίξεις στον αναλυτικό υπολογισμό συναρτήσεων τρωτότητας, αυτό το Κεφάλαιο εξετάζει διεξοδικά το λογισμικό SPO2FRAG (Εικόνα , για μία πρώιμη έκδοση του λογισμικού βλέπε και [23]), μια εφαρμογή κωδικοποιημένη σε περιβάλλον MATLAB® που επιτρέπει την ταχεία εκτίμηση καμπυλών σεισμικής τρωτότητας για κτίρια, με βάση τα αποτελέσματα της ανάλυσης SPO. Ο αλγόριθμος SPO2IDA βρίσκεται στον πυρήνα του SPO2FRAG, επιτρέποντας στην εφαρμογή να προσομοιώνει τα αποτελέσματα

της IDA χωρίς να εκτελεί πολυάριθμες, περίπλοκες αναλύσεις. Το ιστορικό πίσω από το SPO2FRAG παρουσιάζεται εν συντομία, προκειμένου να τονιστεί η σύνδεση μεταξύ του πλαισίου της PBEE και της λειτουργικότητας του προγράμματος. Η ενότητα είναι αφιερωμένη στη λεπτομερή περιγραφή του ίδιου του προγράμματος, που εξετάζει τις διάφορες υπορουτίνες που αποτελούν το SPO2FRAG, τις εσωτερικές λειτουργίες, τη μεθοδολογία και το διάγραμμα ροής, καθώς και τις διάφορες επιλογές που είναι διαθέσιμες στον χρήστη.

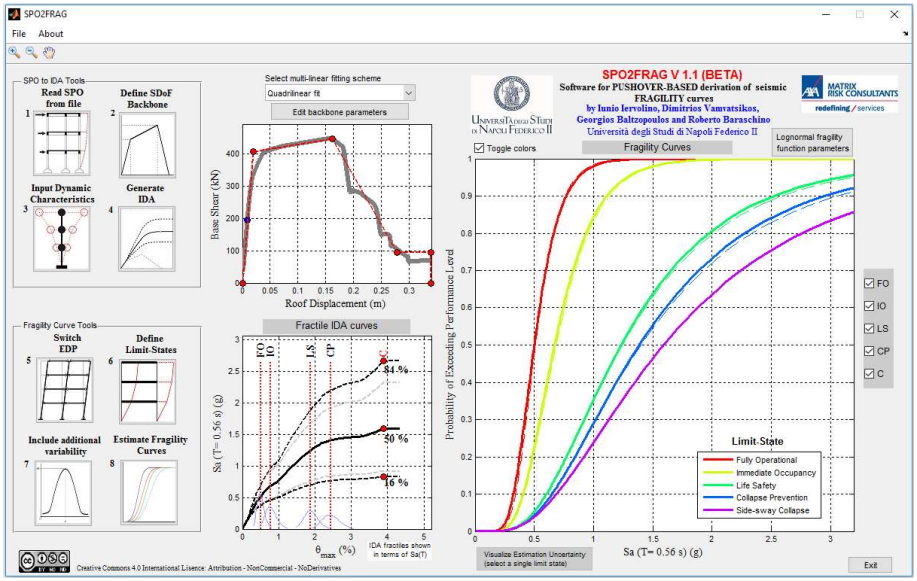

Εικόνα 1. Κυρίως γραφικό περιβάλλον SPO2FRAG που εμφανίζει μια ολοκληρωμένη επεξεργασία του υπολογισμού της καμπύλης τρωτότητας.

Αν και η χρήση των συστημάτων SDOF αρχικά είχε ως κίνητρο την έλλειψη υπολογιστικών πόρων για την εκτέλεση δυναμικής ανάλυσης μεγαλύτερων αριθμητικών μοντέλων, τα τελευταία χρόνια η τάση παραμένει - αλλά για διαφορετικούς λόγους. Η πρόοδος στο PBEE και στην ανάλυση σεισμικής διακινδύνευσης (βλέπε π.χ. [24]) έχει αναδείξει την ανάγκη για μια επαρκή πιθανολογική αναπαράσταση της ανελαστικής συμπεριφοράς των κατασκευών κατά τη διέγερση από σεισμό. Λόγω της εγγενώς στοχαστικής φύσης αυτού του φαινομένου, μια τέτοια πιθανολογική περιγραφή με αναλυτικά μέσα μπορεί να απαιτεί έναν τεράστιο αριθμό δυναμικών αναλύσεων. Για το λόγο αυτό, μέθοδοι που χρησιμοποιούν προσεγγίσεις δομικών συστημάτων σε

επίπεδο SDOF έχουν διατηρηθεί δεόντως στο οπλοστάσιο του PBEE και συνέχισαν να υποβάλλονται σε βελτίωση και ανάπτυξη.

Κοιτάζοντας πίσω, η δυναμική απόκριση των μονοβάθμιων ταλαντωτών υπό επιτάχυνση βάσης βρισκόταν στο προσκήνιο της σεισμικής έρευνας από τα πρώτα της βήματα [25] και παρέμεινε εκεί καθ' όλη τη διάρκεια της εξέλιξής της, καθώς εμφανίστηκαν απλουστευμένες μέθοδοι σεισμικής εκτίμησης και σχεδιασμού κτιρίων που βασίζονταν στην ανάλυση pushover για τον καθορισμό μιας ισοδύναμης, υποκατάστατης μονοβάθμιας κατασκευής [21,26–31]. Τα πιο πρόσφατα χρόνια, με το πλαίσιο PBEE να αποκτά μια ολοένα πιο σταθερή βάση στην κοινότητα της αντισεισμικής μηχανικής, νέες μέθοδοι βασισμένες σε μονοβάθμιους ταλαντωτές άρχισαν να εμφανίζονται ([22,32]). Άλλες μελέτες χρησιμοποίησαν την απόκριση ανελαστικών μονοβάθμιων ταλαντωτών ως μέτρο σεισμικής έντασης [33] και για τη μελέτη των συνήθων πρακτικών επιλογής και τροποποίησης εγγραφών εδαφικής κίνησης για τη διεξαγωγή δυναμικής ανάλυσης χρονοϊστορίας [34,35].

Μερικά από τα ζητήματα που διαπερνούν όλες τις προαναφερθείσες περιπτώσεις είναι: το σχήμα της καμπύλης δύναμης-μετατόπισης του μονοβάθμιου συστήματος, ο υστερητικός νόμος που ακολουθεί κατά τη διάρκεια της κυκλικής φόρτισης και η πιθανή παρουσία κυκλικής υποβάθμισης αντοχής ή/και ακαμψίας στην υστέρηση. Η σχέση δύναμης-μετατόπισης που περιγράφει την απόκριση στη μονοτονική στατική φόρτιση, δηλ. η λεγόμενη και καμπύλη κορμού ή ραχοκοκαλιά, είναι τυπικά μια εξιδανίκευση της καμπύλης pushover που υπολογίζεται για την αντίστοιχη κατασκευή. Αυτή η εξιδανίκευση μπορεί να είναι ένα απλό διγραμμικό σχήμα ή μπορεί επίσης να περιλαμβάνει έναν κλάδο φθίνουσας αρνητικής ακαμψίας και ακόμη και ένα πλατό υπολειπόμενης αντοχής. Η εμφάνιση αρνητικής ακαμψίας μπορεί να οφείλεται σε φαινόμενα P-Δ ή σε απώλεια αντοχής του υλικού (συχνά και τα δύο) και η σημασία της αναπαράστασής της στην αντίστοιχη ραχοκοκαλιά του μονοβάθμιου συστήματος έχει υποστηριχθεί έντονα από προηγούμενη έρευνα [36,37].

Όσον αφορά στην υστερητική συμπεριφορά που θα έπρεπε να χαρακτηρίζει ένα υποκατάστατο σύστημα SDOF προκειμένου να αντιπροσωπεύει καλύτερα την συνολική απόκριση της αντίστοιχης κατασκευής, υπήρξε μια στροφή στη σύγχρονη πρακτική προς τη χρήση φαινομενολογικών κανόνων υστέρησης ([38]) που είναι πιο αντιπροσωπευτικοί της πραγματικής δομικής συμπεριφοράς. Υπάρχουν διάφορες προτάσεις στη βιβλιογραφία σχετικά με

αυτό, τυπικά βασισμένες σε πειραματικά δεδομένα που αναφέρονται σε συγκεκριμένες δομικές τυπολογίες: αναφέρονται, για παράδειγμα, οι μελέτες των Takeda et al. για οπλισμένο σκυρόδεμα[39], Graziotti et al. για μη οπλισμένη τοιχοποιία [40] και Lignos και Krawinkler για μεταλλικές κατασκευές [41]. Συνήθως, το ίδιο μοντέλο που χρησιμοποιείται για την αριθμητική προσομοίωση μιας κατασκευής σε επίπεδο στοιχείου (ειδικά σε περιπτώσεις προσομοίωσης συγκεντρωμένης πλαστικότητας) εκχωρείται επίσης στον ισοδύναμο μονοβάθμιο ταλαντωτή της κατασκευής. Ωστόσο, θα πρέπει να σημειωθεί ότι, στην περίπτωση της παραμετρικής φαινομενολογικής προσομοίωσης των επιδράσεων κυκλικής υποβάθμισης, η βαθμονόμηση πειραματικού μοντέλου σε επίπεδο δομικού στοιχείου μπορεί να μην είναι επαρκώς αντιπροσωπευτική της συνολικής συμπεριφοράς ολόκληρης της κατασκευής και μπορεί να απαιτείται ειδική μελέτη ([42]).

Επίσης, στο κεφάλαιο αυτό εισάγεται και ένα δεύτερο λογισμικό προσανατολισμένο στη σεισμική μηχανική: το πρόγραμμα DYANAS (Εικόνα 2), ένα γραφικό περιβάλλον (GUI) MATLAB που διευκολύνει τον καθορισμό μονοβάθμιων ανελαστικών συστημάτων στην πλατφόρμα πεπερασμένων στοιχείων OpenSees (Open System for Earthquake Engineering Simulation; [43]) βελτιστοποιεί την εκτέλεση δυναμικών αναλύσεων χρονοϊστορίας και επιτρέπει τη μεθοδική επεξεργασία των τελικών αποτελεσμάτων. Οι μέθοδοι ανάλυσης και οι επιλογές μετέπειτα επεξεργασίας των αποτελεσμάτων, επικεντρώνονται στη διευκόλυνση μεθόδων δυναμικής ανάλυσης που χρησιμοποιούνται συχνά στα πλαίσια του PBEE.

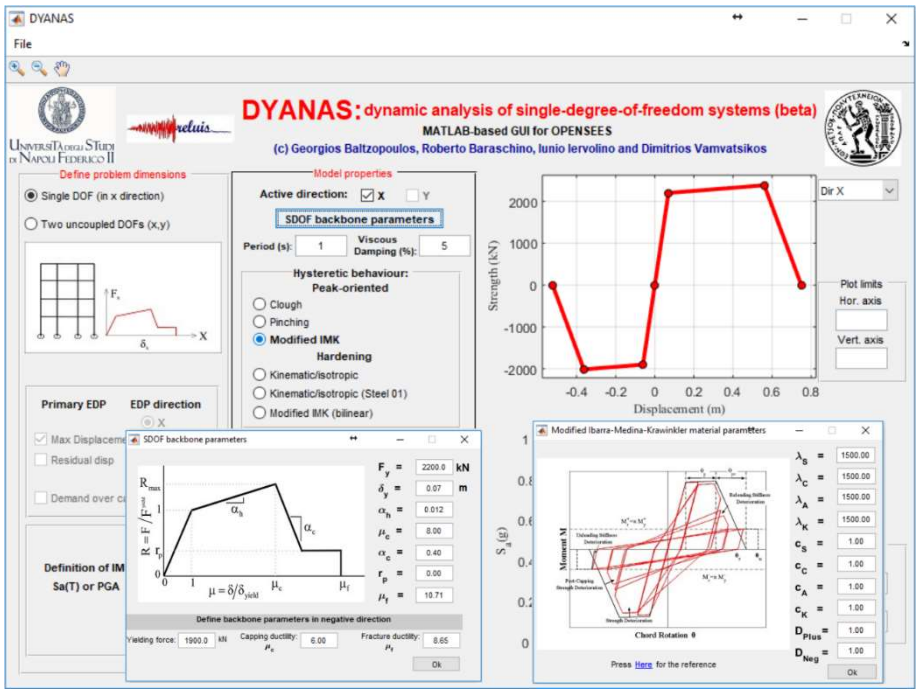

Εικόνα 2. Κύριο παράθυρο GUI και δευτερεύοντα παράθυρα διαλόγου κατά τον καθορισμό των δυναμικών χαρακτηριστικών ενός μονοβάθμιου ταλαντωτή, της καμπύλης κορμού (ασύμμετρη σε αυτήν την περίπτωση) και του υστερητικού μοντέλου.

Τα στοιχεία γραφικής διαδραστικότητας του λογισμικού με το χρήστη εκτελούνται σε περιβάλλον MATLAB. Η αλληλεπίδραση με το OpenSees πραγματοποιείται με χειρισμό αρχείων Tcl/Tk (μια γενική γλώσσα δέσμης ενεργειών που έχει επεκταθεί με εντολές ειδικά για το OpenSees; [44]) μέσω συναρτήσεων MATLAB, σε μια διαδικασία που περιγράφεται στο κείμενο της ενότητας. Το OpenSees είναι μια ανοιχτή πλατφόρμα πεπερασμένων στοιχείων που αναπτύχθηκε για το PBEE. Από την έναρξή του, το OpenSees έχει δει εκτεταμένη χρήση για αριθμητική ανάλυση σε δομικά, γεωτεχνικά και σεισμικά προβλήματα αξιοπιστίας ([45]). Στο παρελθόν, διάφορα GUI έχουν δημιουργηθεί γύρω από το OpenSees, με σκοπό να διευκολύνουν τον ορισμό αριθμητικών μοντέλων και την επακόλουθη εκτέλεση αναλύσεων. Τέτοια παραδείγματα είναι το λογισμικό Build-X [46] και η εφαρμογή GID [47] που προορίζονται και τα δύο για να βοηθήσουν τον ορισμό μοντέλων κτιρίων πολλαπλών βαθμών ελευθερίας, καθώς και η διαδικτυακή πλατφόρμα των Dolšek et al. [48] και η διαδραστική εφαρμογή II-DAP [49] που λειτουργούν

σε επίπεδο μονοβάθμιων ταλαντωτών. Το DYANAS είναι μια νέα προσθήκη σε αυτήν τη λίστα και είναι, κατά κύριο λόγο, ένα εργαλείο PBEE που ενσωματώνει ένα πλήθος λειτουργιών προσανατολισμένων στην αποτελεσματική σεισμική ανάλυση απλών κατασκευών ([50]). Το DYANAS επιτρέπει στους χρήστες να ορίζουν εύκολα ανελαστικούς μονοβάθμιους ταλαντωτές με κλασική ιξώδη απόσβεση, κατά τμήματα γραμμικές περιβάλλουσες μονότονης φόρτισης και μια επιλογή από έξι εξελικτικούς ή κρατυνόμενους υστερητικούς νόμους που έχουν ήδη εφαρμοστεί στο OpenSees. Στη συνέχεια, το GUI δίνει στους χρήστες την ευκαιρία να εκτελούν μη γραμμικές δυναμικές αναλύσεις με μεγάλο αριθμό επιταχυνσιομετρικών καταγραφών, υποστηρίζοντας IDA, ανάλυση πολλαπλών λωρίδων, ανάλυση cloud και B2B-IDA. Για κάθε συνεδρία ανάλυσης, οι χρήστες μπορούν να ορίσουν έναν ή δύο μη συζευγμένους ταλαντωτές SDOF. Στην τελευταία περίπτωση, αυτά μπορούν να εκτελεστούν ταυτόχρονα, χρησιμοποιώντας εγγραφές εδαφικής κίνησης δύο συνιστωσών. Τέλος, το λογισμικό έχει τη δυνατότητα να επεξεργάζεται αποτελέσματα, να τα αναπαριστά γραφικά για τους χρήστες και επιτρέπει την εξαγωγή αρχείων δεδομένων για περαιτέρω επεξεργασία.

3 ΕΚΤΙΜΗΣΗ ΑΒΕΒΑΙΟΤΗΤΑΣ ΣΤΗ ΣΕΙΣΜΙΚΉ ΔΙΑΚΙΝΔΥΝΕΥΣΗ: ΛΟΓΙΣΜΙΚΟ R2R-EU

Υπενθυμίζοντας ότι και οι δύο όροι στο ολοκλήρωμα της Εξίσωση (1), μπορούν να επηρεαστούν από τη λεγόμενη αβεβαιότητα εκτίμησης, καθώς και οι δύο συναρτήσεις πρέπει να εκτιμηθούν αναλυτικά βάσει πεπερασμένων τυχαίων δειγμάτων απόκρισης. Αυτό το κεφάλαιο ασχολείται κυρίως με την αβεβαιότητα εκτίμησης που επηρεάζει τη συνάρτηση τρωτότητας και στο επίκεντρο αυτού του κεφαλαίου βρίσκεται η παρουσίαση του λογισμικού PBEE R2R-EU (record-to-record estimation uncertainty) (Εικόνα 3), το οποίο αναπτύχθηκε σε περιβάλλον MATLAB® με διττό σκοπό: (i) εκτίμηση της σεισμικής τρωτότητας της κατασκευής, με βάση τη δυναμική ανάλυση, και (ii) ποσοτικοποίηση της αβεβαιότητας εκτίμησης, που προέρχεται ειδικά από τη διασπορά της σεισμικής δομικής απόκρισης από ένα επιταχυνσιογράφημα σε αλλο, και ο βαθμός στον οποίο αυτή η αβεβαιότητα μεταδίδεται στην ποσοτικοποίηση της σεισμικής διακινδύνευσης, όπως για παράδειγμα στην ετήσια συχνότητα αστοχίας. Το λογισμικό R2R-EU εξετάζει διάφορες στρατηγικές μη γραμμικής ανάλυσης που χρησιμοποιούνται στο PBEE, όπως

ανάλυση IDA, MSA ή νέφους, η τελευταία εντός πλαισίου της μεθόδου Cornell [51]. Το λογισμικό προσφέρει πολλές εναλλακτικές μεθόδους για τον ορισμό της συνάρτησης τρωτότητας και εφαρμόζει μια σειρά στατιστικών μεθόδων που βασίζονται σε επαναδειγματοληψία ή/και προσομοίωση και αναφέρονται διεθνώς υπό τον όρο bootstrap [52], στη μέθοδο *delta* [53] και στην άμεση εφαρμογή τύπων γνωστών από τη στατιστική θεωρία για συγκεκριμένες κατανομές.

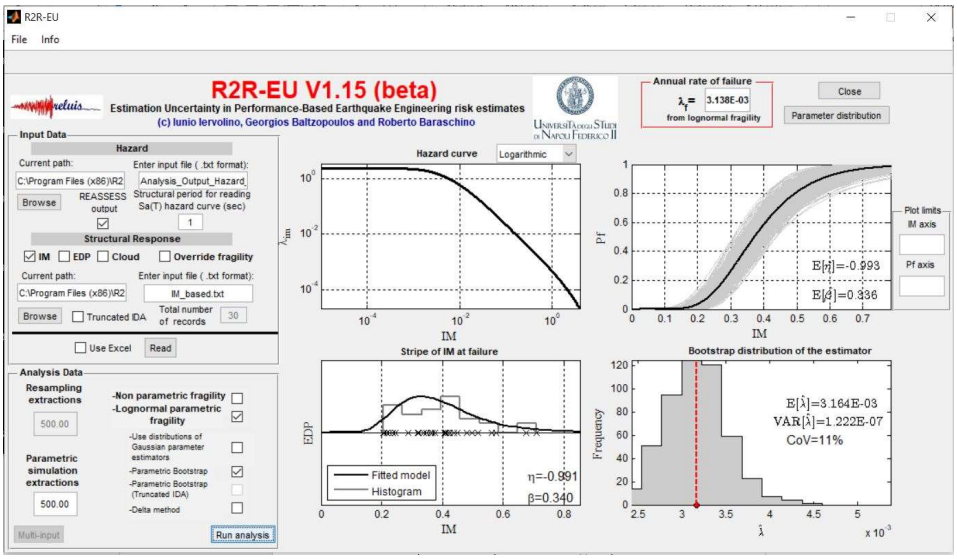

Εικόνα 3. Γραφικό περιβάλλον του λογισμικού R2R-EU

Το εργαλείο R2R-EU ασχολείται με τον καθορισμό της σεισμικής τρωτότητας της κατασκευής και με την ποσοτικοποίηση της αβεβαιότητας εκτίμησης που εμπεριέχει η συχνότητα αστοχίας, τουλάχιστον όσον αφορά στο τμήμα της που μπορεί να αποδοθεί στη διασπορά της σεισμικής απόκρισης μεταξύ καταγραφών διέγερσης. Με τα αποτελέσματα της δυναμικής ανάλυσης ως δεδομένα, η στρατηγική για την αναλυτική αποτίμηση μιας συνάρτησης τρωτότητας συχνά καταλήγει σε μία από δύο προσεγγίσεις: την προσέγγιση που βασίζεται στη σεισμική ένταση IM και την προσέγγιση που βασίζεται στις αποκρίσεις EDP. Και στις δύο περιπτώσεις, οι δύο παράμετροι $\{\eta, \beta\}$ είναι γενικά άγνωστες και ένας τρόπος για να ληφθούν σημειακές εκτιμήσεις αυτών των παραμέτρων, είναι η χρήση του (τυχαίου) δείγματος αποκρίσεων που προκύπτουν από την ανάλυση. Όπως τονίστηκε, για παράδειγμα στο [8], εφόσον η σεισμική τρωτότητα και επικινδυνότητα συνάγονται από δείγματα,

είναι απλώς εκτιμήσεις των αντίστοιχων πραγματικών τιμών και επομένως επηρεάζονται από την αβεβαιότητα εκτίμησης. Στην πραγματικότητα, ο εκτιμητής του λ_f, που δηλώνεται ως $\hat{\lambda}_f$, και που εκτιμάται χρησιμοποιώντας ένα συγκεκριμένο τυχαίο δείγμα σεισμικών αποκρίσεων, μπορεί να θεωρηθεί τυχαία μεταβλητή εξαρτώμενη του δείγματος. Αν κάποιος επαναλάμβανε τον υπολογισμό χρησιμοποιώντας διαφορετικά σετ επιταχυνσιογραφημάτων, καθόλα ισοδύναμα με το αρχικό, θα λάμβανε διαφορετικές τιμές συχνότητας αστοχίας κάθε φορά.

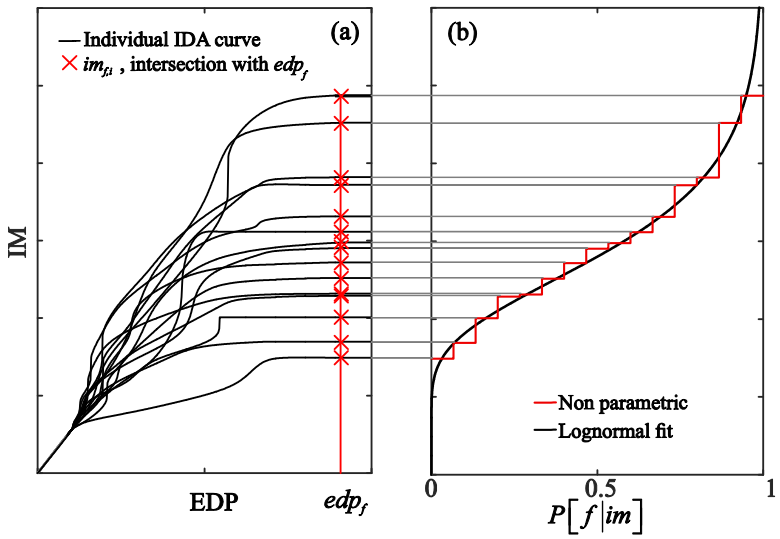

Εικόνα 4. Σχηματική αναπαράσταση εκτίμησης σεισμικής τρωτότητας μέσω επαυξητικής δυναμικής ανάλυσης.

Ένας ευρέως χρησιμοποιούμενος τρόπος έκφρασης της σεισμικής τρωτότητας παρέχεται από τη λεγόμενη προσέγγιση βασισμένη στη σεισμική ένταση. Η τρωτότητα που βασίζεται σε IM συνεπάγεται την εισαγωγή μίας νέας τυχαίας μεταβλητής, IM_f που μπορεί να θεωρηθεί ως η σεισμική ένταση που μπορεί να προκαλέσει δομική αστοχία [54].

Με αυτόν τον ορισμό, η τρωτότητα μπορεί να εκφραστεί ως η συμπληρωματική αθροιστική συνάρτηση κατανομής του IM_f. Επιστρέφοντας στο παράδειγμα της IDA, μπορεί κανείς να αποκτήσει τη χαμηλότερη τιμή IM που, για κάθε επιταχυνσιογράφημα, προκαλεί το να φτάσει η κατασκευή στην αστοχία, βρίσκοντας το ύψος $im_{f,i}$, $i=\{1,2,\ldots,n\}$, όπου η i-οστή καμπύλη

IDA τέμνει την κατακόρυφη γραμμή $EDP = edp_f$, όπως φαίνεται στο σχήμα. Αυτές $im_{f,i}$ οι τιμές μπορούν να θεωρηθούν ως ένα τυχαίο δείγμα της μεταβλητής IM_f . Στη συνέχεια, μπορούν να χρησιμοποιηθούν κοινές στατιστικές μέθοδοι για την προσαρμογή ενός παραμετρικού μοντέλου κατανομής πιθανοτήτων στο δείγμα, όπως το λογαριθμικό κανονικό μοντέλο που φαίνεται ως μαύρη γραμμή στην Εικόνα 4b; Εναλλακτικά, μπορεί κανείς ακόμη και να υποθέσει ότι οι παρατηρούμενες τιμές του δείγματος προσεγγίζουν την τρωτότητα με μη παραμετρικό τρόπο, που απεικονίζεται επίσης στο Εικόνα 4b ως βαθμηδόν αύξουσα συνάρτηση. Ωστόσο, εάν κάποιος επαναλάμβανε τη διαδικασία πολλές φορές, εκτελώντας κάθε φορά IDA με διαφορετικό σύνολο εγγραφών, είναι αναμενόμενο ότι κάθε επανάληψη θα οδηγεί σε διαφορετική καμπύλη τρωτότητας. Αυτή η μεταβλητότητα θα αντανακλάται στη συνέχεια στην εκτιμώμενη συχνότητα αστοχίας μέσω της Εξίσωσης (1), και μπορεί να ληφθεί ένα ποσοτικό μέτρο σύμφωνα με την Εξίσωση (2):

$$CoV_{\hat{\lambda}_f} = \frac{\sqrt{VAR\left[\hat{\lambda}_f\right]}}{E\left[\hat{\lambda}_f\right]}, \quad (2)$$

όπου ο συμβολισμός $CoV_{\hat{\lambda}_f}$ υποδεικνύει τον συντελεστή μεταβλητότητας του εκτιμητή της συχνότητας αστοχίας, και $VAR\left[\hat{\lambda}_f\right]$, $E\left[\hat{\lambda}_f\right]$ δηλώνουν τη διακύμανση και την αναμενόμενη τιμή του, αντίστοιχα. Στην πραγματικότητα, στην περίπτωση αμερόληπτων εκτιμητών, $CoV_{\hat{\lambda}_f}$ παρέχει το μέσο σχετικό σφάλμα εκτίμησης.

Ο Πίνακας 1 δείχνει τις προσεγγίσεις που εφαρμόζονται στο R2R-EU για την αξιολόγηση των καμπυλών τρωτότητας και τις μεθόδους για την ποσοτικοποίηση της αβεβαιότητας εκτίμησης. Επιτρέπουν επίσης την ποσοτικοποίηση της αβεβαιότητας εκτίμησης στο ποσοστό αστοχίας, που χρησιμοποιείται σε συνδυασμό με μεθοδολογίες στατιστικών συμπερασμάτων. Αυτές οι μεθοδολογίες, που συνοψίζονται στον πίνακα και εν μέρει συζητούνται στο [8], είναι: παραμετρικό ή μη-παραμετρικό bootstrap, η εφαρμογή θεωρητικών αποτελεσμάτων για την κανονική κατανομή και η

μέθοδος δέλτα, η οποία βασίζεται στην ανάπτυξη σε σειρά Taylor, είτε του ολοκληρώματος υπολογισμού της σεισμικής διακινδύνευσης, είτε της κλειστής λύσης από τη μέθοδο σεισμικής αξιοπιστίας του Cornell.

Πίνακας 1. Μεθοδολογίες που εφαρμόζονται στο λογισμικό R2R-EU για την ποσοτικοποίηση της αβεβαιότητας εκτίμησης.

Τυχαία μεταβλητή	*Δυναμική ανάλυση*	*Μοντέλο τρωτότητας*	*Μέθοδος ποσοτικοποίησης της αβεβαιότητας εκτίμησης*
IM-based	IDA	Lognormal	Parametric bootstrap, probability theory, Delta method
		Non-Parametric	Bootstrap (resampling)
EDP-based	IDA/MSA	Lognormal	Parametric bootstrap
		Τρι-παραμετρικό μοντέλο Shome & Cornell [55]	Bootstrap (resampling)
		Normal probability paper	Bootstrap (resampling)
		Least squares fit	Bootstrap (resampling)
	Cloud	-	Delta method for Cornell's method

4 ΣΧΕΤΙΚΑ ΜΕ ΤΟΝ ΑΠΑΙΤΟΥΜΕΝΟ ΑΡΙΘΜΟ ΚΑΤΑΓΡΑΦΩΝ ΣΕΙΣΜΙΚΗΣ ΚΙΝΗΣΗΣ ΣΤΗΝ ΕΚΤΙΜΗΣΗ ΤΗΣ ΣΕΙΣΜΙΚΗΣ ΔΙΑΚΙΝΔΥΝΕΥΣΗΣ: ΕΦΑΡΜΟΓΗ ΤΗΣ ΣΤΑΤΙΣΤΙΚΗΣ ΘΕΩΡΙΑΣ ΣΤΗ ΣΕΙΣΜΙΚΗ ΜΗΧΑΝΙΚΗ

Ο αριθμός των εγγραφών που χρησιμοποιούνται συνήθως για μη γραμμική δυναμική ανάλυση υπαγορεύεται κυρίως από τους μεγάλους χρόνους υπολογισμού που απαιτούνται για την εκτέλεση πολύπλοκων δομικών μοντέλων σε υψηλά επίπεδα μη γραμμικότητας. Ωστόσο, ο αριθμός των εγγραφών καθορίζει άμεσα το μέγεθος δείγματος δομικής απόκρισης που θα χρησιμοποιηθεί για την εκτίμηση της τρωτότητας και, τελικά, του ποσοστού αστοχίας

Προηγούμενη έρευνα για το θέμα, προσανατολισμένη στο PBEE, έχει συζητήσει τον αριθμό των καταγραφών σεισμικής κίνησης που θα έπρεπε να χρησιμοποιηθούν για την εκτίμηση της κατανομής των EDP σε ένα μόνο επίπεδο (ή λωρίδα) έντασης [2,6]. Στο [9] εξετάστηκε η αβεβαιότητα εκτίμησης γύρω από την παραμετρική τρωτότητα για απλουστευμένα δομικά συστήματα, ενώ [10] εξετάστηκε η επίδραση του μεγέθους δείγματος σεισμικών αποκρίσεων στα διαστήματα εμπιστοσύνης διαφόρων παραμέτρων συναρτήσεων τρωτότητας. Η επίδραση της αβεβαιότητας εκτίμησης στο παραμετρικό μοντέλο τρωτότητας που προκύπτει από την ανάλυση νέφους εξετάστηκε στο [19]. Σε ορισμένες από αυτές τις προηγούμενες μελέτες που εξέτασαν την αβεβαιότητα εκτίμησης για τις παραμέτρους τρωτότητας (π.χ., [9,10]) αναγνωρίστηκε ότι χρειαζόταν περαιτέρω έρευνα για να διερευνηθεί η επίδραση αυτής της αβεβαιότητας στο πραγματικό τελικό αποτέλεσμα, δηλαδή την εκτίμηση της σεισμικής επικινδυνότητας.

Ο στόχος αυτού του Κεφαλαίου είναι να διερευνήσει περαιτέρω το ζήτημα του αριθμού των καταγραφών εδαφικής κίνησης που απαιτείται να χρησιμοποιηθούν σε εφαρμογές αντισεισμικής μηχανικής και να παρουσιάσει μεθοδολογίες που να μπορούν να εφαρμοστούν ως εργαλεία για τη λήψη τεκμηριωμένων αποφάσεων σχετικά με τον απαιτούμενο αριθμό των επιταχυνσιογραφημάτων, προκειμένου να επιτευχθεί μια δεδομένη αποδεκτή τιμή του $CoV_{\hat{\lambda}_f}$. Δύο διακριτές διαδρομές ακολουθούνται παράλληλα για να επιτευχθεί αυτός ο στόχος: μια αναλυτική προσέγγιση που βασίζεται στη μέθοδο αξιοπιστίας Cornell [51] και μια υπολογιστική προσέγγιση βασισμένη στην IDA. Στην πρώτη περίπτωση, διερευνώνται ορισμένες πρόσθετες απλουστεύσεις, οι οποίες χρειάζονται για να καταστήσουν δυνατή μια έκφραση κλειστής μορφής για το $CoV_{\hat{\lambda}_f}$. Το αναλυτικό αποτέλεσμα στη συνέχεια αξιολογείται με τη βοήθεια ανάλυσης νέφους [54] που εφαρμόζεται για μερικούς μονοβάθμιους ανελαστικούς ταλαντωτές. Στην υπολογιστικά προσανατολισμένη περίπτωση, μια συλλέγεται μια σχετικά μεγάλη δεξαμενή επιταχυνσιογραφημάτων και χρησιμοποιείται για την εκτέλεση IDA για μια ποικιλία αντισεισμικά σχεδιασμένων πλαισίων. Σε αυτό το πλαίσιο, εξετάζονται διάφορες οριακές καταστάσεις και εναλλακτικά IM. Με βάση αυτά τα αποτελέσματα των IDA, χρησιμοποιείται μια μεθοδολογία Monte-Carlo για την προσομοίωση της κατανομής πιθανότητας του εκτιμητή $\hat{\lambda}_f$, για ένα ευρύ φάσμα μεγεθών τυχαίου δείγματος αποκρίσεων.

Ως κύρια συμπεράσματα που μπορούν εξαχθούν από αυτή τη μελέτη, είναι πως η διασπορά των σεισμικών αποκρίσεων μας κατασκευής αποτελεί μόνο μέρος της ιστορίας, με το $CoV_{\hat{\lambda}_f}$ να εξαρτάται επίσης από το σχήμα του καμπύλη κινδύνου κάθε συγκεκριμένης τοποθεσίας. Το συμπέρασμα που απορρέει αυτού του ευρήματος είναι ότι για κατασκευές που βρίσκονται σε τοποθεσίες που χαρακτηρίζονται από διαφορετικά επίπεδα σεισμικότητας, ενδέχεται να απαιτούνται διαφορετικό αριθμό επιταχυνσιογραφημάτων για να επιτευχθεί το ίδιο επίπεδο εμπιστοσύνης στην εκτίμηση της σεισμικής διακινδύνευσης, ακόμη και στην περίπτωση παρόμοιων κατασκευών που αναμένεται να εμφανίσουν την ίδια ετήσια συχνότητα αστοχίας. Η επίδραση της επικινδυνότητας στο $CoV_{\hat{\lambda}_f}$ μπορεί να συνοψιστεί από την κλίση της καμπύλης κοντά στα επίπεδα έντασης που είναι πιο σημαντικά για την πρόκληση αστοχίας: όσο πιο απότομη είναι η τοπική κλίση της καμπύλης τόσο μεγαλύτερη είναι η αβεβαιότητα εκτίμησης πίσω από το $\hat{\lambda}_f$.

Το δεύτερο μέρος του κεφαλαίου διερευνά το ζήτημα του αριθμού των επιταχυνσιογραφημάτων, συμβατών με το φάσμα σχεδιασμού που χρησιμοποιείται για δυναμική ανάλυση, όταν ο στόχος είναι η εκτίμηση της μέσης ανελαστικής απόκρισης. Η εξέταση των ληφθέντων δομικών αποκρίσεων αποκάλυψε ότι οι τα στατιστικά μεγέθη της απόκρισης ως συνάρτηση του μεγέθους του δείγματος δεν συμπεριφέρθηκαν όπως αναμενόταν για τυχαία δείγματα, δηλαδή, οι σεισμικές αποκρίσεις δεν φαινόταν να είναι ανεξάρτητες και να ακολουθούν την ίδια κατανομή. Αυτό συνεπάγεται ότι ο καθορισμός του αριθμού των επιταχυνσιογραφημάτων που θα χρησιμοποιηθούν για δυναμική ανάλυση μέσω στατιστικών παραμέτρων όπως το τυπικό σφάλμα εκτίμησης, μπορεί να είναι κατάλληλος στην περίπτωση της απλής τυχαίας δειγματοληψίας, αλλά να είναι ακατάλληλος στο πλαίσιο επιλογής καταγραφών συμβατών με το φάσμα σχεδιασμού. Με άλλα λόγια, μπορεί να είναι εκ προοιμίου ακατάλληλη η επίκληση της αβεβαιότητας εκτίμησης, όταν πρόκειται για επιλογή επιταχυνσιογραφημάτων βάσει φιλοσοφίας των αντισεισμικών κανονισμών.

5 ΣΕΙΣΜΙΚΉ ΤΡΩΤΟΤΗΤΑ ΚΤΙΡΙΩΝ ΑΝΤΙΣΕΙΣΜΙΚΑ ΣΧΕΔΙΑΣΜΕΝΩΝ ΜΕΣΩ ΔΥΝΑΜΙΚΗΣ ΑΝΑΛΥΣΗΣ ΠΟΛΛΑΠΛΩΝ ΛΩΡΙΔΩΝ

Στον ισχύοντα ιταλικό οικοδομικό κανονισμό (NTC [56,57]), ο οποίος είναι παρόμοιος με τον Eurocode 8 ή EC8 [58], η επιτελεστικότητα των κατασκευών πρέπει να επαληθεύεται για τις σεισμικές δράσεις (βλέπε ένταση εδαφικής κίνησης) με συγκεκριμένες περιόδους επαναφοράς (T_R) υπέρβασης στην τοποθεσία ενδιαφέροντος, οι οποίες εξαρτώνται από τις οριακές καταστάσεις αστοχίας που λαμβάνονται υπόψη για το σχεδιασμό. Σε περίπτωση συνηθισμένων κατασκευών, για παράδειγμα γραφείων ή κατοικιών, απαιτούνται έλεγχοι ασφάλειας έναντι περιορισμού ζημιών και έναντι οριακής κατάστασης ασφάλειας της ζωής έναντι επιπέδων έντασης εδαφικής κίνησης που αντιστοιχούν σε T_R 50 και 475 έτη, αντίστοιχα. Ωστόσο, η σεισμική δομική αξιοπιστία που προκύπτει από το σχεδιασμό, δηλαδή την ετήσια συχνότητα των σεισμών που οδηγούν σε δομική αστοχία, δεν ελέγχεται ρητά αν και οι σεισμικές δράσεις σχεδιασμού έχουν πιθανολογικό προσδιορισμό.

Για να αντιμετωπιστεί ποσοτικά η σεισμική διακινδύνευση στην οποία εκθέτει τις κατασκευές ο σχεδιασμός που συμμορφώνεται με τον κανονισμό, ένα μεγάλο ερευνητικό έργο πραγματοποιήθηκε στην Ιταλία μεταξύ 2015 και 2017. Στο έργο, με το όνομα *Rischio Implicito – Norme Tecniche per le Costruzioni* [59], κτιριακές κατασκευές που ανήκουν σε μια ποικιλία δομικών τύπων, όπως μη-οπλισμένη τοιχοποιία (URM), οπλισμένο σκυρόδεμα (RC), προκατασκευασμένο σκυρόδεμα (PRC), δομικό χάλυβα (S) και σεισμικά μονωμένα κτίρια από οπλισμένο σκυρόδεμα (BI), σχεδιάστηκαν σύμφωνα με το NTC για έναν αριθμό τοποθεσιών που διαθέτουν διαφορετικά επίπεδα σεισμικής επικινδυνότητας (Μιλάνο, Νάπολη και Λάκουϊλα) και τοπικές εδαφικές συνθήκες (A και C σύμφωνα με την ταξινόμηση EC8). Τα κτίρια προορίζονται για κατοικία και βιομηχανική χρήση και, για κάθε τυπολογία, εξετάστηκαν διάφορες αρχιτεκτονικές/δομικές διαμορφώσεις [60].

Η σεισμική δομική αξιοπιστία των σχεδιασμένων κατασκευών εκτιμήθηκε ως προς τη μέση ετήσια συχνότητα αστοχία έναντι κατάρρευσης και έναντι χρηστικότητας μέσω αποτροπής ζημιών. Οι συχνότητες υπολογίστηκαν εντός του πλαισίου PBEE, που ενσωματώνει τη σεισμική τρωτότητα και την καμπύλη επικινδυνότητας για την τοποθεσία σχεδιασμού. Η τρωτότητα

υπολογίστηκε για ορισμένα επίπεδα IM μέσω μη γραμμικής δυναμικής ανάλυσης χρησιμοποιώντας τρισδιάστατα (3D) δομικά αριθμητικά προσομοιώματα.

Στην πραγματικότητα, στο ερευνητικό έργο RINTC η τρωτότητα υπολογίστηκε μόνο ως μεμονωμένες πιθανότητες αστοχίας σε δέκα επίπεδα IM, και δεν υπολογίστηκαν καμπύλες τρωτότητας, καθώς δεν χρειάζονται απαραίτητα για τον υπολογισμό των συχνοτήτων αστοχίας [11]. Από την άλλη πλευρά, οι παραμετρικές καμπύλες τρωτότητας των διαφόρων κτιρίων που σχεδιάστηκαν, προσομοιώθηκαν και αναλύθηκαν στο ερευνητικό πρόγραμμα RINTC μπορούν να είναι χρήσιμες για περαιτέρω μελέτες εκτίμησης διακινδύνευσης. Αυτό αποτέλεσε κίνητρο για τη μελέτη που παρουσιάζεται εδώ, όπου παρέχονται οι καμπύλες σεισμικής τρωτότητας για τα μοντέλα που ανήκουν στις πέντε δομικές τυπολογίες και στα δύο κριτήρια αστοχίας που διερευνήθηκαν στο πρόγραμμα.

Μεταξύ της ποικιλίας προσεγγίσεων για την εξαγωγή μιας συνάρτησης τρωτότητας, η μελέτη που παρουσιάζεται εδώ εστιάζει στις λεγόμενες αναλυτικές συναρτήσεις τρωτότητας που αναπτύχθηκαν μέσω μη γραμμικής δυναμικής ανάλυσης τρισδιάστατων μοντέλων. Ειδικότερα, τα αποτελέσματα του MSA (π.χ., [17]), χρησιμοποιώντας σύνολα καταγραφών εδαφικής κίνησης επιλεγμένα με βάσει την τοπική σεισμική επικινδυνότητα, θεωρείται ότι μπορούν να αντικατασταθούν από λογαριθμοκανονικές καμπύλες τρωτότητας για τις κατασκευές του RINTC σε όλες τις τοποθεσίες στις οποίες αναφέρεται ο σχεδιασμός. Οι καμπύλες υπολογίζονται λαμβάνοντας υπόψη μια ποικιλία διαδικασιών ικανών να διαχειριστούν τις αριθμητικές αστάθειες που προκύπτουν από τη μη γραμμική δυναμική ανάλυση ή/και τις περιπτώσεις τοποθεσιών χαμηλής επικινδυνότητας, όπου σπάνια παρατηρούνται αστοχίες. Επιπλέον, αντιμετωπίζεται η αβεβαιότητα στην εκτίμηση των παραμέτρων τρωτότητας [8], που προκύπτει από τη διασπορά της σεισμικής απόκρισης μεταξύ επιταχυνσιογραφημάτων.

Μετά από μια σύντομη παρουσίαση των αποτελεσμάτων του ερευνητικού έργου RINTC, παρουσιάζονται οι καμπύλες τρωτότητας και συζητούνται σε σχέση με τα ζητήματα που προκύπτουν κατά την εξαγωγή τους και κυρίως ανάλογα με την επικινδυνότητα των τοποθεσιών. Ως επαλήθευση των καμπυλών τρωτότητας, οι συχνότητες αστοχίας που υπολογίζονται μέσω των προσαρμοσμένων καμπυλών συγκρίνονται με τα αρχικά αποτελέσματα και οι

διαφορές τους εξηγούνται ποσοτικά. Τα σχήματα που αντιπροσωπεύουν τις λογαριθμικές ευθραυστότητες φαίνονται από την Εικόνα 5 έως την Εικόνα 9.

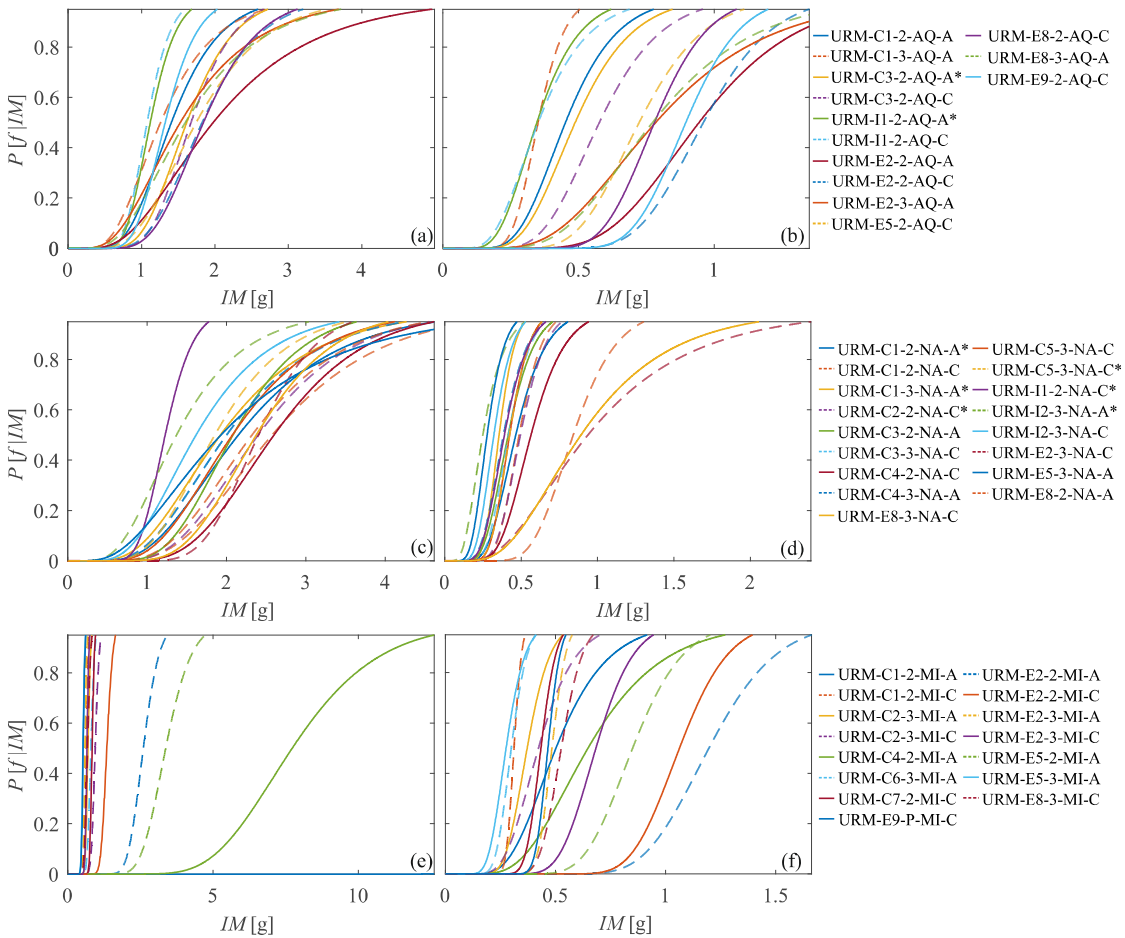

Εικόνα 5. σεισμική τρωτότητα για κτίρια URM. Τα σχήματα δείχνουν καμπύλες για L'Aquila (a,b), Naples (c,d) και Milan (e,f) στο GC και στο UPD αντίστοιχα.

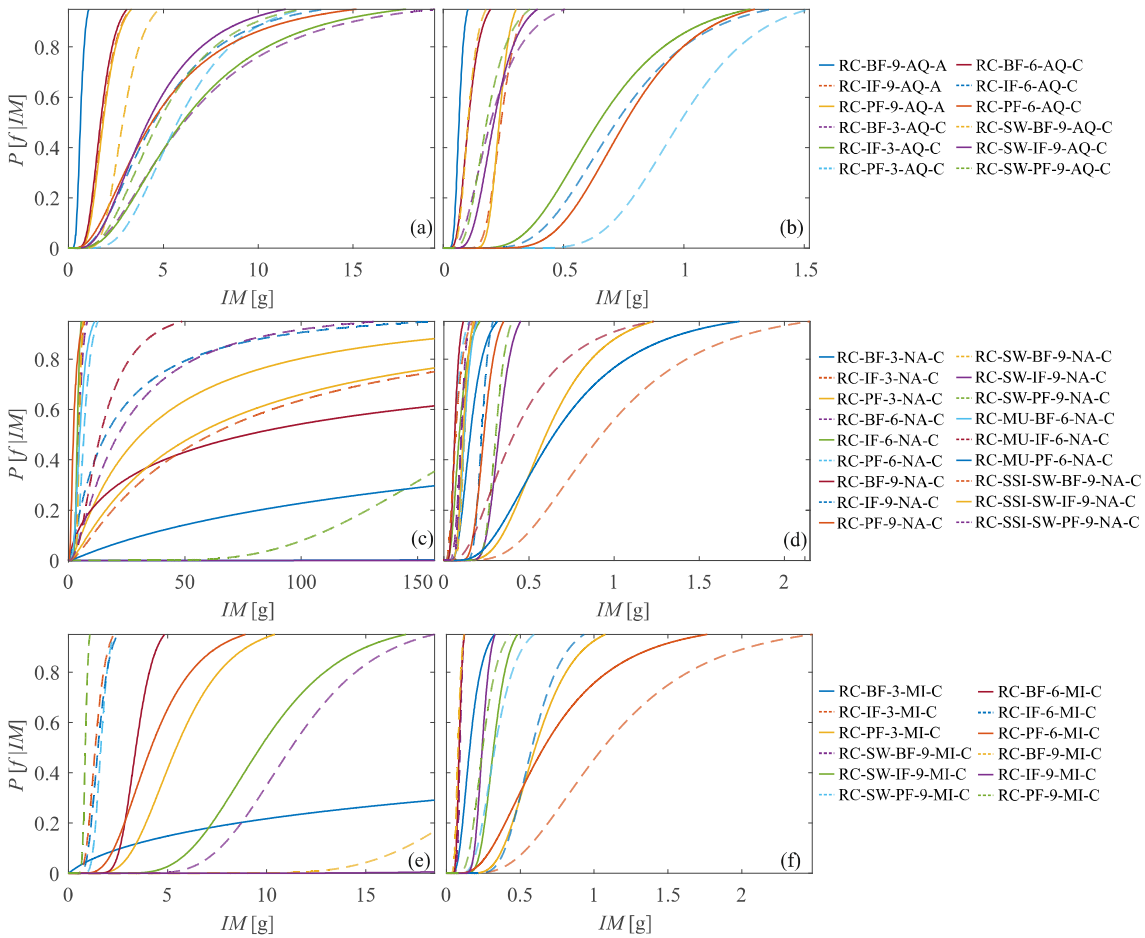

Εικόνα 6. σεισμική τρωτότητα για κτίρια RC. Τα σχήματα δείχνουν καμπύλες για L'Aquila (a,b), Naples (c,d) και Milan (e,f) στο GC και στο UPD αντίστοιχα.

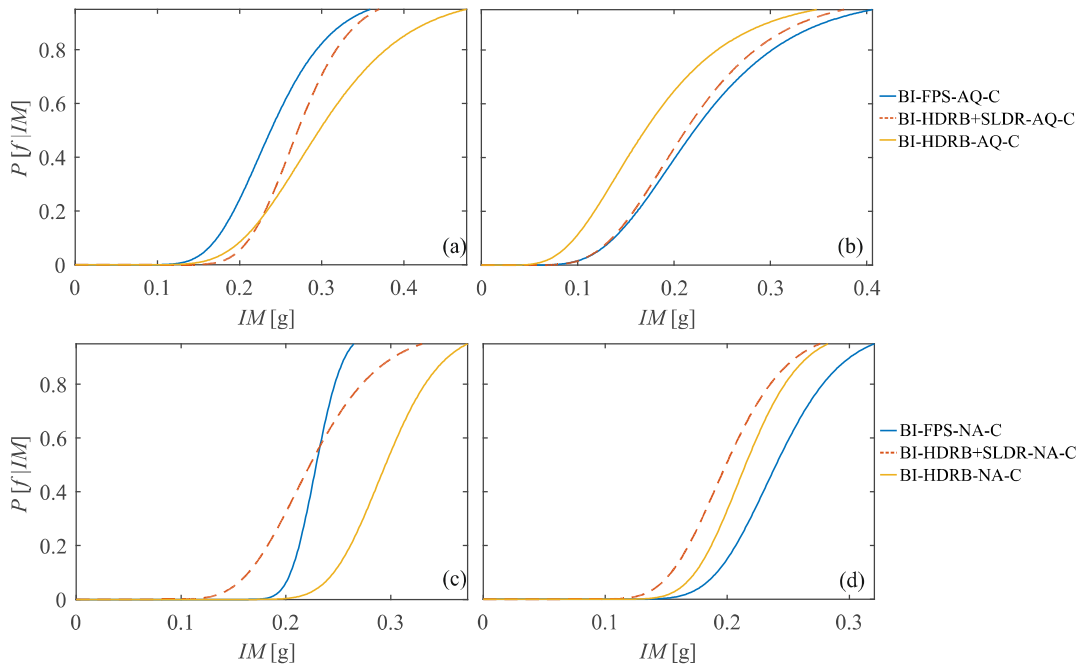

Εικόνα 7. σεισμική τρωτότητα για κτίρια BI. Τα σχήματα δείχνουν καμπύλες για L'Aquila (a,b), Naples (c,d) και Milan (e,f) στο GC και στο UPD αντίστοιχα.

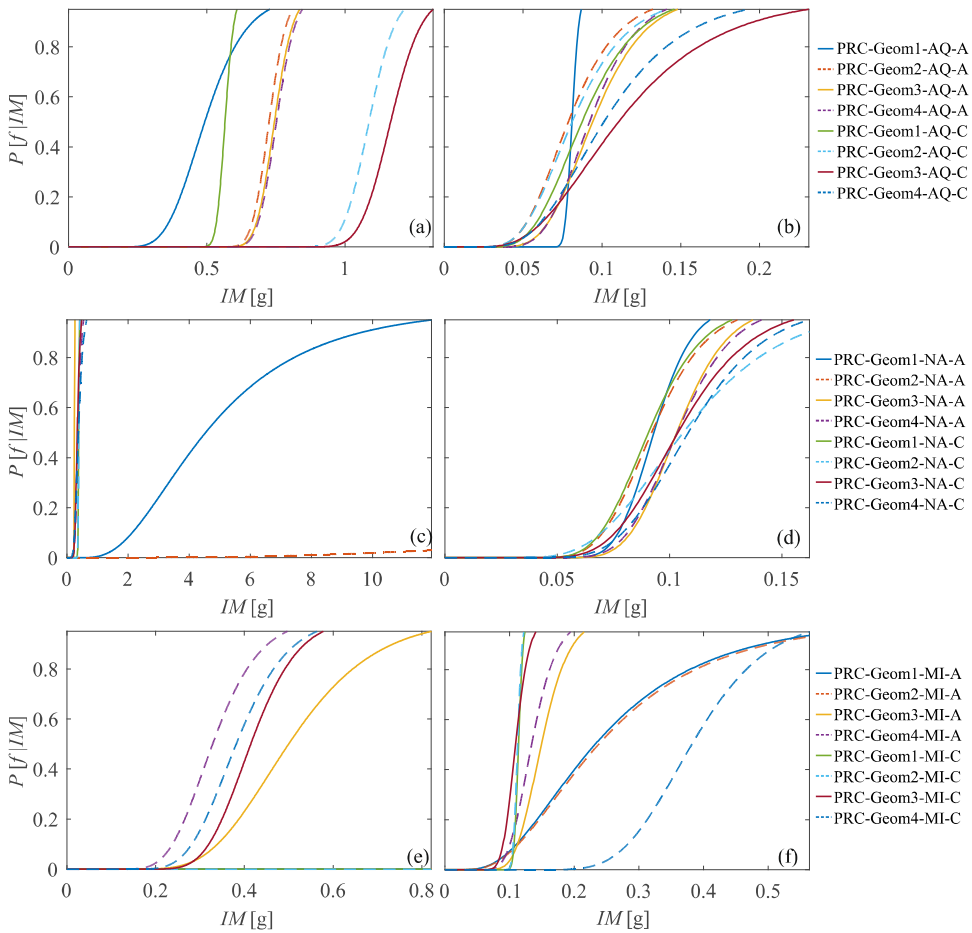

Εικόνα 8. σεισμική τρωτότητα για κτίρια PRC. Τα σχήματα δείχνουν καμπύλες για L'Aquila (a,b), Naples (c,d) και Milan (e,f) στο GC και στο UPD αντίστοιχα.

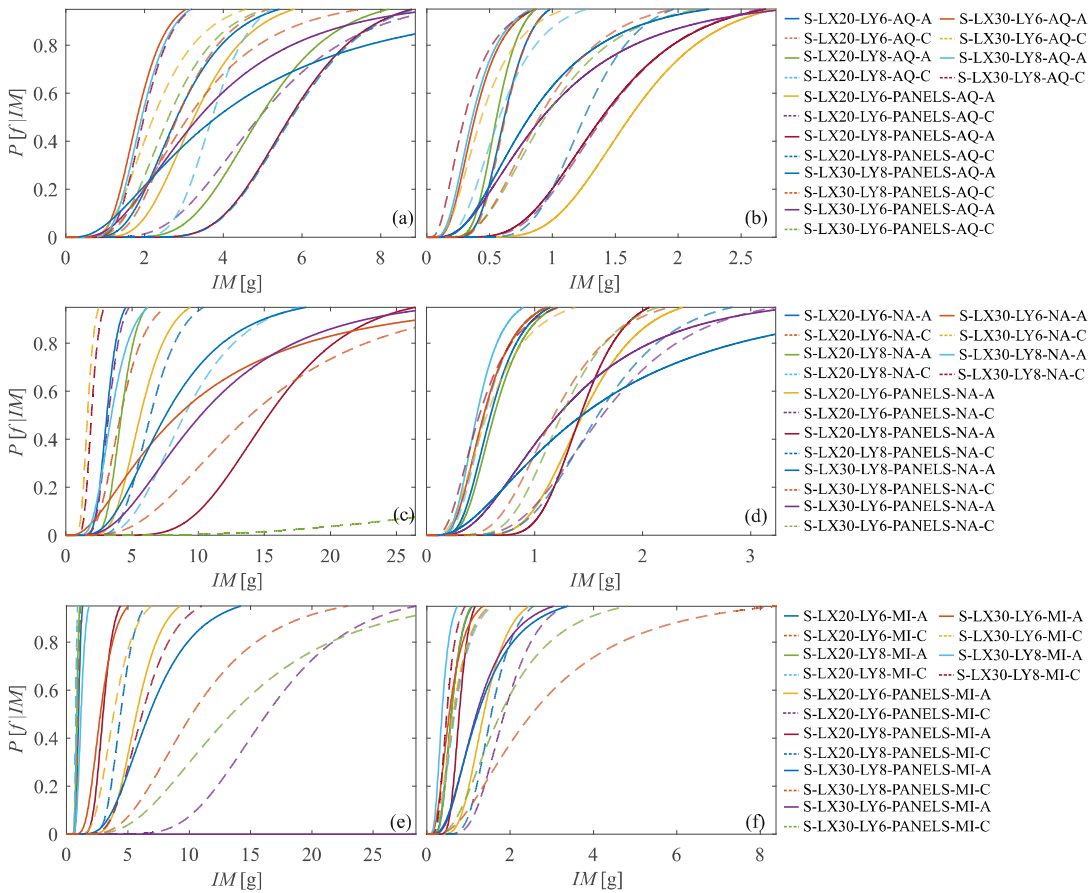

Εικόνα 9. σεισμική τρωτότητα για κτίρια steel. Τα σχήματα δείχνουν καμπύλες για L'Aquila (a,b), Naples (c,d) και Milan (e,f) στο GC και στο UPD αντίστοιχα

6 ΒΙΒΛΙΟΓΡΑΦΙΑ

[1] Cornell CA, Krawinkler H. Progress and Challenges in Seismic Performance Assessment. PEER Cent News 2000;3:1–4.

[2] Cornell CA. Hazard, ground motions and probabilistic assessment for PBSD. vol. 23. 2004.

[3] Krawinkler H, Seneviratna GDPK. Pros and cons analysis of seismic evaluation. Eng Struct 1998;20:452–64. https://doi.org/10.1016/S0141-0296(97)00092-8.

[4] Fragiadakis M, Vamvatsikos D, Aschheim M. Application of nonlinear static procedures for the seismic assessment of regular RC moment frame buildings. Earthq Spectra 2014;30:767–94. https://doi.org/10.1193/111511EQS281M.

[5] Fajfar P. A Nonlinear Analysis Method for Performance-Based Seismic Design. Earthq Spectra 2000;16:573–92. https://doi.org/10.1193/1.1586128.

[6] Shome N, Cornell CA, Bazzurro P, Carballo JE. Earthquakes, records, and nonlinear responses. Earthq Spectra 1998;14:469–500. https://doi.org/10.1193/1.1586011.

[7] Shome N, Cornell CA. Probabilistic seismic demand analysis of nonlinear structures. Reliability of marine structures program technical report RMS-35. Stanford University 1999.

[8] Iervolino I. Assessing uncertainty in estimation of seismic response for PBEE. Earthq Eng Struct Dyn 2017;46:1711–23. https://doi.org/10.1002/eqe.2883.

[9] Gehl P, Douglas J, Seyedi DM. Influence of the number of dynamic analyses on the accuracy of structural response estimates. Earthq Spectra 2015;31. https://doi.org/10.1193/102912EQS320M.

[10] Eads L, Miranda E, Krawinkler H, Lignos DG. An efficient method for estimating the collapse risk of structures in seismic regions. Earthq Eng Struct Dyn 2013;42:25–41. https://doi.org/10.1002/eqe.2191.

[11] Iervolino I, Spillatura A, Bazzurro P. Seismic Reliability of Code-Conforming Italian Buildings. J Earthq Eng 2018. https://doi.org/10.1080/13632469.2018.1540372.

[12] Vamvatsikos D, Allin Cornell C. Incremental dynamic analysis. Earthq Eng Struct Dyn 2002;31:491–514. https://doi.org/10.1002/eqe.141.

[13] Dolsek M. Incremental dynamic analysis with consideration of modeling uncertainties. Earthq Eng Struct Dyn 2009;38:805–25. https://doi.org/10.1002/eqe.869.

[14] Vamvatsikos D, Fragiadakis M. Incremental dynamic analysis for estimating seismic performance sensitivity and uncertainty. Earthq Eng Struct Dyn 2010;39:141–63.

[15] Vamvatsikos D. Seismic Performance Uncertainty Estimation via IDA with Progressive Accelerogram-Wise Latin Hypercube Sampling. J Struct Eng 2014;140:A4014015. https://doi.org/10.1061/(ASCE)ST.1943-541X.0001030.

[16] Bazzurro P, Cornell CA, Shome N, Carballo JE. Three proposals for characterizing MDOF nonlinear seismic response. J Struct Eng 1998. https://doi.org/10.1061/(ASCE)0733-9445(1998)124:11(1281).

[17] Jalayer F, Cornell CA. A Technical Framework for Probability-Based Demand and Capacity Factor Design (DCFD) Seismic Formats. PEER Rep 2003/8 2003:122.

[18] Jalayer F, Cornell CA. Alternative non-linear demand estimation methods for probability-based seismic assessments. Earthq Eng Struct Dyn 2009;38:951–72. https://doi.org/10.1002/eqe.876.

[19] Jalayer F, De Risi R, Manfredi G. Bayesian Cloud Analysis: Efficient structural fragility assessment using linear regression. Bull Earthq Eng 2015;13:1183–203. https://doi.org/10.1007/s10518-014-9692-z.

[20] Luco N, Bazzurro P, Cornell CA. Dynamic Versus Static Computation Of The Residual Capacity Of A Mainshock-damaged Building To Withstand An Aftershock. Proc 13th World Conf Earthq Eng Vancouver, Canada 2004.

[21] Vidic T, Fajfar P, Fischinger M. Consistent inelastic design spectra: Hysteretic and input energy. Earthq Eng Struct Dyn 1994;23:523–37. https://doi.org/10.1002/eqe.4290230505.

[22] Vamvatsikos D, Cornell CA. Direct estimation of the seismic demand and capacity of oscillators with multi-linear static pushovers through IDA. Earthq Eng Struct Dyn 2006;35:1097–117. https://doi.org/10.1002/eqe.573.

[23] Iervolino I, Baltzopoulos G, Vamvatsikos D, Baraschino R. SPO2FRAG V1.0: Software for pushover-based derivation of seismic fragility curves. ECCOMAS Congr. 2016 - Proc. 7th Eur. Congr. Comput. Methods Appl. Sci. Eng. Crete Island, Greece, 5–10 June, vol. 3, 2016, p. 5962–76. https://doi.org/10.7712/100016.2233.11553.

[24] Pinto PE, Giannini R, Franchin P. Seismic Reliability Analysis of Structures. 2004.

[25] Veletsos AS, Newmark NM, Chelapati C V. Deformation Spectra for Elastic and Elastoplastic Systems Subjected to Ground Shock and Earthquake Motions. Proc 3rdWorld Conf Earthq Eng 1965:663–82.

[26] Fajfar P, Gašperšič P. the N2 Method for the Seismic Damage Analysis of Rc Buildings. Earthq Eng Struct Dyn 1996;25:31–46. https://doi.org/10.1002/(SICI)1096-9845(199601)25:1<31::AID-EQE534>3.0.CO;2-V.

[27] Chopra AK, Goel RK. Capacity-demand-diagram methods based on inelastic design spectrum. Earthq Spectra 1999;15:637–55. https://doi.org/10.1193/1.1586065.

[28] Miranda E. Estimation of Inelastic Deformation Demands of SDOF Systems. J Struct Eng 2001;127:1005–12. https://doi.org/10.1061/(asce)0733-9445(2001)127:9(1005).

[29] FEMA. FEMA-440: improvement of nonlinear static seismic analysis procedures.

Prep by ATC FEMA, Washington, DC 2005.

[30] Priestley MJN, Calvi GM, Kowalsky MJ. Displacement-based seismic design of structures. Building 2007;23:1453–60. https://doi.org/10.1016/S0141-0296(01)00048-7.

[31] Guerrini G, Graziotti F, Penna A, Magenes G. Improved evaluation of inelastic displacement demands for short-period masonry structures. Earthq Eng Struct Dyn 2017;46:1411–30. https://doi.org/https://doi.org/10.1002/eqe.2862.

[32] Fragiadakis M, Vamvatsikos D. Fast performance uncertainty estimation via pushover and approximate IDA. Earthq Eng Struct Dyn 2010;39:683–703. https://doi.org/10.1002/eqe.965.

[33] Tothong P, Cornell CA. An empirical ground-motion attenuation relation for inelastic spectral displacement. Bull Seismol Soc Am 2006;96:2146–64. https://doi.org/10.1785/0120060018.

[34] Iervolino I, Cornell CA. Record selection for nonlinear seismic analysis of structures. Earthq Spectra 2005;21:685–713. https://doi.org/10.1193/1.1990199.

[35] Kwong NS, Chopra AK, Mcguire RK. A framework for the evaluation of ground motion selection and modification procedures. Earthq Eng Struct Dyn 2015;44:795–815. https://doi.org/10.1002/eqe.2502.

[36] Ibarra LF, Krawinkler H. Global collapse of frame structures under seismic excitations. 2005.

[37] Adam C, Jäger C. Seismic collapse capacity of basic inelastic structures vulnerable to the P-delta effect. Earthq Eng Struct Dyn 2012;41:775–93. https://doi.org/10.1002/eqe.1157.

[38] Ibarra LF, Medina RA, Krawinkler H. Hysteretic models that incorporate strength and stiffness deterioration. Earthq Eng Struct Dyn 2005;34:1489–511. https://doi.org/10.1002/eqe.495.

[39] Takeda T, Sozen MA, Nielsen NN. Reinforced Concrete Response to Simulated Earthquakes. J Struct Div 1970;96:2557–73. https://doi.org/10.1061/jsdeag.0002765.

[40] Graziotti F, Penna A, Magenes G. A nonlinear SDOF model for the simplified evaluation of the displacement demand of low-rise URM buildings. Bull Earthq Eng 2016;14:1589–612. https://doi.org/10.1007/s10518-016-9896-5.

[41] Lignos DG, Krawinkler H. Deterioration Modeling of Steel Components in Support of Collapse Prediction of Steel Moment Frames under Earthquake Loading. J Struct Eng 2011;137:1291–302. https://doi.org/10.1061/(ASCE)ST.1943-541X.0000376.

[42] Kampenhuber D, Adam C. Degradation parameter for equivalent SDOF systems obtained from cyclic pushover analysis and parameter optimisation. Proc. Second Eur. Conf. Earthq. Eng. Seismol. (2ECEES), Istanbul, Turkey, Aug, 2014, p. 24–9.

[43] McKenna F. OpenSees: A framework for earthquake engineering simulation. Comput Sci Eng 2011;13:58–66. https://doi.org/10.1109/MCSE.2011.66.

[44] Ousterhout JK, Jones K. Tcl and the Tk Toolkit. 2nd editio. Addison Wesley; 2009.

[45] Scott MH, Haukaas T. Modules in OpenSees for the next generation of performance-based engineering. 17th Anal Comput Spec Conf 2006;2006:26. https://doi.org/10.1061/40878(202)33.

[46] Psyrras NK, Sextos AG. Build-X: Expert system for seismic analysis and assessment of 3D buildings using OpenSees. Adv Eng Softw 2018;116:23–35. https://doi.org/10.1016/j.advengsoft.2017.11.007.

[47] Papanikolaou VK, Kartalis-Kaounis T, Protopapadakis VK, Papadopoulos T. GiD+ OpenSees interface: an integrated finite element analysis platform. Greece Lab R/C Mason Struct Aristotle Univ Thessaloniki 2017.

[48] Dolšek M, Šebenik Ž, Klinc R, Dolenc M, Brozovič M. Web Application for the Selection of Characteristic Ground Motions. 6th Int. Conf. Earthq. Geotech. Eng. Christcurch, New Zealand, 1-4 Novemb., 2015.

[49] Elkady A, Lignos DG. Interactive Interface for Dynamic Analysis Procedures (II-DAP): Version 1.0 Manual and Examples. 2018.

[50] Vamvatsikos D, Cornell CA. Applied incremental dynamic analysis. Earthq Spectra 2004;20:523–53. https://doi.org/10.1193/1.1737737.

[51] Cornell CA, Jalayer F, Hamburger RO, Foutch DA. Probabilistic Basis for 2000 SAC Federal Emergency Management Agency Steel Moment Frame Guidelines. J Struct Eng 2002;128:526–33. https://doi.org/10.1061/(ASCE)0733-9445(2002)128:4(526).

[52] Efron B. The Jackknife, the Bootstrap and Other Resampling Plans. Philadelphia, Pennsylvania: Society For Industrial And Applied Mathematics; 1982.

[53] Oehlert GW. A note on the delta method. Am Stat 1992;46:27–9. https://doi.org/10.1080/00031305.1992.10475842.

[54] Jalayer F, Cornell CA. Direct probabilistic seismic analysis: implementing non-linear dynamic assessments. Stanford University, 2003.

[55] Shome N, Cornell CA. Structural seismic demand analysis: Consideration of collapse. 8th ACSE Spec Conf Probabilistic Mech Struct Reliab 2000:PMC2000-119.

[56] CS.LL.PP. Norme tecniche per le costruzioni. Gazz Uff Della Repubb Ital 2008;29.

[57] CS.LL.PP. Aggiornamento delle Norme tecniche per le costruzioni. Gazz Uff Della Repubb Ital 2018;42.

[58] CEN. EN 1998-1 - Eurocode 8: design provisions for earthquake resistance of structures, Part 1: general rules, seismic actions and rules for buildings. European Committee for Standardization, Rue de Stassart, 36 B-1050 Brussels: 2004.

[59] RINTC-Workgroup. Results of the 2015-2017 implicit seismic risk of code-conforming structures in Italy (RINTC) project. ReLUIS Report, Rete Dei Lab Univ Di Ing Sismica (ReLUIS), Naples, Italy 2018.

[60] Iervolino I, Dolce M. Foreword to the Special Issue for the RINTC (The Implicit Seismic Risk of Code-Conforming Structures) Project. J Earthq Eng 2018. https://doi.org/10.1080/13632469.2018.1543697.

TABLE OF CONTENTS

LIST OF FIGURES

LIST OF TABLES

ABSTRACT

In the framework of performance-based earthquake engineering (PBEE) the most notable task is the problem of evaluating the rate of earthquakes leading a structure to fail in meeting a performance objective, that can be intended as a measure of seismic reliability. In one of its simplest forms this calculation includes two terms: the annual rate of earthquakes able to cause structural failure; the rate of exceeding a certain value of a ground motion intensity measure (IM); the conditional probability that structural response given a certain IM level, exceeds the performance objective threshold, the so-called *fragility function*. In the state-of-the-art approach, fragility can be analytically evaluated via several procedures that all require non-linear dynamic analysis of a structural numerical model subjected to set of ground motions. The main disadvantages of the dynamic-analysis-based derivation of fragility functions is the computational burden involved and the amount of effort that has to go into modelling highly non-linear structural behaviour so that engineers find themselves strongly motivated to look for approximate alternatives and for such reasons due tools have been developed. First one is SPO2FRAG, an application coded in MATLAB® environment that permits the computer-aided evaluation of seismic fragility functions for buildings, based on the results of static non-linear-analysis. Second tool is DYANAS, a MATHWORKS MATLAB®-based graphical user interface that expedites the definition of inelastic SDOF systems in the OpenSees finite element platform, streamlines the execution of dynamic analyses under suites of base-acceleration time histories and allows for methodical processing of the final results.

Both terms needed for seismic reliability assessment can be affected by so-called estimation uncertainty, since both functions have to be deduced from available and limited data. For such reason the tool R2R-EU was developed in MATLAB with a dual purpose: (i) estimating structure-specific seismic fragility, based on dynamic analysis, and (ii) quantifying estimation uncertainty, emanating specifically from record-to-record variability of seismic structural response, and the extent to which that uncertainty propagates unto risk metrics, such as the failure rate

Concept of estimation uncertainty has been then used to investigate the record sample size required to achieve quantifiable levels of mean relative estimation error on seismic risk metrics. The mean relative estimation error depends on both the dispersion of structural responses and the shape of the

hazard curve at the site, This dependence was shown to hold in the context of Cornell's reliability method and of fragility functions derived via the so-called intensity-based approach.

Finally, fragility curves were assessed for the buildings designed within the RINTC project. The study provides the seismic fragility curves for code-conforming Italian buildings analysed in the RITNC project. Lognormal fragilities refer to global collapse failure and usability preventing damage, which are the performances considered in the project, and are derived via state-of-the-art methods and include consideration of the uncertainty in the estimation of their parameters. The curves are made available to be possibly used for further risk analyses, and also enable a discussion of the fragility fitting issues as a function on the site's hazard.

Chapter 1 –INTRODUCTION

1.1 Background and motivations

In the framework of performance-based earthquake engineering (PBEE, [1]) the most notable task is the problem of evaluating the rate of earthquakes leading a structure to fail in meeting a performance objective (a situation often referred, in the framework of construction codes, to as *exceedance of a limit state*). This calculation, in one of its simplest forms, can be performed by an implementation of the total probability theorem:

$$\lambda_f = \int_{im} P\left[EDP > edp_f \,|IM = im \right] \cdot \left| d\lambda_{im} \right| . \qquad (1)$$

Equation (1) introduces two interfacing random variables, the so-called engineering demand parameter (*EDP*) and the seismic intensity measure (*IM*) that in this context will be both assumed scalar, for simplicity. The other terms appearing in the equation are: the annual rate of earthquakes able to cause structural failure, λ_f ; the rate of exceeding a certain value of a ground motion *IM*, that is λ_{im} ; the conditional probability, $P\left[EDP > edp_f \,|IM = im \right]$, that structural response given a certain *IM* level, exceeds the performance objective threshold, edp_f ; the so-called *fragility function*. *EDP* is a generic term used for any measure of structural response of engineering significance, that can be used to check or determine if the structure has failed to meet a given performance objective due to, for example, excessive stress or deformation. Examples of

often-used *EDP*s for building structures are inter-storey drift ratio or roof-level displacement. In this context, failure can be expressed as the exceedance of a predefined threshold *EDP*-value; i.e., $EDP > edp_f$. On the other hand, an *IM* can be some direct instrumental measure of ground motion amplitude, such as peak ground acceleration (*PGA*), or a quantity of elastic response, such as spectral pseudo-acceleration at various periods, $Sa(T)$. The term λ_{im} is a measure of the seismic hazard at a specific site and can be evaluated by means of probabilistic seismic hazard analysis and $|d\lambda_{im}|$ is the absolute value of its differential.

In the state-of-the-art approach, fragility can be analytically evaluated via several procedures that all require non-linear dynamic analysis of a structural numerical model subjected to set of ground motions, selected consistently with the seismic hazard of the site [2]. Analysis aims at the generation of samples of structural response given samples of ground motions.

The main disadvantages of the dynamic-analysis-based derivation of fragility functions is the computational burden involved and the amount of effort that has to go into modelling highly non-linear structural behaviour. The combination of numerical model complexity, required number of runs and the need for elaborate result post-processing can add-up to such demands of human and computing resources that engineers find themselves strongly motivated to look for simpler, approximate alternatives. The most notable simplifying alternative, one that has been with PBEE in various forms since its early years, involves making recourse to an equivalent single-degree of freedom (SDOF) non-linear system. One key point in this approximation is the assignment of a force-deformation law governing the SDOF system's response to monotonic lateral loading, typically referred to as the *backbone curve*. The definition of this backbone is typically based on the (numerically-evaluated) response of the original multiple-degree of freedom (MDOF) structure to a progressively increasing lateral force profile, known as its static push-over (SPO) curve. Due to their approximate nature, SPO-based methods have limitations that have been extensively documented and discussed (e.g., [3,4]). The other key point that is ubiquitous among SPO-based procedures is the calculation of the seismic demand of the equivalent SDOF system and the subsequent estimation of the original MDOF structure's seismic demand (e.g. [5]).

As previously introduced, the evaluation of the fragility function is often based on the results of non-linear dynamic analysis of a complex or simplified numerical model, which is subjected to a sample of ground motions, in order to capture the *record-to-record variability* of structural response (e.g., [6,7]). Thus, when a structure's probability of failure-given-intensity is inferred from a sample of structural responses from dynamic analysis, that only constitutes an estimate of the fragility function. As a consequence, any seismic risk metric calculated on the basis of that fragility, such as the failure rate, is also an estimate, henceforth indicated as $\hat{\lambda}_f$, of the unknown *true* value λ_f. In other words, any probabilistic model for structural fragility that is based on that limited sample of structural responses, will be affected by estimation uncertainty and that uncertainty will be propagated to the estimator of the failure rate $\hat{\lambda}_f$ (e.g., [8]).

Past PBEE-oriented research on the topic has seen discussion on the number of records that ought be used for estimating the distribution of *EDP*s at a single level (or *stripe*) of intensity [2,6]. The effect of estimation uncertainty on parametric fragility was investigated and in some of these previous studies that examined estimation uncertainty for the fragility parameters (e.g., [9,10]) it was recognized that further research was needed to investigate the effect of this uncertainty to the actual end result; i.e., the failure rate estimate.

In this context, this thesis is focused towards achieving the following distinct objectives:

- provide tools and methodologies to evaluate seismic fragility function by of means simplified pushover-based approaches;
- provide operational tools for the quantification of estimation uncertainty behind seismic risk estimates due to record-to-record variability of structural response;
- investigate the choice of the number of records to use for dynamic analysis to achieve quantifiable levels of mean relative estimation error on seismic risk metrics;
- investigate the use of parametric fragility functions within the context of an Italian research project (RINTC, [11]) that examined code-designed buildings belonging to different structural typologies.

1.2 Outline of the thesis

In **Chapter 2**, typical dynamic analysis methods in the context of PBEE are recalled first. Subsequently, concepts at the base of the software SPO2FRAG are illustrated before that the main features and operational outline of the tool are described and some numerical examples are provided. In the second part, the software for dynamic analysis of single-degree-of-freedom, DYANAS, is introduced with its structure and user interface. Finally, illustrative applications are provided as well.

In **Chapter 3**, the concept of estimation uncertainty in seismic risk evaluation and fragility function evaluation is recalled first. Then, the software R2R-EU, developed for estimating structure-specific seismic fragility, based on dynamic analysis, and quantifying estimation uncertainty, emanating specifically from record-to-record variability of seismic structural response, is described. Finally, two applications, one of which using results from the RINTC projects (*Rischio Implicito delle strutture progettate secondo le Norme Tecniche per le Costruzioni* – implicit seismic risk of code-conforming Italian buildings), are developed.

Chapter 4, in the first part advocates the use of quantitative criteria to determine the sample size of ground motion records, based on the statistical inference concept of estimation uncertainty, for estimating the annual failure rate. In particular, analytical and numerical means to investigate the record sample size required to achieve quantifiable levels of mean relative estimation error on seismic risk metrics are introduced. The second part, as a step backwards, asks another type of question, whether the statistical concepts previously introduced are an appropriate tool for addressing the minimum number of records mandated by modern codes.

Chapter 5 aims at discussing the seismic fragility curves for code-conforming Italian buildings developed within the RINTC project. Fragilities refer to two different structural failure criteria, global collapse failure and usability preventing damage, are derived via state-of-the-art methods and include consideration of the uncertainty in the estimation of the parameters. In conclusion, the impact of the fragilities on the failure rate estimation is deepened.

In **Chapter 6** general outcomes derived from the topics faced off in the previous sections are finally summarized.

Chapter 2 – SEISMIC FRAGILITY ASSESSTMENT VIA STATIC AND DYNAMIC NON-LINEAR ANALYSIS: THEORY AND IMPLEMENTATION IN SPO2FRAG AND DYANAS

The following papers have been derived from this Chapter:

- *Baltzopoulos G., Baraschino R., Iervolino I., Vamvatsikos D. (2017) SPO2FRAG: Software for seismic fragility assessment based on static pushover. Bulletin of Earthquake Engineering. DOI: 10.1007/s10518-017-0145-3.*
- *Baltzopoulos G., Baraschino R., Iervolino I., Vamvatsikos D. (2018) Dynamic analysis of single-degree-of-freedom systems (DYANAS): A graphical user interface for OpenSees. Engineering Structures, 177: 395-408.*

2.1. Introduction

The methods used to derive fragility functions can be classified as empirical, analytical or hybrid; the interested reader is referred to [12] for a comprehensive overview. In recent years there has been considerable emphasis on the analytical approach, which is based on numerical models, especially for structure-specific fragility functions. State-of-the-art analytical methods rely on advanced numerical models of the structure subjected to non-linear dynamic analyses. A classic example of such analysis is incremental dynamic analysis (IDA, [13]). IDA accounts for the variability of structural response (i.e., the record-to-record variability) by using a sample of recorded accelerograms as seismic input. IDA entails having each accelerogram in the ensemble scaled in amplitude to increasing levels of intensity (as measured by the selected *IM*) and estimating the structural response at each such level. In fact, because the *IM* typically does not possess full explanatory power with respect to structural response, the variability of the latter with respect to the former has to be captured. Thus, IDA seeks to map seismic structural response statistically, from the first signs of non-linear inelastic behaviour up to eventual collapse. Proposed extensions of this dynamic analysis methodology reserve the possibility of accounting for uncertainty in the numerical model itself (e.g. [14–16]). Alternative-to-IDA dynamic analysis strategies used for estimating structural fragility are *cloud analysis* and *multiple-stripe analysis* (MSA) (e.g. [17–20]). As extension of IDA, another type dynamic analysis called *back-to-*

back IDA (B2B-IDA) has been proposed [21] to evaluate structural response for a structure previously damaged and still not repaired.

As previously introduced, the main disadvantages of the dynamic-analysis-based derivation of fragility functions is the time consumed for performing analysis jointed with and the capacity requested to the user to model non-linear structural behaviour. For these reasons, the use of simplified methods making recourse to a backbone curve of a SDOF system's subjected to dynamic or static excitation has been considered as approximate alternative, with all the limitations involved.

Throughout the years, semi-empirical methods available for this calculation have evolved from *the equal displacement rule* to equations relating strength ratio to ductility per oscillator period (often abbreviated as $R-\mu-T$ relations, e.g., [22]) and eventually to the static pushover to IDA (SPO2IDA) algorithm of [23]. While earlier inelastic-spectra-based approaches were focused on average response of SDOF oscillators with elastic-perfectly plastic or bilinear backbone curves, the more recent SPO2IDA tool has the ability to treat more complex SPO curves and, more importantly, offers direct estimates of the dispersion associated with the record-to-record variability of structural response. These two elements render SPO2IDA particularly suitable for implementation within the PBEE paradigm, since they facilitate the treatment of uncertainty in seismic structural response for limit states approaching global collapse.

After an overview about dynamic analysis methods for PBEE (Section 2.2) and the state of the art in fragility function evaluation (Section 2.3), Section 2.4 comprehensively discusses the earthquake-engineering-oriented software SPO2FRAG (first introduced in [24]), an application coded in MATLAB® environment that permits the computer-aided evaluation of seismic fragility functions for buildings, based on the results of SPO analysis. The SPO2IDA algorithm lies at the core of SPO2FRAG, allowing the application to simulate the results of IDA without running numerous, cumbersome analyses. The background research behind SPO2FRAG is briefly presented, in order to highlight the connection between the PBEE paradigm and the program's functionality. The section is dedicated to the detailed description of the program itself, addressing the various internal modules that comprise SPO2FRAG, the inner workings, methodology and flowchart, as well as the various options

available to the user. Finally, two illustrative examples are presented, along with some evaluation and discussion of the obtained results.

Although the use of SDOF systems was initially motivated by the lack of computational resources for performing dynamic analysis of larger numerical models, in recent years the trend remains - only for different reasons. Advances in PBEE and seismic structural reliability (e.g., [25]) have brought forth the need for an adequate probabilistic representation of structures' post-elastic behavior during earthquake excitation. Due to the inherently stochastic nature of this phenomenon, mainly (but not solely) attributable to the so-called record-to-record variability of seismic response, such a probabilistic description by analytical means may require a prodigious number of dynamic analyses, putting a strain even on modern computational power. For this reason, methods that employ SDOF-level approximations of structural systems have been duly preserved in the arsenal of PBEE and have continued to undergo refinement and development.

Looking back, the dynamic response of yielding SDOF oscillators to base acceleration has been in the limelight of earthquake engineering research since its early steps [26] and remained there throughout its evolution, as simplified methods for seismic assessment and design of buildings appeared that were reliant on pushover analysis to define an equivalent, substitute SDOF structure [22,27–32]. In more recent years, with the PBEE paradigm gaining an ever-steadier foothold in the earthquake engineering community, new SDOF-based procedures began to surface that additionally sought to map the probabilistic distribution of seismic structural response (e.g. [23,33]). Other PBEE-related contexts that employed yielding SDOF oscillators as structural proxies, include the direct use of inelastic displacement as a measure of shaking intensity [34] and the critical scrutiny of prevalent ground motion record selection and modification practices for conducting response history analysis of structures [35,36].

Some of the issues that permeate all of the aforementioned cases are: the shape of the backbone curve of the SDOF system, the hysteretic law it follows during cyclic loading and the potential presence of strength and/or stiffness cyclic degradation in the hysteresis. The force-displacement relationship describing response to monotonic static loading, i.e., the backbone curve, is typically an idealization of the pushover curve obtained analytically for the corresponding structure. This idealization can be a simple bilinear shape, or it

can also include a descending, negative stiffness branch and even a residual strength plateau. The appearance of negative stiffness in a structure's pushover may be due to P-Δ effects or material strength degradation (often both) and the importance of its representation on the equivalent SDOF's backbone has been strongly advocated by past research [37,38].

With regard to the hysteretic behavior that ought to characterize a substitute SDOF system in order to best represent global response of the corresponding structure, there was a shift in modern practice, from the simple, kinematic hardening rules that saw extensive use in the past, towards phenomenological, evolutionary hysteretic rules (e.g., [39]) that are more representative of real structural behavior. Various proposals exist in the literature in this regard, typically based on experimental data that refer to specific structural typologies: for instance, the studies of Takeda et al. for reinforced concrete [40], Graziotti et al. for unreinforced masonry [41] and Lignos and Krawinkler for steel structures [42], are mentioned. Typically, the same model used for a structure's numerical simulation at the element level (especially in cases of concentrated plasticity modelling) is also assigned to the equivalent SDOF oscillator for that structure. However, it should be noted that, in the case of parametric phenomenological modelling of cyclic degradation effects, experimental model calibration at the element level may not be adequately representative of the entire structure's global behavior and a dedicated study may be needed (e.g., [43]).

Section 2.5 introduces an earthquake-engineering-oriented software: DYANAS, a MATHWORKS MATLAB®-based graphical user interface (GUI) that expedites the definition of inelastic SDOF systems in the OpenSees (Open System for Earthquake Engineering Simulation; [44]) finite element platform, streamlines the execution of dynamic analyses under suites of base-acceleration time histories and allows for methodical processing of the final results. The analysis method and post-processing aspects of the software are focused on facilitating dynamic analysis schemes that draw on the PBEE paradigm. The graphical interface components of the software run in MATLAB environment. Interaction with OpenSees is performed by manipulating Tcl/Tk scripts (Tool Command Language – a general scripting language that has been extended with OpenSees-specific commands; [45]) via MATLAB functions, in a process that will be described in the following sections. OpenSees is an open-source, object-oriented finite element platform developed for PBEE. Since its inception,

OpenSees has seen extensive use for numerical analysis in structural, geotechnical and seismic reliability problems (e.g., [46]). In the past, various GUIs have been built around OpenSees, intended to facilitate the definition of numerical models and subsequent running of analyses. Such examples are the Build-X software [47] and the GID interface [48] that are both intended for aiding the definition of multi-DOF building models, as well as the web platform of Dolšek et al. [49] and the II-DAP interactive interface [50] that operate on the SDOF level. DYANAS is a new addition to this list and is, primarily, a PBEE tool that incorporates a multitude of functions oriented towards efficient seismic analysis of simple structures (e.g., [51]). The software presented, DYANAS, is freely available for research purposes as a software package (http://wpage.unina.it/georgios.baltzopoulos/software/software_page.html) and is also distributed as open-source code, obtainable at https://github.com/georgebaltz/SDOF-OSEES. DYANAS allows users to easily define yielding SDOF oscillators with classical viscous damping, piece-wise linear monotonic backbones and a choice of six evolutionary or hardening hysteretic rules that are already implemented in OpenSees (to follow). Subsequently, the GUI gives users the opportunity to perform non-linear dynamic analyses to large sets of accelerometric input, supporting IDA, multiple-stripe analysis, cloud analysis and B2B-IDA. For each analysis session, users may define a single, or two uncoupled, SDOF oscillators. In the latter case, these can be run simultaneously, using bidirectional ground motion records. Finally, the software has the capability to post-process results, graphically represent them for the users and allows exporting figures and data files for further elaboration. The remainder of the Section 2.5 is organized in the following fashion: first, an outline of the dynamic analysis methods prevalent in PBEE and supported by the GUI is given. Subsequently, a description of the software's function, structure and capabilities is provided. Then, a sub-section dedicated to a few illustrative applications that showcase specific aspects of the software's utility as a PBEE tool are to be found, followed by some closing remarks and discussion.

2.2. Dynamic analysis methods for PBEE

As previously introduced, the primary use of dynamic structural analysis in PBEE is as a means of quantifying the ability of a structure to meet certain performance objectives, in a probabilistic framework. An understanding of this

can be obtained through Equation (1), that looks at part of the PEER framing equation [2] to provide the annual rate of a structure's failure to meet some performance objective, λ_f, which is a measure of seismic risk.

While the concept of structure-specific fragility functions sees extensive use in PBEE and seismic risk analysis, in order to determine such a functional relationship between *EDP* and *IM* as $P\left[EDP > edp_f \left| IM = im \right. \right]$ by analytical means, engineers may need to resort to a number of non-linear dynamic analyses of a numerical model of the structure, according to some methodology that maps the distribution of *EDP* for various *IM* levels. The methods used most frequently to obtain this *EDP-IM* mapping for seismic response are IDA, MSA and cloud analysis. For this reason, the three dynamic analysis methodologies (plus a variant of IDA) are briefly outlined below.

2.2.1 Incremental dynamic analysis

IDA consists of running a series of dynamic analyses for a non-linear structure, using a suite of accelerograms that are progressively scaled upwards in amplitude in order to represent a broad range of *IM* levels. Structural response, in terms of some *EDP*, is being continuously registered at each *IM* level; thus, for each acceleration record, a continuous *EDP-IM* relationship is obtained, termed an IDA curve (Figure 1a). A common way of summarizing IDA results for the entire suite of records, is to calculate the 16,50 and 84% fractile IDA curves of *EDP* given *IM* or vice-versa. As can be seen in the figure, while individual-record IDA curves can be non-monotonic, the fractile curves generally are. In fact, for structures susceptible to dynamic instability, when a record is scaled up to levels that can induce such behavior, the IDA curve tends to become horizontal, indicating almost-infinite increase in *EDP* for small *IM* increments; thus IDA flat-lines are taken to indicate structural collapse (for further details the interested reader is referred to [13]. It is mentioned in passing that IDA has already found its way into guidelines for practicing engineers that espouse PBEE principles (e.g., FEMA-P695, [52]).

2.2.2 Multiple-stripe analysis

MSA, like IDA, has the objective of calculating *EDP*-responses of a structure at various, increasing *IM* levels. The difference from IDA is that MSA does not necessarily resort to scaling the same suite of accelerograms to reach these *IM* levels, but may instead use different sets of (scaled or unscaled) records at each *IM* level (e.g., [19]). Ideally, these record sets should be selected to reflect site-

specific seismic hazard at each *IM* level, thus rendering the calculated seismic structural demand hazard-consistent (e.g., [53]). A schematic example of MSA results is given in Figure 1b, where it can be seen that *EDP* response samples, sometimes termed "*EDP*-stripes", have been obtained for six *IM* levels (note that in the context of IDA and due to the continuous nature of IDA curves, apart from *EDP*-given-*IM*, one may also calculate "*IM*-stripes" for a given *EDP* value).

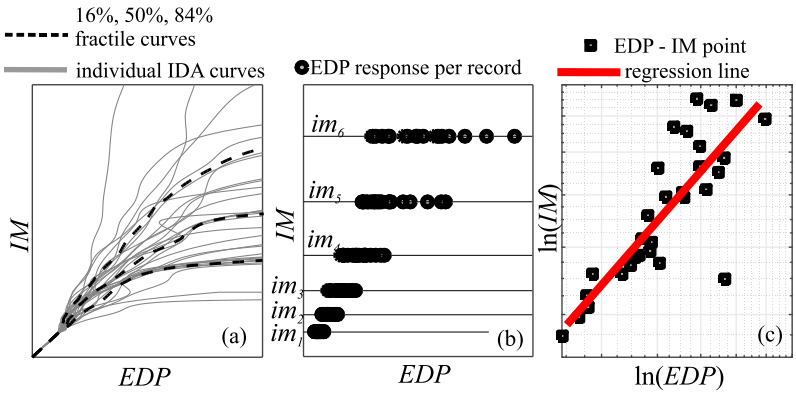

Figure 1. Illustrating the dynamic analysis methods most frequently used in PBEE: thirty IDA curves of a yielding SDOF oscillator and corresponding 16,50,84% EDP-given-IM fractile curves (a); EDP responses of a non-linear structure at six IM levels obtained via MSA (b); logarithmic-scale scatter plot of EDP-IM responses obtained via cloud analysis and corresponding ordinary least squares regression line (c).

2.2.3 Cloud analysis

Cloud analysis gets its name from the fact that it uses sets of unscaled acceleration records, meaning that, typically, only a single record will correspond to each *IM* level (besides it being not-very-likely to find many records with, say, the exact same *PGA* or $Sa(T)$ value, the very nature of this method calls for an even spread of intensity values within the range of interest). This results in a "cloud" of points in the *EDP-IM* plane, such as the scatter-plot shown in Figure 1c. With the cloud method, a probabilistic relation between *EDP* and *IM* can be obtained by means of linear regression and its assumptions of homoscedastic, Gaussian residuals (e.g., [20]). Regression of cloud analysis *EDP-IM* data can find application in some simplified seismic reliability methods; the interested reader is referred to [54] for further details.

2.2.4 Back-to-back incremental dynamic analysis

Besides traditional IDA, an extended version thereof has also been suggested in the past [21]. This extension of IDA was intended to provide a probabilistic description of seismic response for structures that have already been damaged by a mainshock earthquake (MS) and are susceptible to the effect of aftershocks (AS) before any repairs can take place. In this type of analysis, henceforth referred to as *back-to-back* IDA, the analyzed structure is first subjected to an initial set of accelerograms, let us call them the MS record set, each scaled to produce the same predefined *EDP* level. At the end of each single-run MS analysis, a damaged incarnation of the structure has been produced; this is allowed to revert to at-rest conditions and is subsequently subjected to a second set of records, let us call these the AS set, that are scaled upwards in the traditional IDA manner. Figure 22provides a schematic representation of this procedure. The end result, as in traditional IDA, is a set of continuous *EDP-IM* curves, the difference being that these curves no longer describe the seismic behavior of the original structure, but that of the structure that has been subjected to a specific damaged state. Also note, that the MS-AS characterization of the two record sets employed in this discussion is purely conventional and was used for designating the order with which the two shocks are considered in the analysis, without implying that they must be part of the same seismic sequence.

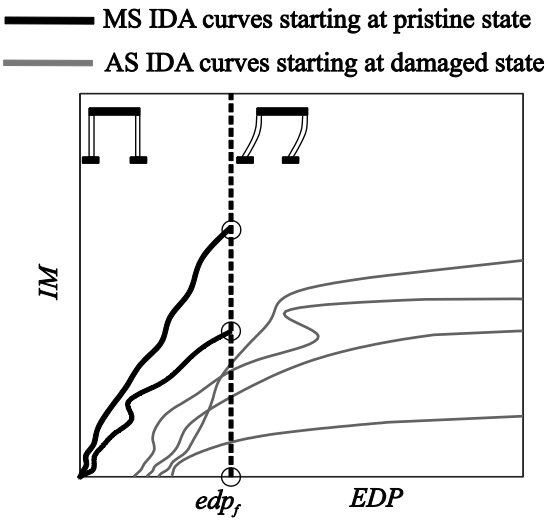

Figure 22. Schematic representation of back-to-back IDA: a "mainshock" record acting on a structure in pristine condition is scaled until a limit state

threshold edp_f is reached, then IDA is performed for a set of "aftershock" records, acting on the structure damaged by the mainshock record; the procedure is repeated for a predefined number of "mainshock" accelerograms, each followed by a set of "aftershock" accelerograms.

2.3. State- of the art in fragility function evaluation

Given the output of dynamic analysis, the strategy for analytically evaluating a fragility function often branches into one of two approaches: the *IM*-based approach and the *EDP*-based approach; *IM*-based fragility estimation is suitable within the IDA framework, while *EDP*-based can be applied in both IDA and MSA settings. In both cases, it is assumed that a threshold *EDP*, edp_f, can be defined, so that its exceedance will be tantamount to failure, that is, $P\left[f \left| IM = im \right.\right] = P\left[EDP > edp_f \left| IM = im \right.\right]$. In the *IM*-based approach, a new random variable (RV) needs to be introduced: the *IM*-value causing failure, denoted as IM_f, which is, in principle, different for each record. After the analysis has been concluded and the IDA curves become available, a sample of the RV can be obtained by finding the intersection $im_{f,i}$ between the vertical line passing through edp_f and the *i*-th IDA curve, $i = \{1, 2, ..., \mathrm{n}\}$ (Figure 3a). The fragility function may then be considered as the probability of IM_f being equal or lower than the level of seismic intensity possibly occurring at the site: i.e., $P\left[f \left| IM = im \right.\right] = P\left[IM_f \le im \right]$. It is also possible to assign a parametric model to the distribution of IM_f and a typical choice is the lognormal model, which is completely defined by mean η and standard deviation β of the logarithm of IM_f. In that case, fragility can be expressed using the standard Gaussian function, $\Phi(\cdot)$, according to Equation (2):

$$P\left[f \left| IM = im \right.\right] = P\left[IM_f \le im \right] = \Phi\left(\frac{\ln(im) - \hat{\eta}}{\hat{\beta}} \right) \qquad (2)$$

The two parameters $\{\eta, \beta\}$ are generally unknown and one way to obtain estimates of these parameters, $\{\hat{\eta}, \hat{\beta}\}$, is by using the sample of responses resulting from IDA according to Equation (3):

$$\begin{cases} \hat{\eta} = \dfrac{1}{n} \cdot \sum_{i=1}^{n} \ln\left(im_{f,i}\right) \\ \hat{\beta} = \sqrt{\dfrac{1}{n-1} \cdot \sum_{i=1}^{n} \left[\ln\left(im_{f,i}\right) - \hat{\eta}\right]^2} \end{cases}, \tag{3}$$

where n represents the number of IDA curves and is therefore equal to the number of records used and $im_{f,i}$ is the intensity that one needs to scale the i-th record (out of n in total), in order to cause failure of the structure.

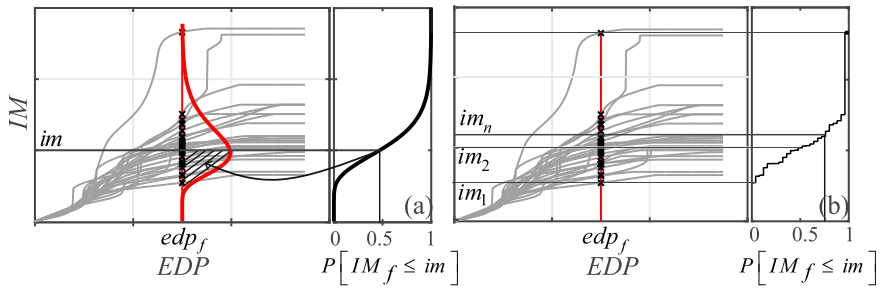

Figure 3: Fragility assessment using IDA curves assuming either a parametric (lognormal) probabilistic model for the distribution of IM_f (a) or a non-parametric representation (b).

Of course, it is not necessary to assume a parametric model for *IM*-based fragility; in fact, a non-parametric representation can be obtained directly from the sample of IM_f values, according to Equation (4):

$$P\left[\, f \,\middle|\, IM = im \right] = \frac{1}{n} \cdot \sum_{i=1}^{n} I_{\left(im_{f,i} \le im\right)}, \tag{4}$$

where $I_{\left(im_{f,i} \le im\right)}$ is an indicator function that returns 1 if $im_{f,i} \le im$ or 0 if $im_{f,i} > im$ (Figure 3b). The use of estimation uncertainty as a means for determining the number of records to use in *IM*-based fragility derivation is explored in Section 3.2.

Structural fragility can also be expressed as the complementary cumulative distribution function of IM_f, by following an *EDP*-based approach. In fact, the *EDP*-based method works both for IDA and MSA; in this case, *EDP* responses are obtained at discrete (fixed) *IM* levels. When these *EDP* responses are plotted against the corresponding *IM*s, they are arranged in horizontal

stripes (e.g., Figure 1b), one for each level of shaking intensity considered. By counting the fraction of records in each stripe that cause the exceedance of the limit state threshold, edp_f, the estimation of the fragility parameters $\left\{\hat{\eta},\hat{\beta}\right\}$ can be carried out via maximum likelihood, according to Equation (5), which is from [55]:

$$\left\{\hat{\eta},\hat{\beta}\right\}=\arg\max_{\eta,\beta}\left[\sum_{j=1}^{u}\left(\ln\binom{n}{q_j}+q_j\cdot\ln\left\{\Phi\left[\frac{\ln\left(im_j\right)-\eta}{\beta}\right]\right\}+\right.\right.$$
$$\left.\left.+\left(n-q_j\right)\cdot\ln\left\{1-\Phi\left[\frac{\ln\left(im_j\right)-\eta}{\beta}\right]\right\}\right)\right], \quad (5)$$

where u is the number of *IM* levels considered (i.e., the number of stripes, each stripe containing responses from *n* records), and $q_j=\sum_{i=1}^{n}I_{\left(edp_{ij}>edp_f\right)}$ is the number of failures observed at the stripe corresponding to $IM=im_j$ (Figure 4 a), when edp_{ij}, $i=\{1,..,n\}$, $j=\{1,..,u\}$ represents the single structural response recorded at the *i*-th record of the *j*-th stripe. In this formulation, cases of non-convergent analysis (referred to as *collapse* cases) due to the numerical model coming too close to highly-non-linear behaviour associated with incipient instability, say c_j in number, are also counted in q_j and are therefore accounted for, despite the potential lack of a credible *EDP* value [56]. At this point it should be noted that, in cases where the observed numbers of failure q_j remain excessively low over all stripes considered, the maximum likelihood estimates implied in Equation (5) can suffer from numerical problems. One viable alternative for considering fragility, consistent with the *EDP*-based approach, is the three-parameter-per-intensity model adopted by Shome and Cornell [56], given by Equations (6)

$$\begin{cases} P\left[f \left| IM = im_j \right. \right] = P\left[\bar{C} \mid IM = im_j \right] \cdot P\left[EDP > edp_f \left| \bar{C}, IM = im_j \right. \right] + \\ \quad + P\left[C \mid IM = im_j \right] = \left(1 - \frac{c_j}{n} \right) \cdot \left\{ 1 - \Phi \left[\frac{\ln\left(edp_f \right) - \hat{\eta}_{\ln\left(EDP_j \right)}}{\hat{\beta}_{\ln\left(EDP_j \right)}} \right] \right\} + \frac{c_j}{n} \\ \hat{\eta}_{\ln\left(EDP_j \right)} = \left(n - c_j \right)^{-1} \cdot \sum_{i=1}^{n-c_j} \ln\left(edp_{ij} \right) \\ \hat{\beta}_{\ln\left(EDP_j \right)} = \sqrt{\left(n - c_j - 1 \right)^{-1} \cdot \sum_{i=1}^{n-c_j} \left[\ln\left(edp_{ij} \right) - \hat{\eta}_{\ln\left(EDP_j \right)} \right]^2} \end{cases}, \quad (6)$$

where $P\left[C \mid IM = im_j \right]$ is the probability of collapse, $P\left[\bar{C} \mid IM = im_j \right]$ is its complement, i.e., the probability of non-collapse, c_j is the number of observed collapse cases at the *j*-th stripe, according to the previous definition, and $\hat{\eta}_{\ln\left(EDP_j \right)}$, $\hat{\beta}_{\ln\left(EDP_j \right)}$ are the mean and the standard deviation of the logarithm of *EDP*, at $IM = im_j$, provided by structural analysis and not affected by numerical instability (no-collapse cases). Note that this approach provides fragility at the discrete intensities $IM = im_j$, rather than as a continuous function of *IM*. However, it is also possible to fit a continuous parametric model for the probability of collapse, as an alternative to the empirical fractile c_j / n, by means of logistic regression [57] according to Equation (7):

$$P\left[C \mid IM = im_j \right] = \frac{1}{1 + e^{-\left(\alpha_0 + \alpha_1 \cdot im_j \right)}} . \quad (7)$$

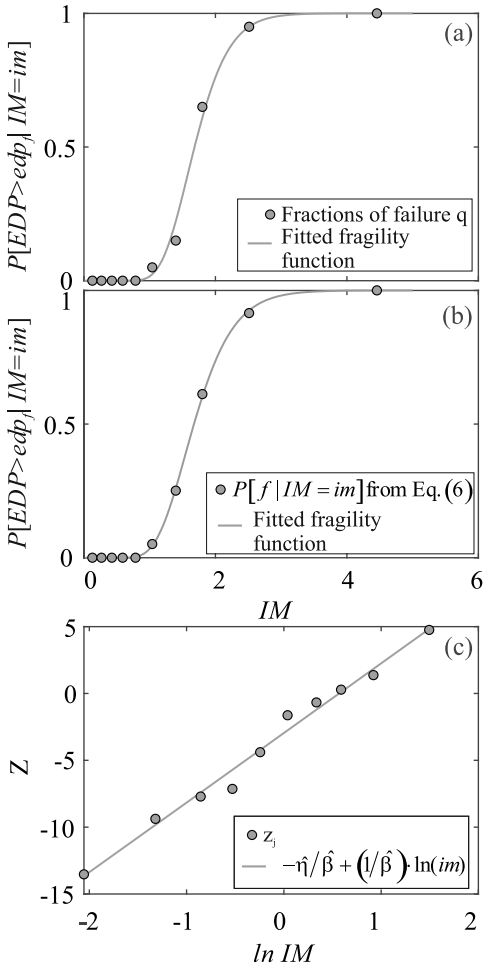

Figure 4. Maximum likelihood fit of a lognormal fragility function to the results of MSA (a); fit of lognormal fragility by means of non-linear least squares (b); fit of lognormal fragility on normal probability paper (c).

Another alternative procedure is to obtain estimates of the parameters $\left\{\hat{\eta},\hat{\beta}\right\}$ by means of least squares fitting, which can be done in one of two ways. One method consists of plotting the failure probabilities per stripe, $P\left[\left. f\right|IM=im_j\right]$ obtained from Equation (8), on normal probability paper and estimating the parameters via least squares fitting of a line. For this procedure, the values of the standard normal variable, Z ,corresponding to the failure probabilities are calculated as $z_j=\Phi^{-1}\left(P\left[\left. f\right|IM=im_j\right]\right)$, for which it can be assumed that, on

a *normal probability paper* [58], a linear relationship of the form $Z = -\hat{\eta}/\hat{\beta} + \left(1/\hat{\beta}\right) \cdot \ln(im)$ should hold; e.g., Figure 4c. In this case, the least squares estimate for $\left\{\hat{\eta}, \hat{\beta}\right\}$ is known to be the one given by Equations (8):

$$\begin{cases} \hat{\beta} = \dfrac{\sum_{j=1}^{u}\left(z_j - \overline{z}\right)^2}{\sum_{j=1}^{p}\left(z_j - \overline{z}\right) \cdot \left[\ln\left(im_j\right) - \overline{\ln\left(im\right)}\right]} \\ \hat{\eta} = \overline{\ln\left(im\right)} - \dfrac{\overline{z}}{\hat{\beta}} \\ \overline{z} = u^{-1} \cdot \sum_{j=1}^{u} z_j \\ \overline{\ln\left(im\right)} = u^{-1} \cdot \sum_{j=1}^{u} \ln\left(im_j\right) \end{cases}, \tag{8}$$

which are derived directly from the normal equations of the least-squares problem; e.g., [59]. It should be noted that if the probability of failure decreases with increasing seismic intensity, input data may be ill-conditioned and the fragility fitting may be not reliable.

The second method entails fitting a fragility function by minimizing the sum of squared errors according to Equation (9):

$$\left\{\hat{\eta}, \hat{\beta}\right\} = \arg\min_{\eta,\beta}\left(\sum_{j=1}^{u}\left\{\left(1 - \frac{c_j}{n}\right) \cdot \left\{1 - \Phi\left[\frac{\ln\left(edp_f\right) - \hat{\eta}_{\ln\left(EDP_j\right)}}{\hat{\beta}_{\ln\left(EDP_j\right)}}\right]\right\} + \frac{c_j}{n} - \Phi\left(\frac{\ln\left(im_j\right) - \eta}{\beta}\right)\right\}^2\right), \tag{9}$$

which is akin to performing a non-linear least squares regression, Figure 4b.

2.4. Simplified approach via non-linear static analysis: SPO2FRAG software

The conceptual basis of SPO2FRAG lies in simulating the results of incremental dynamic analysis using SPO alone. Therefore, the principal assumptions behind IDA and the methodologies for fitting *IM*-based analytical

fragility models on IDA results are also relevant in this case and merit briefly recalling them.

IDA collects the responses of a non-linear structure to a suite of accelerograms, as these accelerograms are progressively scaled in amplitude to represent increasing levels of seismic intensity. These structural responses are typically represented by a scalar quantity, the *EDP*. Examples of *EDP*s often used for buildings are maximum roof drift ratio (RDR) and maximum interstorey drift ratio over all floors (IDR). Furthermore, a scalar *IM* is chosen to represent seismic intensity; e.g., *PGA* or first-mode spectral acceleration, $Sa(T_1)$. One basic assumption is that such an *IM* is sufficient, that is, the *EDP* random variable conditioned on the *IM* is independent of other ground motion features needed to evaluate the seismic hazard for the site, such as magnitude and source-to-site distance (e.g., [60]). Another closely related assumption is the so-called *scaling robustness* of the chosen *IM*, meaning that using records scaled to the desired amplitude of the *IM*, rather than records where said amplitude occurred naturally, will not introduce bias into the distribution of structural responses obtained (e.g., [35]). This allows plotting *EDP* against *IM* as each individual record is scaled upwards, resulting in an IDA curve.

It is assumed that in the numerical model of the structure employed for IDA, stiffness and strength degradation under dynamic loading are acceptably represented. Consequently, failure of the analysis to provide an *EDP* value after scaling a record to a certain *IM* level can be attributed to the onset of dynamic instability, which would physically correspond to the structure's side-sway collapse (see also [61]). For presentation purposes, this numerical onset of collapse can be displayed at the end of the IDA curve as a horizontal segment of ever-increasing *EDP*-values for a fixed *IM* value, or a flat-line (see Figure 5). In cases where global collapse is deemed to occur at lower IMs due to non-simulated modes of failure (e.g., shear or axial failure of columns) an appropriate flatline may be used instead to terminate the IDA curve earlier.

An effective way of summarizing IDA results is to calculate and plot counted fractile curves of either *EDP* for fixed *IM* or vice-versa [51]. Usually, fractile IDA curves at 16%, 50% and 84% are chosen for presentation, corresponding to the mean plus/minus one standard deviation of a Gaussian distribution. As a matter of fact, as introduced in Section 2.3, analytical derivation of fragility functions typically involves fitting a parametric probability model to the results of dynamic analysis and the model chosen is

very often lognormal. One way of defining the fragility function for a limit state is to assume that there exists a threshold (maximum allowable) value of some *EDP*, edp_f, whose exceedance also signals failure, i.e., exceedance of the limit state, according to Equation (10).

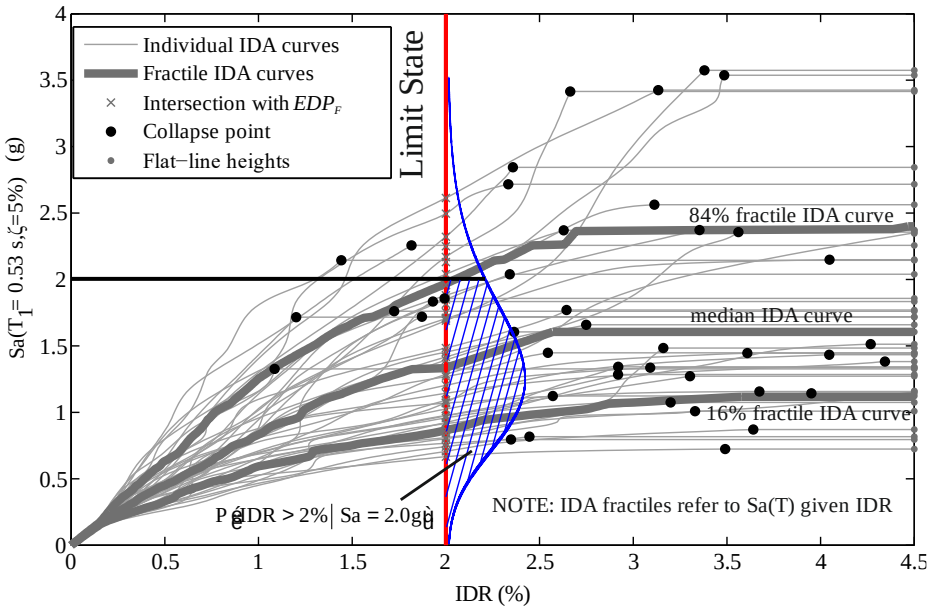

Figure 5. Example of IM-based derivation of structural fragility using IDA curves (limit state defined as exceedance of a 2% IDR value).

$$P\left[f \left| IM = im \right.\right] = P\left[EDP > edp_f \left| IM = im \right.\right] = P\left[IM_f \le im \right]. \qquad (10)$$

An alternative way of looking at this fragility definition, within the IDA framework, can be stipulated by considering a random variable representing the *IM* level at which to scale a specific record in order to fail the structure (i.e., causing the event $EDP > edp_f$), denoted as IM_f. In this case, the fragility function can be written as the probability of this random variable being equal or lower than the level of seismic intensity possibly occurring at the site, according to Equation (10) – see also [18]. By making the assumption that IM_f follows a lognormal distribution, the fragility function will be completely defined by estimating the two parameters of the underlying Gaussian, i.e., the mean of the logs η and the logarithmic standard deviation β. These parameters can be estimated using the sample of $IM_{f,i}$ values shown in Figure

5 as the intersection of the individual IDA curves and the $EDP = edp_f$ vertical line. As a consequence, it is possible to write the fragility function via the standard Gaussian function $\Phi(\bullet)$, as in Equation (2).

As evidenced in Figure 5, the *IM*-based approach is particularly convenient when global collapse becomes the limit state of interest: any vertical line intersecting all the records' flat-lines will provide the empirical distribution for collapse intensity to which a model such as the lognormal appearing in Equation (2) can be fitted. This, in turn, may be used to compute the failure rate via Equation (1). In general, though, pinpointing a fixed value of edp_f that signals the transition between limit states can be hard due to the uncertainties involved.

It should be highlighted that when using IDA to estimate the fragility $P\left[f \left| IM = im \right. \right]$, the two already mentioned assumptions of sufficiency and robustness to scaling are endorsed by default, due to the very nature of the analysis. In what follows, it will be assumed that first mode spectral acceleration, $Sa(T_1)$, is a *sufficient-enough IM* with respect to roof and interstorey drifts for the structures considered and thus the problem of fragility estimation will be treated as site-independent.

2.4.1 SPO2IDA

SPO analysis finds application in the context of earthquake engineering as part of several approximate procedures that relate the inelastic seismic response of structures to that of some equivalent SDOF system. The popularity of such methods can be attributed to their inherent simplicity and eventual adoption by normative documents and guidelines on seismic structural design/assessment. Some of the earlier examples of SPO-based procedures made recourse to elastic-perfectly plastic or bilinear SDOF equivalent oscillators and relied on inelastic displacement ratio predictive Equations or $R - \mu - T$ (strength ratio – ductility – period) relations to obtain estimates of their average inelastic response. More recently, the trend has been shifting towards accounting for the variability of inelastic seismic response around its central value and towards expanding the limits of structural assessment to include global collapse (e.g., [62]). The latter of these trends practically translates into the adoption of more elaborate numerical models for the structure and consequently SPO curves that trace monotonic response to lateral loading down the (in-cycle) strength-

degradation descending branch and along an eventual residual strength plateau. This, in turn, gives rise to the need for analytical models that predict the response of SDOF systems with more complex backbone curves, such as the quadrilinear depicted in Figure 6.

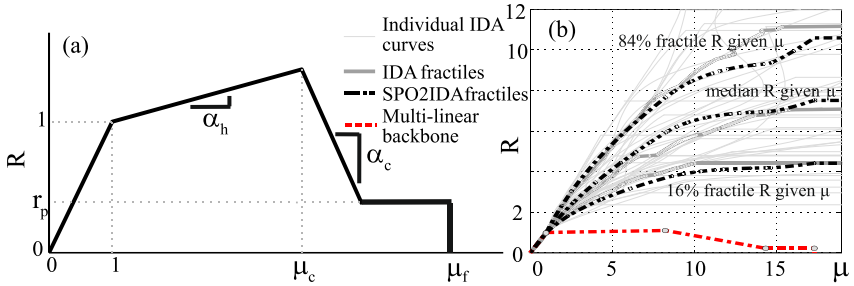

Figure 6. Quadrilinear monotonic backbone curve in dimensionless $\{R,\mu\}$ *coordinates and defining parameters (a), SPO2IDA prediction against actual quadrilinear-backbone SDOF oscillator (T=0.56s) IDA curves obtained using all forty-four components of the FEMA P695 far-field ground motion set (b).*

In this format, the quadrilinear backbone can be completely defined by five parameters shown in Figure 6(a): the hardening slope α_h (positive ratio of post-yield stiffness to elastic stiffness), the capping-point ductility μ_c (point where loss of strength with increasing deformation begins), the post-capping slope α_c (negative slope corresponding the ratio of the negative post-capping stiffness divided by the initial elastic stiffness), the height of the residual strength plateau r_p (ratio of residual strength divided by yield strength) and the fracture ductility μ_f (point corresponding to sudden, complete loss of strength). It is recalled that ductility is defined as the ratio of displacement response to yield displacement, $\mu = \delta/\delta_y$, while the strength ratio $R = Sa(T)/Sa(T)_y$ is defined as the ratio of the spectral acceleration intensity to its value causing yield, or, equivalently, the ratio of the elastic seismic force over the yield base shear of the system (R is sometimes encountered in the literature under the term *strength reduction factor*).

[23] proposed a set of semi-empirical analytical Equations aimed at predicting the median and (record-to-record) variability of peak seismic response of SDOF oscillators featuring quadrilinear SPOs. These Equations use the SPO parameters α_h, μ_c, α_c, r_p, μ_f and period of natural vibration T as

predictor (independent) variables to estimate the SDOF structure's 16%, 50% and 84% fractile IDA curves in $\{R, \mu\}$ coordinates. For this reason, this set of Equations has been named SPO2IDA. The Equations that comprise SPO2IDA were fit against the responses of SDOF oscillators with critical viscous damping ratios, ζ, equal to five percent and with hysteretic behavior exhibiting moderate pinching but no cyclic degradation of stiffness or strength. These oscillators were subjected to a suite of thirty recorded ground acceleration time-histories, recorded on firm soil and most likely unaffected by near-source directivity effects. An example of an SPO2IDA prediction for a quadrilinear-backbone SDOF system, plotted against the actual (individual and fractile) IDA responses for these thirty accelerograms, can be found in Figure 6(b). The limits of applicability for SPO2IDA in terms of the independent variables are the following: $0.10s \le T \le 4.0s$, $0.0 \le \alpha_h \le 0.90$, $1.0 < \mu_c \le 9.0$, $0.02 \le |\alpha_c| \le 4.0$ and $0.0 \le r_p \le 0.95$.

The key observation behind the development of SPO2IDA was the relatively consistent behavior of the IDA fractile curves corresponding to the various segments of the underlying SPO (i.e., hardening, softening, residual). This behavior is visible in Figure 6(b), where the SPO is plotted along with the IDA fractiles (both calculated and predicted). While an almost-constant ascending slope characterizes the initial post-yield IDA segments, this gives way to gradual flattening upon crossing of the capping point. This flattening is temporarily arrested when the residual plateau is encountered, but only until the fracture point leads to the flat-lines that indicate collapse. Although analytically complex, SPO2IDA is an algorithm that has proven well-suited to computer implementation. SPO2FRAG fully exploits SPO2IDA's potential as a PBEE tool by surrounding it with a set of modules that render the SPO-based estimation of seismic structural fragility practical. The complete conceptual and operational details are presented in the following sections.

2.4.2 Definition of an equivalent SDOF system

The choice of an equivalent SDOF system for a given structure lies at the core of all SPO-based analysis methods. This choice entails the definition of the SDOF oscillator's mass, m^*, yield strength, F_y^*, yield displacement, δ_y^* and as many of the dimensionless backbone parameters (see Figure 6a) as are

applicable to the case at hand (i.e., depending on whether one is opting for a bilinear, trilinear or full quadrilinear approximation of the SPO curve).

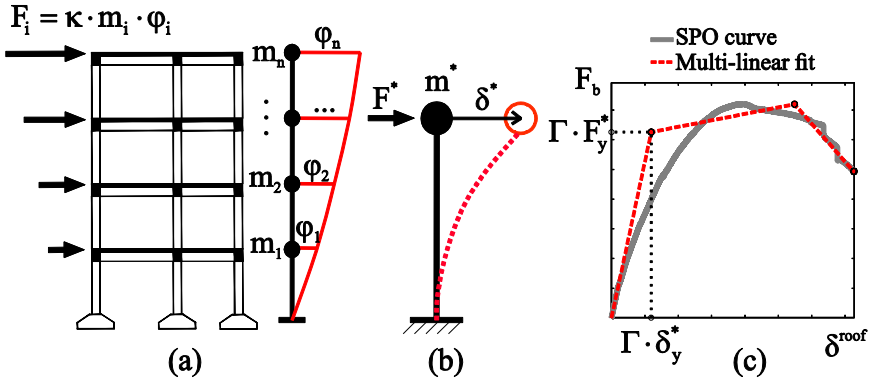

Figure 7. Definition of equivalent SDOF system: SPO analysis of the strtucture (a), definition of dynamic characteristics of the SDOF system (b), definition of monotonic backbone of the SDOF system based on SPO curve (c).

With reference to Figure 7, we assume that a generic *n*-storey frame building is subjected to a lateral load profile $F_i = \kappa \cdot m_i \cdot \varphi_i$, where F_i is the force acting on the *i*-th storey, m_i represents floor mass, the elements φ_i define a dimensionless displacement profile, which is assumed constant with unit value at roof level ($\varphi_n = 1$), and κ is a scale factor with dimensions of acceleration. By gradually increasing the scale factor κ , recording the displacement response of the deforming structure at roof level, δ^{roof} , and plotting that displacement against base shear, $F_b = \sum_{i=1}^{n} F_i$, we obtain the SPO curve - Figure 7(c). This curve is used to determine the monotonic backbone of an SDOF system whose mass, m^* , is given as a function of the structure's floor masses by $m^* = \sum_{i=1}^{n} m_i \cdot \varphi_i$ and whose reaction force F^* and displacement δ^* are related to the structure's base shear and roof displacement by dividing with the modal participation factor Γ ($F^* = F_b / \Gamma$ and $\delta^* = \delta^{roof} / \Gamma$) , which is calculated as $\Gamma = m^* \Big/ \sum_{i=1}^{n} m_i \cdot \varphi_i^2$ [5].

The period of vibration of the equivalent SDOF system, T^*, is calculated as $T^* = 2\pi \cdot \sqrt{\frac{m^* \cdot \delta_y^*}{F_y^*}}$. As indicated by Figure 7(c), the definition of F_y^* and δ_y^* depends on the piece-wise linear approximation adopted for the SPO curve. As far as specific methodologies towards obtaining said approximation are concerned, the literature offers some variety but little consensus. Normative documents such as Eurocode 8 [63], FEMA-356 [64] and FEMA-273 [65] suggest some procedures for obtaining elastic-perfectly-plastic or bilinear approximations for the backbone of the equivalent SDOF based on ad-hoc criteria such as *area balancing* [63]. Furthermore, when it comes to trilinear or quadrilinear SPO fits that bring to the table a larger number of parameters to be estimated, such simple rules are not enough. In fact, more advanced methods towards constructing trilinear SPO curve approximations were proposed in FEMA-440 [66], ASCE/SEI 41-06 [67] as well as by [68] and [62].

Recently, [69] set forth a set of rules for obtaining quadrilinear approximations that may potentially include a residual strength plateau. In that work, the optimization of the piece-wise linear fit was performed by comparing the IDA curves of the multi-linear-backbone SDOF oscillator with those of the system sporting the exact backbone. For this reason, this was considered the most suited algorithm for inclusion within SPO2FRAG's modules. In the aforementioned study, the authors paid particular attention to systems with SPOs exhibiting notable changes of stiffness already from the early, low-base-shear stages, e.g., Figure 7(c). Such a behavior, which can be due to, for example, gradual cracking of reinforced concrete (RC) members is especially challenging when it comes to pinpointing a nominal yield point for the equivalent SDOF system. It was concluded that the elastic segment of the equivalent system's backbone should correspond to a secant stiffness at an early point on the SPO curve, at around 5% to 10% of maximum base shear. This is due to the fact that when the elastic stiffness attributed to the equivalent system, F_y^* / δ_y^*, significantly departs from the initial tangent stiffness of the actual structure, the IDA curves corresponding to the linearized backbone display poor fit with respect to the IDAs of the *exact* backbone at the comparatively low-seismic-intensity region. This is especially relevant in cases where absence of a clearly defined elastic segment and high initial curvature characterizes the SPOs.

2.4.3 Consideration of MDOF effects

Once an equivalent SDOF oscillator has been fully determined, SPO2IDA can provide an approximation for the three fractile IDA curves of this SDOF system in $\{R, \mu\}$ coordinates, as already discussed (see Figure 8a). The predicted IDAs can be regarded as fractiles of strength ratio, $R_{x\%}$, given μ, with $x = \{16\%, 50\%, 84\%\}$. However, two further steps are needed before this result can be used to obtain a meaningful estimate for the fragility of the original MDOF structure. First of all, the SDOF IDA curves must be transformed from $\{R, \mu\}$ into an *IM – EDP* format appropriate for the structure. Second step is to address the variability of response at the nominal yield point $R = \mu = 1$. Prior to this point, the three IDA $R_{x\%}$ fractiles of the SDOF system coincide, corresponding to zero response variability around the median. On the other hand, the MDOF structure does exhibit response variability at that point. If the nominal yield point corresponds to the structure remaining in the elastic range, some limited variability will exist due to higher-mode contributions to base shear. Higher variability may be expected when the nominal yield corresponds to deformation levels where the structure is already manifesting some non-linear behavior (e.g., Figure 7c). In either case, the missing amount of variability should be estimated and injected back into the SDOF-derived approximation of the IDA curves. This is especially important when fragility for low-damage limit states is being sought. These operations are schematically presented in Figure 8b.

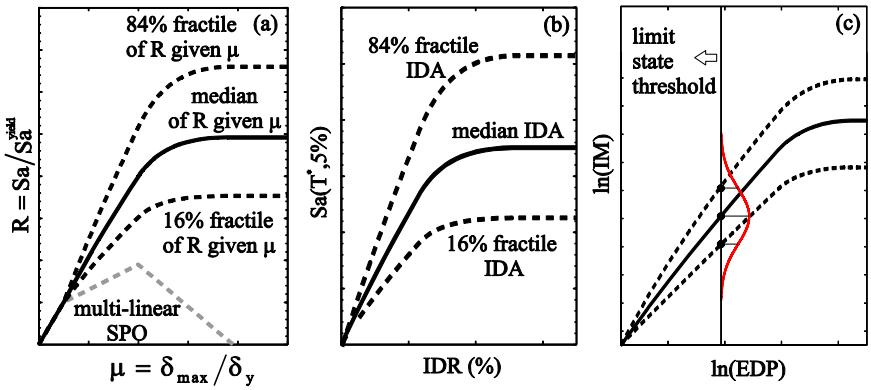

Figure 8. Schematic representation of the conceptual basis of SPO2FRAG: (a) obtaining SPO2IDA-predicted IDA fractiles for the equivalent SDOF system, (b) transforming the SDOF IDA curves to MDOF IM-EDP coordinates, (c)

fitting Gaussian models to the transformed IDA fractiles according to the IM-based procedure (c).

Since the restoring force of the SDOF system depends on spectral acceleration at its natural period, T^*, the transformation of *IM* is the most immediate operation: the 16%, 50% and 84% fractiles of $Sa\left(T^*,5\%\right)$ are obtained from their counterpart R fractiles according to $Sa\left(T^*,5\%\right)_{x\%} = R_{x\%} \cdot \frac{\delta_y}{\Gamma} \cdot \left(\frac{2\pi}{T^*}\right)^2$, $x \in \{16,50,84\}$.

The passage from ductility demand to RDR and IDR can be performed according to Equation(11), where h_i denotes the height of the i-th storey and Γ_{eff} is an *effective* modal participation factor that can be used instead of Γ:

$$\begin{cases} RDR = \Gamma_{eff} \cdot \dfrac{\mu \cdot \delta_y^*}{\sum_{i=1}^{n} h_i} \\ IDR = COD \cdot RDR \end{cases} \tag{11}$$

In Equation (11), the notation COD stands for *coefficient of distortion* (e.g., [70]). COD is defined as the ratio of maximum IDR to the roof drift and is a function of R. This is expressed by Equation (12), where δ_i represents the SPO displacement of the *i*-th storey at base shear level $R \cdot F_y$ and $H = \sum_{i=1}^{n} h_i$ the total building height:

$$COD = \frac{\max_i \left\{ \left(\delta_i - \delta_{i-1} \right) / h_i \right\}}{\delta_n / H} \tag{12}$$

On the other hand, the effective modal participation factor Γ_{eff} appearing in Equation (11) is intended to account for higher-mode effects and possible early (prior to nominal yield) non-linear behavior; for an example see [71]. Note that Γ_{eff} can be simply substituted by Γ when such effects are not of concern. In the context of SPO2FRAG, Γ_{eff} corresponds to an approximate analytical model that was developed using IDA results obtained for twenty-eight plane, steel and RC moment-resisting frames (MRFs) having two to eight storeys,

first-mode periods within 0.25s-2.00s and using both distributed and concentrated plasticity models. The proposed functional form for Γ_{eff} is:

$$\begin{cases} \Gamma_{eff} = \Gamma + R^2 \cdot \left(\sum_{i=1}^{n} m_i \Big/ \sum_{i=1}^{n} m_i \cdot \varphi_i - \Gamma \right) \cdot \left[\dfrac{Sa(T_2)}{Sa(T^*)} - 1 \right] \times \\ \quad \times \left[1 - 0.5 \cdot \left(\dfrac{T^*}{T_1} \right)^{1/2} \right], \ 0 < R \le 1 \\ \Gamma_{eff} = \Gamma + \left(\sum_{i=1}^{n} m_i \Big/ \sum_{i=1}^{n} m_i \cdot \varphi_i - \Gamma \right) \cdot \left[\dfrac{Sa(T_2)}{Sa(T^*)} - 1 \right] \times \\ \quad \times \left[1 - 0.5 \cdot \left(\dfrac{T^*}{T_1} \right)^{1/2} - 1.7 \cdot \left(\dfrac{R-1}{R_{50\%}^{col} - 1} \right)^{1/2} + \right. \\ \quad \left. + 1.3 \cdot \left(\dfrac{R-1}{R_{50\%}^{col} - 1} \right)^{1/2} \cdot \left(\dfrac{T^*}{T_1} \right)^{1/2} \right], \ 1 < R \le R_{50\%}^{col} \\ \Gamma_{eff} = \Gamma + \left(\sum_{i=1}^{n} m_i \Big/ \sum_{i=1}^{n} m_i \cdot \varphi_i - \Gamma \right) \cdot \left[\dfrac{\widetilde{Sa(T_2)}}{Sa(T^*)} - 1 \right] \times \\ \quad \times \left[0.8 \cdot \left(\dfrac{T^*}{T_1} \right)^{1/2} - 0.7 \right], \ R > R_{50\%}^{col} \\ 1.0 \le \left(T^* / T_1 \right)^{1/2} \le 1.50, \ 1.0 \le \widetilde{Sa(T_2)} \Big/ Sa(T^*) \le 3.0 \end{cases} . \quad (13)$$

In Equation (13), $Sa(T_2)$ represents the geometric mean spectral acceleration at the second-mode period, when all records of the ground motion suite employed by [23] for SPO2IDA are scaled to a common $Sa(T^*)$ value. On the other hand, $R_{50\%}^{col}$ represents the median strength ratio causing collapse, taken as the median SPO2IDA flat-line height.

Note that according to Equation (13), Γ_{eff} can assume values between Γ (lower bound) and $\sum_{i=1}^{n} m_i \Big/ \sum_{i=1}^{n} m_i \cdot \varphi_i$ (upper bound). The upper bound value corresponds to activation of the full structural mass along the vibration mode φ_i. Furthermore, Γ_{eff} depends on R, T^*/T_1, and $Sa(T_2)/Sa(T^*)$. The ratio

T^*/T_1 is a measure of how far the nominal yield point of the equivalent SDOF system trespasses into non-linear territory; higher values of this ratio correspond to SPO curves with considerable initial curvature. The ratio $Sa(T_2)/Sa(T^*)$ is in place to account for the response-amplifying effect of higher modes, when the structure is excited by accelerograms exhibiting larger spectral ordinates at the second-mode period. It has been known for some time that, in MRF structures, such effects persist into the non-linear response range (e.g., [7]).

The second part of the SDOF to MDOF transition consists of adding the missing variability at nominal yield, β_y. [62] suggested that this can be achieved by running a set of linear-elastic response history analyses of the structure. Although that approach may work when nominal yield of the equivalent SDOF system coincides with the linear-elastic limit of the structure, in order to deal with a generic case when the former delves into non-linear territory a semi-empirical relation was developed for the purposes of SPO2FRAG. This relation was calibrated using the same stock of buildings' numerical models as for Equation (13):

$$\begin{cases} \beta_y = \sqrt{\beta_{yo}^2 + \beta_{y,T_2}^2} \\ \beta_{yo} = 1/2 \cdot \ln\left(Sa_{y,84\%}^{bilin} \,/\, Sa_{y,16\%}^{bilin}\right) \\ \beta_{y,T_2} = 0.04 + 0.04 \cdot \dfrac{Sa(T_2)}{Sa(T^*)} \cdot \left[2.6 - 1.6 \cdot \left(\dfrac{T_{\text{sec}}}{T_1}\right)^{1/2}\right] \cdot \\ T_{\text{sec}} = 2\pi \cdot \sqrt{\dfrac{m^* \cdot \delta_y}{F_y}},\ 1.0 \le \left(T_{\text{sec}}/T_1\right)^{1/2} \le 1.5 \end{cases} \tag{14}$$

According to Equation (14), two separate contributions are considered in the estimate of β_y. The term β_{yo} that accounts for early non-linear behavior (i.e., curvature of the SPO curve prior to the nominal yield point) and the term β_{y,T_2} that accounts for purely higher-mode contribution to variability at yield. The other terms introduced in Equation (14) are the secant-to-first-mode period ratio T_{sec}/T_1 and the $Sa_{y,x\%}^{bilin}$ fractiles that determine β_{yo}. The terms $Sa_{y,x\%}^{bilin}$ appearing in Equation (14), correspond to the x% SPO2IDA fractiles of an auxiliary SDOF system, whose bilinear backbone is fitted using only the SPO

segment that precedes the nominal yield point; this means that β_{yo} attains higher values as the nominal yield point advances into the non-linear part of the SPO curve and reduces to zero whenever nominal yield is found on the initial linear segment. The T_{sec}/T_1 ratio used in the calculation of the β_{y,T_2} term is another proxy for early SPO curvature; note that according to Equation (14), the influence of the higher-mode term β_{y,T_2} diminishes for increasing values of T_{sec}/T_1. This is explained by the fact that larger values of T_{sec}/T_1 imply substantial initial curvature of the SPO curve, in which case the competing term β_{yo} tends to account for most of the variability. It should be noted that the combination of employing the Γ_{eff} concept and injecting the missing variability at yield β_y, constitutes a simplified method of dealing with higher-mode effects in the context of SPO analysis that was tailor-made to suit the needs of the SPO2FRAG software; therefore, caution is advised should it be used to confront this complex issue outside this context.

2.4.4 SPO-based fragility

Having thus simulated the three IDA fractile curves, based on the SPO of the structure, the parameters of the lognormal fragility model of Equation (2) can be fitted for each limit-state (Figure 8c). Since the SPO-based IDA approximation does not provide the individual IDA curves, but only fractiles, the fragility parameters can be estimated as:

$$\begin{cases} \eta = \ln\left(Sa^{LS}_{f,50\%}\right) \\ \beta = \ln\left(Sa^{LS}_{f,50\%} \,/\, Sa^{LS}_{f,16\%}\right) \end{cases}. \tag{15}$$

The terms $Sa^{LS}_{f,x\%}$ represent the *x*% fractile of the structural intensity causing exceedance of each limit state LS, as defined when introducing Equation (10) and *IM*-based fragility.

Finally, once the lognormal fragility parameters $\{\eta, \beta\}$ have been estimated from the SPO analysis one may consider two a posteriori modifications. One modification to the median, in order to account for structural damping other than $\zeta = 5\%$ and another modification to the dispersion that accounts for additional response variability due to structural modelling uncertainty. In the

$\zeta \neq 5\%$ case, it is considered that it is sufficient to modify the median and only for limit states nearing collapse. In fact, [68] proposed a modification factor, C_ζ, to be applied to the median collapse intensity of 5%-damped SDOF systems:

$$\begin{cases} R_{50\%}^{col}(\zeta) = C_\zeta \cdot R_{50\%}^{col}(\zeta = 5\%) \\ C_\zeta = 1 - \dfrac{0.07 \cdot \ln \zeta + 0.20}{\left(T^*\right)^{0.38} \cdot \left|\alpha_c\right|^{-0.26} \cdot \mu_c^{-0.44}} \end{cases}. \tag{16}$$

However, even for structures with $\zeta \neq 5\%$, it is desirable to maintain $Sa\left(T^*, 5\%\right)$ as *IM*, since hazard is typically available in terms of 5%-damped spectral ordinates. Therefore, the necessary modification boils down to Equation (17), where η_ζ^{col} represents the logarithmic mean collapsing intensity of a $\zeta \neq 5\%$ structure in terms of $Sa\left(T^*, 5\%\right)$ and $\eta_{\zeta=5\%}^{col}$ is the uncorrected SPO2IDA estimate from Equation (15), that considers $\zeta = 5\%$ by default:

$$\eta_\zeta^{col} = \eta_{\zeta=5\%}^{col} - \ln C_\zeta . \tag{17}$$

Apart from the modification of Equation (17), which is applicable at collapse, a modification factor is also applied to the median failure intensity of any limit states defined by *EDP* thresholds in proximity to collapse. These modification factors are obtained by interpolation, based on the requisite that η increase monotonically with edp_f.

When a single deterministic numerical model of the structure is subjected to IDA, the distribution of the obtained responses reflects record-to-record variability. However, one may also wish to account for uncertainty underlying the mechanical model parameters (such as material strength, member hysteretic behavior, mass distribution, etc.). A simple method for dealing with this issue, adopted by [54], is the so-called first-order assumption, whereby the mean logarithmic failure intensity is itself a normal random variable, depending on the probabilistic configuration of the structural model, with a standard deviation β_U and mean η. Then, the fragility function remains lognormal with the same mean, but with variance $\beta_{tot}^2 = \beta^2 + \beta_U^2$, with β representing response variability estimated directly from SPO2IDA and Equation (15). The

variability due to modelling uncertainty, β_U, can either directly assume a value proposed in the literature (e.g., values suggested in FEMA P-695 for the collapse limit state) or be estimated by combining SPO2IDA and Monte-Carlo simulation, similar to what was suggested by [33], to follow.

2.4.5 Operational outline of SPO2FRAG

The SPO2FRAG tool is essentially a software implementation of the methodology for the SPO-based derivation of seismic fragility functions presented in detail in the preceding section. This engineering application revolves around a graphical user interface (GUI), which is divided in three parts (Figure 5): the SPO to IDA and fragility toolboxes, panels for the visualization of intermediate results (SPO processing and IDA curve generation) and an output panel where the end result in the form of fragility curves is visualized.

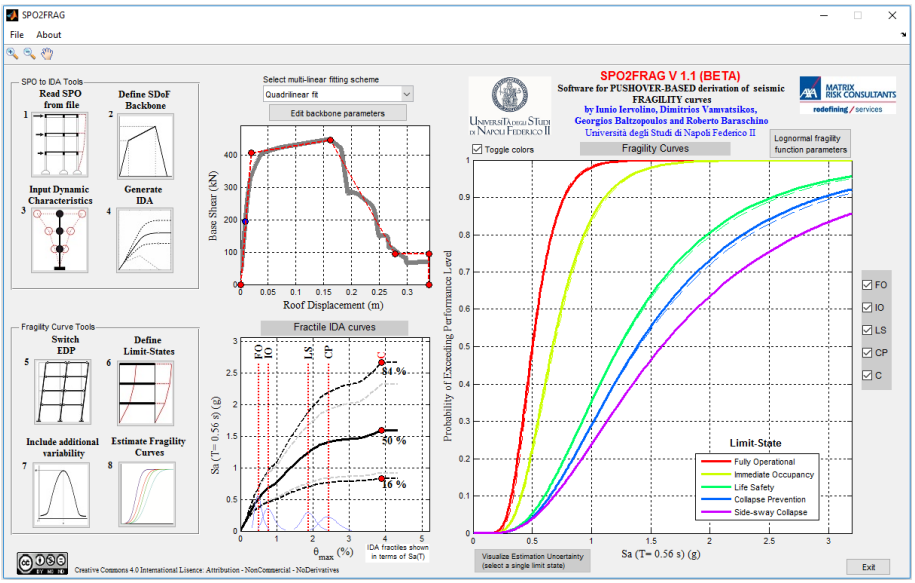

Figure 9. Main SPO2FRAG GUI displaying a completed elaboration of fragility curve calculation.

In operational terms, SPO2FRAG comprises a series of individual modules that function independently and complement one another:

1. input interface;
2. automatic multi-linearization tool;
3. dynamic characteristics interface;
4. SPO2IDA module;
5. *EDP* conversion tool;

6. limit-state definition interface;
7. additional variability management tool;
8. fragility parameter-fitting module.

These modules are organized into two toolboxes on the main GUI and operate according to the flowchart of Figure 10.

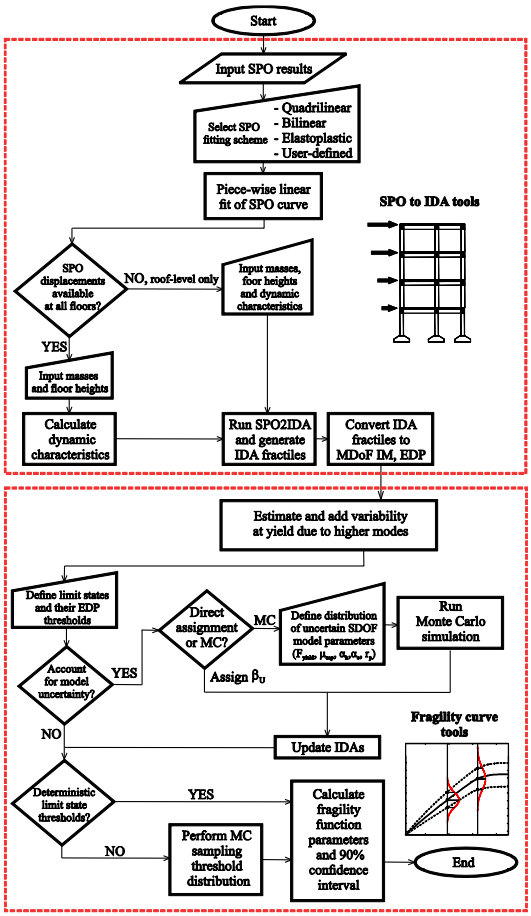

Figure 10. SPO2FRAG flowchart, schematically showing the grouping of the sub-modules into "SPO2IDA tools" and "Fragility curve tools".

2.4.5.1 Data input and definition of equivalent SDOF system

The SPO2FRAG tool does not include structural analysis code and operates on the premise that the necessary static non-linear and any optional modal analysis are performed externally. Therefore, any SPO2FRAG project starts at the data input interface, which reads SPO force-displacement results from either a text or a spreadsheet file.

The user is advised to provide SPO displacements at all storeys (rather than just at roof level) since this lateral deformation profile δ_i can then be used by the program to compute the COD according to Equation (12), permitting a direct SPO-based conversion of RDR to IDR – Equation (11). During input, the SPO curve is subjected to some rudimentary checks for correctness and consistency. Subsequently, the roof displacement – base shear values are forwarded to the automated piece-wise linear fitting module.

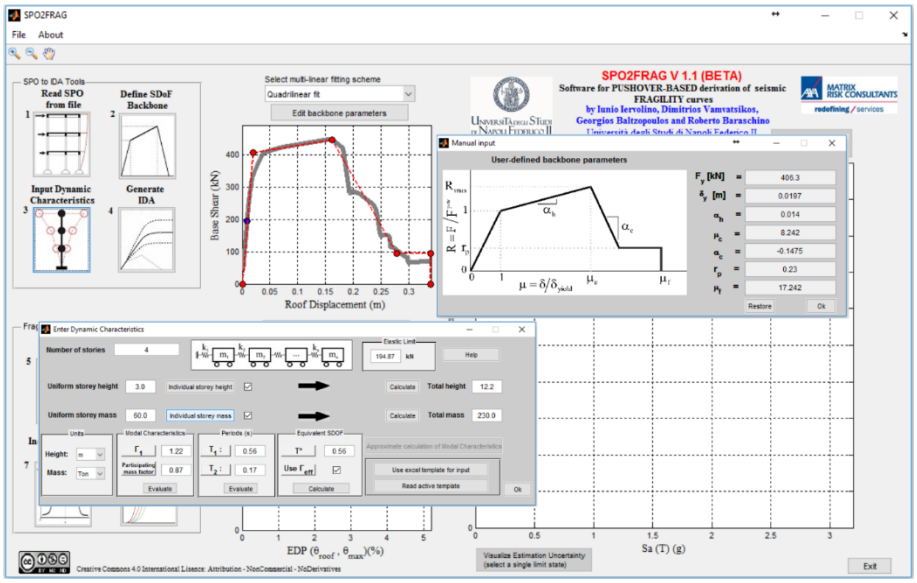

Figure 11. Multi-linear backbone definition for the equivalent SDOF system and input of dynamic and geometric characteristics of the MDOF structure (spring-mass representation is purely indicative) within the SPO2FRAG GUI.

The multi-linear fit module is intended to aid the user in the definition of the equivalent SDOF backbone curve and allows for the options listed below:

- *Quadrilinear fit*; the SDOF backbone curve receives a piece-wise linear fit based on the work of [69], potentially comprising a maximum of four segments: elastic, hardening, softening and residual strength. Corresponding parameter values are determined via a Monte-Carlo-based optimization algorithm.
- *Bilinear fit*; two-segment (elastic-hardening) fit in the spirit of the FEMA-356 displacement coefficient method [64], again according to criteria set forth by [69].

- *Elastic-perfectly plastic fit*; simple bilinear elastoplastic fit based on area balancing, compatible with code prescriptions (e.g., [63]), ending when strength drops below 80% of maximum (or at the last available SPO point).
- User-defined backbone parameters: manual input by the user.

The multitude of fitting-scheme choices is intended to accommodate various levels of refinement in the numerical modelling, at the user's discretion. The user is also given the option to intervene and override any of the automatically assigned backbone parameters.

Once the backbone parameters have been established, data input continues with the dynamic characteristics and geometric configuration of the structure (Figure 11). Additional data required at this stage consist of floor masses and storey heights, the first and second mode vibration periods and the participating mass factor. In cases where the user has provided SPO displacement values at all storeys, SPO2FRAG offers the option of internally approximating the modal participation factor, participating mass and first-mode period. First of all, a segment of the SPO curve is sought that corresponds to linear-elastic response (within a certain tolerance). The force (base shear) and *i*-th floor displacement values at the end of said segment are denoted as F_{el} and $\delta_{el,i}$, $i=\{1,...,n\}$ with n corresponding to the top-most storey, as per the convention of Figure 7. By making the assumption that the lateral force profile sufficiently approximates the first modal load vector, Γ, T_1 and the participating mass, $\tilde{m}$, can be automatically estimated by the program according to Equation (18).

$$\begin{cases} \Gamma \approx \delta_{el,\mathrm{n}} \cdot \left(\sum_{i=1}^{n} m_i \cdot \delta_{el,i} \right) \Big/ \left(\sum_{i=1}^{n} m_i \cdot \delta_{el,i}^2 \right) \\ \tilde{m} \approx \dfrac{\left(\sum_{i=1}^{n} m_i \cdot \delta_{el,i} \right)^2}{\sum_{i=1}^{n} m_i \cdot \delta_{el,i}^2 \cdot \sum_{i=1}^{n} m_i} \\ T_1 \approx 2\pi \cdot \sqrt{F_{el} \Big/ \left(\sum_{i=1}^{n} m_i \cdot \delta_{el,i} \right)} \end{cases} . \qquad (18)$$

This is also the point where the user is called upon to decide whether to opt for the SDOF to MDOF *EDP* conversions using Γ_{eff} as per Equation (13) or to

simply set $\Gamma = \Gamma_{eff}$. The former choice can add accuracy to the approximation for structures with non-negligible higher-mode contribution to the response, while the latter is a cautionary choice for cases when the user desires to employ some particular backbone fit of his own devising.

2.4.5.2 The SPO2IDA module and SDOF to MDOF conversions

Once the data input and multi-linear fit of the SPO curve phases have been concluded, the SPO2IDA module is activated, providing the approximated 16%, 50% and 84% IDA fractile curves in $\{R, \mu\}$ terms. This SPO2IDA output is internally converted into $Sa(T^*, 5\%)$ versus drift coordinates. In cases where the SPO displacements at all storeys have been provided, the default is to convert the IDAs into IDR with the aid of Equation (12); otherwise, RDR is employed, as estimated via Equation (11). In the latter case, the user is still given the option to switch to IDR, using the approximate Equations for the lateral post-yield deformation profile suggested in FEMA P-58-1 [72].

2.4.5.3 Definition of performance limit states

By default, SPO2FRAG recognizes five seismic performance limit states, but the user is given the choice to add or remove limit states for each project. The first four limit states are labeled *fully operational*, *immediate occupancy*, *life safety* and *collapse prevention* (see [73]). The fifth limit state, labeled *side-sway collapse*, is added by SPO2FRAG when the SPO curve exhibits strength degradation in the form of a negative-stiffness branch. This limit state corresponds to dynamic instability and is matched to the IDA flat-lines, without requesting any further user-input. The user may also opt to introduce any non-simulated collapse modes by appropriately truncating the SPO curve, whereby this limit-state (and the corresponding flatlines) more reliably indicate the occurrence of global collapse. For the remainder of the limit states, the user is expected to define thresholds in terms of *EDP* that determine each one's exceedance. Exceedance thresholds may be inserted explicitly or defined on the SPO curve (e.g., at specified values of global ductility or percentage of peak strength loss), via a dedicated tool contained in the limit-state module (Figure 12). An additional option available to the user is to treat some or all of these exceedance thresholds as random variables by assuming that they follow a lognormal distribution. In this case, the threshold *EDP* value is taken as the median value and the user must define the log-standard deviation as well.

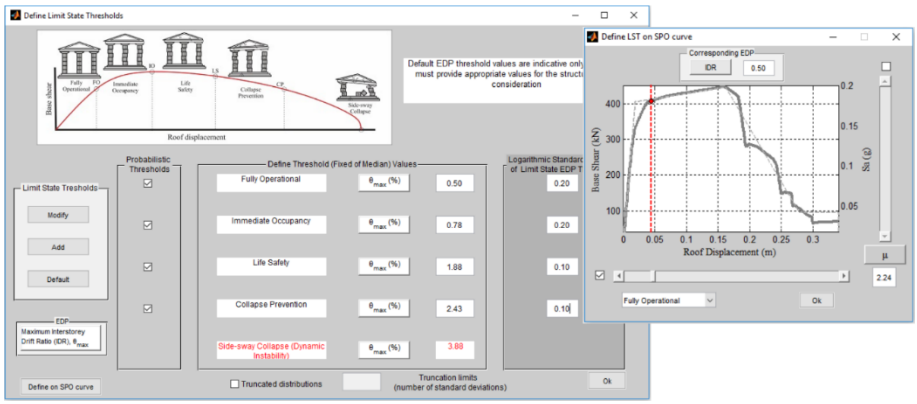

Figure 12. Limit-state threshold definition window and subsidiary tool for operating on the SPO curve while defining the thresholds.

2.4.5.4 Managing additional sources of variability

At this point, even though SPO2FRAG has accumulated sufficient information to be able to proceed with the estimation of the fragility function parameters according to Equation (15), two issues pertaining to the introduction of additional response variability remain to be addressed on an optional basis. The first of these issues is the fact that, prior to nominal yield, the MDOF system exhibits record-to-record variability that has not yet been accounted for in the SDOF to MDOF transformation, resulting in the 16% and 84% IDA fractiles temporarily coinciding with the median for drift values corresponding to $R \leq 1$. This shortcoming can be remedied at this juncture by injecting an estimate for this missing variability at nominal yield, which is then propagated along the IDA 16% and 84% fractiles. Users may employ the values automatically provided by SPO2FRAG, according to Equation (14), or override them with their own values from external analysis (e.g., as suggested by [62]). This addition can be important when the fragilities of high-performance limit states are of interest (i.e., those corresponding to practically unscathed post-earthquake functionality of the building).

The second optional issue concerns cases where one wishes to account for model uncertainty in the fragility curves. This translates to additional response variability, which can be incorporated into the approximated SPO2FRAG IDA curves by symmetrically (in log-space) distancing the 16% and 84% fractiles away from the median. This only leaves the parameter β_U to be determined for each limit state and the corresponding SPO2FRAG module offers two options for doing so (Figure 13). The first option entails user-definition of a β_U value

at one of the predetermined limit states. This value could be obtained from the technical literature and should be appropriate for the structure and the level of modeling sophistication at hand. This additional uncertainty is then propagated along the IDA curves in a manner that ensures their monotonicity.

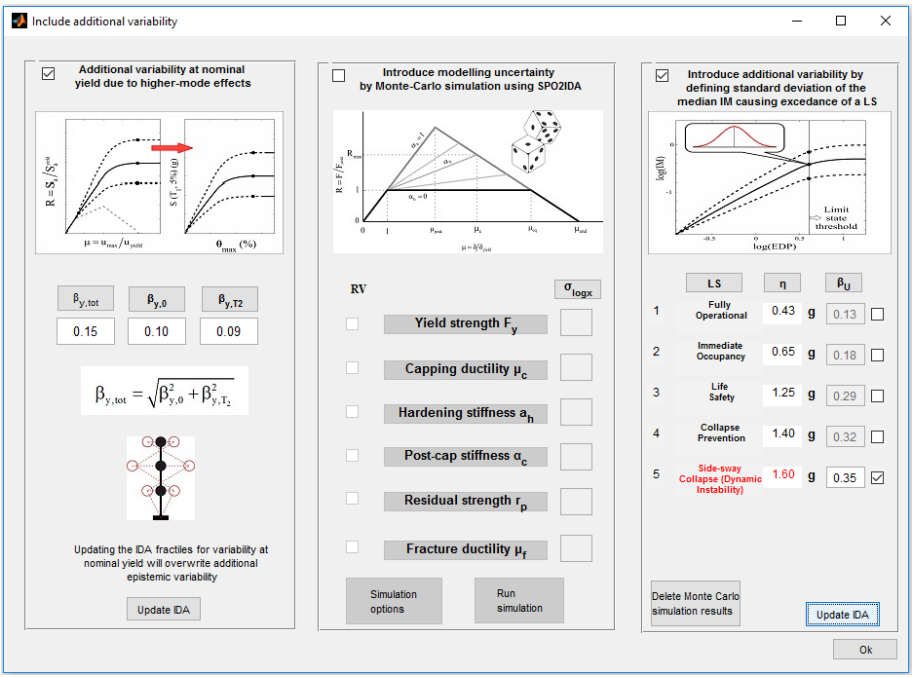

Figure 13. SPO2FRAG's window for the additional variability management module.

The second option is to estimate β_U via a combination of SPO2IDA and Monte Carlo simulation. In this second case, some of the parameters that define the equivalent SDOF backbone are treated as lognormally distributed, independent random variables, whose variance is determined by the user (the median is taken by default as the value defining the current equivalent SDOF backbone). According to this methodology, a number of M Monte Carlo realizations of the backbone are created by sampling from these distributions and subsequently SPO2IDA is used to obtain the median intensity per limit state exceedance for the *j*-th backbone realization, $\left(Sa_{f,50\%}^{LS}\right)_j$, $j=\{1,...,M\}$. Then, β_U can be estimated according to Equation (19).

$$\beta_U = \sqrt{\frac{1}{M-1}\cdot\sum_{j=1}^{M}\left[\ln\left(Sa_{f,50\%}^{LS}\right)_j - \frac{1}{M}\cdot\sum_{i=1}^{M}\ln\left(Sa_{f,50\%}^{LS}\right)_i\right]^2}\ . \qquad (19)$$

This operation follows the spirit of the methodology of [33], the difference being that, in this case, the Monte Carlo simulations are performed by sampling directly the piece-wise linear equivalent SDOF backbones, rather than by executing new SPO analysis runs.

2.4.5.5 Fragility curve parameters

Upon the conclusion of the preceding operations (even without consideration of additional uncertainty) the fragility function estimation module may be activated. At this point, SPO2FRAG will query the user regarding the damping ratio ζ characterizing the structure and the choice of estimator for the dispersion parameter (see also Figure 10). The former information is needed whenever a correction for $\zeta \neq 5\%$ should be applied to the estimated logarithmic mean according to Equation (17), while the latter provides an alternative to the estimation of β given in Equation (15): Instead of using the log-space distance between the 50th and the 16th percentile failure intensities, one may opt to use instead the log-space half-distance between the 84th and 16th percentiles, $\beta = 1/2 \cdot \ln\left(Sa_{f,84\%}^{LS} / Sa_{f,16\%}^{LS}\right)$.

SPO2FRAG uses Equation (15) by default for two reasons. If one selects, among alternative SPO lateral force profiles, the one that leads to the earliest failure of the structure (as recommended by [62]) the SPO-based backbone will correspond to that single collapse mechanism. On the other hand, IDA of the MDOF structure will reveal a variety of collapse mechanisms for different records – see for example [74]. Recognizing that the IDA curves corresponding to the more favorable collapse mechanisms should be more influential towards the shape of the 84% failure intensity fractile, it is to be equally expected that the more unfavorable (e.g., soft-storey mechanisms) similarly dominate the 16% fractile. Hence, one concludes that choosing the most unfavorable SPO lateral load profile could result in the lower (50% and 16%) fractile curves being better approximated through SPO2IDA than the 84% one. The second reason is that Equation (15) may be regarded as compatible with a *truncated IDA* analysis strategy (e.g., [55]), where an analyst chooses to run IDA but only scale records up to a certain *IM* level (e.g., until 50% of records induce collapse). This truncated IDA scheme may be dictated by the desire to avoid

any scaling bias that might lurk above the considered *IM* limit (see for example [36]).

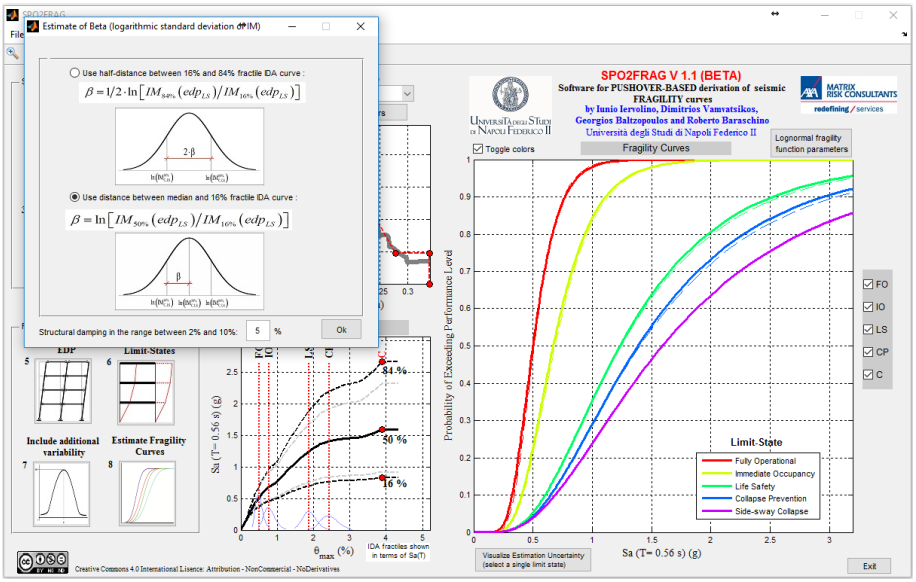

Figure 14. SPO2FRAG's dialogue window upon activation of the fragility-function estimation module.

For all limit states that have been assigned deterministic exceedance thresholds, estimation of the lognormal fragility function parameters $\{\eta, \beta\}$ proceeds as described in detail in paragraph 2.4.4. In cases where some limit states have been assigned exceedance thresholds with an associated lognormal probability density, the fragility function is estimated by means of numerically evaluating, via Monte Carlo, the integral resulting from application of the total probability theorem:

$$P\left[IM_f^{LS} \le im\right] = \int_{EDP_f} \Phi\left[\frac{\ln(im) - \eta_{edp_f}}{\beta_{edp_f}}\right] \cdot f_{EDP_f}\left(edp_f\right) \cdot d\left(edp_f\right). \qquad (20)$$

In Equation (20), $f_{EDP_f}\left(edp_f\right)$ is the probability density function of EDP_f and η_{edp_f}, β_{edp_f} are the logarithmic mean and standard deviation of IM_f^{LS} conditional on the limit state threshold assuming each specific value $EDP = edp_f$. A noteworthy result of normal theory applicable in this case is

that, when $f_{EDP_f}\left(edp_f\right)$ is a lognormal density, then $P\left[IM_f^{LS} \le im\right]$, as given by Equation (20), also follows the lognormal model.

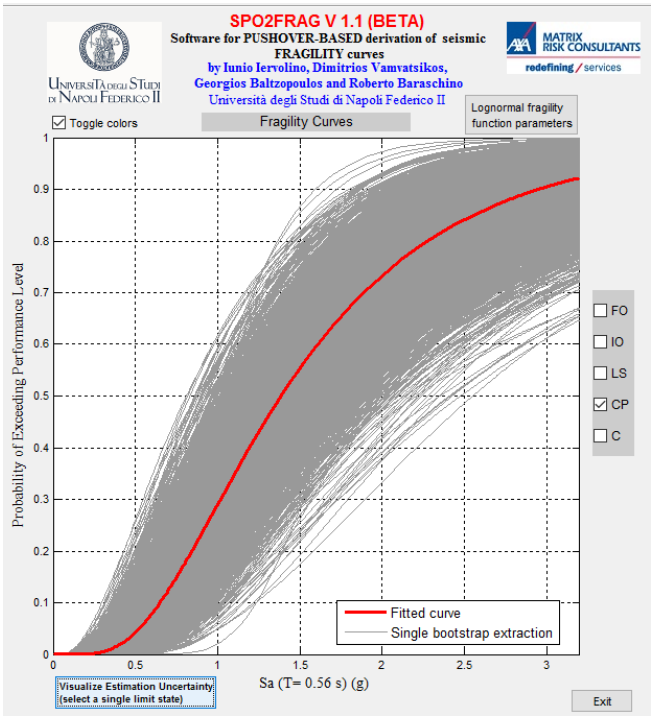

Figure 15. Visualization of estimation uncertainty underlying the fragility parameter estimates with the aid of a parametric-bootstrap-generated set of alternative fragility curves.

2.4.5.6 Consideration of estimation uncertainty

The SPO2FRAG tool estimates seismic fragility according to the *IM*-based procedure described in Section 2.3, by simulating dynamic analysis results via the SPO2IDA algorithm. Since the SPO2IDA Equations were fit against IDA responses to a suite of thirty recorded accelerograms [23], the fragility parameter estimates provided by SPO2FRAG can be implicitly regarded as (fixed-size) sample estimators of a Gaussian model's parameters. As such, the estimators for the mean and variance are probabilistic results that are affected by uncertainty of estimation, i.e., the uncertainty inherent in estimating the mean and variance of a population based on an extracted finite-size sample [75].

Since quantification of estimation uncertainty associated with structural fragility may be of interest for the seismic risk analyst, SPO2FRAG calculates the boundaries of the 90% confidence interval for each limit state's parameter

estimates. Furthermore, SPO2FRAG also provides the user with a visual representation of the estimation uncertainty associated with the fragility curves obtained, shown in Figure 15. The plot depicted is generated using parametric bootstrap [76]. The parametric bootstrap belongs to a family of resampling schemes for the approximate calculation of estimator statistics and is simulation-based. In the case at hand, a fixed number of twenty-five hundred bootstrap samples of size thirty are extracted from the Gaussian distribution defined by the SPO2FRAG-estimated fragility parameters. Then, a new pair of lognormal fragility parameters is re-estimated for each extraction. Finally, the fragility functions corresponding to each bootstrap extraction are plotted against the originally fitted fragility curve, resulting in Figure 15.

2.4.6 Illustrative SPO2FRAG applications

In order to be able to illustrate SPO2FRAG's function and compare the resulting fragility functions with their dynamic-analysis-derived counterparts, two applications on MRFs are presented where seismic fragility functions are obtained both by means of SPO2FRAG and via IDA.

2.4.6.1 Structures, numerical models and set of ground motions used in the analyses

The two case-study structures used in these examples are a four-storey steel MRF and a six-storey RC-MRF. The four-storey steel MRF (Figure 16a) belongs to a set of archetype structures designed and employed for the purposes of the NIST GCR 10-917-8 report [77]. On the other hand, the six-storey RC-MRF (Figure 16c) was designed and used by [78], where information on member detailing can be found.

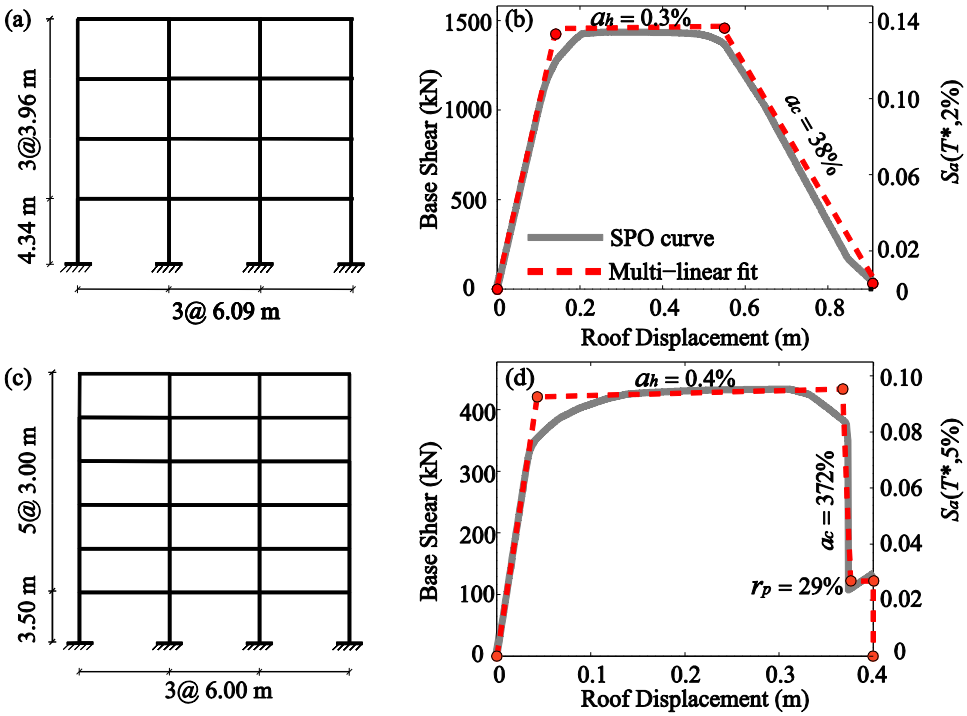

Figure 16. Geometry of centerline idealizations of the two MRFs and corresponding SPO curves. Four-storey steel MRF geometry (a) and SPO (b). Six-storey RC-MRF geometry (c) and SPO (d).

Both frames were modelled numerically using 2D centerline finite element representations in the OpenSees structural analysis platform [79]. Material non-linearity was accounted for using a concentrated plasticity approach. The properties of the monotonic backbone of the plastic hinges at member edges were estimated using the regression Equations suggested by [42] for the steel and those by [80] for the RC frame, while a moderately pinching hysteretic law proposed by [39] was assigned to both. Structural damping of $\zeta = 2\%$ was assumed for the steel and $\zeta = 5\%$ for the RC frame, modelled according to the recommendations of [81]. Geometric non-linearity in the form of $P-\Delta$ effects was also taken into account. The SPO curves of both frames, obtained using first-mode-proportional load patterns, are shown in Figure 16, along with the equivalent SDOF backbone of their SPO2FRAG elaboration.

For the purpose of running IDA with these numerical structural models, a set of eighty recorded accelerograms was assembled. This set includes the twenty-two ground motions of the far-field set in FEMA-P695 [52], which was

enriched by another eighteen records from the Engineering Strong Motion database (http://esm.mi.ingv.it). Both recorded horizontal components at each station are applied to the plane structural models separately. Overall, the ground motion suite includes records from events with magnitude from 6.0 to 7.6, recorded at distances from 5 to 50 km on firm soil (EC 8 classification A, B or C), not containing relevant directivity effects and exhibiting *PGA* in the range from 0.12 to 0.90g.

2.4.6.2 Comparison of IDA- and SPO2FRAG-based fragility estimates

Both structures were subjected to IDA using the set of eighty accelerograms described above, while their SPO curves were used to simultaneously run fragility estimates in SPO2FRAG. In order to limit the number of required analyses to reasonable levels, IDA was run using the hunt-and-fill algorithm proposed by [51]. For both structures, limit state exceedance thresholds were defined in terms of IDR. Immediate occupancy, life safety and collapse prevention IDR thresholds were determined using the SPO results, by imposing the maximum plastic rotation acceptance criteria of FEMA-356 to the critical elements (first-storey columns). The fully operational threshold was set to 0.5% IDR for the RC-MRF and near the nominal yield for the steel MRF. Global collapse was left to be automatically determined by SPO2FRAG based on the predicted flat-line heights of the IDA fractiles for the RC-MRF (thus mainly corresponding to side-sway collapse) while for the steel MRF it was set to the IDR corresponding to 50% loss of strength measured on the SPO curve, by using the relevant in-built tool (e.g., Figure 12) to capture additional modes of failure that may be expected to appear at such large drifts.

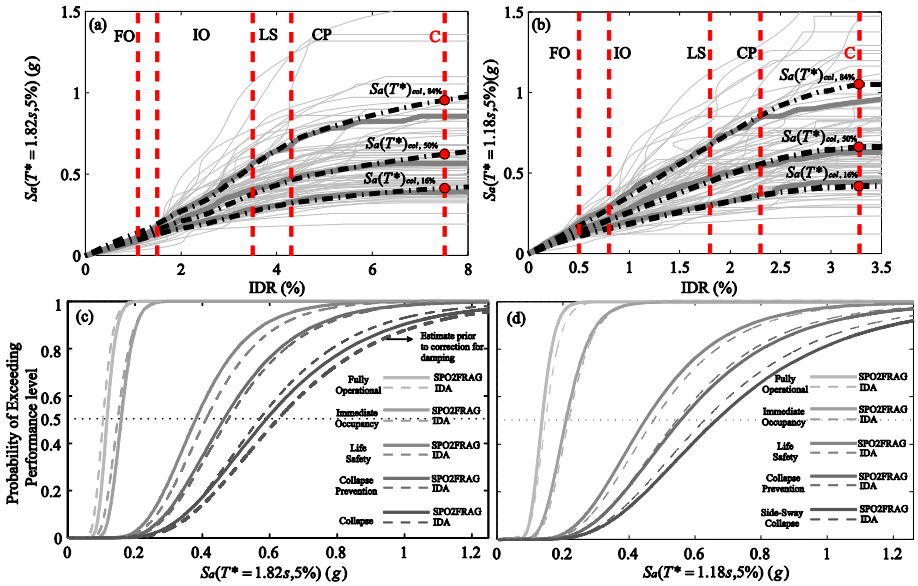

Figure 17. Analytical IDA curves and corresponding SPO2FRAG predictions for (a) the four-storey steel MRF and (b) the six-storey RC-MRF. Comparison of IDA- and SPO2FRAG-based lognormal fragility functions per limit state for (c) the four-storey steel MRF and (d) the six-storey RC-MRF.

Furthermore, for the steel four-storey MRF, Γ_{eff} according to Equation (13) was employed due to the more flexible frame's higher-mode sensitivity and the correction due to $\zeta \neq 5\%$ was applied according to Equation (17). Finally, the default choice of Equation (15) was employed for the estimation of dispersion in both cases (see also Figure 14).

In Figure 17 the IDA results, for both structures, can be seen with the SPO2FRAG predictions superimposed. Additionally, the fragility curves obtained for each limit state by SPO2FRAG are presented for comparison with the same curves derived from the IDA results using Equation (21) for the estimate of β, where the index $i=\{1,...,N\}$ refers to the response to the *i*-th accelerogram.

$$\beta = \sqrt{\frac{1}{N-1}\cdot\sum_{i=1}^{N}\left[\left(\ln\left(Sa_{C,i}^{LS}\right)-\ln\left(Sa_{C,50\%}^{LS}\right)\right)^2\right]} \qquad (21)$$

The corresponding parameter estimates are provided in Table 1 and Table 2. In order to get an appreciation of the effect that the choice of employing Γ_{eff} (a choice made for the case of the steel MRF alone) bears on these results, it is

mentioned that the SPO2FRAG prediction of median intensity at collapse for the four-storey steel MRF using Γ is 0.60g (compare with 0.59g in Table 1 resulting from using Γ_{eff} instead). On the other hand, for the six-storey RC-MRF, the choice of using Γ_{eff} or Γ leaves the median collapse intensity practically unaffected.

Table 1. Lognormal fragility function parameter estimates from SPO2FRAG and IDA and corresponding annual limit-state exceedance rates (events/year) for the four-storey steel MRF assumed to be situated at L'Aquila.

Limit state	$\exp(\eta)$ (IDA)	β (IDA)	$\exp(\eta)$ (SPO2FRAG)	β (SPO2FRAG)	λ_f (IDA)	λ_f (SPO2FRAG)
Fully Operational	0.105 g	0.223	0.117 g	0.189	$6.7\cdot10^{-3}$	$5.7\cdot10^{-3}$
Immediate Occupancy	0.149 g	0.239	0.159 g	0.197	$4.0\cdot10^{-3}$	$3.6\cdot10^{-3}$
Life Safety	0.410 g	0.340	0.379 g	0.334	$7.1\cdot10^{-4}$	$8.3\cdot10^{-4}$
Collapse Prevention	0.476 g	0.364	0.463 g	0.364	$5.3\cdot10^{-4}$	$5.7\cdot10^{-4}$
Collapse	0.569 g	0.383	0.589 g	0.409	$3.7\cdot10^{-4}$	$3.6\cdot10^{-4}$

Table 2. Lognormal fragility function parameter estimates from SPO2FRAG and IDA and corresponding annual limit-state exceedance rates (events/year) for the six-storey RC-MRF assumed to be situated at Ancona.

Limit state	$\exp(\eta)$ (IDA)	β (IDA)	$\exp(\eta)$ (SPO2FRAG)	β (SPO2FRAG)	λ_f (IDA)	λ_f (SPO2FRAG)
Fully Operational	0.147 g	0.256	0.136 g	0.226	$1.3\cdot10^{-3}$	$1.5\cdot10^{-3}$
Immediate Occupancy	0.217 g	0.278	0.208 g	0.288	$5.5\cdot10^{-4}$	$6.1\cdot10^{-4}$
Life Safety	0.473 g	0.403	0.448 g	0.407	$9.4\cdot10^{-5}$	$1.1\cdot10^{-4}$
Collapse Prevention	0.544 g	0.421	0.555 g	0.434	$6.7\cdot10^{-5}$	$6.6\cdot10^{-5}$
Collapse	0.627 g	0.446	0.662 g	0.458	$4.9\cdot10^{-5}$	$4.4\cdot10^{-5}$

2.4.6.3 Comparing SPO2FRAG and IDA results in the context of seismic risk assessment.

In order to better appreciate the agreement between the SPO2FRAG and IDA results, integration with seismic hazard was performed by plugging Equation (2) into Equation (1), thus obtaining estimates of the annual exceedance rate for each limit state (without considering estimation uncertainty for the sake of simplicity).

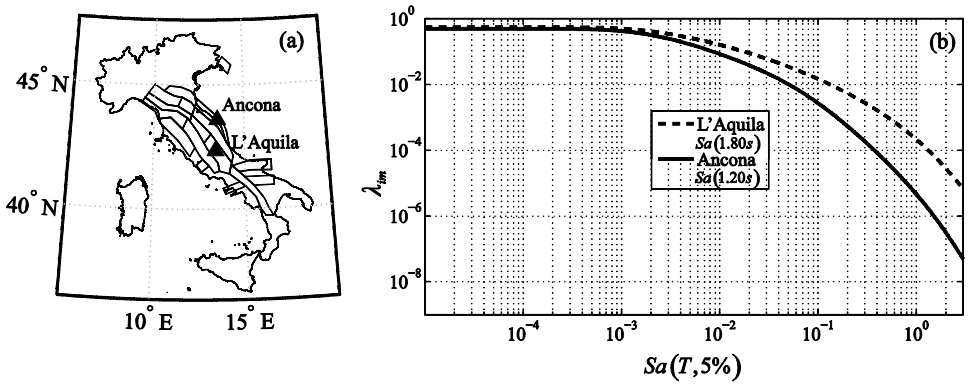

Figure 18. Map of Italy showing the two sites of interest and the seismic sources considered for the seismic hazard calculations (a) and calculated hazard curves to be integrated with structural fragility of the case-study examples (b): annual exceedance rate of $Sa(1.80s,5\%)$ *at L'Aquila and the same for* $Sa(1.20s,5\%)$ *at Ancona. As the* [82] *ground motion prediction Equation is employed, the closest available periods to* T^* *are used for each case to avoid interpolation.*

To be able to do so, it was assumed that the 4-storey steel MRF is situated at a site near the Italian city of L'Aquila and the 6-storey RC-MRF at a site near the Italian port-town of Ancona. For both of these sites, the seismic hazard was calculated with the aid of the REASSESS software [83], assuming firm soil conditions. The hazard at these sites was calculated using the seismic source model from [84], seismicity rates from [85,86] and the ground motion prediction equation proposed by [82]. The annual exceedance rates of the 5%-damped spectral acceleration at T^* are shown in Figure 18. The calculated annual rates of limit-state exceedance are included among the results reported in Tables 1 and 2. The good agreement between the SPO2FRAG and analytically-derived estimate is evident.

2.5. Graphical interface for dynamic analysis of single-degree-of-freedom systems: DYANAS tool.

2.5.1 Software structure and graphical user interface

DYANAS is structured around two main pillars: the various MATLAB-coded pre- and post-processing tools that are incorporated into the GUI and the suite of parametric scripts that run directly on the OpenSees platform. In order to run an analysis defined by the user via the MATLAB GUI, OpenSees must be provided with Tcl/Tk scripts that contain definition of the numerical model, loading, and the analysis' operational parameters, including what response information to save. These Tcl/Tk scripts are divided into two categories: parametric and definition files. Parametric scripts contain all the information necessary for model definition and execution of analysis in OpenSees, as functions of externally-defined placeholder variables or as hard-coded analysis parameters; these files remain unchanged during any analysis session of the software (unless the user decides to make a direct, outside intervention of course). On the other hand, the definition files are constantly over-written by the GUI's pre-processing tools, according to user input and system definition. Once OpenSees concludes a packet of user-requested analyses, output files are created, that are subsequently parsed by the GUI's post-processing MATLAB routines for further elaboration of the raw results. This procedure is schematically depicted in the flowchart of Figure 19.

The pre-processing, (system and analysis definition) functionalities of the GUI can be further split into two main groups: definition of the SDOF system characteristics, such as dynamic properties, backbone curve and the rules governing hysteretic behavior, and definition of the type of analysis, including definition of controlling parameters and handling of dynamic input. The post-processing tools, on the other hand, enable organizing, plotting and extracting specific subsets of the results, in various common formats, useful within the PBEE framework. The remainder of this section describes the salient features of the functionalities outlined above.

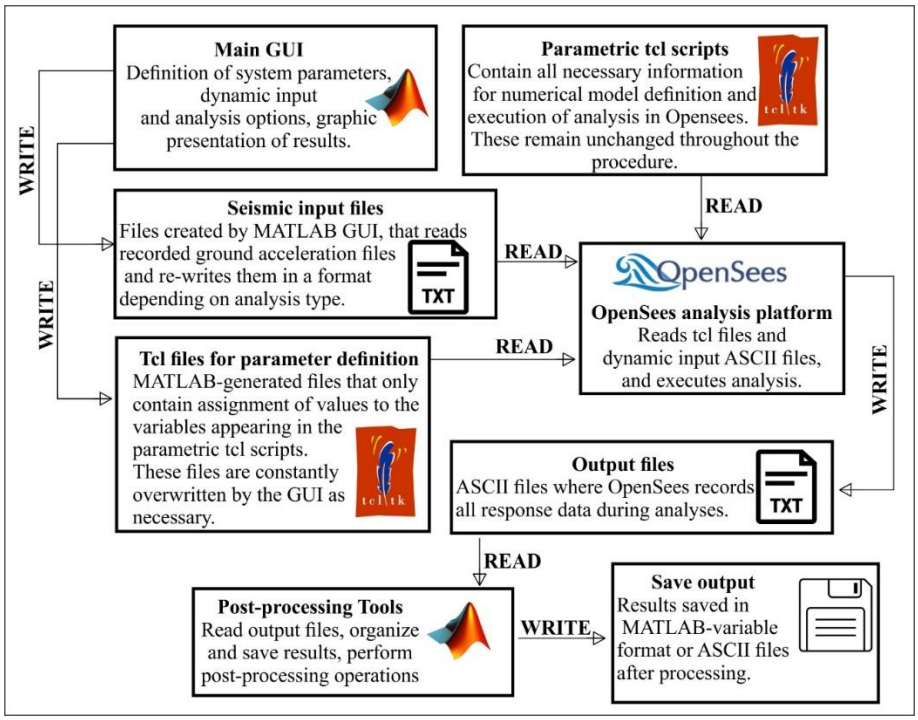

Figure 19. Operational flowchart of the DYANAS GUI's interaction with OpenSees.

2.5.1.1 Definition of oscillator characteristics, engineering demand parameter and seismic intensity measure

The first step in any new analysis session is the definition of the system to be analyzed, that may either be an SDOF oscillator or two uncoupled simple oscillators. In the latter case, two separate SDOF systems are defined and analyzed simultaneously, without any interaction occurring between them. This can be useful in the case of regular, symmetrical structures, for which equivalent SDOF systems may be defined via pushover in both principal directions [87].

In all cases, the SDOF system definition requires the assignment of dynamic characteristics, such as period of natural vibration T and viscous damping ratio ν (modelled as mass-proportional), backbone curve and hysteretic rule. The backbone curve corresponds to a piece-wise linear idealization of the force-displacement response of the system to monotonic loading and is defined by the yield strength and displacement, F_y and δ_y respectively, and up to four

parameters for a quadrilinear case, already defined in previous section, shown in Figure 20.

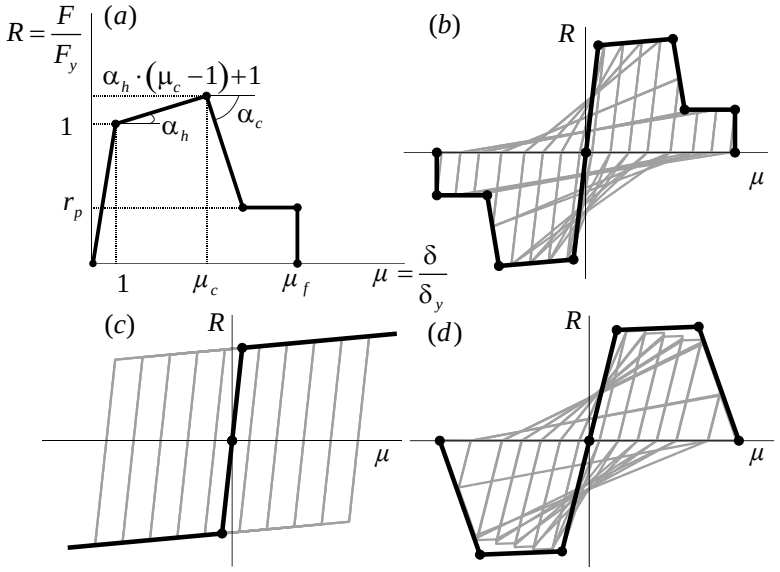

Figure 20. Definition of non-dimensional parameters for the characterization of an SDOF system's piece-wise linear backbone curve (a); backbone curve with descending branch, residual strength plateau and peak-oriented hysteretic loops (b); bilinear, kinematic hardening system (c); trilinear backbone exhibiting peak-oriented hysteretic behavior with moderate cylcic strength degradation.

A sample of the GUI's dialogue windows during the definition of backbone and other properties is provided in Figure 21.

As can be seen in the figure, the software permits the definition of asymmetric backbone curves, with μ_c, μ_f and F_y being allowed to differ in the two directions, while maintaining the same elastic stiffness. Regarding the choice of hysteretic constitutive law, several options that have been implemented in OpenSees in the past are available [37,39,42,88–90]. These are divided into two broad categories of peak-oriented and hardening hysteretic rules and some of them allow for evolutionary behavior, including cyclic strength and stiffness degradation. It should be noted that association of a backbone curve with a descending branch is meaningful only for the peak-oriented hysteretic behavior group; in such cases that include softening branches, in-cycle strength degradation can also emerge during dynamic response (whenever cycles exceed the μ_c limit – see also [91]). By means of

the “quasi-static cyclic” analysis type, the software offers the user a means to visualize the effect of each hysteretic rule on displacement-controlled cyclic loading.

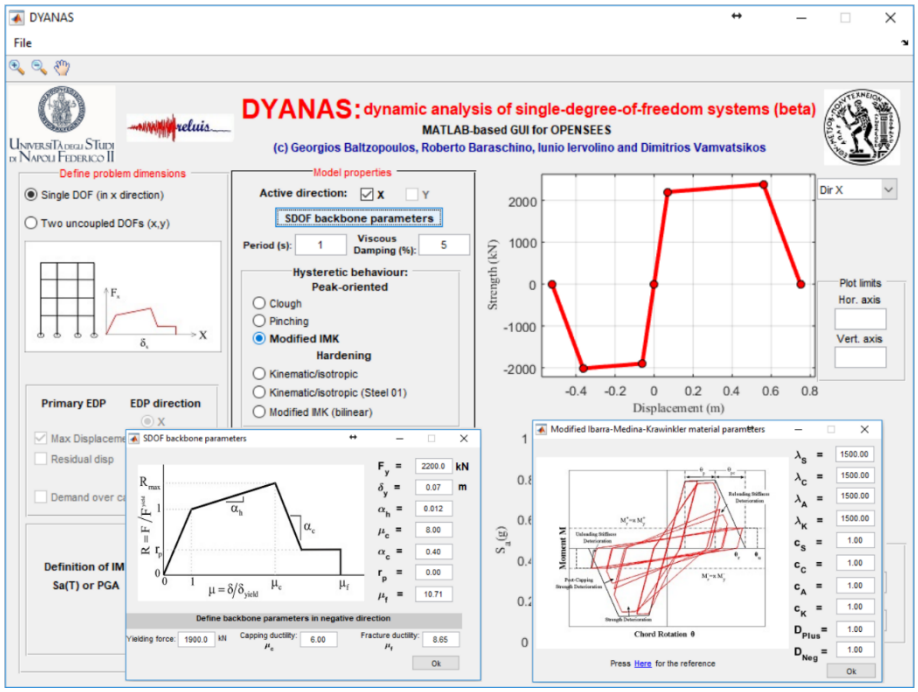

Figure 21. Main GUI window and subsidiary dialogue windows during definition of a SDOF oscillator’s dynamic characteristics, backbone curve (asymmetrical in this case) and hysteretic model.

The second preliminary step, prior to proceeding to the analysis, is to select the *EDP* and *IM* that will be employed. For such simple structures as these SDOF oscillators, the choice of *EDP* is limited to the peak transient displacement in either horizontal direction, δ_X and δ_Y, the residual displacements in both directions and the demand over capacity ratio, D/C. The D/C ratio expresses, in non-dimensional form, how close the structure comes to exhausting a threshold *EDP*. It also provides a means of defining an *EDP* that takes response in both directions into account, according to the definition in Equation (22), which is valid for all converging runs, where δ_f^X and δ_f^Y are the “failure” displacements in the corresponding directions (i.e., the *EDP* thresholds).

$$D/C = \max\left\{\delta_X/\delta_f^X, \delta_Y/\delta_f^Y\right\} \tag{22}$$

Although the actual choice of *IM* can be deferred until the analysis definition phase (the default option being $Sa(T)$ at the *X*-direction oscillator's vibration period), in the case of bi-directional ground motion (i.e., definition of two SDOF systems) the user should also determine how that *IM* is to be calculated: for example, $Sa(T)$ can be taken as the maximum between the values of the two components, $Sa_{\max}(T)$, or as the geometric mean of the two, $Sa_{gm}(T)$.

2.5.1.2 Running IDA and back-to-back IDA

Due to the particular shape of individual IDA curves, when attempting to adequately represent them by scaling all records at a fixed, constant step in terms of *IM*, the number of dynamic analyses that may be needed can prove overly time-consuming, even in the case of SDOF systems. DYANAS seeks to optimize required analysis time, by incorporating a MATLAB-programmed implementation of the "hunt-and-fill" algorithm [51], whereby the number of runs for each record is determined on the fly during analysis. According to this algorithm, after a few test-runs at characteristic *IM* levels, the software begins to determine the scale factor of the next run based on the history of previous results, resulting on a set of *EDP-IM* points on the curve – black dots in Figure 22 – that may be closer or farther apart between curves, in an attempt to use approximately the same number of runs for all curves, regardless of flat-line height. Then, the complete IDA curve (intermediate points – colored segments in Figure 22) is obtained by means of piece-wise interpolation between these calculation points on the *IM-EDP* plane. Both spline and linear interpolation are possible, with the former being the default option in DYANAS, as it results in smoother IDA curves.

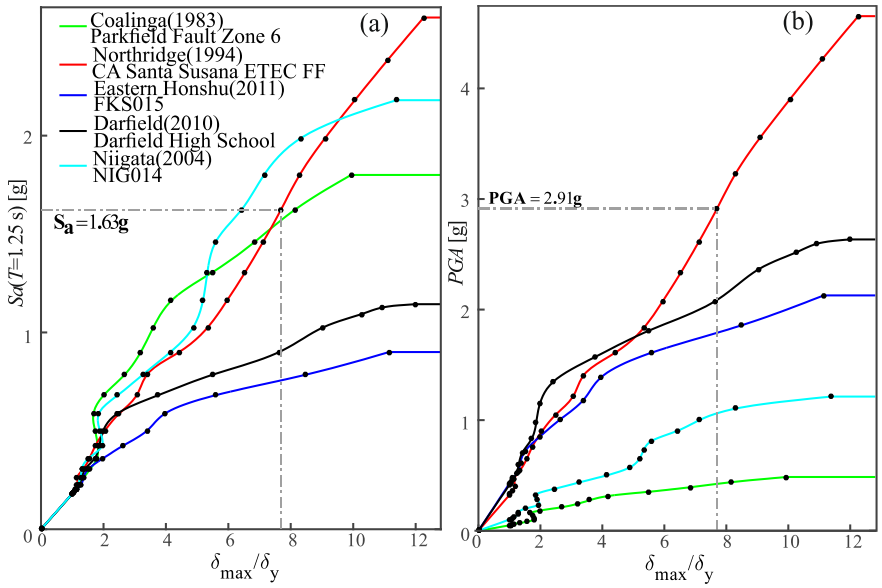

Figure 22. Conversion of IDA curves from five records between IMs: from $Sa\left(T=1.25\text{ s}\right)$ *(a) to PGA (b). The highlighted calculation point on one of the five records used for this example (event, year and recording station reported in the legend) shows the re-mapping of that point between the two panels, the PGA-to-spectral-ordinate ratio for that record being* $2.91/1.63$*. Herein the hunt-and-fill algorithm was stopped prior to evening out the total number of runs per curve, when each flatline was adequately captured.*

An additional advantage, provided by this computational strategy, is the possibility for nigh-instantaneous change of *IM*, once a set of IDA curves has been obtained. This *IM*-change operation can prove useful in a variety of situations, such as when a set of distinct structures must all have their seismic vulnerability functions expressed in a common *IM* [92] or when the same requirement occurs for the two principal orientations of a single structure [93] or simply for studying the relative merits of choosing one *IM* over another [60]. This is also demonstrated in Figure 22, where the conversion of a set of five IDA curves from spectral pseudo-acceleration, $Sa\left(T\right)$, at period $T=1.25\text{ s}$ to *PGA* is shown. Given that each explicit calculation point from the trace-IDA implementation, shown in the figure as a black dot upon the spline-interpolated curve, corresponds to a specific scale factor applied to that record, each *EDP* value at any of these points can be reassigned to the value that the new *IM* assumes on the record's scaled spectrum. After this re-mapping of the

calculation points to the new *IM* (in this example *PGA*) is complete, spline interpolation based on the new *IM-EDP* points provides the converted IDA curves.

The same computational strategy is also followed in the case of back-to-back IDA, with the only difference being in the management/definition of seismic input (to follow). At the conclusion of either of these types of analysis (IDA or back-to-back IDA) a set of post-processing options are available to the user: change of *IM* or *EDP*, extraction of *IM* or *EDP* stripes that can be saved into MATLAB-variable or text file formats and saving the analysis results for later use. Change of *EDP* offers a choice between δ_X , δ_Y , residual displacements and D/C ratio. Switching *EDP* is trivial, as all necessary *EDP* responses are recorded and saved during every single run. Conversion to different *IM*s, on the other hand, follows the re-interpolation procedure outlined earlier. For single-component ground motion, change of *IM* entails switching to a spectral ordinate at a different period T and/or different viscous damping ratio ν , with defaults being the *X*-direction SDOF's period of natural vibration and five percent, respectively. In the case of bidirectional motion, the definition of the *IM* with respect to the two horizontal acceleration components can also be changed among the already-mentioned alternatives being: $Sa(T)$ of either single component, $Sa_{\max}(T)$ or $Sa_{gm}(T)$.

Finally, the post-processing tools of the GUI can provide the extraction of text or MATLAB files containing IDA results organized as either vectors of *EDP* responses given *IM* ("*EDP* stripes") or *IM* causing exceedance of a specific *EDP* value ("*IM* stripes"). Such output formats may come handy when attempting to fit a parametric probabilistic model to a fragility function (the interested reader is referred to [55], for the nuances of fitting such a model in the *IM*- and *EDP*-based case). For *IM* stripe extraction (example provided in Figure 23), the software finds the intersection of each spline-interpolated IDA curve with the vertical line passing through the user-defined *EDP* threshold; the lowest *IM* value is returned in the case of non-monotonic IDA curves that intersect the line at more than one point. For *EDP* stripes, the user defines a vector of desired *IM* values and the software returns the intersections with the corresponding horizontal lines; for IDA curves that have already flat-lined below a given *IM* level, the information that the structure has collapsed is returned.

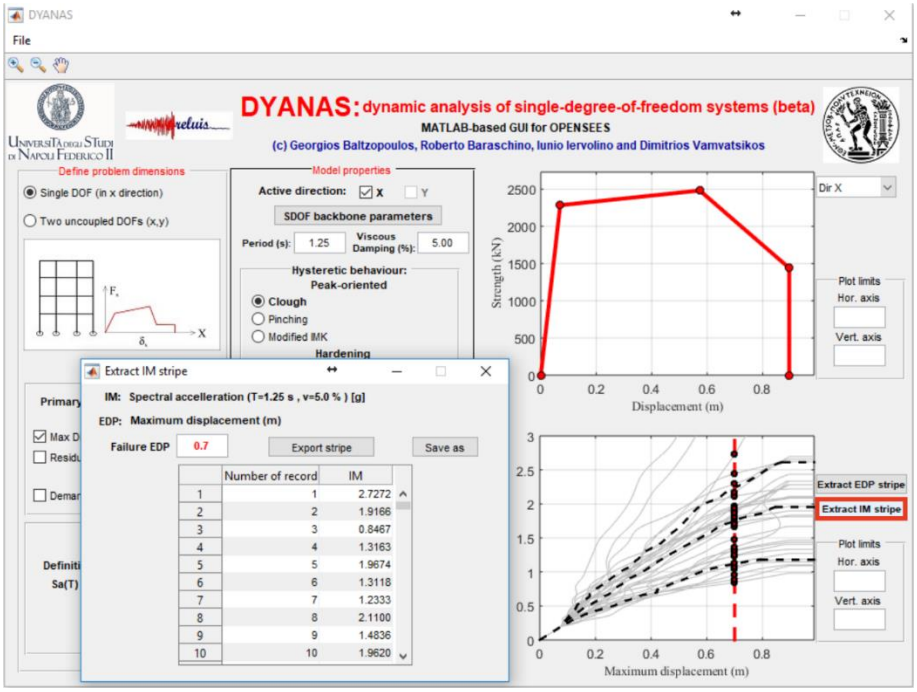

Figure 23. Extraction of an IM stripe from a set of IDA curves. The EDP threshold is defined in the homonymous dialogue window and the intersections with the curves are displayed in the main GUI lower-right window.

2.5.1.3 Running multiple-stripe and cloud analysis

To conduct MSA, the user must define all *IM* levels for which *EDP* responses are needed beforehand, via the dedicated dialogue window of the GUI (Figure 24), and subsequently assign a set of records to each *IM* stripe. Each stripe must be assigned a specific *IM* value and all records in the stripe will be then scaled to match that value (exception to that rule is cloud analysis, see below). Internally, analysis is run using the same MATLAB and OpenSees (Tcl/Tk) routines as for IDA, with the difference that record scaling is completely pre-determined at the start of the analysis and a different seismic input file has to be read at each single run. Note that, in the case of MSA, a change of *IM* requires re-running the analysis from scratch (unlike IDA – see above) while *EDP* still can be changed at will after completion of the analysis.

In the present GUI application and for reasons of convenience, cloud analysis is also managed via the MSA window, as one may imagine it as a single-record-per-stripe MSA. The user simply has to define a single *IM* stripe with a nominal intensity value, which is disregarded, and check the "do not

scale records" box; in that case the software will realize that could analysis is in order and will display the results accordingly, as shown in Figure 24. For both MSA and cloud analysis, *EDP* stripes can be exported in text- or MATLAB-file format, reducing to *IM-EDP* pairs in the latter case.

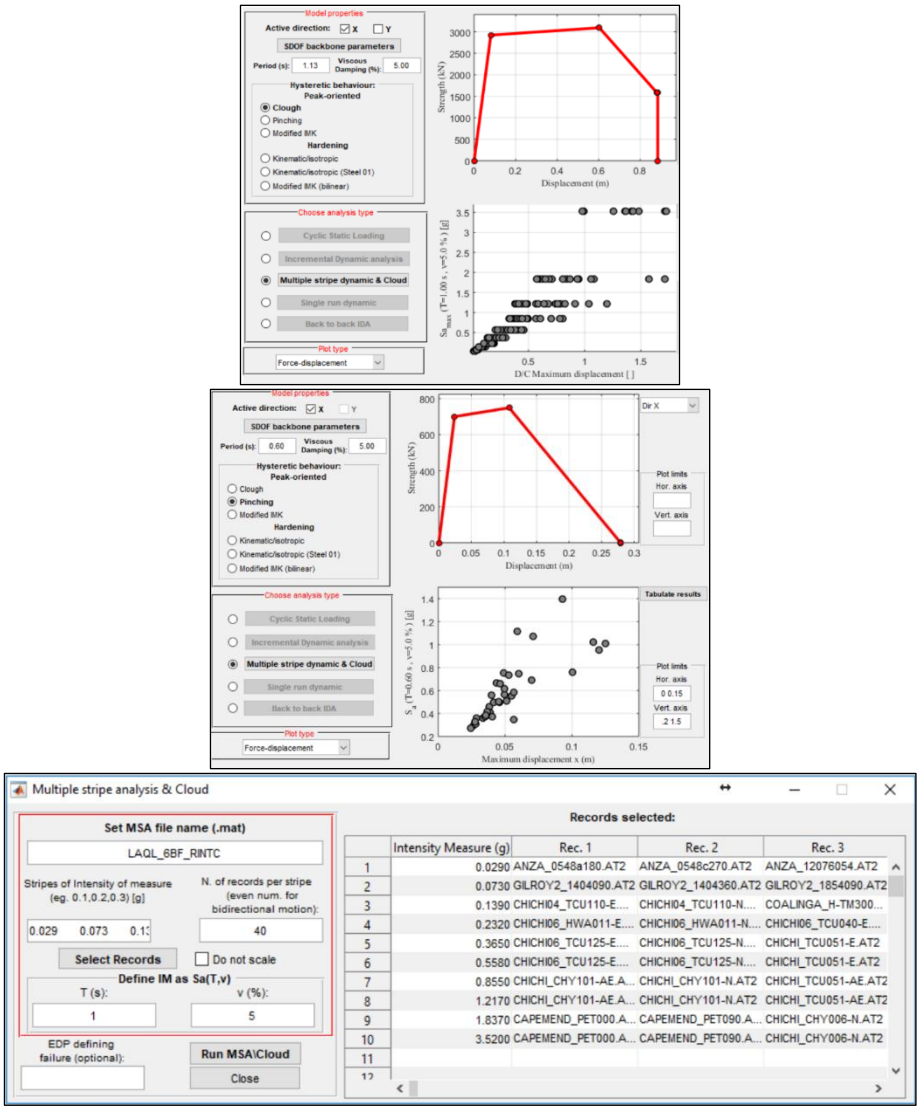

Figure 24. Main GUI window snapshots displaying the results of MSA (upper panel) and cloud analysis (middle panel); MSA dialogue window, showing the setting-up of an analysis at ten levels of seismic intensity (lower panel). All records in each stripe will be scaled to match that stripe's predefined IM level, unless the "Do not scale" checkbox is ticked, in which case cloud analysis runs.

2.5.1.4 Seismic input

Seismic input can be defined by selecting sets of ASCII files, each containing a recorded acceleration time-history. The software can parse two standard accelerograms formats, namely the Pacific Earthquake Engineering Research NGA database format [94] and the Engineering Strong Motion database format [95]. In either case, the necessary information for running the analyses are extracted/computed from the selected files (units, duration, sampling rate, elastic response spectrum) and passed on to the corresponding MATLAB routines, while the actual accelerometric data are written into temporary files suitable for being read by OpenSees. As an alternative to these standard formats, the user may use simple ".txt" ASCII files that contain a single column of acceleration values and will be inquired by the software to provide units and sampling rate.

The software, at this stage, is distributed equipped with two folders that already contain two sets of accelerograms: one is the suite of thirty single-component records used for calibrating the SPO2IDA tool and the other is the twenty-two bidirectional ground motion "far-field" set of FEMA-P695 [52]. Both record sets consist of accelerograms recorded on firm soil, predominantly during California events of magnitude six or greater.

For IDA or cloud analysis, a single set of records must be selected by the user, while, in the case of MSA, different sets may be assigned to each predefined *IM* level (stripe), all containing the same number of records. Cloud analysis in particular, is defined via the MSA control panel, by suspending record scaling, as discussed above. Back-to-back IDA on the other hand, requires two sets of records: the first set, referred to as the MS set, is used to perform a preliminary IDA analysis, that serves to determine the scale factors necessary to induce the predefined *EDP* value, associated with some structural limit state, across the entire MS record set. During any type of analysis, each record is followed by an appendix of zero acceleration entries for a duration of five times the elastic period of the system, intended to provide time for the residual velocity at the end of the excitation to be damped down to negligible values. This is performed internally in OpenSees, without tampering with the records, so that the next shock will find the system at rest. This procedure is implemented to achieve increased precision in the calculation of residual displacements, which is especially important in the case of back-to-back IDA.

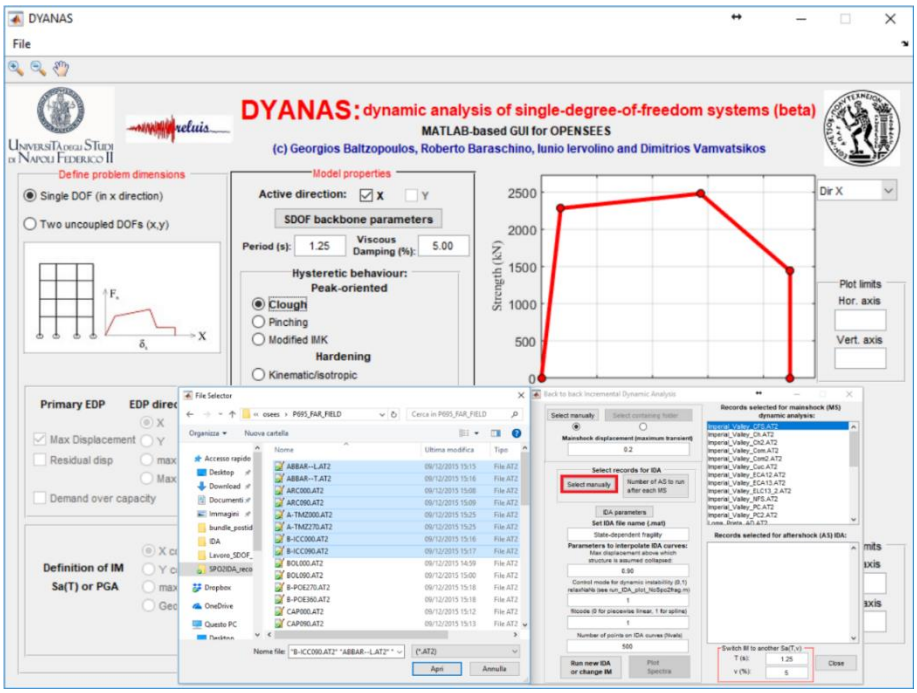

Figure 25. Selection of accelerograms for running back-to-back IDA; the MS record set list has been already filled and the record-selection dialogue window is open for designating the AS set.

The second set of accelerograms, referred to as the AS set, is used to run an IDA that always follows one of the MS records (the user is actually free to use the same set to represent both MS and AS if one so desires, or two sets of different size). In other words, each scaled AS record acts on a structure that has already experienced the predefined transient maximum *EDP* value and has had some time to come to quasi-rest conditions. In Figure 25 the analysis-parameter definition panel for back-to-back IDA is shown, with the AS acceleration-file selection-window open. The user is additionally given the option to define the number of AS IDAs that are going to be run per MS record, ranging from one to the number of records in the AS set. When the number of IDAs requested per MS is less than the number of AS accelerograms defined, a random extraction is performed from among the AS records (independent extractions are performed for each MS record). A final option available to the user for back-to-back IDA, is that one may request that all MS-AS pairs be created so that no AS record is ever used twice, provided that an adequate number of records has been provided.

In the case of bidirectional ground motion, record assignment proceeds as in the single-component-of-motion case, with the difference that all record sets must be even in number, so that they may be divided in two halves and re-assigned to each of the two directions. Pairing of the records follows the ASCII dictionary alphabetical order of the filenames, by assigning any two consecutive records first in the *X* and then the *Y* direction. This is intended to take advantage of the fact that, in most strong ground motion databases, accelerograms recorded by two streams of the same station will be typically saved under filenames differing by only a few characters.

2.5.2 Illustrative applications

In this section, some applications are provided as examples, in order to illustrate DYANAS' functionality in more practical terms. The first example uses a pair of relatively regular and symmetrical buildings, for which equivalent SDOF structures are considered in each principal direction, to provide applications of IDA and MSA. The second example deals with cloud analysis, while the third application presents the use of back-to-back IDA. In order to consolidate the usefulness of the GUI as a PBEE tool, some of these examples involve the calculation of fragility functions for SDOF structures, based on IDA results. However, it should be clear that the primary scope of the software is to use non-linear dynamic analysis to provide *EDP-IM* relationships, one natural use of which is the assessment of seismic structural fragility.

2.5.2.1 Two equivalent SDOF systems representing both principal directions of a building

For this example application, four static pushovers were used, corresponding to the two principal directions of two code-conforming, RC moment-resisting frame buildings. These two buildings, a three-storey frame with masonry infills and a six-storey bare frame, were designed according to the current Italian seismic code and subsequently numerically modelled [96]. The scope of these numerical models, which were also used to obtain the pushover curves, was the analytical assessment of seismic collapse risk implicit in the Italian code's provisions, via non-linear dynamic analysis [97]. Considering both buildings in either direction, pushover analysis was performed using a force distribution according to the modal load of each direction's predominant elastic mode shape. Thus, four equivalent SDOF systems with tri- or quadri-linear backbones were derived from these static pushover curves (for further details, see [98])

and a Clough-type, peak-oriented model without cyclic deterioration [88], was assumed to govern hysteretic response.

The two equivalent SDOF oscillators corresponding to the three-storey infilled frame had vibration periods of 0.28 and 0.31 s while those of the six-storey bare frame were 1.11 and 1.25 s. As can be seen in Figure 26, the bare RC frame is characterized by similar maximum attainable base shear and displacement capacity in both directions. On the other hand, the infilled frame exhibits higher maximum resistance in one direction with respect to the other. This is due to the increased presence of openings in the masonry infills along the direction parallel to the building's facade, resulting in lower infill-contribution to lateral strength in that direction. Furthermore, it can be seen that this building is characterized by different ultimate displacement capacity per principal direction.

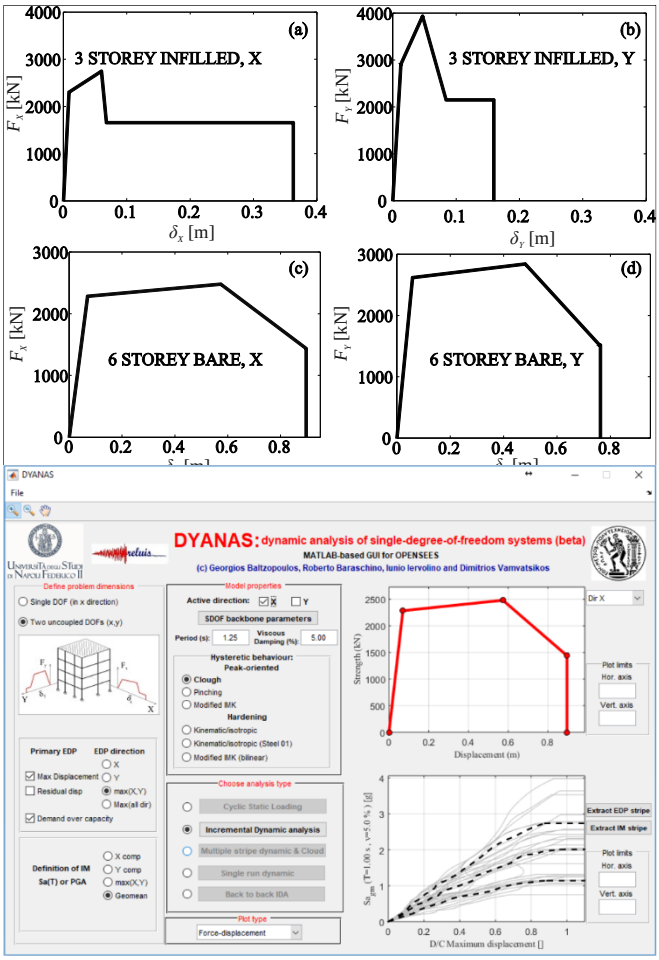

Figure 26. Piecewise-linear idealizations of the RC frames' static pushovers: three-storey frame with masonry infills, direction X (a) and direction Y (b), six-storey bare frame direction X (c) and direction Y (d). Below the pushovers, the GUI main window is shown in post-analysis of the six-storey frame.

2.5.2.2 Incremental dynamic analysis for estimation of collapse fragility

In this exercise, each pair of equivalent SDOF systems, corresponding to a single RC building, was subjected to IDA using a suite of thirty, two-component acceleration records. These accelerograms were recorded on firm soil during events of magnitude ranging from 6.1 to 7.6, at distances from the fault plane 44 km or less and are considered to not exhibit impulsive characteristics due to directivity; during IDA, the same scale factor was applied to both horizontal components with each pair thus always maintaining their as-

recorded relative amplitudes. In order to be able to express the seismic collapse fragility of these structures in terms of a common *IM*, the geometric mean of the two components' spectral acceleration at one second period, $Sa_{gm}\left(T=1.0\text{ s}\right)$, was arbitrarily selected and all IDA curves were converted to that *IM*. For each building three collapse fragility functions were calculated, two curves considering each principal direction *X*, *Y* separately and one corresponding to the entire building, i.e., considering both directions at once. In the first two cases, the *EDP* was set to δ_X or δ_Y and *IM* stripes were extracted at δ_f^X and δ_f^Y, respectively. In the third case, the D/C ratio according to Equation (22) was taken as *EDP* and the *IM* stripe for $D/C=1$ was obtained. It follows from Equation (22) that, if one were to name failure in the two directions f_X, f_Y and since failure of the entire structure can be seen as the union of the two events, $P\left[f\left|IM=im\right.\right]=P\left[f_X\cup f_Y\left|IM=im\right.\right]=P\left[D/C>1\left|IM=im\right.\right]$. In all cases, lognormal seismic fragility functions are estimated according to Equation (2), where $im_{f,i}$ represents the *i-th* record's (lowest) scaled *IM* value causing exceedance of the threshold (i.e., the *i*-th element of the *IM* stripe at that threshold, according to the nomenclature used earlier), η and β are parameters defined in Equation (3).

The resulting fragility curves are shown in Figure 27. At this point, it may be useful to recall that the procedure outlined above (as well as those in the following illustrative applications) is inextricably linked to the requisites behind conducting a pushover-based SDOF simplification of a real structure. The main requisites are the predominance of the first mode going into the inelastic response range and that the structure be characterized by sufficient symmetry and regularity for response in the two principal directions to remain largely uncoupled and unaffected by torsion (e.g., [87]). For this reason, extending evaluations that are based on an equivalent SDOF systems' seismic response, to the actual corresponding multi-DOF structure, may require additional effort to account for the influence of higher modes (see for example [62,99]). This being an illustrative example intended to demonstrate the capabilities of this software, with no pretense of using the result for seismic risk assessment of any real structure, considerations need not and will not depart from the SDOF level.

With these premises in mind, it can be seen from the figure that, in the case of the infilled RC frame (Figure 27a), separate evaluation of collapse fragility along the principal directions results in quite different probability distributions of collapse intensity, with median collapse intensities in the *X* and *Y* directions being $\exp(\eta_X)=1.97$ g and $\exp(\eta_Y)=1.19$ g, respectively. In this case of one direction nominally exhibiting greater seismic vulnerability than the other by a wide margin (when the two are viewed as separate structural systems during analysis) it happens that the entire system's collapse fragility almost coincides with the most vulnerable one, with $\exp(\eta)=1.17$ g.

On the other hand, in the case of the bare RC frame (Figure 27b), collapse fragilities derived separately for each direction are more uniform, with $\exp(\eta_X)=2.31$ g and $\exp(\eta_Y)=2.12$ g. However, in this case, the simplified analysis executed for this example indicates that the total building vulnerability is greater than the worst of the two nominal vulnerabilities obtained by the separate analyses, with a median collapse intensity of $\exp(\eta)=1.86$ g.

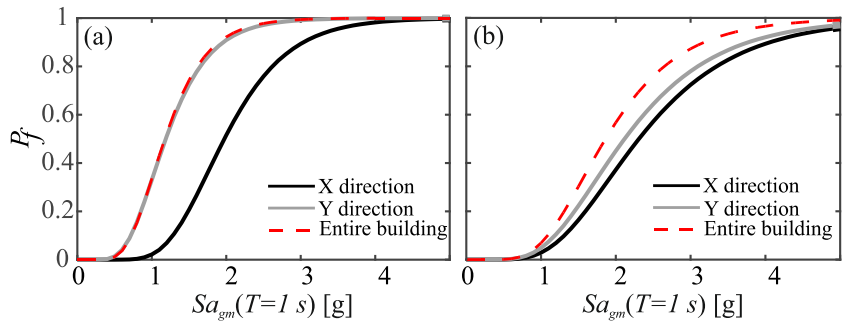

Figure 27. Collapse fragilities estimated separately for each principal direction and for the entire structure. Fragility curves of the three-storey infilled RC frame (a) and those of the six-storey bare RC frame (b).

2.5.2.3 Multiple-stripe analysis using different sets of records per level of seismic intensity

In this example, a six-storey bare RC frame building is used, designed for a site in L'Aquila, Italy [96]. Details on the equivalent SDOFs in the two principal directions of the structure can be found in [98], while the backbone curve in the *X* direction is shown in the upper left panel of Figure 24. In order to calculate site-specific seismic risk for that building, [97] selected hazard-consistent sets of records at ten different levels of seismic intensity, when said intensity was

expressed in terms of $Sa_{\max}\left(T=1.0\text{ s}\right)$. Thus, twenty pairs of bidirectional acceleration time-histories were obtained, for each *IM* level, and were assigned to an MSA via the GUI (Figure 24). In this case, definition of *IM*-type, i.e., maximum-among-horizontal-components spectral acceleration $Sa_{\max}$, has to be defined prior to running the analysis, in order to ascertain correct scaling of the records. *EDP* for the analysis was defined as a D/C ratio by setting threshold displacements in both directions, corresponding to a roof drift of the actual building of three percent. The resulting *EDP* vs. *IM* plot from the analysis can be seen in Figure 28, where the dashed line at $D/C=1$ separates the converging runs between those causing failure to the right and those who do not, to the left. Note that in the two highest *IM* levels, $Sa_{\max}\left(T=1.0\text{ s}\right)=1.837\text{ g}$ and 3.52 g, two and ten cases, respectively, reached collapse and are thus not present on the plot; collapsed cases per stripe are reported separately by the GUI.

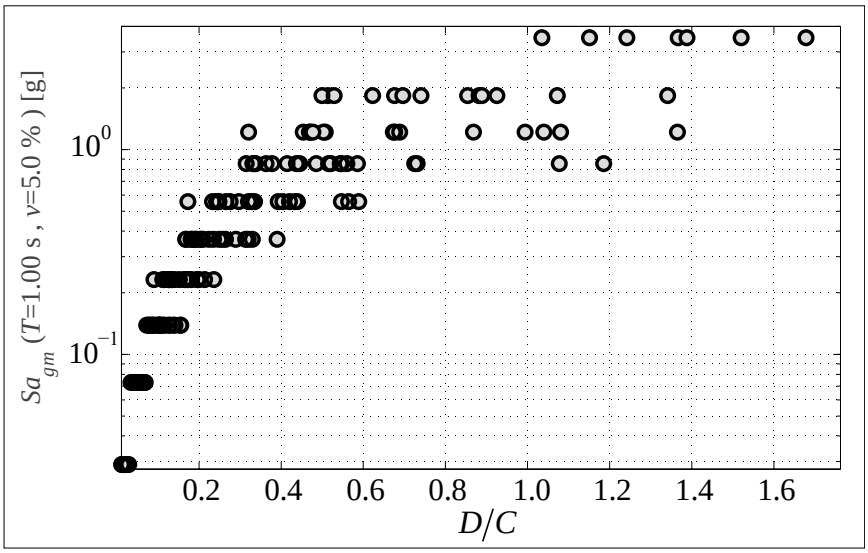

Figure 28. MSA results shown in a semi-logarithmic EDP-IM plot obtainable via the "export figures" option of the software.

2.5.2.4 Running cloud analysis via the MSA panel of the GUI

In this brief example application, the trilinear-backbone SDOF oscillator shown in Figure 29 is used, having vibration period $T=0.60\text{ s}$ and characterized by a moderately-pinched peak-oriented hysteresis [89]. As mentioned previously, in order to run cloud analysis the user has to define a single nominal *IM* stripe in

the MSA panel of the GUI, assign all records to that stripe and select the "do not scale records" option.

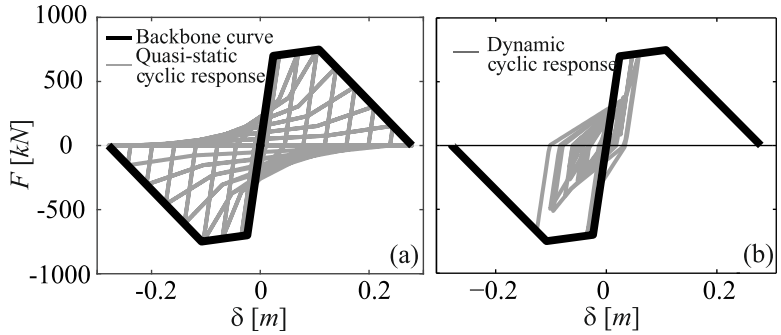

Figure 29. Trilinear backbone curve of the SDOF oscillator used for cloud analysis and cyclic quasi-static response of the peak-oriented pinched hysteretic model (a); cyclic response of the same to a specific accelerogram (b). Both plots can be obtained via the GUI's "export figures" option, following a "cyclic quasi-static" or "single-run dynamic" analysis, respectively.

For this analysis, a set of forty-two single-component records is selected from within the Engineering Strong Motion database (http://esm.mi.ingv.it/), with the criteria of covering a wide range of as-recorded intensity in terms of $Sa(T = 0.60\ \mathrm{s})$, never using both components of the same station for a single event, not using more than three stations from the same event and always exceeding yield acceleration of the oscillator in Figure 29. It is evident that this type of analysis requires a notably lower number of runs with respect to the preceding IDA and MSA examples. The results of the analysis, i.e., an *EDP-IM* scatter plot forming the homonymous "cloud", are shown in Figure 30.

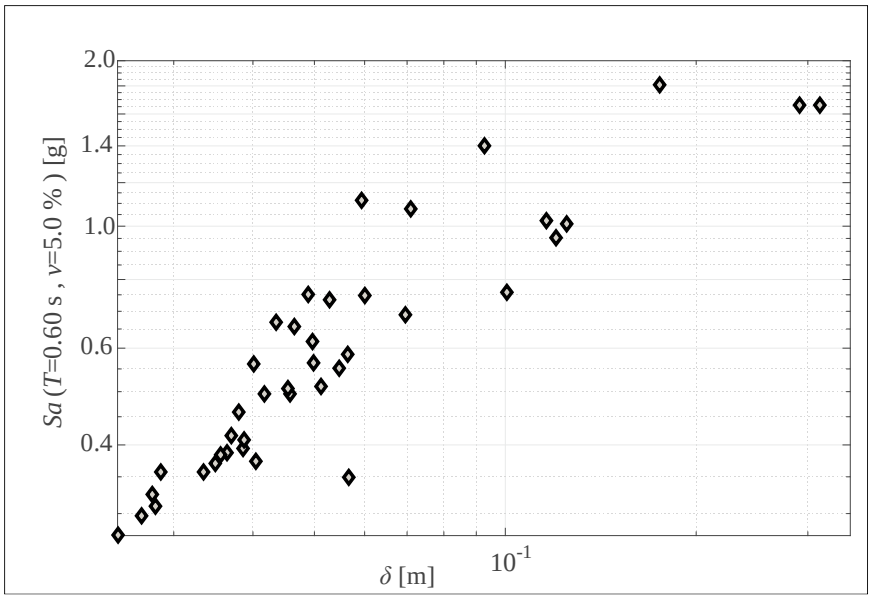

Figure 30. Results of cloud analysis, shown in a logarithmic-scale EDP-IM scatter plot, obtainable via the "export figures" option of the software.

2.5.2.5 Back-to-back incremental dynamic analysis for estimating state-dependent seismic fragility

State-dependent seismic fragility extends the traditional concept of fragility, expressed as the probability of failure for a given *IM* level, $P\left[f \left| IM = im \right. \right]$, to the probability of failure given both the occurrence of a specific intensity and the structure already being in a generic limit state S_i, $P\left[f \left| S_i \cap IM = im \right. \right]$. Such state-dependent fragility functions can find application in seismic reliability analysis that considers damage accumulation phenomena (e.g., [100]) and may be analytically estimated by means of back-to-back IDA (see for example [101]).

For this illustrative example, a simple SDOF structure is assumed, with vibration period $T = 0.50$ s and a horizontal post-yield segment stretching up to a capping ductility $\mu_c = 6.0$, after which lateral strength drops gradually; hysteresis for this system follows the peak-oriented model of [42] and exhibits mild cyclic strength degradation, as shown in Figure 31. Furthermore, it is assumed that a generic limit state, corresponding to this structure having sustained some seismic damage and indicated as S_1, is reached when maximum transient seismic ductility demand, μ, exceeds 9.6. The example

consists of using IDA to estimate the collapse fragility of this SDOF structure at its intact state, indicated as S_0, and back-to-back IDA for estimating the same fragility under the condition that the structure is in the S_1 state due to one or more prior shocks.

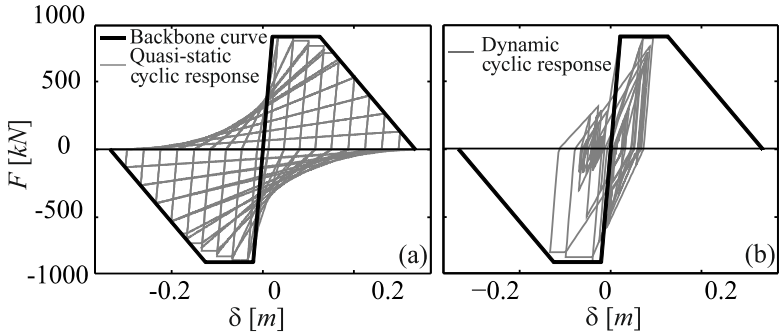

Figure 31. Backbone curve of the SDOF oscillator used for back-to-back IDA and cyclic quasi-static response of the peak-oriented modified Ibarra-Medina-Krawinkler hysteretic model exhibiting mild strength degradation (a); cyclic response of the same to a specific accelerogram (b). Both plots can be obtained via the GUI's "export figures" option, following a "cyclic quasi-static" or "single-run dynamic" analysis, respectively.

As mentioned in passing earlier, back-to-back IDA is preceded by an IDA performed with a suite of accelerograms designated as the MS set. In this case, the MS set consisted of ten records and the preliminary analysis provided the scale factors required to reach the $\mu = 9.6$ threshold that was assumed, by convention, to signify exceedance of S_1 (see Figure 32a). During back-to-back IDA, each MS record is followed by three AS records that are randomly sampled from within a pool of twenty accelerograms, resulting in thirty curves. For this analysis, the thirty single-component records provided with the software are used. It should be noted that the number of records and back-to-back IDA runs used in this example is simply dictated by the need to maintain Figure 32 easily legible by avoiding overcrowding of IDA curves. In fact, these numbers should be chosen on the basis of the confidence that the user desires to be able to place on the estimated fragility parameters; the interested reader is referred to [8] for more details.

By taking the *IM* stripes corresponding to the so-called *flat-line heights* of the IDA curves that, as discussed previously, signify the onset of dynamic instability, collapse fragility curves can be obtained according to Equation (2)

for both S_0 and S_1 initial states. These fragility curves are shown in Figure 32, in terms of both $Sa\left(T=0.50\text{ s}\right)$ and PGA, with the latter being derived from the former almost-instantaneously, via re-interpolation of the IDA curves. In either case, one observes the characteristic shift of the S_1 fragilities to the left of the S_0 curves, quantifying the decrease in capacity (or increase in vulnerability) of the structure, that has befallen a damaged state.

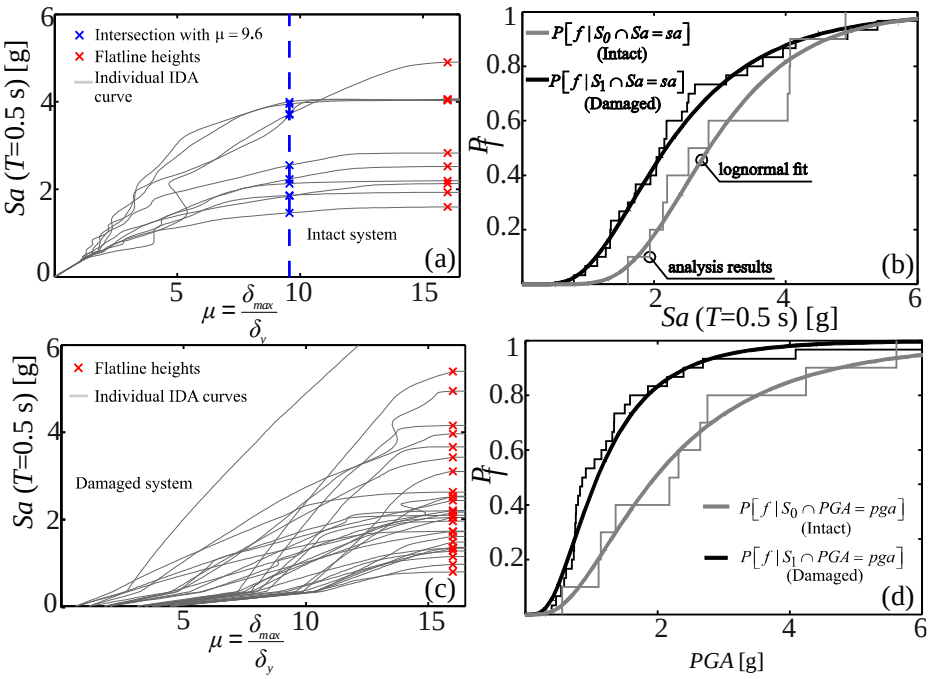

Figure 32 Preliminary IDA used to determine intact state collapse fragility and intensities inducing the S1 limit state threshold (a); back-to-back IDA used to determine collapse fragility given that the structure has previously reached the limit state S1 (b); comparison of collapse fragility curves of the intact and damaged structure, expressed in terms of $Sa\left(T=0.50\text{ s}\right)$ *(c) and in terms of PGA (d), after implementation of the IM conversion tool.*

2.6. Conclusions

This section first introduced SPO2FRAG, an interactive MATLAB®-coded PBEE tool useful for approximate, computer-aided calculation of building fragility functions based on static pushover analysis. SPO2FRAG comes as a standalone application, with various intercommunicating modules nested behind a user-friendly graphical user interface.

The software uses SPO results as a vehicle to obtain an equivalent SDoF representation of the non-linear structure and subsequently goes on to employ the SPO2IDA algorithm to avoid the need for time-consuming dynamic analysis for obtaining probabilistic estimates of seismic response. A series of specifically-developed tools are then called upon to effect and SDoF-to-MDoF response transformation, culminating in the calculation of fragility parameters and going as far as providing information related to the underlying estimation uncertainty. In the preceding sections, the workflow of a complete SPO2FRAG operation was outlined from both the user-end and the software-end.

The viability of SPO2FRAG as a calculation tool was demonstrated by means of two case-study examples, where fragility functions estimated using the software were compared and found in agreement with the analytical solution involving IDA. It was therefore shown that, for regular, symmetric frames (i.e., cases of fist-mode dominated structures for which the fundamental assumptions behind static pushover analysis apply) SPO2FRAG is able to provide expedient solutions to the issue of analytical, building-specific seismic fragility estimation, under the assumptions behind IDA.

Second part of the section was dedicated to the presentation of DYANAS, an open-source, earthquake engineering software. The software is a MATHWORKS MATLAB®-based graphical user interface that interacts with the OpenSees finite element framework and offers engineers an easy way to define and run dynamic analysis of yielding single-degree-of-freedom systems subjected to large suites of earthquake-induced ground motion records. Therefore, the main purpose of this software is to determine the relationship between seismic intensity and engineering demand parameters using any one of several dynamic analysis methods that are frequently used in performance-based earthquake engineering. Incremental dynamic analysis is supported in its traditional form and also in a “back-to-back” format that could allow state-dependent seismic fragility to be estimated. Multiple-stripe and cloud-type analyses are also supported, in cases where the user does not desire to use scaled records to estimate seismic response at different levels of shacking intensity. Much of the software’s utility stems from the post-processing routines, with which it is equipped. These routines, which are also programmed in MATLAB and can be recalled via the user interface, permit the re-interpolation of incremental dynamic analysis curves, thus providing rapid conversion of the curves into alternative intensity measures, such as peak ground acceleration or

spectral ordinates at various periods. Furthermore, at the end of analysis, the user can obtain vectors of intensity measure given engineering demand parameter, or vice versa, thus facilitating further probabilistic seismic demand elaborations for these simple structural systems. Overall, the GUI was shown to be a useful tool within the context of performance-based earthquake engineering, as demonstrated by the illustrative applications provided. DYANAS is freely distributed for research purposes by the University of Naples Federico II under a GNU general public license v3.0.

Chapter 3 – ESTIMATION UNCERTAINTY BEHIND SEISMIK RISK EVALUATION IN PERFORMANCE BASED EARTHQUAKE ENGINEERING: R2R-EU TOOL

The following paper has been derived from this Chapter :

- *Baraschino R., Baltzopoulos G., Iervolino I. (2019) R2R-EU: Software for fragility fitting and evaluation of estimation uncertainty in seismic risk analysis. Soil Dynamics and Earthquake Engineering. 132: 106093.*

3.1. Introduction

Recalling what already introduced, both terms under the integral of Equation (1), can be affected by so-called estimation uncertainty, since both functions have to be deduced from available (i.e., limited) data. Section 3.2 primarily deals with estimation uncertainty affecting the fragility function, then the focus of this Chapter is the presentation of the PBEE software tool R2R-EU (*record-to-record estimation uncertainty*), which was developed in MATLAB® with a dual purpose: (i) estimating structure-specific seismic fragility, based on dynamic analysis, and (ii) quantifying estimation uncertainty, emanating specifically from record-to-record variability of seismic structural response, and the extent to which that uncertainty propagates unto risk metrics, such as the failure rate. The R2R-EU tool considers various consolidated non-linear analysis strategies used in PBEE, such as IDA, MSA or cloud analysis, in the context of Cornell's seismic reliability method [54]. The software (freely available) offers several alternatives for the definition of the fragility function, and implements a series of statistical inference methods based on resampling and/or simulation schemes belonging to the bootstrap family [76], the *delta method* [102] and direct application of formulas from statistical inference theory. In the remainder of this Chapter, first a brief overview of the methodologies for quantification of estimation uncertainty used in R2R-EU is provided, in tandem with a review of the corresponding alternative approaches used for conducting dynamic analysis and for evaluating structural fragility. Subsequently, a brief operational description of the software capabilities is given, and an example application is provided, followed by some concluding remarks.

3.2. Estimation uncertainty in seismic risk and fragility function assessment

As highlighted in the introductory discussion, the R2R-EU tool deals with the definition of structure-specific seismic fragility and with the quantification of that part of estimation uncertainty in the failure rate, that can be attributed to the record-to-record variability of structural response. The latter can be provided by one of the methods mentioned in the introduction; i.e., IDA, MSA and cloud. IDA involves progressively scaling each ground motion in a set, so as to cover a broad range of *IM* levels, and running dynamic analysis, ideally until the numerical model experiences instability that can be interpreted as side-sway structural collapse [56]. A measure of structural response, often termed an *engineering demand parameter* or *EDP*, is being registered at each *IM* level. The output of this analysis is a set of *EDP*-*IM* curves (equal in number to the number of ground motion records used). On the other hand, MSA involves the use of different sets of – ideally unscaled – accelerograms per *IM* level, chosen to represent the seismic scenarios causing that level of shaking at the construction site as indicated by *disaggregation* of seismic hazard [53]. The output of MSA is a set of *EDP* responses at fixed *IM* values (Figure 1b). Cloud analysis uses a set of unscaled accelerograms to perform dynamic analysis so that at each record represents a single *IM* value and corresponds to a single *EDP* response. The output is a cloud of points (Figure 1c), hence the name.

As introduced in Section 2.3, given the output of dynamic analysis, the strategy for analytically evaluating a fragility function often branches into one of two approaches: the *IM*-based approach and the *EDP*-based approach. In both cases, the two parameters $\{\eta, \beta\}$ are generally unknown and one way to obtain estimates of these parameters, $\{\hat{\eta}, \hat{\beta}\}$, is by using the sample of responses resulting from IDA/MSA according to Equation (3) or (5).

Of course, it is not necessary to assume a parametric model for *IM*-based fragility; in fact, a non-parametric representation can be obtained directly from the sample of IM_f values, according to Equation (4). The use of estimation uncertainty as a means for determining the number of records to use in *IM*-based fragility derivation is explored in Chapter 4.

All of the aforementioned approaches for estimating a fragility function (which may entail assigning a parametric model or not; e.g., Figure 3) have been implemented in R2R-EU. They also allow to quantify the estimation

uncertainty in the failure rate, used in conjunction with methodologies of statistical inference. These methodologies, summarized in Table 3 and partly discussed in [8], but also outlined in the following paragraphs, are: parametric or non-parametric resampling plans (generally belonging to the bootstrap family), the application of known results for the distribution of the estimators of the lognormal parameters, and the delta method, which is based on Taylor series expansion of either the risk integral or the formula from Cornell's seismic reliability method.

Table 3. Methodologies implemented in the R2R-EU tool for the quantification of record-to-record estimation uncertainty in PBEE.

Approach	*Dynamic analysis*	*Fragility model*	*Method for quantifying estimation uncertainty*
IM-based	IDA	Lognormal	Parametric bootstrap, probability theory, Delta method
		Non-Parametric	Bootstrap (resampling)
EDP-based	IDA/MSA	Lognormal	Parametric bootstrap
		Shome & Cornell three parameter model per intensity [56]	Bootstrap (resampling)
		Normal probability paper	Bootstrap (resampling)
		Least squares fit	Bootstrap (resampling)
	Cloud	-	Delta method for Cornell's method

3.2.1 Estimators of the Gaussian distribution's parameters

If structural fragility is assumed lognormal, the estimators of the parameters logarithmic mean $\left(\hat{\eta}\right)$ and variance $\left(\hat{\beta}^2\right)$, obtained according, e.g., to Equations (3), have known distributions. The estimator $\hat{\eta}$ is distributed as a Gaussian with mean and variance equal to η and β^2/n respectively (but assumed equal to $\hat{\eta}$ and $\hat{\beta}^2/n$; i.e., η and β^2 are substituted by the available point estimates), while $\hat{\beta}^2 \cdot (n-1)/\beta^2$ is *chi-squared* distributed with $n-1$ degrees of freedom. Since the failure rate is a function of these two stochastically independent RVs, shown here as Equation (23):

$$\hat{\lambda}_f\left(\hat{\eta},\hat{\beta}\right)=\int_{IM}\Phi\left[\left(\ln(im)-\hat{\eta}\right)/\hat{\beta}\right]\cdot\left|d\lambda_{im}\right|, \tag{23}$$

it follows that the mean and variance of $\hat{\lambda}_f$ can be evaluated (in R2R-EU) using their known densities.

3.2.2 Bootstrap

The bootstrap is a statistical inference process, which is based on taking an original data set and generating, so-called, *bootstrap samples* by resampling the original data with replacement. The bootstrap samples have the same size as the original. This resampling process is implemented in R2R-EU for three cases: non-parametric *IM*-based fragility derived from IDA, *EDP*-based fragility using the three-parameter model of Equation (6) and *EDP*-based fragility with parameter estimation via the normal probability paper procedure or least square fit.

3.2.2.1 Resampling for IM-based fragility

In the case of *IM*-based non-parametric fragility, the bootstrap implementation takes the original *n*-size sample of IM_f realizations already available from IDA, $\left\{im_{f,1},im_{f,2},..,im_{f,n}\right\}$, and generates an arbitrary number, *m*, of bootstrap samples $\left\{im^*_{f,1k},im^*_{f,2k},..,im^*_{f,nk}\right\}$, where $k=\{1,..,m\}$. Subsequently, a Monte Carlo simulation is performed, where, for each bootstrap sample, Equation (1) is used to compute a *bootstrap replication* of the failure rate, $\hat{\lambda}^*_{f,k}$. Then, the mean and variance of the failure rate estimator (denoted via the operators $E[\cdot]$ and $VAR[\cdot]$, respectively) are evaluated using the simulations results according to Equation (24):

$$\begin{cases} E\left[\hat{\lambda}_f\right]=\dfrac{1}{m}\cdot\sum_{k=1}^{m}\hat{\lambda}^*_{f,k} \\ VAR\left[\hat{\lambda}_f\right]=\dfrac{1}{m-1}\cdot\sum_{k=1}^{m}\left(\hat{\lambda}^*_{f,k}-E\left[\hat{\lambda}_f\right]\right)^2 \end{cases}. \tag{24}$$

3.2.2.2 Resampling for EDP-based fragility

In the case of *EDP*-based fragility, the bootstrap process starts from a set of $n\times u$ *EDP* responses, available from either MSA or IDA and denoted as

previously by edp_{ij}, obtained from n records $\left(i=\{1,..,n\}\right)$ at each one of *IM* levels $\left(j=\{1,..,u\}\right)$, denoted as $\{im_1, im_2, .., im_u\}$. As a first step, the *EDP* responses at each *IM* level (stripe), are resampled with replacement m times, resulting in new sets of responses at the j-th stripe (i.e., bootstrap samples) $\left\{edp^*_{1j,k}, edp^*_{2j,k}, .., edp^*_{nj,k}\right\}$, $k=\{1,..,m\}$. Subsequently, at each and every j-th, $j=\{1,..,u\}$, stripe of the k-th bootstrap sample, $k=\{1,..,m\}$, the responses $c^*_{j,k}$, corresponding to collapse cases, are identified, and the probabilities of failure, $P^*_k\left[\, f \,|IM=im_j\,\right]$, are calculated according to Equation (6).

In the case of the three-parameter model, the k-th bootstrap replication of the failure rate, $\hat{\lambda}^*_{f,k}$ is evaluated according to a discretized version of Equation (1), reported here as Equation (25):

$$\hat{\lambda}^*_{f,k}=\sum_{j=1}^{u} P^*_k\left[\, f \,|IM=im_j\,\right]\cdot\left|\Delta\lambda_{im_j}\right| \qquad (25),$$

where $\Delta\lambda_{im_j}=\left(\lambda_{im_j}-\lambda_{im_{j-1}}\right)$. This distinction is made due to the fact that the probability of failure is only available at specific, discrete *IM* levels. Finally, after having obtained all bootstrap replications $\hat{\lambda}^*_{f,k}$, the mean and variance of the failure rate estimator are again evaluated according to Equation (24).

In the case of *EDP*-based lognormal fragility whose parameters are estimated via linear fit on normal probability paper, new parameter estimates $\left\{\hat{\eta}^*_k, \hat{\beta}^*_k\right\}$, $k=\{1,..,m\}$, are obtained via Equation (8) for each bootstrap sample. Then bootstrap replications $\hat{\lambda}^*_{f,k}$ are calculated by substituting the parameters $\left\{\hat{\eta}^*_k, \hat{\beta}^*_k\right\}$ into Equations (2) and (1). Finally, Equation (24) is used to obtain the statistics of the failure rate estimator, same as before.

3.2.3 Parametric bootstrap

When a parametric model is assumed for the fragility function, the mean and variance of the failure rate's estimator can be inferred via a parametric version of the bootstrap. In the parametric version, bootstrap samples can be extracted directly from the assumed fragility model, rather than by means of resampling

the original dataset. In R2R-EU this is implemented for both cases of *IM*- and *EDP*-based lognormal fragility (in the *EDP*-based case, when parameter estimation occurs via maximum likelihood).

3.2.3.1 Parametric bootstrap for IM-based fragility

In the *IM*-based case, the *n* values of IM_f obtained from IDA, $\{im_{f,1}, im_{f,2}, .., im_{f,n}\}$, are used to derive the reference lognormal fragility parameters $\{\hat{\eta}, \hat{\beta}\}$ via Equation (3). Subsequently, an arbitrary number *m* of new bootstrap samples, $\{im^*_{f,1k}, im^*_{f,2k}, .., im^*_{f,nk}\}$, $k = \{1, .., m\}$, is extracted from the reference distribution defined by $\{\hat{\eta}, \hat{\beta}\}$, with each new sample being of size *n*. Then, for the *k*-th out of *m* bootstrap samples, a new fragility function (Figure 33a) is evaluated via Equation (3), having parameters $\{\hat{\eta}^*_k, \hat{\beta}^*_k\}$, and the bootstrap replication of the failure rate $\hat{\lambda}^*_{f,k}$ is computed using these parameters and Equation (23). Finally, as in the resampling process, the mean and the variance of the failure rate estimators are calculated via Equation (24).

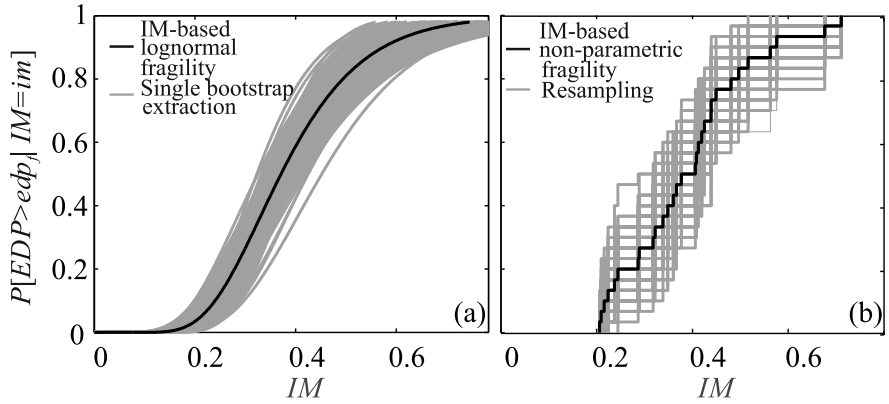

Figure 33. Reference fragility functions (black curves) and 200 bootstrap extractions of lognormal fragility (a) and empirical fragility (b).

3.2.3.2 Parametric bootstrap for EDP-based fragility

In the *EDP*-based case, the reference structural fragility parameters $\{\hat{\eta}, \hat{\beta}\}$ are obtained from the available responses via the binomial maximum likelihood of Equation (5). Then, at the *j*-th stripe, corresponding to $IM = im_j$, $j = \{1, .., u\}$, a

number of *m* bootstrap samples is extracted from the binomial distribution with parameter equal to $p_j = \Phi\left\{\left[\ln\left(im_j\right) - \hat{\eta}\right] \Big/ \hat{\beta}\right\}$ (i.e., the parameter of binomial distribution is the probability of failure). Each sample consists of *n* Bernoulli trials, resulting in $q_{j,k}^*$ failures and $n - q_{j,k}^*$ survivals of the structure at the *j*-th stripe of the *k*-th bootstrap sample. Subsequently, new lognormal parameters $\left\{\hat{\eta}_k^*, \hat{\beta}_k^*\right\}$ are obtained from the $q_{j,k}^*$ failures, via Equation (5). It is assumed that, during the bootstrap replications, the maximum likelihood estimate may run into numerical problems for a number of m_o bootstrap samples, out of a total *m*. With this assumption in mind, the bootstrap replication of failure rate, $\hat{\lambda}_{f,k}^*$, is computed via Equation (1) and then the mean and variance of the estimator can be evaluated according to Equation (26):

$$\begin{cases} E\left[\hat{\lambda}_f\right] = \left(m - m_o\right)^{-1} \cdot \sum_{k=1}^{m-m_o} \hat{\lambda}_{f,k}^* \\ VAR\left[\hat{\lambda}_f\right] = \left(m - m_o - 1\right)^{-1} \cdot \sum_{k=1}^{m-m_o} \left(\hat{\lambda}_{f,k}^* - E\left[\hat{\lambda}_f\right]\right)^2 \end{cases}, \tag{26}$$

which only differs from Equation (24) in the fact that the simulation-based statistics are calculated using a number of $\left(m - m_o\right)$ bootstrap replications of the failure rate; i.e., only those that did not encounter numerical issues.

3.2.4 Delta method

An alternative method for evaluating the mean and variance of $\hat{\lambda}_f$, besides the bootstrap and the properties of the Gaussian function, is the delta method. The delta method uses a Taylor series expansion to approximate the expectation and variance of a RV and has been applied in the context of Cornell's seismic reliability method in [8]. The latter can be implemented using output from cloud analysis, which entails a set of *n* ground motion records with variable intensities and the corresponding sample of *EDP* responses. By performing linear regression of $\ln\left(EDP\right)$ against $\ln\left(IM\right)$ and assuming that the logarithm of the hazard curve, $\ln\left(\lambda_{im}\right)$, can be approximately considered locally linear, the annual failure rate can be estimated in closed-form as $\hat{\lambda}_f \approx k_0 \cdot \left(edp_f / \hat{a}\right)^{-k/b} \cdot \exp\left[\left(k^2/2 \cdot b^2\right) \cdot \left(\hat{\beta}_D{}^2 + \beta_C{}^2\right)\right]$, where k_0 and k are,

respectively, the slope and intercept of the $\ln(\lambda_{im})$ curve linearized around the *IM* corresponding to edp_f, $\hat{a}$ and $\hat{b}$ are the slope and intercept from the linear regression of $\ln(EDP)$ against $\ln(IM)$, $\hat{\beta}_D$ is the standard deviation of the residuals of $\ln(EDP)$ given $\ln(IM)$, which is estimated from the regression and β_C is the logarithmic standard deviation of edp_f ,which is assumed to follow a lognormal distribution. In this context, the statistics of $\hat{\lambda}_f$ can be approximated via Taylor series expansion, which are given in [8]. The delta method can be applied for the failure rate estimator from Equation (23), under the assumption of lognormal fragility. In this case the failure rate is regarded as a function of the fragility parameters, that can undergo a Taylor series expansion, which can also be found in [8] along with the necessary derivatives of $\hat{\lambda}_f$. The advantage of the delta method, over the other procedures implemented in R2R-EU, is that the closed-form expressions need only be evaluated analytically once, after which the statistics of $\hat{\lambda}_f$ can be obtained with less computational effort with respect to the bootstrap.

3.3. R2R software: conceptual framework and implementation

R2R-EU runs behind a Mathworks MATLAB®-based graphical user interface (see Figure 34) which implements all of the methods illustrated in the previous section for evaluating a fragility model and for quantification of estimation uncertainty in the fragility parameters and in the failure rate. Two sets of input data are needed to run R2R-EU: one containing the hazard curve, and another containing the structural responses. For the hazard curve, there is the additional possibility of directly importing output files from the REASSESS software [103]. In all supported cases, after elaborating the hazard and dynamic analysis data, R2R-EU provides the fragility model and the point estimates of the fragility parameters (where applicable), the point estimate of the failure rate and the mean and variance of the failure rate estimator. For the cases where one of the bootstrap schemes is applicable, a simulation-based approximation for the distribution of $\hat{\lambda}_f$ is also provided, in the form of the histogram of requested bootstrap replications. In cases where the chosen fragility model is parametric (lognormal) and inference is conducted via a bootstrap process, the

approximate distributions of $\hat{\eta}$ and $\hat{\beta}$ are likewise provided, in the form of the histograms of the corresponding bootstrap replications. The R2R-EU tool allows to save and export results, in either MATLAB data file or ASCII text file formats. More details on the workflow and input/output options, as well as additional application examples omitted here for reasons of space, can be found in R2R-EU user's manual.

3.3.1 Illustrative Applications

3.3.1.1 IM-based approach

In this section an application of R2R-EU is presented, using as case study structure a four-story, plane, code-conforming, steel perimeter moment resisting frame designed to ASCE-SEI 7-05 criteria and described in the NIST GCR 10-917-8 report. (Figure 34a).

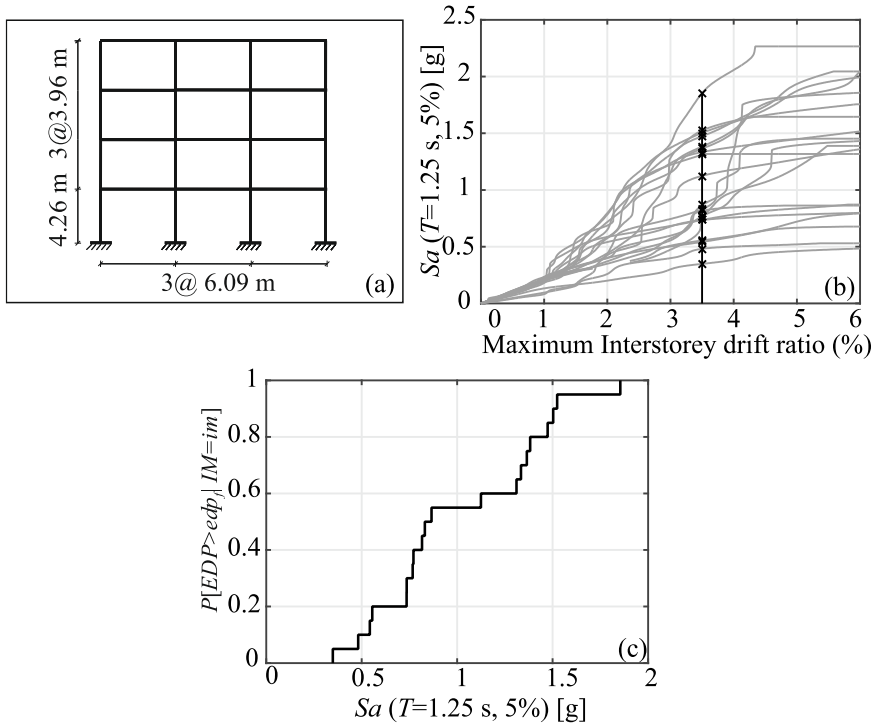

Figure 34. Perimeter frame for the case study of IM-based fragility (a); IDA curves for the case study frame, from twenty records, in terms of maximum interstorey drift ratio and 5% damped spectral acceleration at the structure's first-mode period (b), with crosses marking the IM_f vertical stripe at failure defined by IDR>3.5 %; non-parametric fragility corresponding to the vertical IM_f stripe shown (c).

The structure is ideally located at a site near the town of Amatrice (central Italy; lat. 42.53°, lon. 13.29°), for which the hazard curve (Figure 35), in terms of five-percent-damped spectral acceleration at the frame's first-mode vibration period $Sa\left(T=1.25\,\mathrm{s},5\%\right)$ is obtained using the software REASSESS, considering the seismic source model from . IDA is performed for the structure, using a set of fifty records (selected from NESS1, a dataset of the *Engineering Strong Motion database* [104]), which are scaled upwards until side-sway collapse (Figure 34b). By considering a generic limit state, which is nominally exceeded when a maximum interstorey drift ratio (IDR) above 3.5% is recorded, the R2R-EU software is used for the quantification of the failure rate's estimation uncertainty. To this end, the example uses two of the available strategies: the bootstrap for non-parametric *IM*-based fragility (shown in Figure 34c) and the delta method for lognormal fragility. The exercise is repeated in two versions: the first only uses a randomly selected subset of twenty-out-of-fifty IDA curves, while the entire set of fifty is used on the second go.

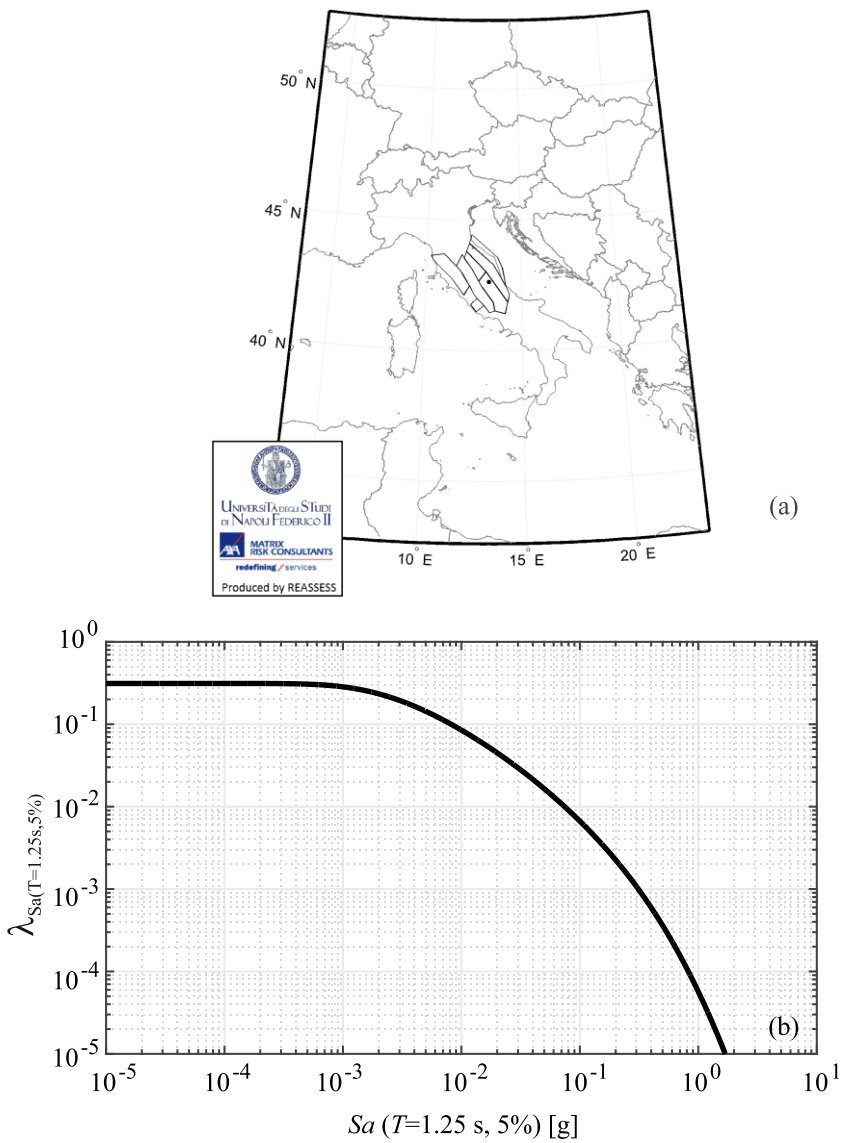

Figure 35. Seismogenic zones considered in the hazard analysis in REASSESS and location of the site (black dot) (a), resulting hazard curve (b).

For the application of the bootstrap resampling method, first the vectors composed by twenty (and later fifty) IM_f values (crosses in Figure 34b) are used to build the empirical fragility curves. In this case, five-hundred bootstrap extractions of the failure rate are requested from R2R-EU, which leads to calculating the mean and variance of the estimator, according to the

methodology outlined in paragraph 3.2.2. These statistics are also calculated by means of the delta method and the whole process is repeated using the structural response results from all fifty records; the results provided by R2R-EU are summarized in Table 4, where the coefficient of variation reported in the last column is calculated as $CoV_{\hat{\lambda}_f} = \sqrt{VAR\left[\hat{\lambda}_f\right]} \Big/ E\left[\hat{\lambda}_f\right]$. The drop in the dispersion of the estimator with the increase in the number of records used, is evident across both inference methods employed.

Table 4. Statistics of the failure rate estimator evaluated using samples of either twenty or fifty records to obtain structural response via IDA.

Method	*Number of records*	$\hat{\lambda}_f$ *[events/year]*	$E\left[\hat{\lambda}_f\right]$ *[events/year]*	$VAR\left[\hat{\lambda}_f\right]$ *[(events/year)^2]*	$CoV_{\hat{\lambda}_f}$
Non-parametric bootstrap (*IM*-based)	20	$1.53 \cdot 10^{-4}$	$1.59 \cdot 10^{-4}$	$2.34 \cdot 10^{-9}$	30%
	50	$1.52 \cdot 10^{-4}$	$1.53 \cdot 10^{-4}$	$4.32 \cdot 10^{-10}$	14%
Delta method	20	$1.36 \cdot 10^{-4}$	$1.41 \cdot 10^{-4}$	$1.82 \cdot 10^{-9}$	30%
	50	$1.48 \cdot 10^{-4}$	$1.48 \cdot 10^{-4}$	$4.68 \cdot 10^{-10}$	15%

3.3.1.2 EDP-based approach: applications from the RINTC project

This application considers six of the structures that were designed, modelled and analysed within the activities of the RINTC project (in italian: *Rischio Implicito delle strutture progettate secondo le Norme Tecniche per le Costruzioni* – implicit seismic risk of code-conforming Italian buildings, deepened in Chapter 5, which is a research project carried out by a consortium of Italian universities (ReLUIS) for the Department of Civil Protection, with the objective of analytically assessing the intrinsic seismic reliability of new code-conforming structures in Italy [11,105]. Within the framework of that project, MSA was used to estimate the seismic reliability for buildings of varying typology and configuration, designed for several Italian sites in order to cover a wide range of seismic hazard levels. For the purposes of this illustrative application of the R2R-EU software, the buildings considered were designed for the site of L'Aquila under soil conditions of *type C*, according to Eurocode 8 classification [106], and belong to the following typologies: unreinforced masonry residential buildings (URM), cast-in-place reinforced concrete residential buildings (RC) and steel industrial buildings (STEEL). The three-dimensional numerical model of each building was subjected to MSA

using ten stripes, each containing twenty records of *hazard-consistent*, bi-directional, ground motion. The shaking intensity, characteristic of each stripe, was selected to correspond to a specific return period (T_r), ranging from 10 years to 10^5 years, and the analysis results were combined with the site-specific hazard to evaluate λ_f for the collapse limit state (among others) [11]. The six buildings used for the application shown here (two of each aforementioned category STEEL, URM, RC) are briefly described below.

STEEL 1: single-storey steel industrial building consisting of 20 m span-length moment-resisting portal frames in the transverse direction, which are repeating every 6 m in the longitudinal sense and are braced via concentric braces at the outermost spans;

STEEL 2: steel structure similar to STEEL 1 only somewhat larger, with axial distance between portal frames and braced span length equal to 8 m;

URM 1: Regular two-story unreinforced masonry structure (configuration type "C2" [107]);

URM 2: Regular in elevation and irregular in plan unreinforced masonry structure (configuration type "I1" [107]);

RC 1: cast-in-place reinforced concrete structure consisting of a nine-story moment-resisting frame with masonry infills, coupled with a shear wall;

RC 2: cast-in-place reinforced concrete structure consisting of a nine-story moment-resisting and shear wall pilotis frame, i.e., designed for interruption of the masonry infills at the ground floor.

Details on the design, numerical modelling and non-linear dynamic analyses of these structures can be found in [108–110].

All three *EDP*-based procedures for MSA available in R2R-EU (i.e., one parametric and two resampling bootstrap processes, see Table 3) were implemented for these six structures. The dynamic analysis results that underlie the R2R-EU elaborations are presented in Figure 36, where structural responses per stripe are given in terms of demand-over-capacity ratios (D/C), these ratios being defined as the *EDP* values normalized by the edp_f that has been assigned to signify conventional collapse for each structure. This means that failure corresponds to D/C exceeding unit value, which has been marked on Figure 36 by a vertical dashed line; on the same figure, all converged-analysis cases with $D/C > 2$ have been incorporated along with non-convergent

analyses into a single point per stripe labelled as *collapses*, that carries a label reporting the number of conventional collapse cases. The results provided by R2R-EU, corresponding to these analyses, in terms of point estimate $\hat{\lambda}_f$ and estimator statistics for the failure rate and fragility parameters (where applicable) are summarized in the Table 4[1]

[1] It should be noted that it has been RINTC practice to refrain from extending hazard calculations to intensities with TR >105 years, so as to avoid extrapolating semi-empirical seismological models, assuming that λf for collapse is at least 10-5 [11]; in the applications presented herein this condition is dropped and the failure rates are solely dependent on the structural responses available.

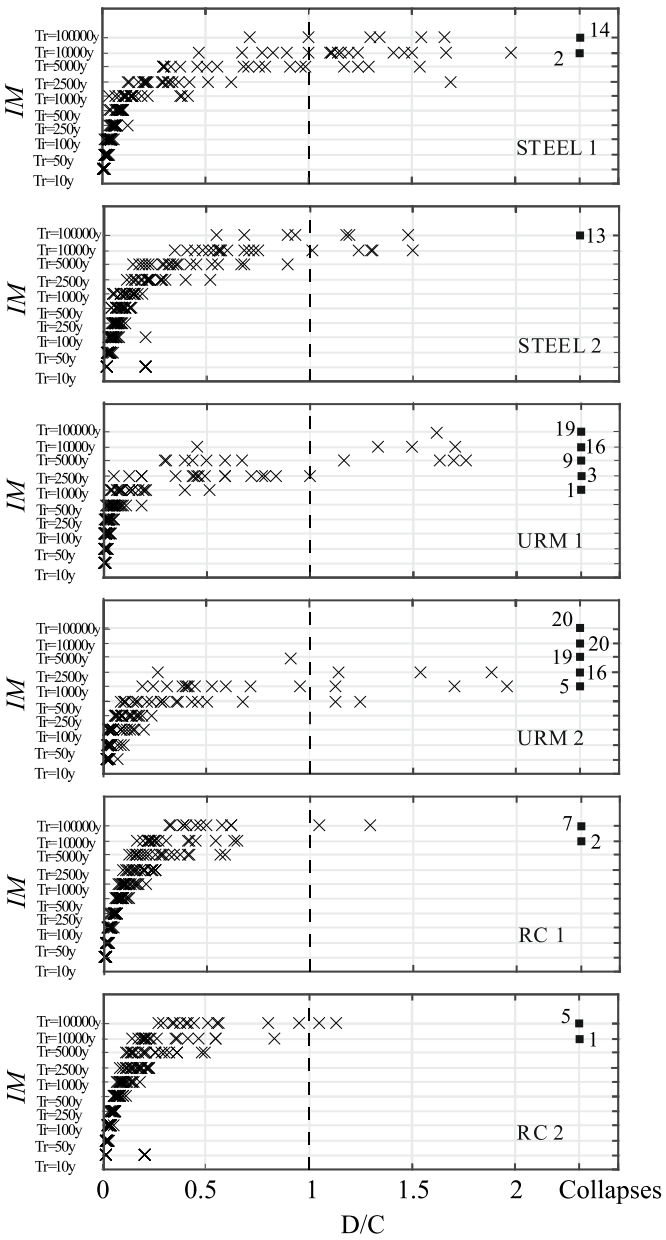

Figure 36. Structural response of the six considered buildings in terms of demand-over-capacity ratios D/C. Crosses represent response values from dynamic analysis that converged with $D/C \leq 2$ *; squares are stand-ins used for indicating the number of conventional collapses at each stripe.*

Table 5. Statistics of the estimator of the failure rate by using all three procedures implemented in R2R-EU for the MSA EDP-based approach.

Lognormal fragility (maximum likelihood)

Building	STEEL 1	STEEL 2	URM 1	URM 2	RC 1	RC 2
$\hat{\lambda}_f$ [events/year]	$2.07 \cdot 10^{-4}$	$9.65 \cdot 10^{-5}$	$3.81 \cdot 10^{-4}$	$1.19 \cdot 10^{-3}$	$5.08 \cdot 10^{-5}$	$3.66 \cdot 10^{-5}$
$(m - m_o)$	500	491	500	495	431	298
$E[\hat{\eta}]$	1.26	1.68	0.52	0.74	1.32	1.47
$VAR[\hat{\eta}]$	$7.26 \cdot 10^{-3}$	$8.59 \cdot 10^{-3}$	$1.79 \cdot 10^{-3}$	$2.04 \cdot 10^{-3}$	$2.51 \cdot 10^{-2}$	$6.85 \cdot 10^{-2}$
$E\left[\hat{\beta}\right]$	$4.51 \cdot 10^{-1}$	$3.78 \cdot 10^{-1}$	$2.35 \cdot 10^{-1}$	$2.28 \cdot 10^{-1}$	$4.98 \cdot 10^{-1}$	$5.37 \cdot 10^{-1}$
$VAR\left[\hat{\beta}\right]$	$6.72 \cdot 10^{-3}$	$5.02 \cdot 10^{-3}$	$2.14 \cdot 10^{-3}$	$1.39 \cdot 10^{-3}$	$1.35 \cdot 10^{-2}$	$2.38 \cdot 10^{-2}$
$E\left[\hat{\lambda}_f\right]$ [events/year]	$2.08 \cdot 10^{-4}$	$9.65 \cdot 10^{-5}$	$3.81 \cdot 10^{-4}$	$1.19 \cdot 10^{-3}$	$5.39 \cdot 10^{-5}$	$4.16 \cdot 10^{-5}$
$VAR\left[\hat{\lambda}_f\right]$ [(events/year)^2]	$1.13 \cdot 10^{-9}$	$1.81 \cdot 10^{-10}$	$2.44 \cdot 10^{-9}$	$2.28 \cdot 10^{-8}$	$1.62 \cdot 10^{-10}$	$1.09 \cdot 10^{-10}$
$CoV_{\hat{\lambda}_f}$	16%	14%	13%	13%	24%	25%

Lognormal fragility (normal probability paper procedure)

Building	STEEL 1	STEEL 2	URM 1	URM 2	RC 1	RC 2
$\hat{\lambda}_f$ [events/year]	$1.42 \cdot 10^{-4}$	$1.06 \cdot 10^{-4}$	$3.10 \cdot 10^{-4}$	$8.09 \cdot 10^{-4}$	$9.98 \cdot 10^{-5}$	$6.15 \cdot 10^{-5}$
m	500	500	500	500	500	500
$E[\hat{\eta}]$	1.36	1.5	0.57	0.20	0.90	1.13
$VAR[\hat{\eta}]$	$2.17 \cdot 10^{-2}$	$2.26 \cdot 10^{-2}$	$2.89 \cdot 10^{-3}$	$3.95 \cdot 10^{-3}$	$1.38 \cdot 10^{-2}$	$2.50 \cdot 10^{-2}$

$E\left[\hat{\beta}\right]$	$2.06\cdot10^{-1}$	$2.39\cdot10^{-1}$	$1.78\cdot10^{-1}$	$1.95\cdot10^{-1}$	$1.57\cdot10^{-1}$	$1.85\cdot10^{-1}$
$VAR\left[\hat{\beta}\right]$	$1.13\cdot10^{-3}$	$1.36\cdot10^{-3}$	$6.03\cdot10^{-4}$	$1.65\cdot10^{-3}$	$3.03\cdot10^{-4}$	$6.87\cdot10^{-4}$
$E\left[\hat{\lambda}_f\right]$ [events/year]	$1.40\cdot10^{-4}$	$1.08\cdot10^{-4}$	$3.10\cdot10^{-4}$	$8.33\cdot10^{-4}$	$9.15\cdot10^{-5}$	$6.44\cdot10^{-5}$
$VAR\left[\hat{\lambda}_f\right]$ [(events/year)^2]	$7.84\cdot10^{-10}$	$4.30\cdot10^{-10}$	$1.51\cdot10^{-9}$	$2.68\cdot10^{-8}$	$1.20\cdot10^{-10}$	$4.70\cdot10^{-10}$
$CoV_{\hat{\lambda}_f}$	20%	19%	13%	20%	12%	34%

Three-parameter model per intensity, Equation (6)

Building	STEEL 1	STEEL 2	URM 1	URM 2	RC 1	RC 2
$\hat{\lambda}_f$ [events/year]	$1.85\cdot10^{-4}$	$9.52\cdot10^{-5}$	$4.10\cdot10^{-4}$	$1.13\cdot10^{-3}$	$4.48\cdot10^{-5}$	$3.24\cdot10^{-5}$
m	500	500	500	500	500	500
$E\left[\hat{\lambda}_f\right]$ [events/year]	$1.88\cdot10^{-4}$	$9.56\cdot10^{-5}$	$4.12\cdot10^{-4}$	$1.12\cdot10^{-3}$	$4.61\cdot10^{-5}$	$3.26\cdot10^{-5}$
$VAR\left[\hat{\lambda}_f\right]$ [(events/year)^2]	$3.03\cdot10^{-10}$	$8.70\cdot10^{-11}$	$2.95\cdot10^{-9}$	$9.45\cdot10^{-9}$	$1.43\cdot10^{-10}$	$9.71\cdot10^{-11}$
$CoV_{\hat{\lambda}_f}$	9%	10%	13%	9%	26%	30%

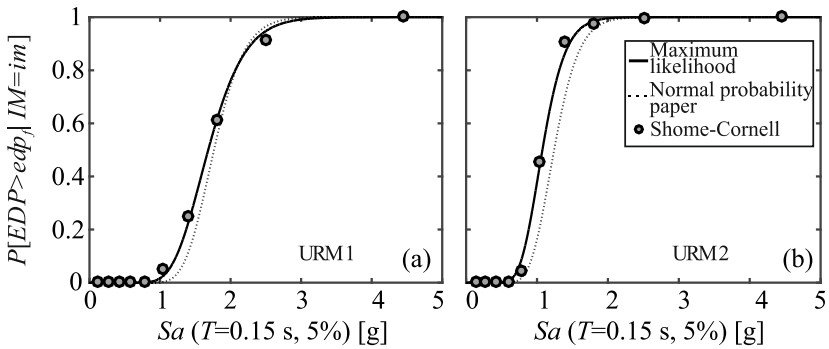

Figure 37. Fragility functions estimated by R2R-EU from the MSA results of the two masonry buildings: URM 1 (a) and URM 2 (b).

3.4 Conclusions

This section dealt with R2R-EU, that is an interactive PBEE software tool that can be used for quantifying the estimation uncertainty in seismic structural risk assessment, due to record-to-record variability of response. R2R-EU takes as input a hazard curve, the results of dynamic analysis, which can be incremental dynamic analysis, multiple stripe analysis or cloud analysis, and a threshold engineering demand parameter that defines the demarcation line for failure. With this input, the software first evaluates the structure-specific seismic fragility function. Subsequently, R2R-EU goes on to calculate a point estimate for the annual failure rate and to evaluate the expected value and variance of the rate's estimator. These calculations can be performed while assuming either a non-parametric representation for structural fragility or a lognormal model or even when employing Cornell's seismic reliability formulation. R2R-EU is available at www.reluis.it.

Chapter 4 – ON NUMBER OF RECORDS FOR RISK ESTIMATION: APPLICATION AND LIMITS OF THE STATISTCAL INFERENCE THEORY IN EARTHQUAKE-ENGINEERING

The following papers have been derived from this Chapter :

- *Baltzopoulos G., Baraschino R., Iervolino I. (2019) On the number of records for structural risk estimation in PBEE. Earthquake Engineering and Structural Dynamics, 48 :489–506.*
- *Baltzopoulos G, Iervolino I., Baraschino R. (2019) Ground motion sample size vs estimation uncertainty in seismic risk, 13th International Conference on Applications of Statistics and Probability in Civil Engineering (ICASP13), Seoul, South Korea, May 26-30.*
- *Baraschino R., Baltzopoulos G., Giorgio M., Iervolino I. (2020) Why determining the number of code spectrum-matched records based on usual statistics is an ill-posed problem, 17th World Conference on Earthquake Engineering, 17WCEE.*

4.1. Introduction

As exposed in the previous sections, the state-of-the-art for PBEE applications entails the analytical estimation of fragility functions by means of various procedures that require multiple dynamic analysis runs of a numerical model of the structure, while the evaluation of λ_{im} for various intensity levels, that is the hazard curve, is typically obtained by means of a probabilistic seismic hazard analysis (PSHA; e.g., [111]). In principle, both PSHA and the analytical derivation of structural fragility involve the use of ground motion records; in the former case this is implicit, as PSHA usually models *IM* via ground motion prediction equations (GMPEs; e.g., [112]), that are semi-empirical models based on recorded strong motion, while in the latter case it is explicit, as one has to select a certain number of accelerograms to conduct the analyses. The number of records typically used for non-linear dynamic analysis is mainly dictated by the large computation times required for running complex structural models at high non-linearity levels. However, the number of records directly determines the structural response sample-size to be used in estimating fragility and, ultimately, the failure rate. As highlighted, for example, in [8], and exposed in the previous Chapter, since these descriptors of seismic fragility and

risk are inferred from samples, they are only estimates of the corresponding true values, and are therefore affected by estimation uncertainty. In fact, the estimator of λ_f, already denoted as $\hat{\lambda}_f$, obtained using a specific sample of ground motions of certain size, can be considered at the same time a RV and a function of the sample. If one were to re-compute $\hat{\lambda}_f$ a number of times using different sets of accelerograms, equal in number to the first one and equivalent in characteristics to the analyst, one would keep obtaining different values for the estimator due to the record-to-record variability of inelastic structural response.[2] In order to illustrate this concept, an example will be provided in the context of IDA. As previously said when IDA stops, it is assumed that a certain threshold value of the *EDP* can be defined, edp_f, such that the condition $EDP > edp_f$ can be held to signify failure (e.g., violation of some limit-state). This implies that seismic fragility can be expressed as the probability of $EDP > edp_f$ conditional to $IM = im$; i.e., $P\left[f|im\right] = P\left[EDP > edp_f \,|IM = im\right]$ (*EDP*-based approach).

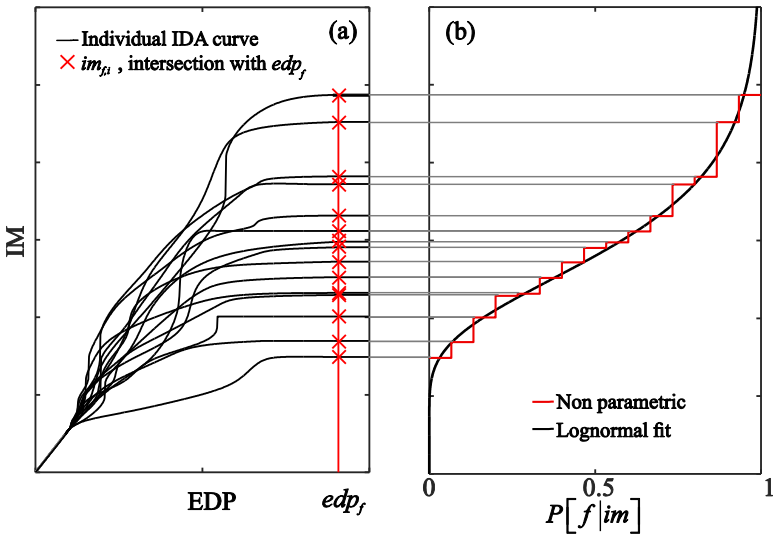

[2] There may be more sources contributing to estimation uncertainty in the fragility and the risk estimate; e.g., when accounting for variability in the numerical model properties that may be based on samples of experimental data (e.g., [155,156]). Nevertheless, the present study deals exclusively with estimation uncertainty related to record-to-record variability of structural response to earthquakes, since the intended focus is on the choice of record sample size.

Figure 38. Schematic representation of possible derivation of seismic fragility functions using incremental dynamic analysis. The intersection of the n IDA curves with the threshold EDP value defining failure (a) provides a sample of failure intensities used to define a cumulative probability function (b).

An alternative, widely-used way of expressing seismic fragility is provided by the so-called *IM*-based approach. *IM*-based fragility entails the introduction of a new RV, IM_f, that can be regarded as the seismic intensity able to cause structural failure [113]. By this definition, fragility can be expressed as the complementary cumulative distribution function of IM_f; i.e., $P\left[f|im\right] \equiv P\left[IM_f \le im\right]$. Returning to the IDA example, one can obtain the lowest *IM* value that causes each record to reach the failure criterion, by finding the height $im_{f,i}$, $i = \{1,2,\ldots,n\}$, where the *i*-th IDA curve intersects the vertical line $EDP = edp_f$, as shown in the figure. These $im_{f,i}$ values can be considered as a sample of IM_f. Common statistical methods ([55]) can then be employed to fit a parametric probability distribution model to the sample, such as the lognormal model indicated by a dark line in Figure 38b; alternatively, one may even assume that the observed sample values approximate the fragility in a non-parametric way, also depicted in Figure 38b as a stepwise function. However, if one were to repeat the procedure over a large number of times, each time performing IDA with a different set of records, it is to be expected that each repetition will lead to a different fragility curve. This variability will then reflect on the evaluated failure rate via Equation (1), and a quantitative measure can be obtained according to Equation (27):

$$CoV_{\hat{\lambda}_f} = \frac{\sqrt{VAR\left[\hat{\lambda}_f\right]}}{E\left[\hat{\lambda}_f\right]}, \tag{27}$$

where the notation $CoV_{\hat{\lambda}_f}$ indicates the *coefficient of variation* of the failure rate estimator, and $VAR\left[\hat{\lambda}_f\right]$, $E\left[\hat{\lambda}_f\right]$ denote its variance and expected value,

respectively.[3] In fact, in the case of unbiased estimators, $CoV_{\hat{\lambda}_f}$ provides the mean relative (with respect to the true value) estimation error.

Past PBEE-oriented research on the topic has seen discussion on the number of records that ought be used for estimating the distribution of *EDP*s at a single level (or *stripe*) of intensity [2,6]. In [9] the estimation uncertainty surrounding parametric fragility for simplified structural systems was examined, while [10] examined the effect of record sample size on the confidence intervals of various fractiles of collapse fragility. The effect of estimation uncertainty on the parametric fragility model stemming from cloud analysis was considered in [20]. The number of records issue has also been studied in a somewhat different context: [114] studied its effect under various proposals for spectral-matching and scaling of accelerograms and [115] paid particular attention to evaluating the ASCE/SEI-7 record selection and scaling procedure. In some of these previous studies that examined estimation uncertainty for the fragility parameters (e.g., [9,10]) it was recognized that further research was needed to investigate the effect of this uncertainty to the actual end result; i.e., the seismic risk estimate.

The objective of this Chapter is to further investigate the issue of the number of records and illustrate methodologies to be used as tools for making informed decisions about the number of accelerograms to employ in earthquake engineering applications, in order to achieve a given value of $CoV_{\hat{\lambda}_f}$. Two distinct paths are followed in tandem to reach this aim: an analytical approach based on the Cornell reliability method [54] and a computational approach based on IDA. In the former case, some additional simplifications are explored, intended to render a closed-form expression for $CoV_{\hat{\lambda}_f}$ tractable. The analytical result is then evaluated with the aid of cloud analysis [113] performed for some simple yielding oscillators, exposed to varying hazard scenarios. In the computationally-oriented case, a relatively large pool of records is assembled and used to run IDA for an assortment of low-rise code-conforming frames and simple inelastic structures. In this context, various limit states and alternative *IM*s are considered. Based on these IDA results, a Monte-Carlo methodology

[3] These are typically unknown; however, estimates are obtainable via methods such as those presented in [8].

is used to simulate statistics of the estimator $\hat{\lambda}_f$, for a wide range of record sample sizes n.

Sections 4.2 and 4.3 are structured in such a way that the analytical treatment to the problem is presented first, starting from the classical approximate seismic reliability formulation, that is the Cornell reliability method. Following that, risk assessments using *IM*-based, parametric and non-parametric, fragility are examined. Subsequently, the procedures for determining the suitable record sample size, by setting thresholds of tolerable estimation uncertainty, are illustrated, also considering spectral-shape-based (advanced) ground motion intensity measures.

Section 4.4 takes a step backwards with respect to previous section and asks another question: are the adopted response statistics an appropriate tool for addressing the minimum number of records mandated by modern codes and for reconciling the disparity with the sample sizes typically used in seismic risk analyses?

Finally, some concluding discussion is provided to summarize the main findings of the study.

4.2. Cornell reliability method

Cornell's seismic reliability method uses some simplifying assumptions to provide an elegant closed-form solution to estimate the annual failure rate $\hat{\lambda}_f$ [54]. The analytical expression is given below as Equation (28), where k is the (absolute value of) the hazard curve's slope, calculated in logarithmic-space at IM_C, that is the *IM* corresponding to the median capacity, λ_{IM_C} is the annual exceedance rate of IM_C at the site of interest, β_C is the standard deviation of the structural failure threshold, $\hat{b}$ and $\hat{\beta}_D$ are the slope parameter and the standard deviation of the logarithm of *EDP* that come with the assumption of an *EDP-IM* relationship as the one expressed by Equation (29).

$$\hat{\lambda}_f = \lambda_{IM_C} \cdot \mathrm{e}^{\frac{1}{2}\cdot\frac{k^2}{\hat{b}^2}\cdot\left(\hat{\beta}_D^2+\beta_C^2\right)} \tag{28}$$

$$\log\left(EDP\right) = \hat{a} + \hat{b}\cdot\log\left(IM\right) + \varepsilon \tag{29}$$

The parameters $\left\{\hat{a},\hat{b},\hat{\beta}_D\right\}$ can be obtained via ordinary least squares linear regression in the context of *cloud analysis* (e.g., [113]), which is typically performed considering *EDP* responses to a set of unscaled accelerograms from dynamic structural analysis, with $\hat{\beta}_D$ estimated as the standard deviation of ε ; i.e., the *regression residual* [59]. The hat symbol over the notation serves as a reminder that these parameters are estimates obtained from finite samples of ground-motion and hence also subject to estimation uncertainty. A graphical representation of the parameters and quantities relevant to the Cornell method is provided in Figure 39.

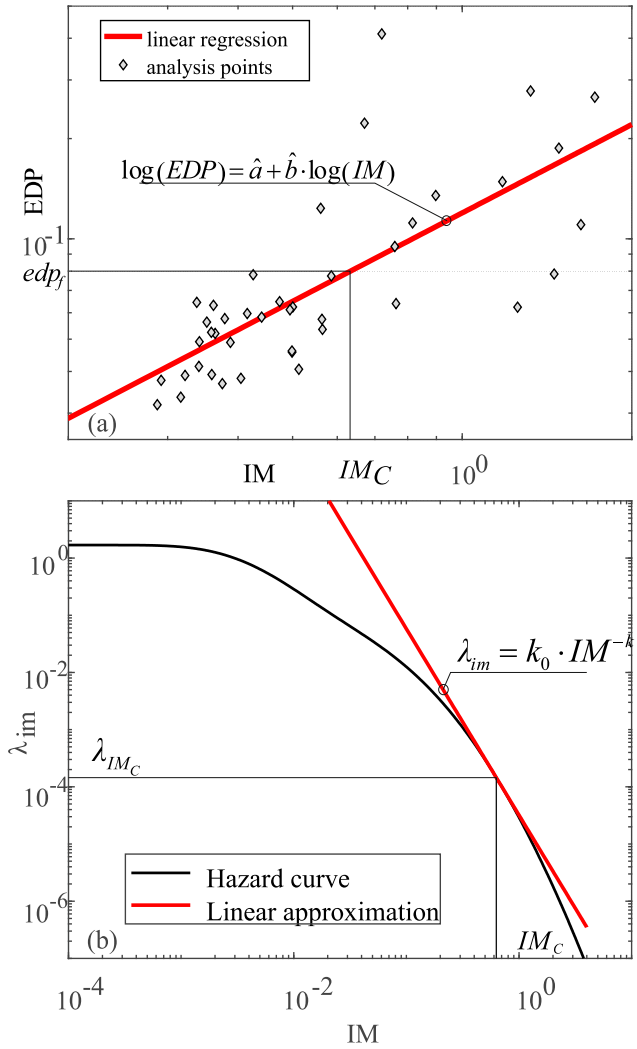

Figure 39. Top: cloud analysis for a simple SDOF inelastic structure situated in Naples, Italy. Bottom: local linearization of the hazard curve assumed in Cornell's seismic reliability method.

In [8], the *delta method* (e.g., [102]) was used to provide analytical expressions that allow calculating the mean and variance of $\hat{\lambda}_f$ in the framework of Cornell's method, reported herein in Equation (30), where $COV[\cdot]$ represents the covariance operator and the derivatives are those of Equation (28). By adopting $CoV_{\hat{\lambda}_f}$ as the measure of estimation uncertainty behind the seismic risk metric $\hat{\lambda}_f$, these two expressions can be used to derive a single formula for its quantification, via Equation (27).

$$\begin{cases} E\left[\hat{\lambda}_f\right] = \hat{\lambda}_f + \frac{1}{2}\cdot VAR[\hat{a}]\cdot\frac{\partial^2\hat{\lambda}_f}{\partial\hat{a}^2} + \frac{1}{2}\cdot VAR\left[\hat{b}\right]\cdot\frac{\partial^2\hat{\lambda}_f}{\partial\hat{b}^2} + \\ \quad + \frac{1}{2}\cdot VAR\left[\hat{\beta}_D^2\right]\cdot\frac{\partial^2\hat{\lambda}_f}{\partial\left(\hat{\beta}_D^2\right)^2} + COV\left[\hat{a},\hat{b}\right]\cdot\frac{\partial^2\hat{\lambda}_f}{\partial\hat{a}\cdot\partial\hat{b}} \\ VAR\left[\hat{\lambda}_f\right] = VAR[\hat{a}]\cdot\left(\frac{\partial\hat{\lambda}_f}{\partial\hat{a}}\right)^2 + VAR\left[\hat{b}\right]\cdot\left(\frac{\partial\hat{\lambda}_f}{\partial\hat{b}}\right)^2 + \\ \quad + VAR\left[\hat{\beta}_D^2\right]\cdot\left[\frac{\partial\hat{\lambda}_f}{\partial\left(\hat{\beta}_D^2\right)}\right]^2 + 2\cdot COV\left[\hat{a},\hat{b}\right]\cdot\frac{\partial\hat{\lambda}_f}{\partial\hat{a}}\cdot\frac{\partial\hat{\lambda}_f}{\partial\hat{b}} \end{cases} . \quad (30)$$

By examining applications of Cornell's method, functional to this study, it was observed that some of the terms of Equation (30) containing second derivatives of $\hat{\lambda}_f$, and especially $\partial^2\hat{\lambda}_f\big/\partial\left(\hat{\beta}_D^2\right)^2$, were providing much smaller contributions to the summations than the other terms of the Taylor expansion. In particular, the term $VAR\left[\hat{\beta}_D^2\right]\cdot\left[\partial\hat{\lambda}_f\big/\partial\left(\hat{\beta}_D^2\right)\right]^2$ was consistently found to be around two orders of magnitude lower than the other terms comprising $VAR\left[\hat{\lambda}_f\right]$. Furthermore, it was observed that $E\left[\hat{\lambda}_f\right]$ can be adequately approximated by the first two terms in the Taylor expansion, i.e., $\hat{\lambda}_f + 1/2\cdot VAR[\hat{a}]\cdot\partial^2\hat{\lambda}_f\big/\partial\hat{a}^2$. Thus, under these hypotheses, some terms can be

dropped from Equation (30) in pursuit of simplification, as they appeared less influential in practical applications (see also the applications that follows), resulting in Equation (31),which provides the approximate estimates for $E\left[\hat{\lambda}_f\right], VAR\left[\hat{\lambda}_f\right]$ to plug into Equation (27).

$$\begin{cases} E\left[\hat{\lambda}_f\right] \approx \hat{\lambda}_f \cdot \left(1 + \dfrac{k^2}{2 \cdot \hat{b}^2} \cdot VAR\left[\hat{a}\right]\right) \\ VAR\left[\hat{\lambda}_f\right] \approx VAR\left[\hat{a}\right] \cdot \left(\dfrac{\partial \hat{\lambda}_f}{\partial \hat{a}}\right)^2 + VAR\left[\hat{b}\right] \cdot \left(\dfrac{\partial \hat{\lambda}_f}{\partial \hat{b}}\right)^2 + \cdot \\ \qquad + 2 \cdot COV\left[\hat{a}, \hat{b}\right] \cdot \dfrac{\partial \hat{\lambda}_f}{\partial \hat{a}} \cdot \dfrac{\partial \hat{\lambda}_f}{\partial \hat{b}} \end{cases} \tag{31}$$

With reference to Figure 39, by denoting the abscissa of the cloud analysis point corresponding to the *i*-th ground motion as $\log\left(im_i\right)$ and representing the sample mean and standard deviation of the logarithms of these records' *IM* values by:

$$\overline{\log\left(im\right)} = 1/n \cdot \sum_{i=1}^{n} \log\left(im_i\right) \text{ and } s_{\log(im)} = \sqrt{1/n \cdot \sum_{i=1}^{n} \left[\log\left(im_i\right) - \overline{\log\left(im\right)}\right]^2},$$

respectively, then it is known [59] that:

$$\begin{cases} VAR\left[\hat{a}\right] \approx \dfrac{\hat{\beta}_D^2}{n} \cdot \left(1 + \dfrac{\overline{\log\left(im\right)}^2}{s_{\log(im)}^2}\right) \\ VAR\left[\hat{b}\right] \approx \dfrac{\hat{\beta}_D^2}{n \cdot s_{\log(im)}^2} \\ COV\left[\hat{a}, \hat{b}\right] \approx \dfrac{\hat{\beta}_D^2}{n} \cdot \left(\dfrac{-\overline{\log\left(im\right)}}{s_{\log(im)}^2}\right) \end{cases} . \tag{32}$$

By combining Equations (27), (31), (32) and substituting the partial derivatives of $\hat{\lambda}_f$ (that can be obtained from Equation (28), but are also given explicitly in [8]), then Equation (33) is obtained. In that Equation,

$\gamma = \log\left(IM_C\right) - \frac{k}{\hat{b}^2} \cdot \left(\hat{\beta}_D^2 + \beta_C^2\right)$ and $\log\left(IM_C\right) = \left[\log\left(edp_f\right) - \hat{a}\right] \Big/ \hat{b}$ is the log of the median structural capacity.

$$CoV_{\hat{\lambda}_f} \approx \frac{\hat{\beta}_D \cdot k \cdot \sqrt{s_{\log(im)}^2 + \overline{\log\left(im\right)}^2 - 2 \cdot \overline{\log\left(im\right)} \cdot \gamma + \gamma^2}}{\sqrt{n} \cdot \hat{b} \cdot s_{\log(im)} \cdot \left[1 + \frac{k^2}{2 \cdot \hat{b}^2} \cdot \left(1 + \frac{\overline{\log\left(im\right)}^2}{s_{\log(im)}^2}\right) \cdot \frac{\hat{\beta}_D^2}{n}\right]} \approx \frac{\frac{\hat{\beta}_D \cdot k}{\hat{b} \cdot s_{\log(im)}} \cdot \sqrt{\overline{\log\left(im\right)}^2 - 2 \cdot \overline{\log\left(im\right)} \cdot \gamma + \gamma^2}}{\sqrt{n}} \quad . \tag{33}$$

The simplifications, when passing unto the second (approximate) equality, are due to the observations that $s_{\log(im)}^2 + \overline{\log\left(im\right)}^2 = 1/n \cdot \sum_{i=1}^{n} \left[\log\left(im_i\right)\right]^2 = \overline{\log\left(im\right)^2}$, and that for most typical earthquake engineering applications $\hat{\beta}_D$ in natural log scale will be in the 0.20-0.60 range [116], so for a number of records n of more than ten, the term $1 + \left(k^2 / 2 \cdot \hat{b}^2\right) \cdot \left(1 + \overline{\log\left(im\right)}^2 \Big/ s_{\log(im)}^2\right) \cdot \left(\hat{\beta}_D^2 / n\right)$ will tend to unity. Thus, apart from the non-surprising fact that $CoV_{\hat{\lambda}_f}$ varies inversely proportional to $\sqrt{n}$, the equation suggests that it depends, among other things, also on the shape of the hazard curve, around a region of the curve that corresponds to the structural capacity.

To better illustrate the implications of Equation (33), three yielding single-degree-of-freedom (SDOF) systems were considered; these SDOFs all had natural vibration period $T = 0.70s$ and bilinear backbone curves following a peak-oriented hysteretic rule exhibiting some mild cyclic strength degradation [42]. Each structure was assumed situated at a site of the same subsoil category (class B according to [63]; i.e., soil with thirty-meter shear wave velocity $v_{s,30}$ between 360 and 500 *m/s*), but characterized by varying levels of seismic hazard. Three Italian sites were chosen for this example, namely Milan (representing a low seismic hazard), Naples (medium hazard) and L'Aquila (high seismic hazard; see also [117]). Hazard curves in terms of spectral acceleration at their vibration period $Sa\left(T = 0.7s\right)$ were obtained for all three

sites using the REASSESS software [103], considering the seismic source model from [84]. The yield displacement d_y for all structures was set corresponding to a uniform-across-sites yield annual frequency of 0.0021. The hazard curves at the three sites are shown in Figure 40. Finally, cloud analysis was performed using three sets of forty-two records and the MATLAB-OpenSees [44] interface DYANAS (Section 2.5) (the analysis for the SDOF situated at the Naples site is shown in Figure 39). The ground motion records were selected from within the NESS flat-file [104,118] to provide coverage of a relatively wide range of $Sa\left(T=0.7s\right)$ values.

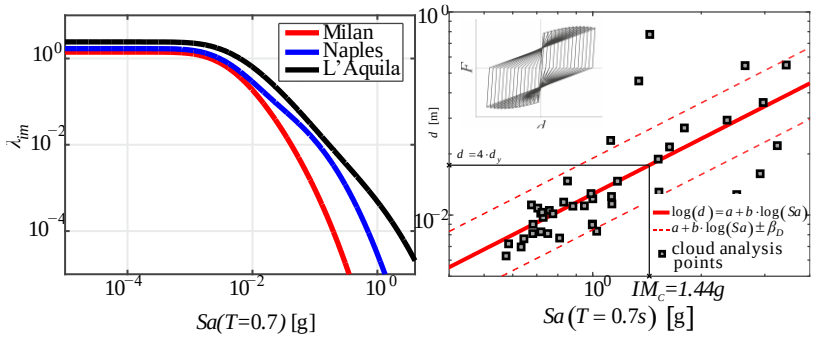

Figure 40. Hazard curves calculated for the three Italian sites (left) and cloud analysis for the SDOF structure assumed at a site near L'Aquila (right). The peak-oriented, degrading hysteretic behavior characterizing these inelastic SDOF oscillators used in the examples of Cornell's reliability method is also shown.

Using all of these results, $CoV_{\hat{\lambda}_f}$ was evaluated for various cases of failure threshold edp_f, set at ductility demands (ratio of maximum-to-yield displacement d/d_y) of four, six and eight. The results of these calculations are presented in Table 6, along with the values assumed by the parameters involved in the intermediate computations. The corresponding example of cloud analysis for the L'Aquila SDOF structure, considering $d/d_y=4$ as the failure threshold, is shown in Figure 40.

The last two columns of Table 6 provide a direct evaluation for the simplifications adopted in Equation (31): a comparison of the results for $CoV_{\hat{\lambda}_f}$ given by the delta method implemented as presented in [8] – i.e., computing $CoV_{\hat{\lambda}_f}$ by substituting Equations (30) into Equation (27) – and the simplified

Equation (33). It emerges, from this comparison, that the latter remains a good approximation of the former. Regarding the resulting $CoV_{\hat{\lambda}_f}$ values themselves, it can be seen that passing from a hazard curve slope-at-median-capacity k of around 2.0 at the high-hazard site (L'Aquila) to about 3.5 for the low-hazard site (Milan), this metric of estimation uncertainty for the failure rate of nominally identical structures more than doubles. Recalling the inverse proportionality of $CoV_{\hat{\lambda}_f}$ to $\sqrt{n}$, according to Equation (33), this result implies that more than four times as many records would be needed to reduce estimation uncertainty for the risk estimate of the SDOF structure in Milan, to the same level as that of the structure in L'Aquila. This difference appears despite the fact that estimated dispersion of structural response $\hat{\beta}_D$ and failure rate $\hat{\lambda}_f$ are very similar for both structures. The same effect is observed at a single site, when considering the failure rate for limit states associated with progressively higher inelasticity levels: for the L'Aquila structure, changing the *EDP* threshold from four- to eight-times d_y resulted in an increase to $CoV_{\hat{\lambda}_f}$ from 0.15 to 0.25, as k increased from around 2.0 to 2.5 due to IM_C moving farther to the right of the hazard curve.

Table 6. Application of Equation (33) to inelastic SDOF systems at sites with varying severity of seismic hazard.

	L'Aquila			Naples	Milan
d/d_y	4	6	8	4	4
$\hat{a}$		-2.06		-2.12	-2.27
$\hat{b}$		0.91		0.88	0.88
$\hat{\beta}_D$		0.406		0.425	0.424
IM^C [g]	1.44	2.24	3.08	0.63	0.19
$k_0 \left[\times 10^{-5}\right]$	50	59.7	74.1	3.19	0.03
k	2.065	2.351	2.569	3.258	3.574
$\lambda_{IM^C} \left[\times 10^{-4}\right]$	2.37	0.89	0.41	1.41	1.11

$\hat{\lambda}_f \left[\times 10^{-4}\right]$		3.638	1.553	0.795	4.834	4.85
$CoV_{\hat{\lambda}_f}$	Eq. (30)	0.17	0.21	0.28	0.4	0.45
	Eq. (33)	0.15	0.18	0.25	0.38	0.44

The observations stemming from these illustrative examples, albeit quite evident from Equation (33), can be summarized as follows: for a fixed sample-size of ground motions, the variability, due to estimation uncertainty, of the seismic risk estimator $\hat{\lambda}_f$ does not increase only with β_D, but also with increasing (negative) slope of the hazard curve around the intensity where mean response matches the failure threshold. In other words, the number of dynamic analyses required to reduce the estimation uncertainty of a given structure's failure rate to a specific level, will increase with increasing severity of the limit state. Furthermore, for seismic risk analysis studies at sites where the curve drops off at steeper slopes one may need a larger number of dynamic analyses to achieve a specific target coefficient of variation, with respect to a similar analysis performed at a site with a milder-sloping curve and with all else being equal structure-wise. At first sight, one might be tempted to treat these observations with some caution, as they could be influenced by the simplifying assumptions of Cornell's reliability method (see [119] for a discussion). However, the same observations are also generally confirmed under a more rigorous context of seismic risk assessment, as discussed in the following.

4.3. Influence of the site-specific Hazard curve

In this section, the issue of estimation uncertainty is treated for cases of direct application of Equation (1), with the structure-specific fragility function $P\left[f \left| im \right.\right]$ being obtained via IDA. Case-study structures used in this context are three SDOF systems at three sites as before and two four-story, plane, code-conforming, moment-resisting frames: a steel perimeter frame, designed to ASCE-SEI 7-05 criteria and described in [77], and a reinforced concrete bare frame (i.e., without masonry infills) designed according to EN-1998-1 (see [78] for structural details). The only differences of the SDOF structures with respect to the previous example is that softening post-peak behavior has been modelled on their backbones to allow collapse prediction (e.g., [37]) and d_y has been re-

adjusted in order to ensure that, for collapse, an arbitrary yet uniform $\hat{\lambda}_f = 4.3 \cdot 10^{-4}$ results across all sites, when $Sa(T = 0.7s)$ is used as *IM*. The steel multiple-degree-of-freedom (MDOF) structure is placed at the L'Aquila site and the reinforced concrete one at the Naples site. Center-line models built in OpenSees are used for both frames; some basic geometrical information and static pushover curves are shown in Figure 41(a,b). For all structural models, IDA is performed using a set of two-hundred ground motions that are scaled upwards until dynamic instability is observed, signifying side-sway collapse. These records were selected primarily from within the NESS database (http://ness.mi.ingv.it/ [104,118]) and, to a lesser extent, from the NGA-West2 database [120]. The selection criteria were to obtain records exhibiting some of the highest available naturally recorded spectral ordinates at the first-mode vibration periods of the examined structures (to keep scaling-up during IDA to a minimum), to exclude records potentially affected by near-source directivity or recorded at very soft soil sites and to avoid over-representation of any single event.

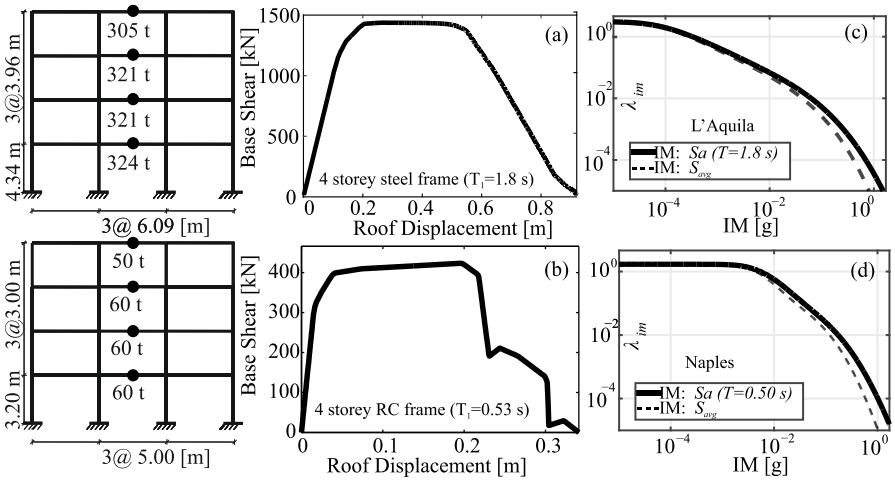

Figure 41. Basic information on the structures and hazard used in the examples. Dimensions and static pushover curves (first-mode proportional lateral load) for the two code-conforming, four-story, inelastic MDOF frame structures. Steel perimeter moment-resisting frame (a) and reinforced concrete moment-resisting frame (b). Hazard curves in terms of two IMs, $Sa(T_1)$ and S_{avg}, are shown for the L'Aquila (c) and Naples site (d).

In all cases, seismic fragility functions are estimated via the two-hundred records according to the *IM*-based procedure (e.g., [113]) for the collapse limit-state; additionally, limit-states characterized by various threshold $\left(edp_f\right)$ interstory drift ratios (IDRs) are considered for the two frames. This is done assuming, alternatively, lognormal and non-parametric fragility functions according to Equations (2) and (4) respectively, where $im_{f,i}$ represents the *i*-th record's (lowest) scaled *IM* value causing exceedance of the threshold (i.e., referring again to Figure 38, the intersection of the *i*-th record's IDA curve with the vertical $EDP = edp_f$ line), $\hat{\eta}$ and $\hat{\beta}$ are the point estimates of the lognormal fragility's parameters, taken as the mean and standard deviation of the logs of $im_{f,i}$, and n is the total number of records.

IDA curves are initially obtained in terms of 5% damped, first-mode spectral acceleration $Sa\left(T_1\right)$ but, thanks to the use of the hunt-and-fill algorithm [51], they are subsequently converted into another two more *efficient* IMs that account for spectral shape: average spectral acceleration S_{avg} ([92,121]) and I_{N_p} [122], given by Equations (34) and (35), respectively (discussion on *IM* efficiency to follow).

$$S_{avg} = \sqrt[n]{\prod_{i=1}^{n}\left[Sa\left(T_i\right)\right]} \tag{34}$$

$$I_{Np} = Sa\left(T_1\right)\cdot\left[S_{avg}/Sa\left(T_1\right)\right]^{0.40} \tag{35}$$

Spectral ordinates at different periods T_i are used to define these IMs for each structure. Both S_{avg} and I_{Np} for the SDOF structures use $T_i = \{0.7\text{s}, 1.0\text{s}, 1.4\text{s}\}$ while S_{avg} for the MDOF frames uses each structure's first-mode period T_1 and another three periods approximately corresponding to $\{0.3\cdot T_1, 1.5\cdot T_1, 2\cdot T_1\}$. Hazard curves for these structure-specific IMs are provided in Figure 41 (c,d) for the frames and Figure 42 for the SDOF systems.

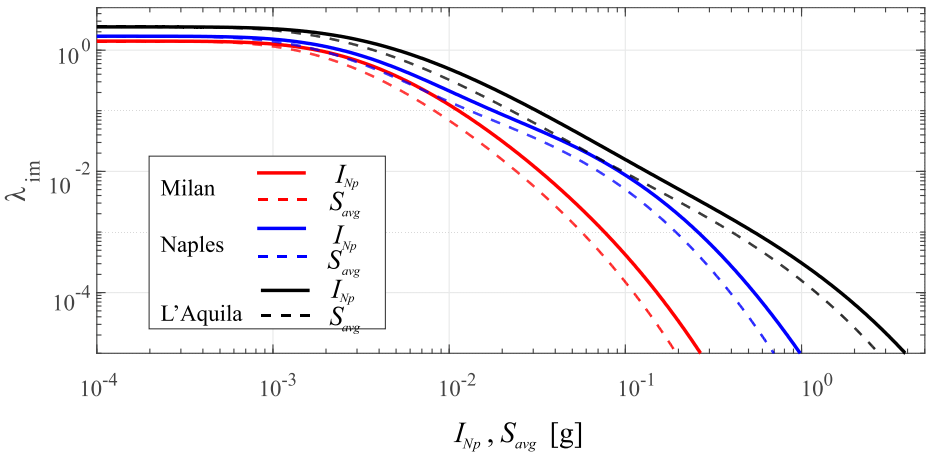

Figure 42. Hazard curves for the structure-specific IMs INp and Savg that were used for the collapse risk estimates of the example SDOF structures at the three Italian sites of Milan, Naples and L'Aquila.

For each structure, limit-state and *IM*, the two-hundred-record IDA-based fragilities are treated as the reference - *true* - fragility functions for the purposes of the study. Following the derivation of the fragility functions from the vectors of $im_{f,i}$ provided by IDA, Monte Carlo simulation is used to calculate the relationship of $CoV_{\hat{\lambda}_f}$ against n. The simulation entails randomly sampling l times from the reference distribution of *IM* levels causing failure, IM_f , for different sample sizes $n = \{2,3,...,200\}$.[4] The reference distribution sampled during the simulation is alternatively considered the lognormal function estimated from the two-hundred-record IDA via Equation (2) and the non-parametric version of the same. In the former case, new lognormal fragility parameters are fitted to each individual sample according to Equation (2), while in the latter, Equation (4) is directly applied to the sample and considered as fragility function. Examples of the resulting simulated fragility realizations are shown in Figure 43 and Figure 44 for the lognormal and non-parametric case, respectively. Both figures refer to the collapse fragility of the four-story steel frame at the L'Aquila site, expressed in terms of both $Sa(T = 1.8s)$ and S_{avg} . Each panel displays the reference two-hundred-record fragility function and

[4] Although this type of simulation is reminiscent of resampling schemes such as the bootstrap, the two methods are only coincident when samples of equal size to the original two-hundred are being extracted.

five-thousand simulated fragility realizations for sample sizes $n=\{20,50,100\}$. These plots provide a visual representation of the effect of estimation uncertainty on structural fragility, as increasing the sample size of structural responses results in the simulated curves clustering more tightly around the sampled reference fragility.

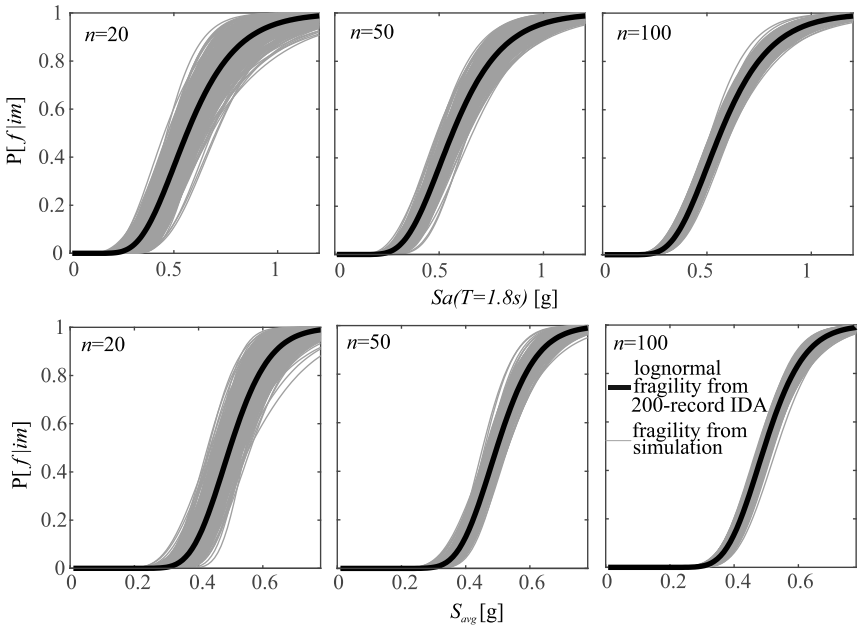

Figure 43. Plots of lognormal collapse fragility functions, produced during Monte-Carlo simulations that sample $n=\{20,50,100\}$ *failure intensities from the lognormal distribution derived from the two-hundred-record IDA of the steel, four-story frame. Top row shows fragilities in terms of* $Sa(T=1.8s)$ *and bottom row in terms of* S_{avg} *. Each panel displays five-hundred simulations.*

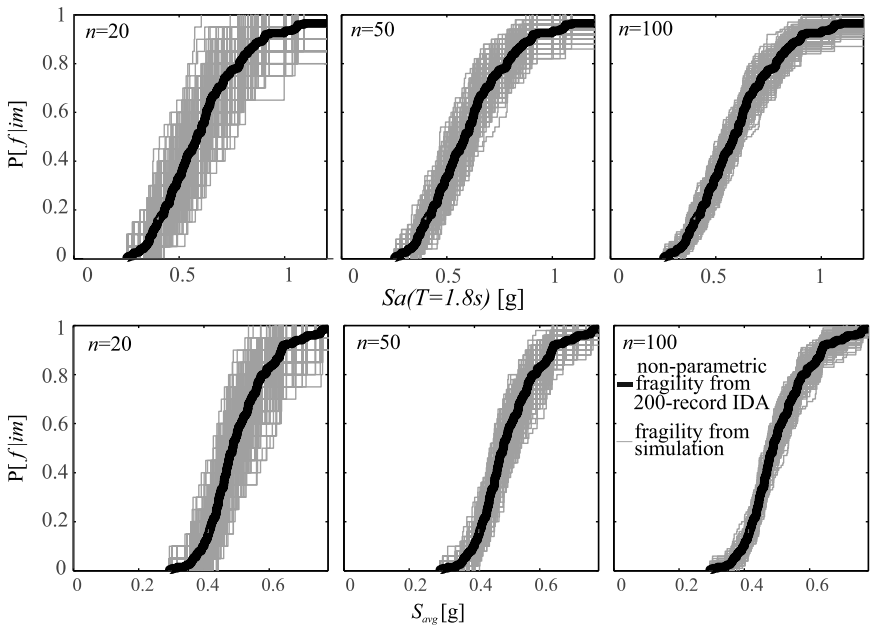

Figure 44. Non-parametric collapse fragility functions, produced during Monte-Carlo simulations that sample $n=\{20,50,100\}$ *failure intensities from their empirical distribution resulting from the two-hundred-record IDA of the four-story steel frame. Top row shows fragilities in terms of* $Sa(T=1.8s)$ *and bottom row in terms of* S_{avg} *, with each panel displaying five-hundred simulations. Corresponding simulations performed under the assumption of a lognormal fragility model are shown in Figure 43.*

In either case, using Equation (1) leads to a point estimate of the failure rate at the *j*-th simulation $\hat{\lambda}_{f,j}$, $j=\{1,2,...,l\}$, with a total of $l=5000$ simulations used for each application. Finally, by substituting $VAR\left[\hat{\lambda}_f\right]$ and $E\left[\hat{\lambda}_f\right]$ in Equation (27) with their estimates from the Monte Carlo simulation-generated sample, $CoV_{\hat{\lambda}_f}$ is approximated for each $\mathbb{I}$ according to Equation (36).

$$CoV_{\hat{\lambda}_f} \approx \frac{\sqrt{\frac{1}{l-1}\cdot\sum_{j=1}^{l}\left(\hat{\lambda}_{f,\mathrm{j}}-\frac{1}{l}\cdot\sum_{k=1}^{l}\hat{\lambda}_{f,\mathrm{k}}\right)^2}}{\frac{1}{l}\cdot\sum_{j=1}^{l}\hat{\lambda}_{f,\mathrm{j}}} \qquad (36)$$

The results of this procedure are shown in Figure 45 for the three SDOF systems, in Figure 46 for the steel frame and in Figure 47 for the reinforced concrete frame. In these figures, $CoV_{\hat{\lambda}_f}$ is plotted against n for the various limit states and *IM*s considered, and the record sample sizes corresponding to coefficients of variation of 0.10 and 0.20 are denoted for select cases to facilitate comparison.

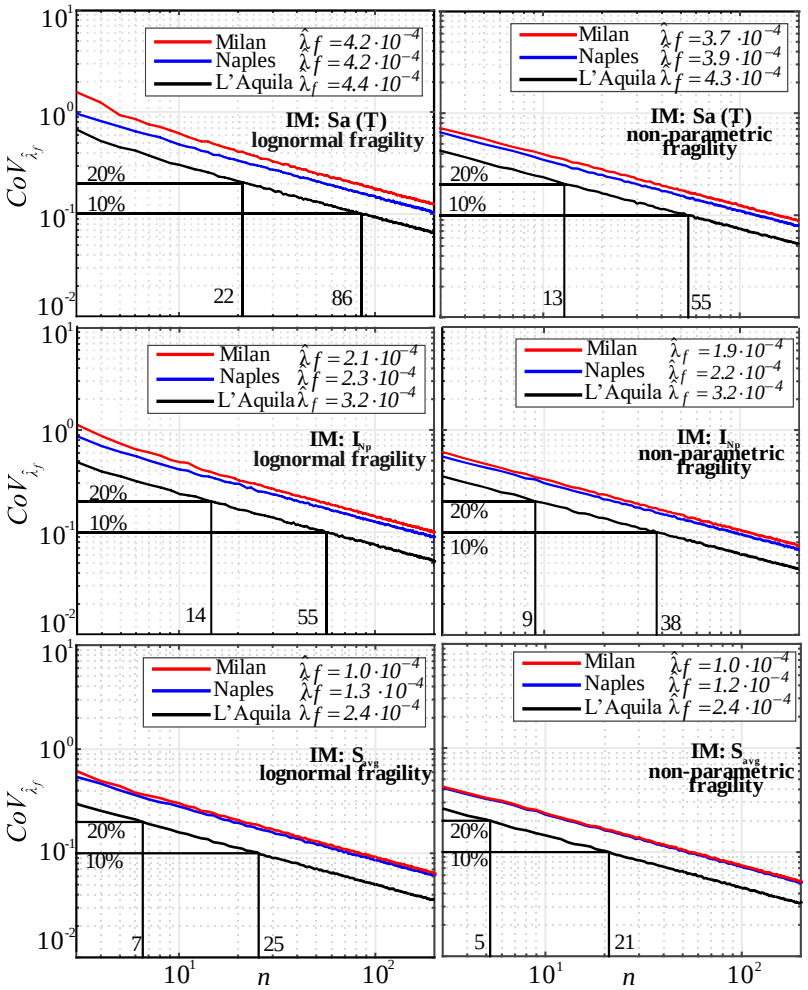

Figure 45. $CoV_{\hat{\lambda}_f}$ against n calculated via Monte Carlo simulation for the three SDOF structures considered.

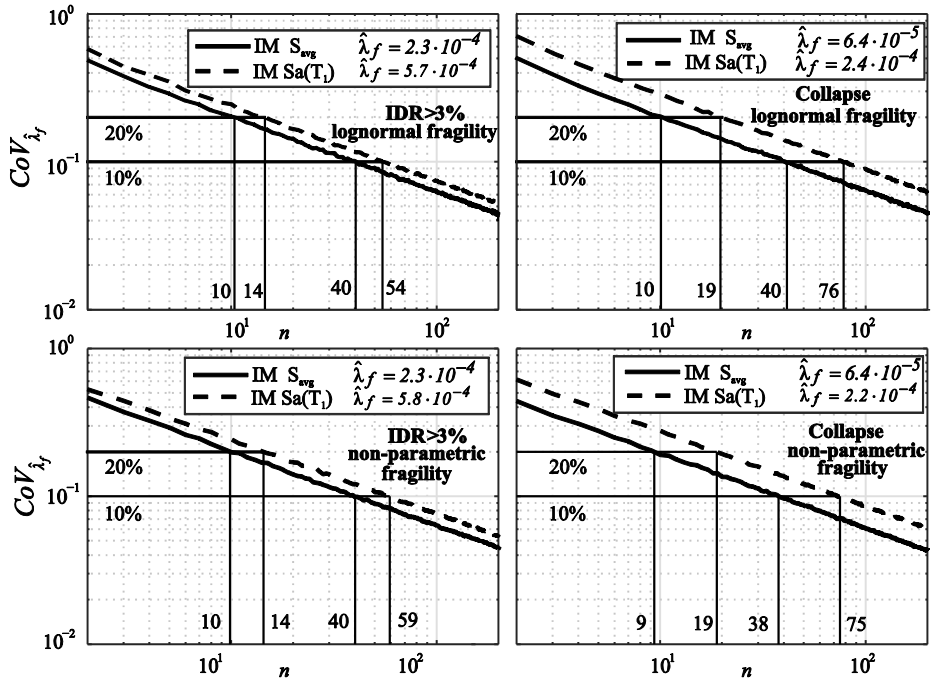

Figure 46. $CoV_{\hat{\lambda}_f}$ against n calculated via Monte Carlo simulation for the four-story steel frame considered at the L'Aquila (high hazard) site.

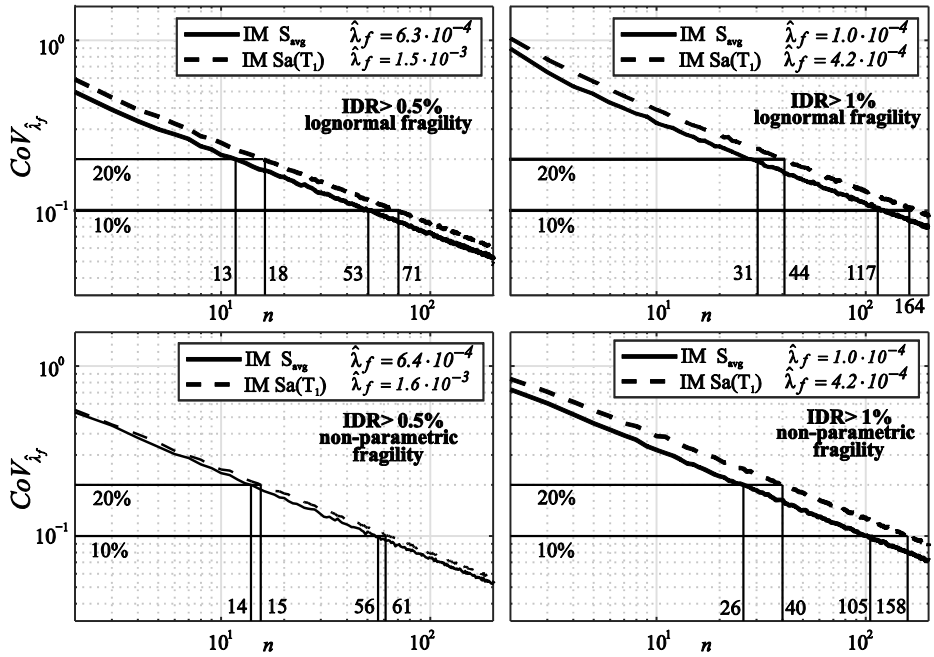

Figure 47. $CoV_{\hat{\lambda}_f}$ *against* $\mathbb{I}$ *calculated via Monte Carlo simulation for the four-story reinforced concrete frame considered at the Naples (medium hazard) site.*

From these results, it can be observed that $CoV_{\hat{\lambda}_f}$ from Monte Carlo simulation is very nearly inversely proportional to $\sqrt{n}$, especially for $n \geq 3$, as suggested by Equation (33). Thus, all of these curves are almost linear in the logarithms with a slope of $-1/2$, i.e., $\log\left(CoV_{\hat{\lambda}_f}\right) \approx \log(\Delta) - 1/2 \cdot \log(n)$. It is, therefore, useful to calculate the log-space intercept of these curves, $\log(\Delta)$, equal to $\Delta = \sqrt{n} \cdot CoV_{\hat{\lambda}_f}$ in linear scale, by least-squares fitting. This information is reported in Table 7 along with the logarithmic standard deviation β_{IM_f} of the fragility curve for each case, where the hat from β_{IM_f} is omitted to indicate the reference two-hundred record-based estimate, presumed close to the true value. It is evident that Δ bears direct correspondence to the numerator of Equation (33) and that cases exhibiting higher Δ values are subject to larger estimation uncertainty of $\hat{\lambda}_f$ than cases with lower Δ, given parity of record sample size.

From the figures and table, it can be observed that for the limit states associated with more severe levels of inelastic response, the lognormal assumption for fragility leads to higher $CoV_{\hat{\lambda}_f}$ than the non-parametric approach. On the other hand, for limit states corresponding to smaller drifts, both the lognormal and non-parametric approach lead to similar levels of estimation uncertainty for the failure rate of the structures examined. This difference hints at the unsurprising fact that the effect of the hazard curve's shape on the failure rate's estimation uncertainty is, in reality, somewhat more complex than just due to the slope at median capacity, since both of these representations of the fragility function share the same median IM_f.

This notwithstanding, the behavior of $CoV_{\hat{\lambda}_f}$ with varying conditions of site-specific seismic hazard observed within these results, is generally consistent with the observations made previously, on the basis of the analytical approximation derived from Cornell's method. In fact, at sites with hazard curves that slope downwards at steeper angles near the median capacity $\hat{\eta}_{IM_f}$, the dispersion of the estimator $\hat{\lambda}_f$ increases for structures with equal sample

sizes and ostensibly equal λ_f. This is observed among the SDOF systems examined, as well as between the two MDOF structures. The same effect is also observed at the same site and structure, when different limit-states are concerned: the collapse and $IDR > 3\%$ limit-states for the steel frame exhibit almost identical $\hat{\beta}_{IM_f}$ values, but the collapse case is associated with larger dispersion of $\hat{\lambda}_f$. This can be explained by the fact that collapse is associated with a higher $\hat{\eta}_{IM_f}$ than $IDR > 3\%$ (in terms of $Sa(T = 1.8s)$ $e^{\hat{\eta}_{IM_f}} = 0.56g$ and $0.37g$, respectively). Thus, $CoV_{\hat{\lambda}_f}$ for the collapse limit state is influenced by a steeper portion of the hazard curve than for $IDR > 3\%$. This is analogous to what was observed when implementing Equation (33) in Cornell's method, with increasing failure thresholds for the same structure.

Table 7. Logarithmic intercept Δ *of* $CoV_{\hat{\lambda}_f}$ *as a function of* n, $\log\left(CoV_{\hat{\lambda}_f}\right) = \log(\Delta) - 1/2 \cdot \log(n)$, *calculated via two-hundred record IDA for various structures, IMs, site seismic hazard and limit-states.*

Site	Structure	Limit-state	*IM*	β_{IM_f}	Fragility	Δ
Milan (low hazard)	Inelastic SDOF *T=0.70s*	Collapse	*Sa(T1)*	0.443	Lognormal	1.874
					Non-parametric	1.247
			INp	0.340	Lognormal	1.453
					Non-parametric	1.047
			Savg	0.222	Lognormal	0.945
					Non-parametric	0.745
Naples (medium hazard)	Inelastic SDOF *T=0.70s*	Collapse	*Sa(T1)*	0.444	Lognormal	1.521
					Non-parametric	1.108
			INp	0.341	Lognormal	1.271
					Non-parametric	0.960
			Savg	0.222	Lognormal Non-parametric	0.881
						0.727
	Four-story reinforced concrete frame *T1=0.53s*	*IDR*>0.5%	*Sa(T1)*	0.314	Lognormal	0.856
					Non-parametric	0.791
			Savg	0.216	Lognormal	0.734
					Non-parametric	0.747
		IDR>1%	*Sa(T1)*	0.389	Lognormal	1.344
					Non-parametric	1.247
			Savg	0.255	Lognormal	1.113

					Non-parametric	1.020
L'Aquila (high hazard)	Inelastic SDOF *T=0.70s*	Collapse	$Sa(T_1)$	0.443	Lognormal	0.956
					Non-parametric	0.737
			I_{Np}	0.340	Lognormal	0.747
					Non-parametric	0.614
			S_{avg}	0.222	Lognormal	0.505
					Non-parametric	0.455
	Four-story steel moment resisting frame $T_1=1.82s$	Collapse	$Sa(T_1)$	0.335	Lognormal	0.884
					Non-parametric	0.866
			S_{avg}	0.194	Lognormal	0.637
					Non-parametric	0.616
		IDR>3%	$Sa(T_1)$	0.329	Lognormal	0.745
					Non-parametric	0.761
			S_{avg}	0.227	Lognormal	0.631
					Non-parametric	0.640

4.3.1 Number of records and efficient intensity measures

The term *efficiency* is used in the literature to denote the property of an *IM* to produce lower dispersion of structural responses, conditional to that *IM*, than alternative, less efficient *IM*s (see for example [6,60]). Efficiency is specific to a given structural typology, *EDP* and level of non-linearity (e.g., [122,123]). Past research has shown that for *EDP*s related to story- and roof-drifts and for limit states nearing side-sway collapse, scalar *IM*s that reflect spectral shape at multiple periods, such as S_{avg} and I_{Np}, are more efficient than the classical $Sa(T_1)$ [60,121–124]. High efficiency is typically cited as an important and desirable characteristic, precisely because it implies that a smaller number of dynamic analysis runs will be required to achieve a given dispersion level for the estimator of a seismic-risk-related parameter (e.g., [2]). In fact, even though most studies that have investigated *IM* efficiency tend to focus on the record-to-record variability of structural response, this is actually intended as a proxy for the estimation uncertainty underlying the risk metrics, whose reduction is the end objective. It is, therefore, quite natural to directly observe the effect of this property on estimation uncertainty, via statistics such as $CoV_{\hat{\lambda}_f}$.

In this respect, there are two main observations to be made, on the basis of the mean relative error results obtained for the example applications. The first observation regards cases with $\Delta > 1$; i.e., combinations of the more severe limit states, low-to-medium hazard and adoption of the classical $Sa(T_1)$ as *IM*. In

these situations, the reciprocal relation of $CoV_{\hat{\lambda}_f}$ with $\sqrt{n}$, means that achieving an arbitrary low coefficient of variation of, say, 10% would require sample sizes in excess of one-hundred records, which verges on the impracticable. This hints at a more pressing need to adopt efficient *IM*s in such cases.

The second observation, is that when switching to more efficient *IM*s, the reductions in the dispersion $\hat{\beta}_{IM_f}$ are not always consistently reflected in the reductions of the number of records required to maintain any given $CoV_{\hat{\lambda}_f}$ level. For example, switching from $Sa(T_1)$ to S_{avg} results in about 30% reduction in $\hat{\beta}_{IM_f}$ for both the $IDR > 0.5\%$ state of the Naples frame and the $IDR > 3\%$ limit state of the L'Aquila frame; however, this translates to a 25% reduction in the number of records required to maintain any level $CoV_{\hat{\lambda}_f}$ in the latter case, but only 8% in the former. Similarly, performing the same operation for the collapse case of the SDOFs at the Milan and Naples sites results in the same 50% reduction in $\hat{\beta}_{IM_f}$, which translates in a 75% reduction in the corresponding number of records for the structure in Milan, but only 66% for the one in Naples.

Apart from these observations, a comment should be made about the fact that the two-hundred-record point estimate $\hat{\lambda}_f$ shifts when switching *IM*. This effect is mainly related to the sensitivity of response to seismological parameters when records are scaled (see, for example, [60]), which can be different for each *IM-EDP* combination. However, this is not an issue that is directly related to estimation uncertainty and for this reason, further discussion thereof falls beyond the scope of this article.

4.3.2 Target mean relative error and interquantile range of the risk estimate

The preceding discussion and illustrative applications showcased the influence of various parameters on $CoV_{\hat{\lambda}_f}$ and provided some typical ranges of values that it is expected to take for given sample sizes. It was highlighted that the mean relative estimation error, in the case of *IM*-based fragility, varies with n according to $CoV_{\hat{\lambda}_f} = \Delta/\sqrt{n}$, with Δ depending on the choice of *IM* and

consequent record-to-record variability of structural response and on the shape of the corresponding hazard curve. The examples provided indicate that, for the simple inelastic structures examined, $\Delta \in (0.45, 1.9)$, which translates into $CoV_{\hat{\lambda}_f}$ ranging roughly from $0.45/\sqrt{n}$ for a combination of efficient *IM* and high seismicity site (mild slope of the hazard curve around average structural capacity) to about $1.9/\sqrt{n}$ for the other extreme of less efficient *IM* and low seismicity site (steeper curve). Given that the hazard curve should be known prior to embarking on dynamic analysis and that the literature is rife with studies on the efficiency of various *IM*s for specific *EDP*s, one should be able to assess the required number of records to be $n = (\Delta / CoV_{tar})^2 \approx \left[(0.45 \div 1.9) / CoV_{tar} \right]^2$, where CoV_{tar}, is a target value for the coefficient of variation of the risk estimate. Once the dynamic analysis has been concluded and structural response results have become available, it will also be possible to use other tools for assessing estimation uncertainty, such as those presented in [8].

In this context, it may be useful to illustrate the consequences of setting a target $CoV_{\hat{\lambda}_f}$ of, say, 0.10 or 0.20 on the precision of the risk estimate, by linking these values to another measure of the estimator's scatter around the mean: the 5th to 95th interquantile range, $\hat{\lambda}_{f,0.95} - \hat{\lambda}_{f,0.05}$ [75]. This statistic can be calculated from the approximations to the distribution of $\hat{\lambda}_f$ obtained by the Monte Carlo simulations for each $\mathbb{I}$, an example of which is provided in Figure 48. The examples in the figure refer to the *IDR>1%* limit state for the reinforced concrete frame and collapse of the steel frame, in both cases using S_{avg} as *IM*, and are given for $n = \{20, 50, 100\}$. The distribution plots clearly showcase the reduction in dispersion of the risk estimator, with increasing sample size of records.

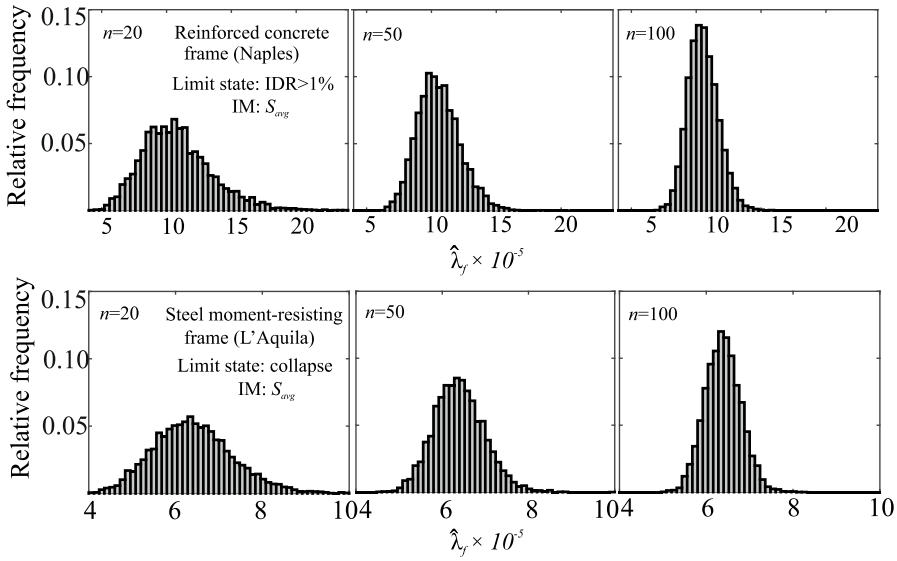

Figure 48. Distributions of the seismic risk estimators $\hat{\lambda}_f$, approximated via Monte Carlo simulation, for record sample sizes $n=\{20,50,100\}$. The top row corresponds to the IDR>1% limit state of the reinforced concrete frame situated at the Naples site and the bottom row to collapse of the steel frame situated at the L'Aquila site. The IM employed in both cases S_{avg}. The ordinate reports relative frequency, i.e., the number of simulated $\hat{\lambda}_f$ point estimates contained in each bin of the histogram divided by the total number of simulations.

On the other hand, the interquantile range $\hat{\lambda}_{f,0.95}-\hat{\lambda}_{f,0.05}$ is plotted in Figure 49, normalized by the point estimate at $n=200$: $\hat{\lambda}_f^{(n=200)}$. This is shown for two cases of collapse annual rate: that of the steel four-story frame, using non-parametric fragility in terms of S_{avg}, and that of the SDOF structure at the Naples site, using non-parametric fragility in terms of $Sa(T_1)$ this time. The underlying implication behind plotting the ratio $\hat{\lambda}_f / \hat{\lambda}_f^{(n=200)}$, is that $\hat{\lambda}_f^{(n=200)}$ should be close to the true rate and thus the interquantile range appears as a percentage of that value. From the figure, it can be observed that normalized $\hat{\lambda}_{f,0.95}-\hat{\lambda}_{f,0.05}$ ranges corresponding to the same value of $CoV_{\hat{\lambda}_f}$ are almost identical between the two cases, even if the latter requires more records to achieve those $CoV_{\hat{\lambda}_f}$ values than the former. Furthermore, it can be seen that the

width of this range shrinks from around 0.70 at $CoV_{\hat{\lambda}_f} = 0.20$, to about 0.33 at $CoV_{\hat{\lambda}_f} = 0.10$. These normalized $\hat{\lambda}_{f,0.95} - \hat{\lambda}_{f,0.05}$ widths suggest that mean relative errors in the environs of 10%, and not larger than 20%, should be regarded as acceptable target levels of accuracy in estimation, as higher $CoV_{\hat{\lambda}_f}$ levels imply that the width of this interquantile range would approach the reference $\hat{\lambda}_f^{(n=200)}$ value in size. In terms of the required number of records, setting $CoV_{tar} = 0.10$ and assuming that, as discussed previously, Δ will be maintained under 1.0 by judicious selection of *IM* to avoid impractical sample sizes, $\mathbb{N}$ would result within a range from forty to one-hundred ground motions, depending on *IM* efficiency with respect to all relevant *EDP*s and site-specific hazard and considering the results of the MDOF frames as representative. In fact, for the simple inelastic SDOF structures this number starts from as low as around twenty ground motions.

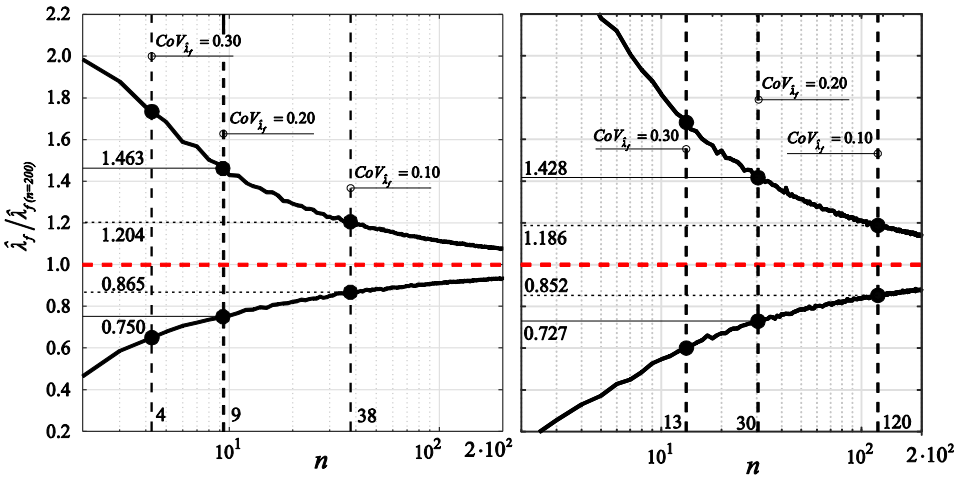

Figure 49. Interquantile range $\hat{\lambda}_{f,0.95} - \hat{\lambda}_{f,0.05}$ as a function of n, normalized by the two-hundred-record point estimate $\hat{\lambda}_f^{(n=200)}$. The $\hat{\lambda}_{f,0.95} - \hat{\lambda}_{f,0.05}$ range was calculated from the Monte Carlo approximations of the distributions of $\hat{\lambda}_f$ for various sample sizes: cases of collapse limit-state for the steel frame (non-parametric fragility in terms of S_{avg}, left panel) and collapse limit-state for the SDOF system located at the Naples site (non-parametric fragility in terms of $Sa(T_1)$, right panel). Record numbers corresponding to $CoV_{\hat{\lambda}_f}$ of 0.10, 0.20 and 0.30 for each case are highlighted by dashed black lines.

4.4. Use of statistics tools when dealing with code-based record selections

4.4.1 Single-stripe analysis and seismic code provisions

Structures are typically designed to enter into the range of inelastic response, during an earthquake that causes a certain shaking intensity to be exceeded. Said design usually entails satisfying specific performance objectives, such as damage reparability or safety of human life. In structural analysis, failure to meet such seismic performance goals is often defined on the basis of exceeding some threshold value of a global measure of inelastic displacement, such as RDR or IDR. As previously mentioned, such response measures are sometimes generically termed *EDP*s and their failure-threshold values can be denoted by edp_f.

In seismic risk assessment, single-stripe dynamic runs of a structure's computer model, aim at estimating the probability of failure at some specific ground motion *IM* level (im), $P\left[EDP > edp_f \,|IM = im\right]$, which can, in turn, involve estimating the conditional mean and variance of the *EDP* at that intensity, $\hat{\mu}_{EDP|IM=im}$ and $\hat{\sigma}^2_{EDP|IM=im}$, where the hat symbols are used to denote both the estimator and the point-estimates of the parameters of an underlying distribution. In fact, point estimates for the two parameters can be respectively obtained from the arithmetic mean, $\overline{x}$, and mean squared error, s^2, of the sample of *EDP* values in the stripe given by Equation (37):

$$\begin{cases} \overline{x} = n^{-1} \cdot \sum_{j=1}^{n} edp_j \\ s^2 = (n-1)^{-1} \cdot \sum_{j=1}^{n} \left(edp_j - \overline{x}\right)^2 \end{cases}, \tag{37}$$

where n is the number of available responses (and records), edp_j, $j = \{1,..,n\}$ are the structural responses given that $IM = im$. In cases where $\hat{\mu}_{EDP|IM=im}$ is estimated as the arithmetic mean of the stripe's sample of *n EDP* responses, as per the equation, the *standard error* (SE) of $\hat{\mu}_{EDP|IM=im}$ can be approximated by $s/\sqrt{n}$ (approximated in the sense that the point estimate of the standard deviation is used in lieu of the true value $\sigma_{EDP|IM=im}$; [75]). This well-known result of statistical inference theory, is often used to highlight the importance of adopting *efficient* intensity measures; i.e., IMs that tend to reduce the

conditional variance $\hat{\sigma}^2_{EDP}$ (henceforth omitting for brevity the condition $IM = im$, which is left implied), and consequently reduce the number of runs/records needed to maintain a desired SE for $\hat{\mu}_{EDP}$, since the required number is proportional to $\hat{\sigma}^2_{EDP}$ (e.g., [2]). The records used are typically scaled to the desired *IM* level and may also be selected on the basis of approximately representing the conditional distribution of spectral ordinates given $IM = im$ (e.g., [53]); in both cases each record is assumed to represent a possible manifestation of future shaking at the site and the corresponding structural response is considered a random sample.

Single-stripe analysis is also used during code-based seismic design, where dynamic analysis is typically only needed for the verification of a single performance objective, which is associated with a specific return period of the seismic actions. Whenever modern seismic codes, such as EC8 and ASCE/SEI 7, allow or require non-linear dynamic analysis to be employed for seismic design in this manner, this usually entails comparing the average of the *EDP* values, which are obtained from a number of non-linear runs that use spectrum-compatible records, with a permissible value that can still be denoted as edp_f, as shown in Figure 50. The evident similarities of this code-mandated procedure with a single-stripe analysis in PBEE context, may lead to the reflex reaction of calculating the sample statistics $\bar{x}$ and s^2 from Equation (37) and of treating $s/\sqrt{n}$ as the SE of some $\hat{\mu}_{EDP}$, with the consequent repercussions on perceived accuracy of the estimate of the mean. However, the question begs to be asked: is the implicit assumption that $\bar{x}$ and s^2 are statistics of a simple random sample of *EDP*s (and therefore point estimates of the mean and variance of an underlying distribution) still valid under the *spectrum compatibility* condition imposed on the records?

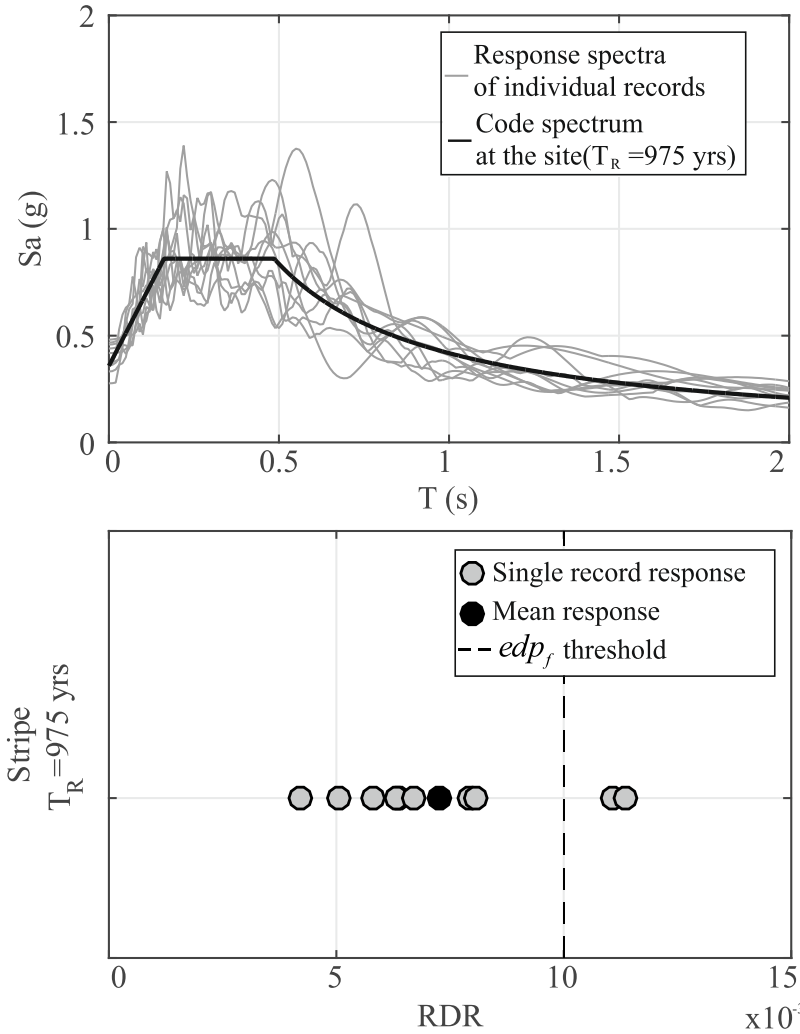

Figure 50. Records selected using the Italian code's EC8-style design spectrum with 5% probability of exceedance in 50 years (i.e., return period of 975 years) and corresponding stripe of structural responses.

At this point, consideration should be given to the issue of spectrum compatibility that standards, such as EC8 or ASCE/SEI 7, require for the record sets. While the codes themselves do not quantify how closely the mean spectrum of the selected records should match the target (bar some lower bound limit imposed on the mean), dedicated practice- and research-oriented software (e.g., [125–128]) tend to operate on a basis of best-fit-possible, employing various optimization algorithms, mainly limited by the size of ground motion database available. It is also noteworthy that the codes do not impose any

quantitative limitation on the variability that single records may exhibit around the target. Regarding the lower bound, EC8 stipulates that the mean spectrum of the selected record set should not undercut the design spectrum by more than ten percent at any period within the range of interest. It also contains a provisional clause that mentions scaling recorded ground motions to the site-specific design peak ground acceleration (*PGA*), but past research advises against this for medium-to-long period structures from as early as [6] and it is not strictly necessary to do so for achieving a good overall match to the target spectrum.

4.4.2 Selection of spectrum-compatible record sets

For the purposes of this study, a ground motion pool of almost three-thousand single-component acceleration records was assembled from within the ESM and NGA-West2 databases. These records came from seventy-eight worldwide shallow crustal events of moment magnitude ranging from 5.4 to 8.0 (seventy-five events from ESM and three from NGA-West2, with no overlap between databases). From within this strong motion dataset, multiple code-spectrum-compatible sets were selected. The target spectrum considered for record selection was the one shown in Figure 50, i.e., the Italian code's EC8-style design elastic spectrum with 5% exceedance probability in 50 years[5] at an Italian site near the town of L'Aquila with soil class B. This spectrum is for all purposes equivalent to an EC8 spectrum.

The goodness-of-fit metric adopted for quantifying the proximity of a single scaled record's spectrum to the target spectrum is denoted as δ_j, and is given by Equation (38):

$$\delta_j = \sqrt{\frac{1}{w} \cdot \sum_{i=1}^{w} \left(\frac{SF_j \cdot Sa_j(T_i) - Sa_{TARGET}(T_i)}{Sa_{TARGET}(T_i)} \right)^2} \quad , \tag{38}$$

where δ_j is the goodness-of-fit of the generic *j*-th record of the set, $Sa_{TARGET}(T_i)$ and $Sa_j(T_i)$ are the spectral acceleration values at period T_i of the target (code) spectrum and of the selected record, respectively, SF_j is the scale factor

[5] Strictly speaking, only the PGA ordinate of the spectrum corresponding to rock site conditions has exactly that probability of exceedance; other spectral ordinates may correspond to slightly different probabilities, since the code spectrum's form is only an approximation of a uniform hazard spectrum.

determined for that record and w is the total number of vibration periods considered. In this study, goodness-of-fit was evaluated at the same periods T_i as those used in [125], while the period interval, in which the spectrum matching conditions ought to be met, was $T \in [0, 2s]$, where it is implied that $Sa(T = 0s)$ denotes the *PGA*. In this light, scaling the records to the target *PGA* becomes moot, since that ordinate is also included in the matching interval.

Matching scaled records to the target spectrum was based on minimizing the sum of individual-to-target distances, according to Equation (39):

$$\begin{aligned} \{Sa_j(T_i), SF_j\} &= \underset{Sa_j(T_i), SF_j}{\arg\min} \left\{ \sum_{j=1}^{n} \sqrt{\frac{1}{w} \cdot \sum_{i=1}^{w} \left(\frac{SF_j \cdot Sa_j(T_i) - Sa_{TARGET}(T_i)}{Sa_{TARGET}(T_i)} \right)^2} \right\} = \\ &= \underset{Sa_j(T_i), SF_j}{\arg\min} \left\{ \sum_{j=1}^{n} \delta_j \right\} \end{aligned} \quad , \quad (39)$$

where $\{Sa_j(T_i), SF_j\}$, $i = \{1, .., w\}$, $j = \{1, .., n\}$ is the set of spectral ordinates and scale factors that together fully define the scaled record set selected. In this approach, the SF to apply to each of the accelerograms in the ground motion pool is part of the optimization process. The numerical problem of minimizing the sum of distances, $\sum_{j=1}^{n} \delta_j$, was solved using the Monte-Carlo-based algorithm proposed in [127] via a suitable modification of the code provided therein. In order to limit potential bias, that could be induced in the estimate of seismic response from scaling the records ([80,129]), a maximum admissible scale factor of ten was imposed.

It clearly emerges from the above that this algorithm tends to search for a fit of the record set to the target, by minimizing the dispersion of the single scaled records around it. On the other hand, an explicit measure of the distance between the mean of the selected records and the target, δ_m, can be provided by Equation (40):

$$\delta_m = \sqrt{\frac{1}{w} \cdot \sum_{i=1}^{w} \left\{ \frac{1/n \cdot \sum_{j=1}^{n} \left[SF_j \cdot Sa_j(T_i) \right] - Sa_{TARGET}(T_i)}{Sa_{TARGET}(T_i)} \right\}^2} \quad . \quad (40)$$

Although the optimization process given by Equation (39) provides a fit between the mean spectrum of the selection and the target only implicitly, since $\sum_{j=1}^{n}\delta_j$ is minimized rather than δ_m, it has the advantage of maintaining dispersion of spectral ordinates within each set as low as possible. As already mentioned, the codes have no explicit requirements for limiting said dispersion, but some authors have advocated keeping it as low as possible [125].

The matching process provided forty-five non-overlapping sets for a series of specific sample sizes $n=\{3,5,7,10,15,17,20\}$. In other words, for every sample size n considered, the records contained in one set are never repeated in any other set of the same size; this was achieved by excluding from the pool the records already belonging to sets constructed during previous selections. The number of forty-five distinct record sets for every n, was an upper limit that was imposed due to database limitations and the need to maintain a minimum goodness-of-fit over all selections, which translates into maintaining the mean squared normalized deviation from the target spectrum, $\delta = n^{-1}\cdot\sum_{j=1}^{n}\delta_j$, below 0.40 in all cases. In Figure 51, δ is plotted for all selected records at $n=\{3,7,20\}$ against order of selection.

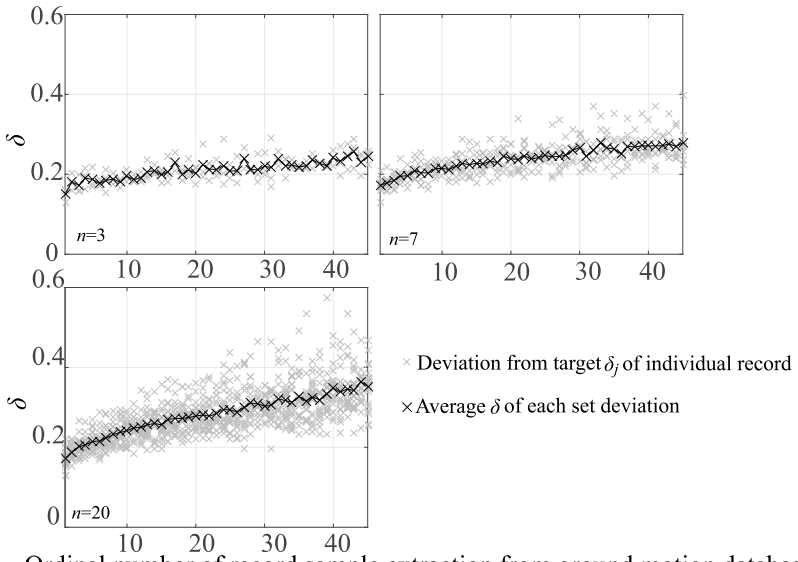

Figure 51. Goodness-of-fit (normalized deviation from target spectrum) for code-compatible record selections against extraction number for sample size of three, seven and twenty.

It is evident that δ tends to increase with each subsequent selection, which is to be expected, as the records that led to the best fit of all previous selections are removed from the database to avoid overlap. The fact that this trend is not strictly monotonic is due to the Monte-Carlo basis of the optimization algorithm used to implement Equation (39). In Figure 52, the target spectrum is shown, along with record sets consisting of three, seven and twenty ground motions, all coming from the multiple extractions described above. For sample sizes of three and seven, the selected sets exhibiting the lowest squared normalized deviation from the target δ, and those exhibiting the best fit to them mean, i.e., lowest δ_m, are shown for comparison.

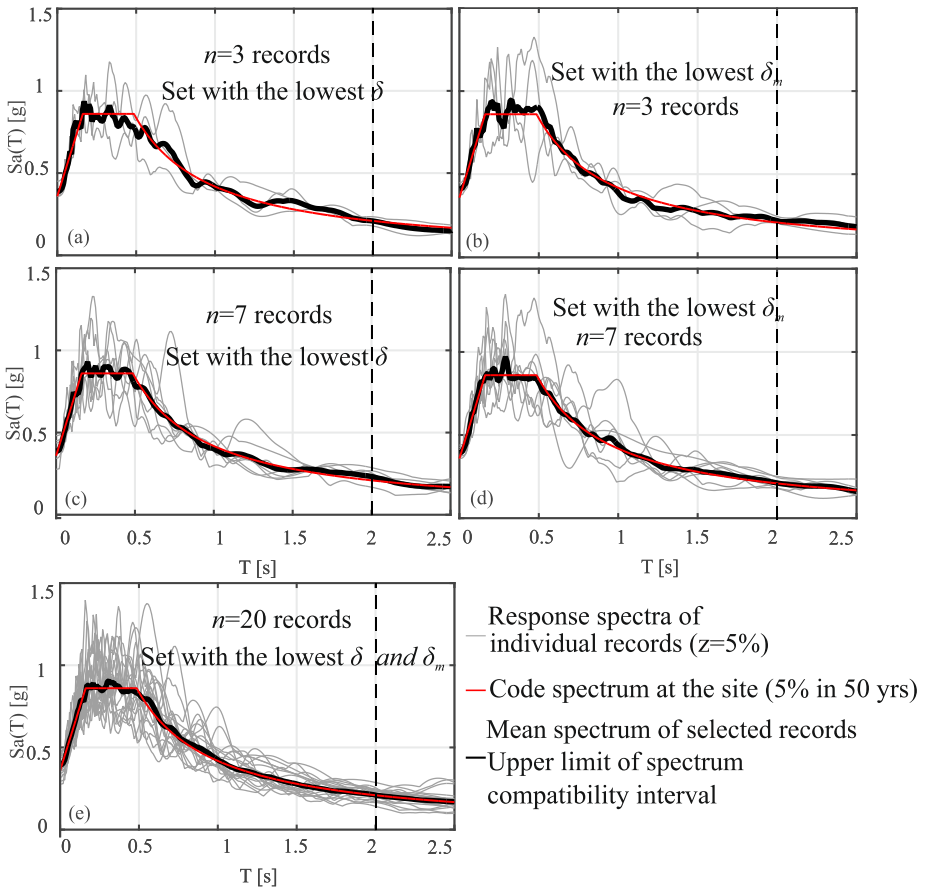

Figure 52. Spectrum-compatible ground motion suites composed of three records (a-b), seven records (c-d) and twenty records (e).

From Figure 51 it can be seen that the intra-set variability of spectral shape generally tends to diminish for smaller sample sizes. It can also be observed from the same figure, that δ tends to increase going to the right (for subsequent record selections), which is an effect of database depletion and explains why the selections were limited to forty-five sets, maintaining $\delta < 0.40$. On the other hand, Figure 52 attests to the fact that minimizing the distance of individual records from the target achieves a good fit of their mean as well, since there is hardly any discernible difference in the goodness-of-fit between panels a and b, which show the best individual record and best mean fit, respectively, for $n = 3$ and likewise between c and d for $n = 7$ (for twenty records δ and δ_m are minimized for the same selection). Furthermore, this figure also confirms the previous observation, that the intra-set variability of spectral ordinates tends to decrease when less records are used to achieve the same goodness-of-fit between their mean and the target spectrum.

4.4.3 Impact of the records' set size on the response statistics

The three-hundred and fifteen record suites assembled according to the procedure described in the previous section (seven set sizes times forty-five sets) were used to run response-history analysis of a non-linear numerical model of a four-storey plane, code-conforming reinforced concrete frame with first mode period $T_1 = 0.53s$ (see Figure 53 and [78] for more information on the structure and detailing). The sample intra-set means of the IDR and RDR responses that were obtained for each record set, denoted respectively as μ_{IDR}^{intra}, μ_{RDR}^{intra}, are shown in Figure 54. These were calculated as the arithmetic means $\bar{x}$, of the corresponding *EDP*, via Equation (37).

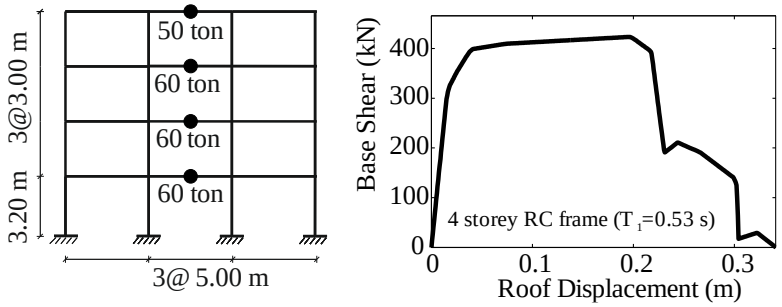

Figure 53. Basic dimensions and static pushover curve for the code-conforming, four-story, inelastic MDOF reinforced concrete moment-resisting frame structure used in the example.

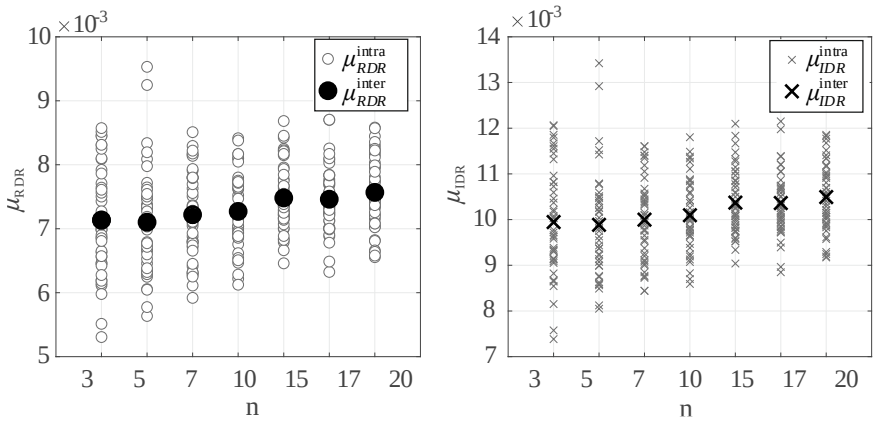

Figure 54. Intra- and inter-set response means (left panel RDR, right panel IDR), for the code-conforming reinforced concrete frame, plotted against sample size.

Also shown in the figure are the inter-set means, μ_{IDR}^{inter} and μ_{RDR}^{inter}, calculated as the average of the intra-set means, according to Equation (41):

$$\mu_{EDP}^{\text{inter}} = m^{-1} \cdot \sum_{k=1}^{m} \mu_{EDP,k}^{\text{intra}} , \tag{41}$$

where m is the total number of record sets available ($m = 45$ in this case) and $\mu_{EDP,k}^{\text{intra}}$ is the arithmetic mean of IDR or RDR responses of the *k*-th record set, $k = \{1,..,m\}$. The relatively low average drift values can be attributed to overstrength and capacity design, which lead to moderate plastic rotations exclusively at the beam ends for this return period of seismic actions.

It can be noted that previous studies report that code (i.e., uniform hazard) spectrum-matched record sets tend to overestimate the central tendency of inelastic response, also when the records are scaled to a common $Sa(T)$ ordinate ([115,130,131]). Be that as it may, it can be observed from the figure that, despite some small fluctuations, the inter-set averages μ_{IDR}^{inter} and μ_{RDR}^{inter} do not appear to vary much with sample size up to $n = 10$, but do exhibit a small increase for larger sample sizes. In fact, Figure 55 indicates that, for record sample sizes $n = \{3,7\}$, where the sets are expected to share a significant amount of records between the two size groups, the intra-set average IDR responses, μ_{IDR}^{intra}, obtained from progressively selecting new sets of increasing δ, fall around the inter-set average without exhibiting any evident strong trends

with the selection order. On the other hand, for $n = 20$, there appears to be some increasing trend of μ_{IDR}^{intra} with the selection order of the corresponding record set. In fact, μ_{IDR}^{inter} for the twenty-record sets is larger than that of the lower sample sizes of thee and seven; this is a consequence of the increasing variance of spectral ordinates around the target for $n = 20$ which also affects the mean, due to the non-linear relationship between the spectra and the inelastic response (this can also be appreciated by looking at the first couple of selections at $n = 20$, whose spectra are expected to be as close to the target as are their $n = 3$ counterparts, and whose mean is also similar). From this observation it follows that if the goal of the analysis is to evaluate the average response conditional to the code design spectrum, there may be a bias-inducing effect of the record set size.

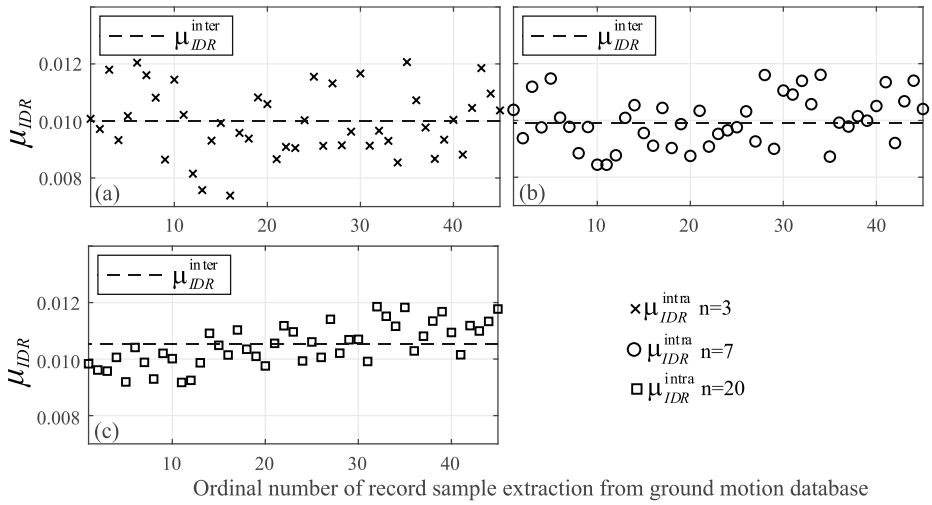

Figure 55. Variation of intra-set mean IDR response with selection order of the corresponding record set, for set size of three, seven and twenty records.

At first glance, this relatively stable behavior, at least the one exhibited by the smaller sample sizes, can tempt the observer to mistake the inter-set average μ_{IDR}^{inter} for an estimator of the mean of an underlying distribution. But if this were the case, one would also expect the sample standard deviations of the IDR responses from Equation (37), s_{IDR}, to also vary randomly around some central value. However, the fact of the matter is that is not the case at all, as shown in Figure 56. In this figure, the calculated s_{IDR} values for each set were plotted against the record selection order, as was previously done for the goodness-of-

fit measure (Figure 51) and for the means (Figure 54). This plot is repeated for the coefficient of variation, $CoV_{IDR} = s_{IDR} / \mu_{IDR}^{\text{intra}}$. On both of these graphs, the least-square regression lines of s_{IDR} and CoV_{IDR} against selection order $m = \{1, 2, .., 45\}$ are displayed, with separate regressions performed for each record set size of $n = \{3, 7, 20\}$. Instead of a random variation around some central value, an increasing average trend with selection order is observed, where selection order is a proxy for decreasing goodness-of-fit, as shown in Figure 51. Not only that, but the dispersion of structural response, expressed by either s_{IDR} or the normalized value CoV_{IDR} , also appears to increase, on average, with sample size; this is clearly indicated by the fact that the regression lines are arranged one underneath the other, with $n = 20$ leading with the larger average dispersions and the other two following in decreasing order with sample size.

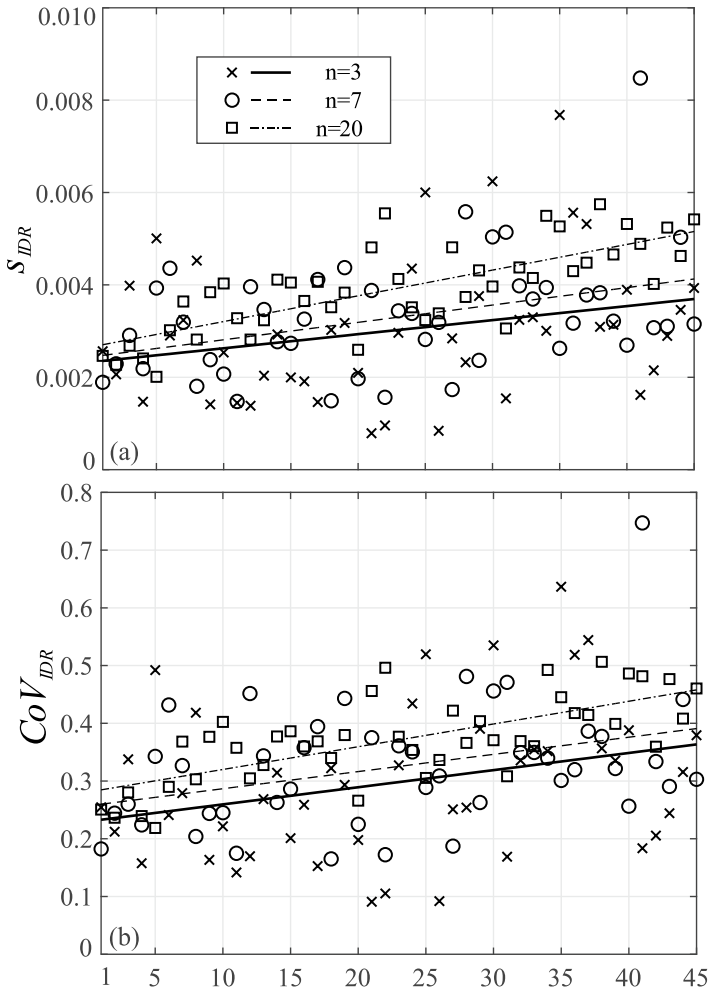

Figure 56. Standard deviation (left) and coefficient of variation of IDR (right) for each set of three, seven and twenty records, plotted against selection order and with a regression line displayed.

This behaviour implies a dependence of the dispersion of IDR from sample size, which means that it is not possible to predict the standard error of the average response of a larger set by using the mean squared error calculated from a smaller set via Equation (37). An explanation for this, is that the structural responses from records selected according to the matching criteria in Equation (39), do not represent a simple random sample of any distribution. In other words, the responses obtained from a record set of a certain size, are not independent realizations of a random variable. This is because matching the

same spectrum induces a dependence between responses, due to the increased intra-set spectral similitude observed in Figure 51 at smaller set sizes; given the important role of spectral shape in determining the distribution of inelastic-displacement-related *EDP*s (e.g., [122,132]) this lower dispersion in inter-set spectral shape can carry over to the responses. This correlation of spectral shape and inelastic response can also partly explain the increasing trend of s_{IDR} observed with respect to the selection order: since subsequent selections excluded all previously extracted records to avoid overlapping (i.e., avoid the presence of the same record in more than one set of the same size), the best-fit candidates are gradually removed from the selection pool. Consequently, the dispersion of the records' spectral ordinates from the target increases in subsequent selections and the dispersion of inelastic response also reflects that increase.

However, the issue remains that the simple random sample assumption is a *sine qua non* condition, both for using sample statistics, such as those of Equation (37), as estimators of the parameters of some underlying distribution, as well as for calculating the corresponding SE. Thus, one logical conclusion that can be drawn from what evidence was drawn from this example, is that the use of statistical inference tools, only suitable in the case of simple random sampling, to determine ground motion sample size in the context of code-mandated spectrum-compatibility may be an ill-posed problem, because the underlying assumption of the corresponding structural responses being independent and identically distributed does not appear to hold.

4.5. Conclusions

The complexity of numerical models that simulate the seismic response of structures in the non-linear range grows at a pace that rivals advances in computing power. This leads to computational costs for analytical seismic risk assessments that remain at constantly high levels, rendering the issue of the appropriate number of response-history analyses to run, ever topical. Sections 4.2 and 4.3 advocate the use of quantitative criteria to determine the sample size of ground motion records, based on the statistical inference concept of estimation uncertainty. This offers earthquake engineers a means of making an informed decision, by weighing computation costs against precision of the risk estimates. The study focused exclusively on the use of naturally-recorded acceleration time-histories (possibly modified by scaling-in-amplitude only),

which is becoming the norm, in part thanks to the widespread recent availability of online strong motion repositories. In order to quantify estimation uncertainty, the coefficient of variation of the estimator of annual failure rate, $CoV_{\hat{\lambda}_f}$, was chosen. The main conclusions to be drawn from this study are listed here.

- A closer look at Cornell's simplified, analytical seismic reliability formulation, showed that the record-to-record dispersion of structural responses is only part of the story, with $CoV_{\hat{\lambda}_f}$ also depending on the shape of the site-specific hazard curve. The implication of this finding, is that for structures located at sites characterized by different seismicity levels, different numbers of runs may be required to reach the same level of confidence in the risk estimate between sites, even for the case of similar structures expected to exhibit the same failure rate. The effect of hazard on $CoV_{\hat{\lambda}_f}$ can be summarized by the slope of the curve near intensity levels that are most relevant for causing failure: the steeper the local drop-off of the curve the greater the estimation uncertainty behind $\hat{\lambda}_f$. These observations were generally corroborated by numerical simulations, based on incremental dynamic analysis of simple inelastic systems and two code-conforming frames.
- Both analytical and numerical investigations showed that the mean relative error of the failure rate follows a relation of the type $CoV_{\hat{\lambda}_f} = \Delta/\sqrt{n}$ and suggest that the parameter Δ, as a rule of thumb (based on the applications developed in this study), varies between around 0.45 and 1.9 for various limit-states that can be defined in terms of maximum drift thresholds, ranging from moderate inelasticity to side-sway collapse. The lower value corresponds to cases where advanced, efficient scalar seismic intensity measures are employed combined with a mild-sloping hazard curve with slope $k \approx 2$ around median structural capacity, and the higher one to the use of traditional intensity measures, such as first-mode spectral acceleration, coupled with locally steeper hazard curves, e.g., with slope $k \approx 3.5$.
- It was observed that, for nominally equivalent structures, variations in the choice of intensity measure and/or site-specific hazard can cause the number of records required to achieve a level of $CoV_{\hat{\lambda}_f}$ around 0.10

to vary from the low tens to a couple of hundred. This, once again, highlights the importance of selecting efficient intensity measures in performance-based earthquake engineering, which becomes an almost-necessity in the case of collapse failure estimation at low-seismicity areas, keeping the number of ground motions needed to achieve a 10% coefficient of variation for the failure rate estimate within the range of forty to one-hundred.

- Finally, it was observed that the reduction in the dispersion of structural response via efficient intensity measures, despite its importance, does not tell the whole tale with regard to the corresponding reduction in computational costs, which can also be site-dependent.
- On a concluding note, in the applications presented herein, the general trend was that less records are needed to reach the same level of mean relative error in the risk estimates for sites exposed to higher seismic hazard, than for sites exposed to lower hazard levels; however, this result may be a rule-of-thumb that is not necessarily generalizable independently of the shape of particular site-specific hazard curves. Generally speaking, it was shown that the results and observations presented can be useful in practical applications of seismic risk assessment, by providing a quantitative basis for determining the required number of records for risk-targeted dynamic analysis. This number can be defined by setting a target of desired precision for the risk estimate in terms of the mean relative error, $CoV_{\hat{\lambda}_f}$.

Differently, Section 4.4 investigates the issue of the number of code-spectrum-compatible records used for dynamic analysis, when the objective is estimating mean inelastic structural response. Spectrum-compatibility was defined as the property of a set of scaled acceleration records, whose mean spectrum is as good a match to the target code spectrum as possible. The premise that motivated this investigation, was that the use of well-known concepts from inference theory, such as estimation uncertainty, while suitable for determining the appropriate sample size of input ground motions in other apparently similar earthquake-engineering applications, may not be applicable in this case. In the context of this investigation, a Eurocode-8 type design spectrum for an Italian site was used as reference and numerous spectrum-compatible sets, without overlap of records between them, were selected from a large pool of three thousand acceleration waveforms. This selection was

repeated for various sizes of the record set, between three and twenty. It was observed that record selection based on goodness-of-fit of the mean to the target, led to less inter-set variability of the spectral ordinates for the smaller sample sizes. Non-linear dynamic analysis was performed for the numerical model of a plane four-storey inelastic frame for all base-acceleration inputs selected. Examination of the obtained structural responses revealed that response statistics as a function of sample size did not behave as expected for random samples, i.e., the responses did not appear to be independent and identically distributed. This implies that determining the number of spectrum-compatible records to use in this context via statistical tools, such as the standard error of the mean, suitable in the case of simple random sampling, is an ill-posed problem. In other words, it may be conceptually inappropriate to invoke considerations of estimation uncertainty, when dealing with code-based record selection.

Chapter 5 –SEISMIC FRAGILITY OF ITALIAN CODE-CONFORMING BUILDINGS BY MULTI-STRIPE DYNAMIC ANALYSIS OF THREE-DIMENSIONAL STRUCTURAL MODELS

The following paper has been derived from this Chapter :

- *I. Iervolino, R. Baraschino, A. Belleri, D. Cardone, G. Della Corte, P. Franchin, S. Lagomarsino, G. Magliulo, A. Marchi, A. Penna, L. R.S. Viggiani and A. Zona (2021). Seismic fragility of Italian code-conforming buildings by multi-stripe dynamic analysis of three-dimensional structural models. Journal of Earthquake Engineering (submitted)*

5.1. Introduction

In the current Italian building code (NTC hereafter; [133,134]), somewhat similar to Eurocode 8 or EC8 [135], structural performance has to be verified with respect to seismic actions (i.e., ground motion intensity) with specific return periods (T_R) of exceedance at the site of interest, which depends on the limit-state(s) considered for design. In case of ordinary (e.g., office or residential) structures, for example, safety verifications for damage limitation and life safety limit states are required against ground motion intensity measure (*IM*) levels corresponding to T_R of 50 and 475 years, respectively. However, seismic structural reliability resulting by design, that is the annual frequency of earthquakes lading to structural failure, is not explicitly controlled although design seismic actions have a probabilistic determination.

To quantitatively address the seismic risk that the code-conforming design exposes structures to, a large research project was carried out in Italy between 2015 and 2017. In the project, named *Rischio Implicito – Norme Tecniche per le Costruzioni* [107], structures belonging to a variety of structural types; i.e., un-reinforced masonry (URM); reinforced-concrete (RC); precast reinforced concrete (PRC); steel (S) and base isolated reinforced-concrete buildings (BI) were designed according to NTC for a number of sites featuring different hazard levels (Milan, Naples, and L'Aquila) and local site conditions (A and C according to EC8 classification). The buildings are for residential and industrial occupancy and, for each typology, various architectural/structural configurations were considered [105].

The seismic structural reliability of the designed structures was assessed in terms of mean annual failure rate of global collapse and usability-preventing damage. The rates were computed within the PBEE framework, that is integrating the seismic structural fragility and the hazard curve for the design site. The fragility was computed for some *IM* levels via non-linear dynamic analysis using three-dimensional (3D) structural numerical models.

In fact, in the RINTC project structural fragility was only obtained as lumped probabilities at ten *IM* levels, and fragility curves were not fitted, as they are not strictly needed to compute the failure rates [11]. On the other hand, parametric fragility curves of the several buildings designed, modelled, and analyzed in the RINTC project can be useful for a critical discussion of the vulnerability of code-conforming structures and for further risk assessment studies. This motivated the study presented herein, where the hazard-consistent seismic fragility curves are provided for the models belonging to the five structural typologies and both failure criteria investigated in the project.

Among the variety of approaches to derive a fragility function, the study herein presented focuses on so-called analytical fragility functions developed via non-linear dynamic analysis of 3D models. In particular, the results of the MSA (e.g., [18]), using hazard-consistent ground motion record sets, are considered to fit lognormal fragility curves for the RINTC structures at all the sites design refers to. The curves are obtained considering a variety of procedures able to manage the numerical instabilities arising from non-linear dynamic analysis and/or the cases of low-hazard sites, where failures are rarely observed. Moreover, the uncertainty in estimation (i.e., [8]) of the fragility parameters, arising from the record-to-record variability of structural response [6], is also addressed.

The remainder of the Chapter is structured such that the structure and results of the RINTC project are briefly recalled first. Then the three methods for lognormal fragility fitting are discussed, along with the resampling procedures to account for uncertainty in the parameters' estimation. Subsequently the fragility curves are presented and discussed with respect to the issues arising in deriving them and mostly depending on sites' hazard. As a validation of the fragilities, the failure rates computed via the fitted curves are compared to the results of those originally the rate of earthquakes causing failure of the structure and differences quantitatively explained. Some final remarks close the Chapter.

5.2. The RINTC framework

In this section the RINTC context is given. In particular, the design, modeling, and analysis of the buildings is briefly recapped for readability, although for typology-specific details the reader is referred to the cited specific references.

5.2.1 Life safety and damage limitation design

According to the NTC, seismic design actions derive from probabilistic seismic hazard analysis or PSHA [136]. Structural systems must withstand the design seismic action with the return period of exceedance depending on *the limit state* of interest at the construction site. For ordinary residential and industrial structures, that is, those examined in the RINTC project, mandatory design limit states are *damage limitation* (SLD) and *life safety* (SLV). Their corresponding design actions on rock site conditions are derived from the 5% damped spectral pseudo-accelerations, $Sa_{SLD}(T)$ and $Sa_{SLV}(T)$, obtained from site-specific elastic design spectra that are close approximations of the 50- and 475-year return period uniform hazard spectra (UHS) at the site. Elastic design spectra for soil site conditions different from rock are obtained by conventional modification via soil-class-specific adjustments.

Figure 57 (left) shows the official (current) Italian seismic hazard map in terms of peak ground acceleration (*PGA*) with 475-year return period of exceedance on rock and the code-prescribed horizontal elastic response spectra for the three considered design sites, representative of low-, mid- and high-hazard in the country, indicated as MI, NA and AQ, respectively

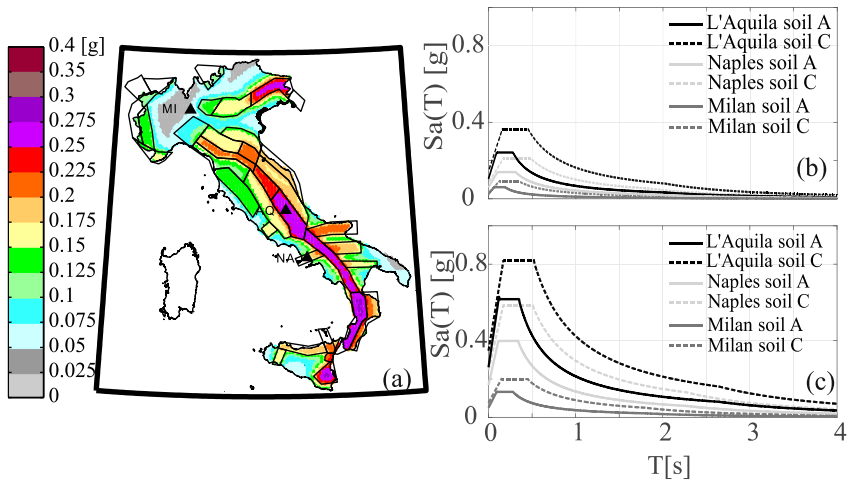

Figure 57. (a) Italian seismic source zones and official hazard map in terms of PGA with 475-year return period of exceedance on rock; for the considered

sites design elastic spectra corresponding to 50-year return period (b) and 475-year return period (c) (in the spectra, T is the natural vibration period).

Figure 57 (right) shows the design spectra at the sites for the two soil site conditions (A and C according to EC8 classification) for the two design limit states. In case that linear analysis is employed, the code allows to introduce a behavior factor, *q*, to obtain inelastic design spectra. Those assumed in the project are recalled in the next section for each typology.

5.2.2 Residential URM buildings

URM buildings considered in this work are two- or three- story buildings made of perforated clay units with mortar joints designed for the three sites on both the soil conditions (A and C). Different (in plan) architectural configurations, either regular or irregular according to the definition provided by NTC, were considered as to represent typical Italian residential buildings: regular configurations are indicated as C (C1-C7), E2, E8, E9, while those irregular as I, E5 (see [110,137] for details). As an example, Figure 58a shows the plan of a C-type configuration building, which is regular in both plan and elevation; Figure 58b,d,e show the plan of the E2, E8 and E9 building, regular in both plan and elevation; Figure 58f shows the plan of the E5 and I configurations.

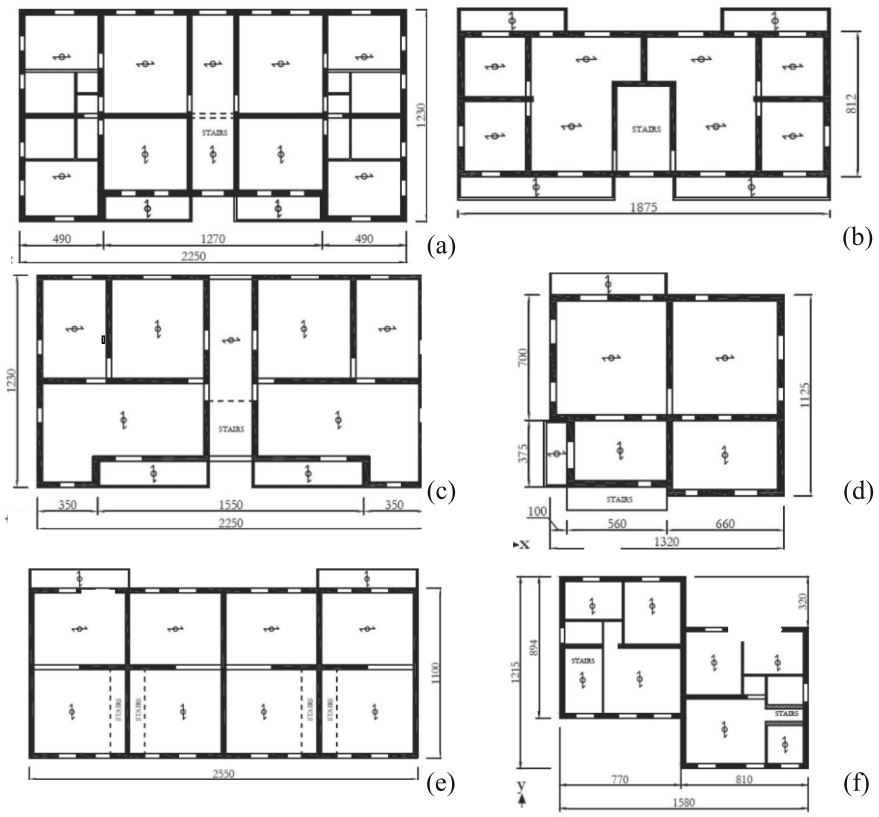

Figure 58. Architectural plan configurations: C (a), E2 (b), E8 (c), E5 (d), E9 (e), I (f).

The applied design methods are: simple building (SB) rules, linear static analysis (with equivalent frame, LSA-F, or with cantilever modelling, LSA-C), and non-linear static analysis (NLSA). In case of LSA, design seismic action was determined by the elastic response spectra divided by a behavior factor q equal to 3.6. The adoption of different design methods allowed designing the same structural configurations in sites with different seismicity with little margin of verification. In fact, linear analysis methods, much more conservative than non-linear static analysis and the rules for the implicit design of simple buildings, are applicable only in sites with lower seismicity. Table 8 shows the forty-five building-site combinations examined in this study.

Table 8. ID of the URM structures under investigation. Building ID is organized as typology-configuration – number of floors – site – soil condition. The

asterisk indicates that structure has been designed according to the recent update Italian building code provisions [134].

Site	**Soil condition**	
	A	C
L'Aquila (AQ)	URM-C1-2-AQ-A URM-C1-3-AQ-A URM-C3-2-AQ-A* URM-I1-2-AQ-A* URM-E2-2-AQ-A URM-E2-3-AQ-A URM-E8-3-AQ-A	URM-C3-2-AQ-C URM-I1-2-AQ-C URM-E2-2-AQ-C URM-E5-2-AQ-C URM-E8-2-AQ-C URM-E9-2-AQ-C
Naples (NA)	URM-C1-2-NA-A* URM-C1-3-NA-A* URM-C3-2-NA-A URM-C4-3-NA-A URM-I2-3-NA-A* URM-E5-3-NA-A URM-E8-2-NA-A	URM-C1-2-NA-C URM-C2-2-NA-C* URM-C3-3-NA-C URM-C4-2-NA-C URM-C5-3-NA-C URM-C5-3-NA-C* URM-I1-2-NA-C* URM-I2-3-NA-C URM-E2-3-NA-C URM-E8-3-NA-C
Milan (MI)	URM-C1-2-MI-A URM-C2-3-MI-A URM-C4-2-MI-A URM-C6-3-MI-A URM-E2-2-MI-A URM-E2-3-MI-A URM-E5-2-MI-A URM-E5-3-MI-A	URM-C1-2-MI-C URM-C2-3-MI-C URM-C7-2-MI-C URM-E2-2-MI-C URM-E2-3-MI-C URM-E8-3-MI-C URM-E9-3-MI-C

5.2.3 Residential RC buildings

Three-, six-, and nine-story RC moment-resisting frame (MRF) buildings and nine-story RC shear walls (SW) buildings were designed for each of the three sites with different levels of seismicity (soil C for all sites and soil A only for AQ), including considerations on soil-structure interaction and modelling uncertainty for some selected cases [107,138].

The buildings were intended for residential use and are all 5×3 bays characterized by regularity in plan (Figure 59d) and elevation. The floor area of the buildings is approximately $21.4\times11.7\text{m}^2$, which is common for all cases. The ground floor height and all other story heights are $3.4m$ and $3.05m$, respectively. The RC frames include knee-joint beams designed to bear the staircases.

Three different structural configurations (i.e., bare-, infilled-, and pilotis-frames, hereafter denoted as BF, IF, and PF, respectively; Figure 59a,b,c) were considered. From a design point of view, the structural members of BF and IF are identical in dimensions and reinforcement detailing (i.e., current practice is to consider infills in design only as a gravity load and associated mass, so BF and IF only differ in terms of assessment models), while the vertical structural members at the ground floor of PF were strengthened to account for the infill reduction, as per code requirements. SW buildings are symmetrically arranged along the perimeter, are $35cm$ thick with height varying with site and floor (plan in Figure 59e).

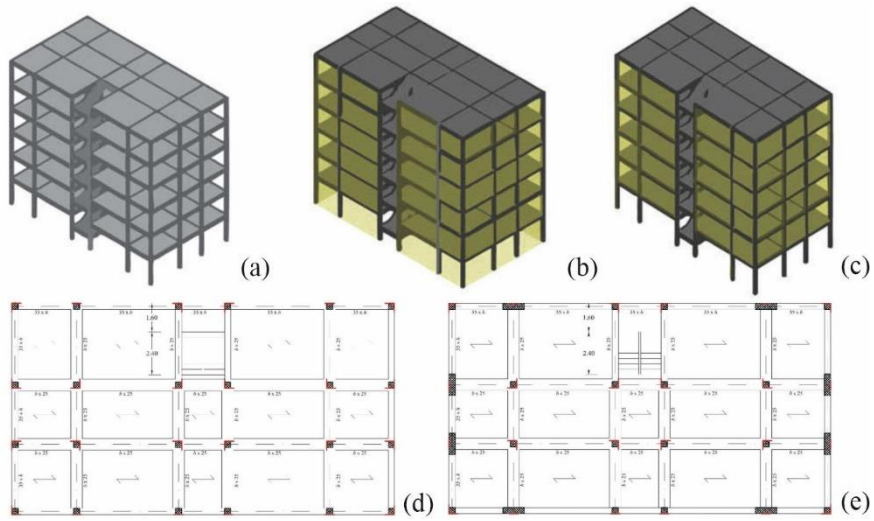

Figure 59. (a) six story bare frame (BF); (b) six story infilled frame (IF); (c) six story pilotis frame (PF); (d) MRF building floor plan; (e) SW building floor plan.

For each site, seismic design was performed by means of modal response spectrum (MRS) analysis. The reference design strength was assigned by the design response spectrum obtained from the horizontal elastic response

spectrum for soil C (Figure 57b) divided by a behavior factor $q = 3.9$ (for multi-story RC frames in low ductility class; note that masonry infills are not explicitly accounted for in the NTC code-conforming design, hence the reference to BF alone covering all frames). For more details on the structural design and subsequent numerical modelling, see [109]. Note also that, for some RC structures soil-structure-interaction (SSI) and model uncertainty (MU) was also considered in modelling [138], even if these are not considered in the fragility derivation herein.

Table 9. ID of the RC structures under investigation. Building ID is organized as typology – configuration – number of floors – site – soil condition.

Site	**Soil condition**	
	A	C
L'Aquila (AQ)	RC-BF-9-AQ-A RC-IF-9-AQ-A RC-PF-9-AQ-A	RC-BF-3-AQ-C RC-IF-3-AQ-C RC-PF-3-AQ-C RC-BF-6-AQ-C RC-IF-6-AQ-C RC-PF-6-AQ-C RC-SW-BF-9-AQ-C RC-SW-IF-9-AQ-C RC-SW-PF-9-AQ-C
Naples (NA)	-	RC-BF-3-NA-C RC-IF-3-NA-C RC-PF-3-NA-C RC-BF-6-NA-C RC-IF-6-NA-C RC-PF-6-NA-C RC-BF-9-NA-C RC-IF-9-NA-C RC-PF-9-NA-C RC-SW-BF-9-NA-C RC-SW-IF-9-NA-C RC-SW-PF-9-NA-C RC-MU-BF-6-NA-C RC-MU-IF-6-NA-C

		RC-MU-PF-6-NA-C RC-SSI-SW-BF-9-NA-C RC-SSI-SW-IF-9-NA-C RC-SSI-SW-PF-9-NA-C
Milan (MI)	-	RC-BF-3-MI-C RC-IF-3-MI-C RC-PF-3-MI-C RC-BF-6-MI-C RC-IF-6-MI-C RC-PF-6-MI-C RC-BF-9-MI-C RC-IF-9-MI-C RC-PF-9-MI-C RC-SW-BF-9-MI-C RC-SW-IF-9-MI-C RC-SW-PF-9-MI-C

5.2.4 BI reinforced-concrete buildings

A series of six-story infilled RC moment resisting frame isolated buildings was designed. Three different isolation systems have been considered: double-curvature friction pendulums (FPS), high-damping rubber bearings (HDRB), and a hybrid system made of HDRB's and sliders (SLDR). Buildings were designed only for mid- and high- hazard sites (Naples and L'Aquila), on soil C (see Table 10 for buildings ID), considering not rational to design of isolation systems for structures located in low-hazard sites. The seismic response of isolated buildings has been evaluated by accounting for the non-linear behavior of both the isolation system and the superstructure. For more details on the structural design and subsequent numerical modelling; see [139] updated and revised as in [140] and [141].

Table 10. ID of the BI structures under investigation. Building ID is organized as typology– configuration–site–soil condition.

Site	**Soil condition**	
	A	C

L'Aquila (AQ)	-	BI-FPS-AQ-C BI-HDRB+SLDR-AQ-C BI-HDRB-AQ-C
Naples (NA)	-	BI-FPS- NA-C BI-HDRB+SLDR-NA-C BI-HDRB-NA-C

5.2.5 Industrial PRC buildings

Single-story industrial PRC buildings were designed at the three sites with different hazard levels (on soil A and C). Each building features 4×1 bays, with columns and prestressed principal beams, longitudinal gutter beams, prestressed roof elements, and vertical/horizontal cladding Figure 60a,b shows the plan and elevation views of the prototype buildings, respectively. The columns were assumed to be fixed at the base (pocket foundations) and to be connected at the top to both the transverse and longitudinal beams through dowel connections. The roof system consists of precast double-tee elements, which are pinned to the beams by means of dowel connections and connected to each other by steel elements in conjunction with a cast-in-situ concrete slab (slab thickness of $50mm$) ensuring a roof rigid diaphragm behavior. The vertical cladding panels are connected to the beams and columns by means of mechanical connections made of steel elements.

Each building, typically intended for industrial use, has an overhead travelling crane (not modelled, but accounted for in the design), thus there are corbels in the precast columns supporting steel runway beams. The beams have variable cross-sections varying width and height along the longitudinal and transversal directions, respectively, while columns have rectangle cross-sections.

For each site, four different configurations were considered to represent the typical industrial constructions in Europe, varying four geometry parameters of the frames. Those parameters are summarized Table 11 where transverse and longitudinal bay widths and story- and crane-bracket heights are indicated as L_X , L_Y , H , and H_c . The considered buildings are listed in Table 12.

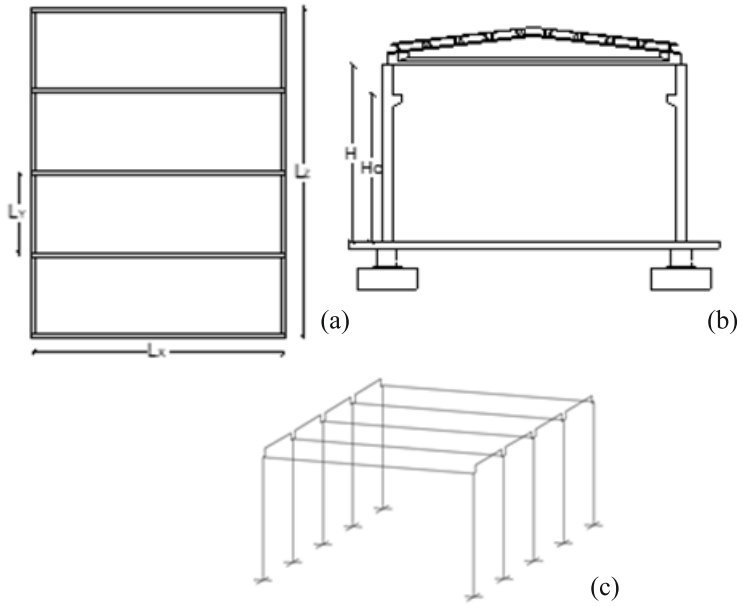

Figure 60. Prototype PRC buildings in plan view (a), transversal frame (b) and numerical model (c).

The seismic design of the buildings was performed by means of MRS analysis for two horizontal and vertical directions at each site. The design response spectrum was obtained from the horizontal elastic response spectra (Figure 57b) divided by a behavior factor $q = 2.5$, which was prescribed by NTC for low ductility class precast buildings with isostatic (see [142–144]).

Table 11. Geometry parameters for the prototype PRC buildings.

Geometry	L_X **[m]**	L_Y **[m]**	H **[m]**	H_c **[m]**
Geom1	15	6	6	4.5
Geom2	20	8	6	4.5
Geom3	15	6	9	7.5
Geom4	20	8	9	7.5

Table 12. ID of the PRC structures under investigation. Building ID is organized as typology-configuration – site – soil condition.

Site	**Soil condition**	
	A	C
L'Aquila (AQ)	PRC-Geom1-AQ-A	PRC-Geom1-AQ-C

	PRC-Geom2-AQ-A PRC-Geom3-AQ-A PRC-Geom4-AQ-A	PRC-Geom2-AQ-C PRC-Geom3-AQ-C PRC-Geom4-AQ-C
Naples (NA)	PRC-Geom1-NA-A PRC-Geom2-NA-A PRC-Geom3-NA-A PRC-Geom4-NA-A	PRC-Geom1-NA-C PRC-Geom2-NA-C PRC-Geom3-NA-C PRC-Geom4-NA-C
Milan (MI)	PRC-Geom1-MI-A PRC-Geom2-MI-A PRC-Geom3-MI-A PRC-Geom4-MI-A	PRC-Geom1-MI-C PRC-Geom2-MI-C PRC-Geom3-MI-C PRC-Geom4-MI-C

5.2.6 Industrial steel buildings

Twenty-four single-story industrial steel buildings equipped with an overhead travelling crane were designed as case studies i.e., four geometries in the three considered sites (L'Aquila, Naples, and Milan) each allowing two options for soil conditions (A and C). As shown in Figure 61, the prototype buildings are made of five equally-spaced transverse single-span duo-pitch portal frames connected through longitudinal beams at the apex, eaves, and crane-supporting bracket levels. Lateral loads are sustained by the MRF system in the transverse direction while the resistance in the longitudinal direction is assigned to diagonal concentric braces symmetrically placed in the outer spans of the frame, i.e., concentrically braced frames (CBFs) with cross-cut braces at the ground level and single braces at the crane-bracket level, respectively. Purlins, supporting the roof cladding and transferring loads from the roof cladding to the rafters, were placed on the rafters with a constant interval. Roof cross braces were arranged in the outer bays to transfer lateral loads to the vertical braces. Full-strength bolted end-plate connections were designed between the apex and eaves, including haunches to improve the structural performance as well as to facilitate the construction; the base connections of the columns and the purlin-rafter connections were designed as pinned; full-strength gusset plate connections were designed to connect the braces.

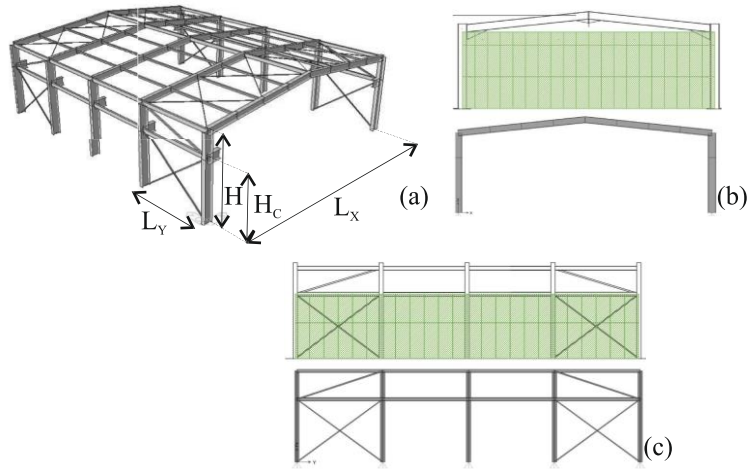

Figure 61. (a) prototype steel frame building; (b) cladding panels distribution in the longitudinal direction; (c) cladding panels distribution in the transverse direction.

As for PRC buildings, for each site, four different configurations were considered varying transverse and longitudinal bay widths and story- and crane-bracket heights; denoted as L_X, L_Y, H, and H_c, as provided in Table 13 and shown in Figure 61a.

Table 13. Geometry parameters for the prototype S buildings.

Geometry	L_X **[m]**	L_Y **[m]**	H **[m]**	Hc **[m]**
1	20	6	6	4.5
2	20	8	6	4.5
3	30	6	9	7.5
4	30	8	9	7.5

The seismic design of the case studies was made in *low ductility class*; seismic actions in horizontal and vertical directions were obtained through MRS analysis from the elastic spectra applying a *q* factor equal to 4.0). The cross-section designs of structural members for the twenty-four combinations of the considered four geometry types, three sites, and two soil conditions, resulted in nine different design solutions, as detailed in [108].

The three-dimensional models adopted for the MSA of the designed case studies include geometric and material non-linearities. Geometric non-linearities were considered through the large displacements and small strains approach, exploiting the corotational coordinate transformation, allowing for

the description of the non-linear geometric effects due to the displacements induced in the structure as well as to the brace member imperfections. Material non-linearities were included using distributed plasticity in all structural elements (columns, beams, and braces) while lumped plasticity was used to model the out-of-plane behavior of the gusset plates at braces' ends, according to the modelling strategy adopted for the braces [145].

In addition to the bare-frame models of the considered case studies, models incorporating the non-linear behavior of the cladding panels were developed. The number of panels employed in each case study varies, because of the different geometries. A schematic representation of the cladding panel distribution is given in Figure 61b,c for the longitudinal and transverse façades, respectively. Table 14 shows all the analyzed buildings.

Table 14. ID of the S structures under investigation. Building ID is organized as typology-geometry – site – soil condition.

Site	**Soil condition**	
	A	C
L'Aquila (AQ)	S-LX20-LY6-AQ-A S-LX20-LY6-PANELS-AQ-A S-LX20-LY8-AQ-A S-LX20-LY8-PANELS-AQ-A S-LX30-LY6-AQ-A S-LX30-LY6-PANELS-AQ-A S-LX30-LY8-AQ-A S-LX30-LY8-PANELS-AQ-A	S-LX20-LY6-AQ-C S-LX20-LY6-PANELS-AQ-C S-LX20-LY8-AQ-C S-LX20-LY8-PANELS-AQ-C S-LX30-LY6-AQ-C S-LX30-LY6-PANELS-AQ-C S-LX30-LY8-AQ-C S-LX30-LY8-PANELS-AQ-C
Naples (NA)	S-LX20-LY6-NA-A S-LX20-LY6-PANELS-NA-A S-LX20-LY8-NA-A S-LX20-LY8-PANELS-NA-A S-LX30-LY6-NA-A S-LX30-LY6-PANELS-NA-A S-LX30-LY8-NA-A	S-LX20-LY6-NA-C S-LX20-LY6-PANELS-NA-C S-LX20-LY8-NA-C S-LX20-LY8-PANELS-NA-C S-LX30-LY6-NA-C

	S-LX30-LY8-PANELS-NA-A	S-LX30-LY6-PANELS-NA-C S-LX30-LY8-NA-C S-LX30-LY8-PANELS-NA-C
Milan (MI)	S-LX20-LY6-MI-A S-LX20-LY6-PANELS-MI-A S-LX20-LY8-MI-A S-LX20-LY8-PANELS-MI-A S-LX30-LY6-MI-A S-LX30-LY6-PANELS-MI-A S-LX30-LY8-MI-A S-LX30-LY8-PANELS-MI-A	S-LX20-LY6-MI-C S-LX20-LY6-PANELS-MI-C S-LX20-LY8-MI-C S-LX20-LY8-PANELS-MI-C S-LX30-LY6-MI-C S-LX30-LY6-PANELS-MI-C S-LX30-LY8-MI-C S-LX30-LY8-PANELS-MI-C

5.2.7 Failure criteria

The seismic performance of all the structures was assessed by carrying out non-linear dynamic analysis on three-dimensional computer models (see the next section). Structural reliability was assessed with respect to the exceedance of two damage states, *global collapse* (GC) and *usability-preventing damage* (UPD). The GC criterion was, in general, defined based on the deformation capacity (the *EDP* is either the RDR or the maximum IDR) corresponding to a certain level of post-peak strength deterioration; i.e. 50% of the maximum base-shear on the SPO curves of the structures for each horizontal direction (Figure 62a). This is the case of the URM, RC and PRC buildings; however, there are some exceptions or adjustments required for some structural typologies. For the URM buildings, the collapse criteria were defined based on the MIDR of single-wall elements corresponding to a 50% drop of the maximum base-shear from SPO analysis, which was carried out under several load patterns (i.e., uniform or inverted triangular) in both horizontal directions, and the minimum value was defined as the collapse limit threshold. Some adjustments were made in the cases the dynamic deformation capacity was found to be lower than the SPO-based threshold value (possibly because of torsional effects and cyclic degradation). In particular, the threshold was adjusted to the MIDR

corresponding to a 35% drop of the maximum base-shear on the static capacity curve. Particularly to PRC buildings, a local collapse condition corresponding to the attainment of the maximum shear strength of the beam-column dowel connections, which is critical for this structural type, was also considered. Given that the S buildings have different load-resisting systems in two horizontal directions, the collapse criteria were defined individually for each of them: 10% RDR was selected for the direction with the MRF system following indications by FEMA 350 [146], whereas the collapse in the CBF system corresponds to the attainment of the maximum strain range, defined as the difference between minimum and maximum strain responses measured at the cross-sections of brace members under seismic excitation. For the latter, the strain range threshold was set according to past studies on local collapse in brace members due to low-cycle fatigue [145]. The collapse condition for BI reinforced concrete buildings occurs either if the superstructure fails or if the base isolation system fails. The superstructure failure criterion is analogous to the one used for the RC buildings, while the failure of the base isolation was defined based on the device-specific criteria. For HDRBs, in particular, three different failure modes were considered, i.e.: cavitation, buckling, and shear failure. The global collapse of the isolation system was conventionally deemed to occur when (at least) 50% of the devices of the isolation system simultaneously fail due to cavitation, shear or buckling. For FPSs, the global collapse was deemed to occur when the first device reaches an ultimate displacement in extra-stroke regime, defined considering a limit value of contact pressure and other issues related to sliding material degradation.

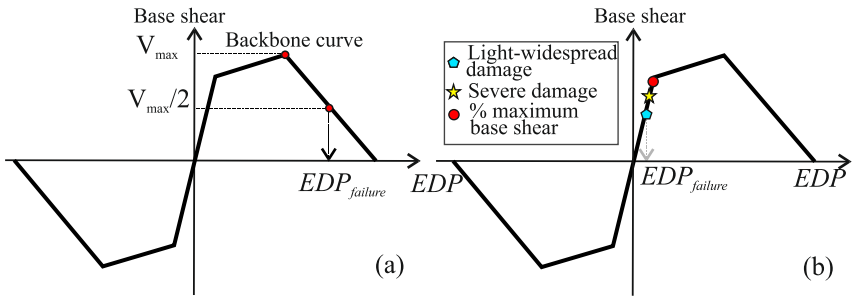

Figure 62. General definition for the GC failure criterion (RC, URM, PRC, and BI) (a) and UPD failure criteria (b). In the latter case, failure is defined as the first occurring among the three conditions defined within the text.

UPD follows a multi-criteria approach (Figure 62b) that considers the onset of any of the following three conditions:

- a widespread light damage condition: light damage in 50% of the main non-structural elements (e.g., infills);
- a severe damage condition: at least one of the non-structural elements reached a severe damage level leading to significant interruption of use;
- attainment of 95% of the maximum base-shear of the structure.

These three conditions particularized for each structural typology are summarized in Table 15.

Table 15. Criteria for UPD based on multi-criteria approach for each structural typology.

Typologies	**Multi-criteria approach for *UPD***		
	a	b	c
URM	Light-widespread damage in 50% of masonry walls (computed in terms of resisting area) in each direction	At least one of masonry walls reached the drift limit corresponding to a certain level of strength deterioration in the case of the phenomenological non-linear beam or attainment of the toe-crushing condition in the case of the microelement mechanical model	The attainment of 95% of the maximum base-shear of the structure
RC BI	Light-widespread damage in 50% of masonry infills and partitions	At least one of the masonry infills or partitions reached 50% strength drop from its maximum resistance	The first attainment of 95% of the maximum base-shear of the structure

PRC	1% inter-story drift ratio	At least one cladding panel reached the maximum strength of the panel-structure connection, with possible panel overturning	-
S	Widespread light damage in 50% of the cladding (sandwich) panels, in each horizontal direction	At least one panel-to-frame connection reached its maximum strength	Having attained 95% of the maximum base-shear of the structure

5.2.8 Sites and hazard

To quantify risk of failure and to select records for the non-linear dynamic analysis of structures, hazard curves need to be calculated for the three sites under investigation. Therefore, the curves were computed for the two soil classes (A and C) using as the *IM* the spectral ordinates closer to the first-mode vibration period of the developed structural models. In fact, the $Sa(T)$ at a period close to the fundamental model of the structural model is that considered to develop the fragility curves (to follow). Table 16 summarizes the hazard analysis performed and the corresponding *IM*s.

Table 16. Sites and spectral ordinates where hazard curves were computed.

Site	**Sa(0.15s)**		**Sa(0.5s)**		**Sa(1s)**		**Sa(1.5s)**		**Sa(2.0s)**		**Sa(3.0s)**	
	A	C	A	C	A	C	A	C	A	C	A	C
AQ	ü	ü	ü	ü	ü	ü	-	ü	ü	ü	-	ü
NA	ü	ü	ü	ü	ü	ü	-	ü	ü	ü	-	ü

MI	ü	ü	ü	ü	ü	ü	-	ü	ü	ü	-	-

Hazard curves, expressed in terms of annual exceedance rate, λ_{im}, were computed as described in [11], that is using the seismic zone source model of [84], with the magnitude distribution and rates described in [85], and the ground motion prediction equation by [147], complemented by that of [82] for periods beyond 2s. Hazard analysis was carried out via the OPENQUAKE platform [148]. Hazard curves were discretized in ten *IM* values corresponding to the following return periods T_R in years: $T_R = \{10, 50, 100, 250, 500, 1000, 2500, 5000, 10000, 100000\}$ *years* . No *IM*-values with exceedance return period longer than $T_R = 100000$ *years* were calculated, to avoid large hazard extrapolations.[6]

Seismic fragility of the designed structures was assessed by subjecting the 3D models to non-linear multi-stripe analysis. MSA, like IDA, has the objective of quantifying a damage measure of a structure when *IM* levels increase. MSA, differently from IDA, may use different sets of (scaled or not) records at each *IM*-level. These record sets should reflect the site-specific hazard changes with the intensity of the shaking, for the purpose of rendering the calculated seismic structural demand hazard-consistent [53]. The conditional spectrum approach, which accounts for seismic hazard disaggregation, was thus employed for selecting the ground motion records to be used as input for dynamic analysis.

The selected records were extracted mainly from the Italian accelerometric archive [149] and only if no records with similar spectra were available there, records in the NGAwest2 database [94] were selected instead. The record selection delivered two-hundreds pairs (horizontal components) of records; twenty records for each one of the ten stripes. Hence, two-hundred records have been employed in the analysis of each individual structural model. To reduce the computational demand from non-linear dynamic analysis, the selected records have been post processed to remove the parts of the signal outside the $\{t_{0.05\%}, t_{99.95\%}\}$ range, where $D_{99.90\%} = t_{99.95\%} - t_{0.05\%}$ is the 99.90% significant duration of the record [150], yet keeping synchronization of horizontal components, which are applied simultaneously to the model.

[6] The seismic source model used for the hazard assessment is coherent with the one employed by the Italian code to define the design seismic actions on structures; i.e., [117].

5.2.9 Dynamic analysis and seismic reliability evaluation

In the project, the 3D numerical models for structural analysis were built in OpenSees [79] except for URM buildings that were analyzed using TREMURI [151]. As described, output analysis for each building consists of ten stripes of twenty structural responses obtained from the application of pairs of horizontal accelerograms for each of the two horizontal directions of the 3D model with the member alignments (called *x* and *y* for sake of simplicity).

Defined $EDP_{(x)i,j}$ and $EDP_{(y)i,j}$ as the seismic demand of a structure subjected to the *j*-th record belonging to the *i*-th stripe along the two directions, a structural capacity threshold is defined (as previously seen) for each direction, respectively called $edp_{f,(x)}$ and $edp_{f,(y)}$. For all the structural models, failure with respect to the performance level of interest (GC and UPD) was checked using the maximum demand-over-capacity ratio in the two directions, here defined as $EDP_{i,j}$. In the numerical analysis there were also some cases of numerical instability. If a numerical instability occurs along only one out of two directions, this will be propagated to global response $EDP_{i,j}$. Analysis leads to ten stripes of twenty responses each; Figure 63a,b.

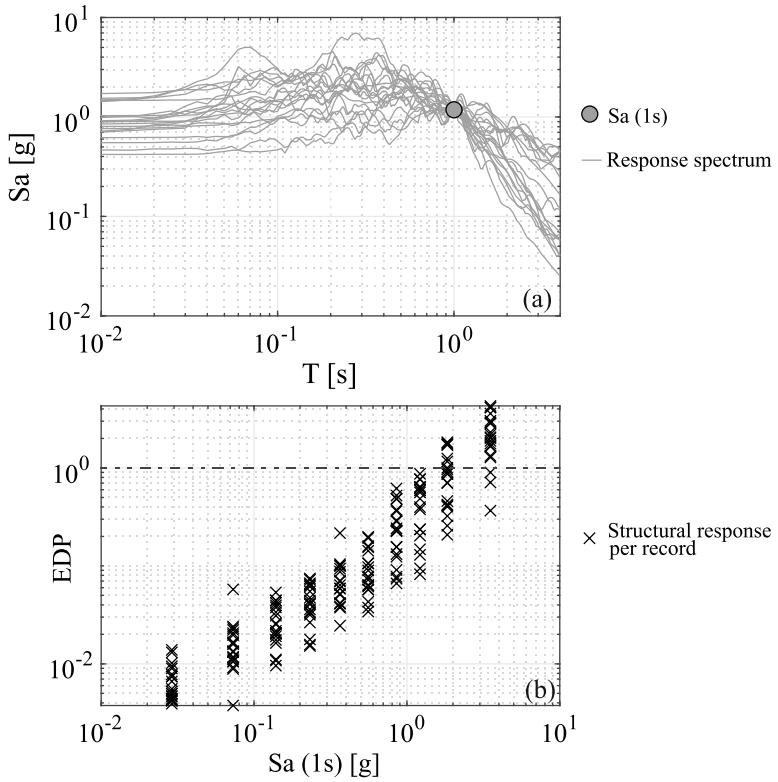

Figure 63. (a) Example of hazard-consistent record-selection for MSA; (b) example of MSA results when the EDP is the demand-to-capacity ratio.

The rate of earthquakes causing failure of the structure, λ_f, was calculated as:

$$\lambda_f = \int_{IM} P\left[f \left| IM = im \right.\right] \cdot \left| d\lambda_{im} \right| \approx \int_{0}^{IM_{T_R=10^5}} P\left[f \left| IM = im \right.\right] \cdot \left| d\lambda_{im} \right| + 10^{-5}, \qquad (42)$$

where $P\left[f \left| IM = im \right.\right]$ is the fragility of the structural model, defined as the probability of violating a structural limit state, edp_f, conditional to the values of a ground motion $IM = im$ and $\left| d\lambda_{im} \right|$ is the absolute value of the derivative of the site-specific hazard curve times $d(im)$. Consistently with what has been previously described, global structural response is defined in terms of demand-over-capacity so edp_f is equal to one. Structural failure was considered to have been reached in cases of numerical instability or the attainment of the collapse criteria in either of the two horizontal directions. Given that collapse is

indicated as C, fragility has been evaluated via an application of the total probability theorem:

$$P\left[f \left| IM = im \right. \right] = P\left[C \left| IM = im \right. \right] + \\ + P\left[EDP > edp_f \left| \overline{C}, IM = im \right. \right] \cdot \left\{ 1 - P\left[C \left| IM = im \right. \right] \right\}, \quad (43)$$

where $P\left[EDP > edp_f \left| \overline{C}, IM = im \right. \right]$ and $P\left[C \left| IM = im \right. \right]$ are, given *IM*, the probability of failure given non-collapse and collapse, respectively.

It was mentioned above that site-specific hazard curves within RINTC project have been evaluated for ten return periods T_R with an upper bound equal to $100000\,years$ so a full evaluation of the failure rate is consequently prevented. Consequently, it has been conservatively assumed that ground-motions having *IM* larger than the *IM* corresponding to $T_R = 100000\,years$, named $IM_{T_{R,\max}}$, will certainly cause structural failure, as shown in the last equality of Equation (42), where 10^{-5} is added to the integral to account for the truncation of the hazard curve at $\lambda_{im} = 10^{-5}$. The discretization of the structural analysis at the ten *IM* levels and the use of twenty pairs of ground motions at each *IM* stripe yielded the following approximation in computing Equations (42) and (43):

$$\begin{cases} \lambda_f \approx 10^{-5} + \dfrac{P\left[f \left| IM = im_1 \right. \right]}{1/T_R\left(im_1\right) - \lim\limits_{IM \to 0} \lambda_f} + \sum\limits_{i=2}^{10} \dfrac{P\left[f \left| IM = im_i \right. \right]}{1/T_R\left(im_i\right) - 1/T_R\left(im_{i-1}\right)}, i = 1,2,...,10 \\ P\left[f \left| IM = im_i \right. \right] \approx \left\{ 1 - \Phi\left[\dfrac{\log\left(edp_f\right) - \mu_{\log(EDP)|im_i}}{\sigma_{\log(EDP)|im_i}} \right] \right\} \cdot \left(1 - \dfrac{N_{C,im_i}}{20} \right) + \dfrac{N_{C,im_i}}{20} \\ \mu_{\log(EDP)|im_i} \approx \dfrac{1}{20 - N_{C,im_i}} \cdot \sum\limits_{j=1}^{20-N_{C,im_i}} \log\left(EDP_{i,j}\right) \\ \sigma_{\log(EDP)|im_i} \approx \sqrt{\dfrac{1}{19 - N_{C,im_i}} \cdot \sum\limits_{j=1}^{20-N_{C,im_i}} \left[\log\left(EDP_{i,j}\right) - \mu_{\log(EDP)|im_i} \right]^2} \end{cases} \quad (44)$$

In the equation $\Phi(\bullet)$ is the cumulative Gaussian distribution function and N_{C,im_i} is the number of numerical instabilities at the im_i stripe.

The main result emerged from the project was that despite the exceedance return period of the design seismic actions being the same at all sites, seismic reliability is not the same for all the sites, but it increases when seismic hazard decreases (see later also). Further research has shown that two different issues could explain this result: (i) the first one related to the requirements that the code imposes regardless of the design seismic actions (e.g., minimum reinforcement requirements and gravity load design) and that are expected to have a larger effect on the seismic safety of structures designed for low-hazard sites [11]; (ii) the ground motion beyond the design return period, which is substantially different for low- and high-hazard sites [152].

5.3. Lognormal fragility fitting

Equation (44) does not require to fit a probabilistic model among different *IM* levels; therefore, the RINTC project has not developed fragility curves based on the 3D structural modelling so far, which is the goal of this study. In the framework of PBEE, two predominant approaches exist to estimate fragility functions analytically, namely *IM*-based and *EDP*-based according to the terminology of [153], the difference lying in the characterization of demand and capacity terms. In the first case, IDA is typically performed to obtain a sample of *IM* causing structural failure and fragility is written as the probability that the random variable represented by the *IM* level causing structural failure (capacity) is equal or lower than the level of seismic intensity occurring at site (demand). Conversely, in the *EDP*-based approach, starting from IDA or MSA results, fragility function is evaluated as the probability that the random variable defined by *EDP* reached by the structure at a fixed *IM* level is larger than the specified capacity. The *IM* to express the fragility is the same as the one to carry out MSA for the considered structural model, that is, spectral pseudo-acceleration at a vibration period close to the fundamental one (see from Table 17 to Table 21 for details).

In the next sub-sections, the considered procedures to fit lognormal fragility functions on the RINTC results are illustrated. More than one procedure has to be considered because a single approach did not converge or provide satisfactory outcomes in all cases. Consistent with the described project's approach, the fitting approach is the *EDP*-based. The fragility fitting procedures are complemented with equations to quantify estimation uncertainty due to the limited sample of structural responses available. Procedures have been

described in Section 2.3 and are here recalled for easier reading using consistent symbology.

5.3.1 Maximum likelihood

If the lognormal probability model is chosen to represent structural fragility, mean η and standard deviation β of the logarithms of the random variable *IM* causing structural failure must be evaluated by means Equation (2), here recalled for easier reading:

$$P\left[f \left| IM = im \right. \right] \triangleq \Phi\left[\frac{\log(im) - \eta}{\beta} \right]. \tag{45}$$

The maximum likelihood (ML) method seeks the parameters $\{\eta, \beta\}$ such that the resulting distribution has the highest likelihood of having generated the observed data (e.g., [55]). As previously mentioned, in MSA, for each of stripe (out of u), a total number n of structural analysis is conducted so that, at the end of the analysis, vectors of the kind $edp_j = \{edp_{j,1}, edp_{j,2}, ..., edp_{j,n}\}$, are available. Each of them can be partitioned in two: one with failure cases, of size q_j, and one of non-failure cases, of size $(n - q_j)$ (the failure cases include collapse cases). The parameters of the lognormal fragility function, $\{\eta, \beta\}$, can be estimated via ML as:[7]

$$\begin{aligned} \{\eta, \beta\} = \arg\max_{\eta,\beta} \left[\sum_{j=1}^{u} \left(\ln \binom{n}{q_j} + q_j \cdot \ln\left\{ \Phi\left[\frac{\ln(im_j) - \eta}{\beta} \right] \right\} + \right. \right. \\ \left. \left. + (n - q_j) \cdot \ln\left\{ 1 - \Phi\left[\frac{\ln(im_j) - \eta}{\beta} \right] \right\} \right) \right] \end{aligned} \tag{46}$$

It has been introduced that because of record-to-record variability the parameters $\{\eta, \beta\}$ are expected to change when the sample of records changes so they are not the true parameters characterizing the structural fragility but only an estimation of them $\{\hat{\eta}, \hat{\beta}\}$. Quantification of the uncertainty estimation

[7] To fit a fragility function, it could advisable, or even required, that MSA is performed up to an *IM* level for which at least 50% of the records lead to failure/collapse, which could imply further stripes (i.e., larger *IM*s) than those routinely considered in the project (e.g., [154]).

(see, among others, [8]) will be briefly recalled later. For sake of simplicity, the terminology $\{\eta, \beta\}$ is from now on used instead of the more accurate $\{\hat{\eta}, \hat{\beta}\}$.

5.3.2 Normal probability paper and least square regression

When the structural vulnerability is low compared to the seismic hazard at the site it may be that only a few failures, if any, are observed at each *IM* level, so that the ML fragility fitting is difficult. In this case, another procedure can be adopted, provided that structural response is available at each stripe:

- for each $IM = im_j$, $j = \{1, 2, \ldots, u\}$, *EDP* data, that is $edp_j = \{edp_{j,1}, edp_{j,2}, ..., edp_{j,n}\}$, are divided in collapse cases, if any, and non-collapse cases, the count of which are $k_{C, IM=im_j}$ and $k_{\overline{C}, IM=im_j}$, respectively (clearly $k_{C, IM=im_j} + k_{\overline{C}, IM=im_j} = n$);
- the probability of failure based on the non-collapse cases is evaluated, for example, as:

$$P\left[EDP > edp_f \left| \overline{C}, IM = im_j \right. \right] = 1 - \Phi\left(\frac{\ln edp_f - \mu_{\ln(EDP_j)}}{\beta_{\ln(EDP_j)}} \right), \qquad (47)$$

  where $\left\{ \mu_{\ln(EDP_j)}, \beta_{\ln(EDP_j)} \right\}$ are the mean and the standard deviation of the logarithms of *EDP* when $IM = im_j$, $i = \{1, 2, \ldots, u\}$;
- the fragility value when $IM = im_i$ is estimated as per Equation (43), where $P\left[C \left| IM = im_j \right. \right] = k_{C, IM=im_j} / n$; alternatively, at any $IM = im_j$, $j = \{1, 2, \ldots, u\}$, value equal to one can be assigned to the analyses for which collapse has been observed and zero for the others, then a logistic regression (not employed to derive the fragility curves employed in the following) can be performed to obtain the sought probability as:

$$P\left[C \left| IM = im_j \right. \right] = \frac{1}{1 + e^{-(\alpha_1 + \alpha_2 \cdot im_j)}}, \qquad (48)$$

  where $\{\alpha_1, \alpha_2\}$ are the regression coefficients;

- at this point *m* fragility values, $P\left[f \left| IM = im_j \right. \right]$, $j = \{1, 2...u\}$, are available; then, a fragility function can be fitted, at least in two ways:
    - via ordinary *least square regression* of $\{\ln im_j, z_j\}$ data, where $z_j = \Phi^{-1}\left\{P\left[f \left| IM = im_j \right. \right]\right\}$ i.e., a Gaussian probability paper [58] (*NPP*),[8] which yields a line the slope is β^{-1} and the intercept is $-\eta/\beta$ as:

$$\{\eta, \beta\} = \arg\min_{\eta,\beta} \left[\sum_{j=1}^{u} \left(\Phi^{-1} \left\{ \frac{k_{C,IM=im_j}}{n} + \left[1 - \Phi\left(\frac{\ln edp_f - \mu_{\ln(EDP_j)}}{\beta_{\ln(EDP_j)}} \right) \right] \times \right. \right. \right. ; \left. \left. \left. \times \left(1 - \frac{k_{C,IM=im_j}}{n} \right) \right\} - \frac{\ln im_j}{\beta} + \frac{\eta}{\beta} \right)^2 \right]$$

(49)

    - Via least square regression (i.e., minimizing the sum of squared errors, *SSE*), which yields the lognormal fragility parameters evaluated in the second Equation (50):

$$\{\eta, \beta\} = \arg\min_{\eta,\beta} \left(\sum_{j=1}^{u} \left\{ \frac{k_{C,IM=im_j}}{n} + \left[1 - \Phi\left(\frac{\ln edp_f - \mu_{\ln(EDP_j)}}{\beta_{\ln(EDP_j)}} \right) \right] \times \right. \right. \left. \left. \times \left(1 - \frac{k_{C,IM=im_j}}{n} \right) - \Phi\left(\frac{\ln im_j - \eta}{\beta} \right) \right\}^2 \right) \quad . \tag{50}$$

In both equations, if the logistic functions is used for the collapse probability, $k_{C,IM=im_j}/n$ is replaced by Equation (48).

[8] A similar approach can be found in [157].

5.3.3 Estimation uncertainty

As previously stated, the parameters $\{\eta, \beta\}$, evaluated from the Equation (46) and both the Equation (50), are only estimates of the true parameters which are unknown. To account for such an uncertainty in estimation, an approximation of the distribution of $\{\eta, \beta\}$ can be derived. A possible procedure would consist of the following steps.

(1) the *EDP* responses at *j*-th *IM* level, $edp_j = \{edp_{j,1}, edp_{j,2}, ..., edp_{j,n}\}$, $j = \{1, 2, \ldots, u\}$, are resampled with replacement, resulting in new sets of responses at the *i*-th stripe (i.e., bootstrap samples) $edp_j^* = \{edp_{j,1}^*, edp_{j,2}^*, ..., edp_{i,n}^*\}$;

(2) at each stripe, collapse cases $k_{C,IM=im_j}^*$ and failure cases q_j^* are evaluated; then $P^*\left[f \left| IM = im_j \right. \right]$, is calculated, e.g. according to the second Equation (44) or as $\left(k_{C,IM=x_j}^* + q_j^*\right) \Big/ n$;

(3) given $P^*\left[f \left| IM = im_j \right. \right]$, Equation (46), first or second Equation (50), depending on the method used to calculate $\{\eta, \beta\}$, can be applied to obtain a new estimation of the fragility parameters that can be indicated as $\{\eta^*, \beta^*\}$;

(4) repeating steps 1-3 an arbitrary number of times, say *k*, provides a distribution of the curve parameters and then of the structural fragility, which can help getting a sense of estimation uncertainty involved in the fragility fitting procedure.[9]

The obtained family of fragility curves provides a sense of the uncertainty in estimation (see next section).

5.4. Results and discussion

5.4.1 Fragility curves

As seen in Chapter 3, the fragility fitting and resampling procedures described above are implemented in R2R-EU software, which was used to get the results presented in this section. For each structural model under investigation, the

[9] Note that this is, factually, a non-parametric resampling plan.

specific method to derive the fragility curves was chosen first using all approaches, then choosing, via expert judgement of the authors, the one better fitting the results of the dynamic non-linear analysis (the results of the three procedures for each model cannot be given here for the sake of brevity). Figures representing the lognormal fragilities are shown from Figure 64 to Figure 68, while lognormal parameters for each structure are listed from Table 17 to Table 21 (along with other values which will be defined later). In all the figures, abscissa axis is limited to the *IM* value corresponding to the 95^{th} percentile of the fragility curve with maximum η (but lower than 3 to keep figures readable) among those belonging to the same structural typology, site and having same failure criteria.

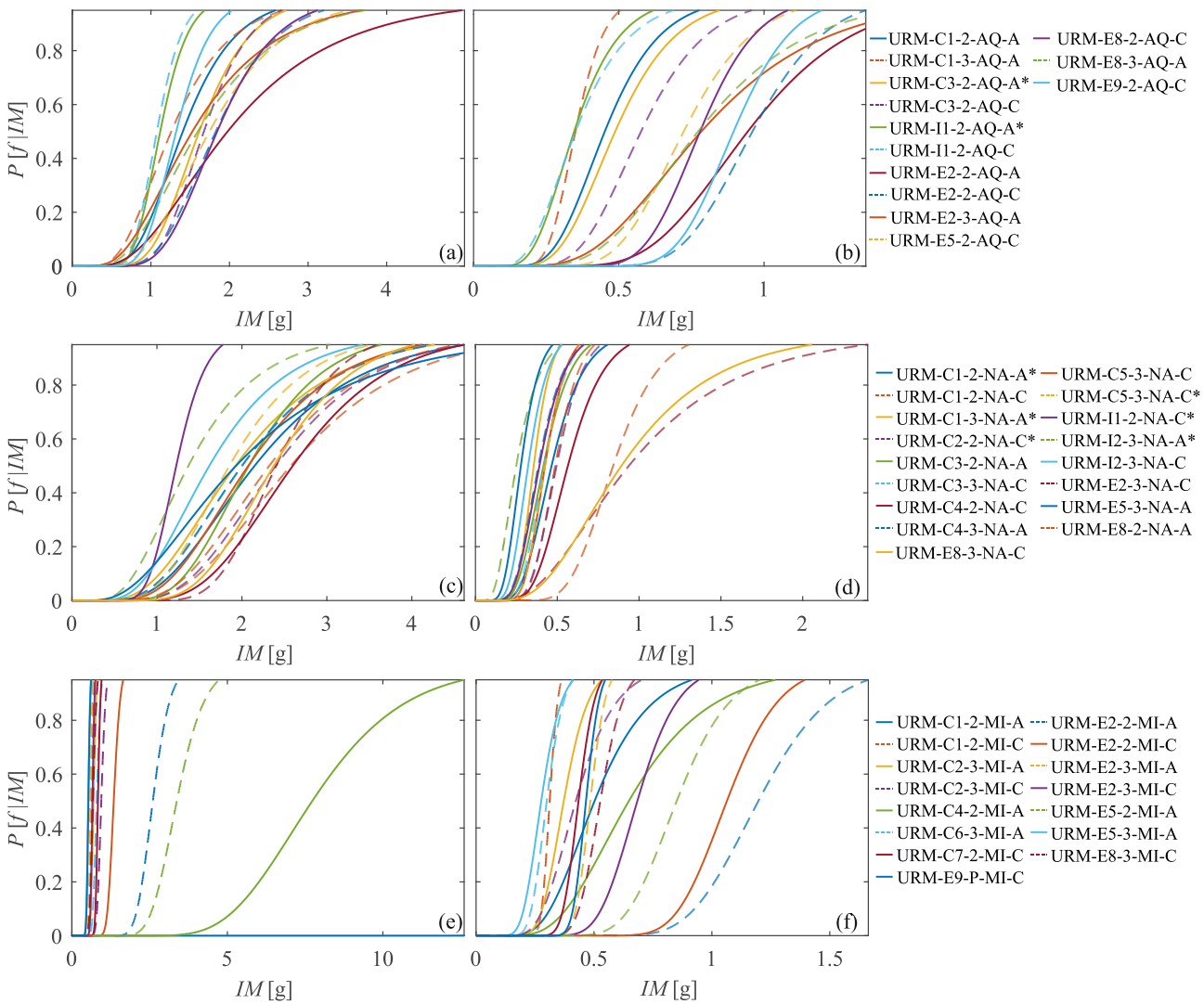
P [f |IM]
IM [g]
(a)
(b)
(c)
(d)
(e)
(f)
URM-C1-2-AQ-A
URM-C1-3-AQ-A
URM-C3-2-AQ-A*
URM-C3-2-AQ-C
URM-I1-2-AQ-A*
URM-I1-2-AQ-C
URM-E2-2-AQ-A
URM-E2-2-AQ-C
URM-E2-3-AQ-A
URM-E5-2-AQ-C
URM-E8-2-AQ-C
URM-E8-3-AQ-A
URM-E9-2-AQ-C
URM-C1-2-NA-A*
URM-C1-2-NA-C
URM-C1-3-NA-A*
URM-C2-2-NA-C*
URM-C3-2-NA-A
URM-C3-3-NA-C
URM-C4-2-NA-C
URM-C4-3-NA-A
URM-E8-3-NA-C
URM-C5-3-NA-C
URM-C5-3-NA-C*
URM-I1-2-NA-C*
URM-I2-3-NA-A*
URM-I2-3-NA-C
URM-E2-3-NA-C
URM-E5-3-NA-A
URM-E8-2-NA-A
URM-C1-2-MI-A
URM-C1-2-MI-C
URM-C2-3-MI-A
URM-C2-3-MI-C
URM-C4-2-MI-A
URM-C6-3-MI-A
URM-C7-2-MI-C
URM-E9-P-MI-C
URM-E2-2-MI-A
URM-E2-2-MI-C
URM-E2-3-MI-A
URM-E2-3-MI-C
URM-E5-2-MI-A
URM-E5-3-MI-A
URM-E8-3-MI-C

Figure 64. Fragility curves for URM buildings. Figures show curves for L'Aquila (a,b), Naples (c,d) and Milan (e,f) at GC and UPD respectively.

Table 17. URM buildings.

ID-building	**Failure criteria**	**Curve fitting method**	***IM***	η	β	***LFM***
URM-C1-2-AQ-A	GC	LSF	Sa(0.15s)	0.341	0.370	0.92
	UPD	LSF	Sa(0.15s)	-0.795	0.330	1
URM-C1-2-MI-A	GC	NPP	Sa(0.15s)	4.241	0.486	5.40E-15
	UPD	NPP	Sa(0.15s)	-0.688	0.365	0.039
URM-C1-2-MI-C	GC	NPP	Sa(0.15s)	-0.452	0.084	1.09E-11
	UPD	NPP	Sa(0.15s)	-1.164	0.091	0.099
URM-C1-2-NA-A*	GC	ML	Sa(0.15s)	0.765	0.468	0.30
	UPD	LSF	Sa(0.15s)	-0.766	0.335	1
URM-C1-2-NA-C	GC	LSF	Sa(0.15s)	0.946	0.421	0.31

ID-building	Failure criteria	Curve fitting method	*IM*	η	β	*LFM*
	UPD	LSF	Sa(0.15s)	-0.719	0.245	1
URM-C1-3-AQ-A	GC	LSF	Sa(0.15s)	0.231	0.463	0.9
	UPD	LSF	Sa(0.15s)	-1.048	0.222	1
URM-C1-3-NA-A*	GC	LSF	Sa(0.15s)	0.654	0.485	0.45
	UPD	LSF	Sa(0.15s)	-1.033	0.236	1
URM-C2-2-NA-C*	GC	LSF	Sa(0.15s)	0.875	0.390	0.36
	UPD	LSF	Sa(0.15s)	-0.702	0.265	1
URM-C2-3-MI-A	GC	NPP	Sa(0.15s)	-0.364	0.104	2.28E-16
	UPD	LSF	Sa(0.15s)	-0.989	0.220	0.50
URM-C2-3-MI-C	GC	NPP	Sa(0.15s)	-0.057	0.120	2.23E-09
	UPD	LSF	Sa(0.15s)	-0.860	0.309	0.57
URM-C3-2-AQ-A*	GC	ML	Sa(0.15s)	0.480	0.317	0.95

ID-building	Failure criteria	Curve fitting method	*IM*	η	β	*LFM*
	UPD	LSF	Sa(0.15s)	-0.718	0.336	1
URM-C3-2-AQ-C	GC	LSF	Sa(0.15s)	0.515	0.282	1
	UPD	LSF	Sa(0.15s)	-0.551	0.308	1
URM-C3-2-NA-A	GC	LSF	Sa(0.15s)	0.733	0.340	0.34
	UPD	NPP	Sa(0.15s)	-0.879	0.323	1
URM-C3-3-NA-C	GC	LSF	Sa(0.15s)	0.694	0.453	0.53
	UPD	LSF	Sa(0.15s)	-0.873	0.277	1
URM-C4-2-MI-A	GC	NPP	Sa(0.15s)	2.045	0.298	1.61E-14
	UPD	NPP	Sa(0.15s)	-0.434	0.409	0.044
URM-C4-2-NA-C	GC	LSF	Sa(0.15s)	0.955	0.349	0.27
	UPD	ML	Sa(0.15s)	-0.572	0.311	1
URM-C4-3-NA-A	GC	LSF	Sa(0.15s)	0.694	0.459	0.41

ID-building	Failure criteria	Curve fitting method	*IM*	η	β	*LFM*
	UPD	LSF	Sa(0.15s)	-0.956	0.324	1
URM-C5-3-NA-C	GC	LSF	Sa(0.15s)	0.729	0.417	0.50
	UPD	LSF	Sa(0.15s)	-0.856	0.245	1
URM-C5-3-NA-C*	GC	ML	Sa(0.15s)	0.616	0.390	0.60
	UPD	LSF	Sa(0.15s)	-0.856	0.245	1
URM-C6-3-MI-A	GC	NPP	Sa(0.15s)	-0.228	0.127	5.72E-21
	UPD	NPP	Sa(0.15s)	-1.205	0.191	0.15
URM-C7-2-MI-C	GC	NPP	Sa(0.15s)	-0.178	0.079	5.25E-24
	UPD	NPP	Sa(0.15s)	-0.834	0.127	0.013
URM-I1-2-AQ-A*	GC	NPP	Sa(0.15s)	0.113	0.249	1
	UPD	LSF	Sa(0.15s)	-1.061	0.354	1
URM-I1-2-AQ-C	GC	ML	Sa(0.15s)	0.073	0.236	1

ID-building	Failure criteria	Curve fitting method	*IM*	η	β	*LFM*
	UPD	NPP	Sa(0.15s)	-1.046	0.409	1
URM-I1-2-NA-C*	GC	LSF	Sa(0.15s)	0.205	0.225	0.99
	UPD	LSF	Sa(0.15s)	-0.940	0.320	1
URM-I2-3-NA-A*	GC	LSF	Sa(0.15s)	0.315	0.484	0.69
	UPD	LSF	Sa(0.15s)	-1.389	0.455	1
URM-I2-3-NA-C	GC	LSF	Sa(0.15s)	0.480	0.456	0.68
	UPD	LSF	Sa(0.15s)	-1.134	0.302	1
URM-E2-2-AQ-A	GC	LSF	Sa(0.15s)	0.681	0.559	0.81
	UPD	LSF	Sa(0.15s)	-0.057	0.302	1
URM-E2-2-AQ-C	GC	LSF	Sa(0.15s)	0.602	0.342	0.98
	UPD	LSF	Sa(0.15s)	-0.041	0.207	1
URM-E2-2-MI-A	GC	LSF	Sa(0.15s)	0.956	0.167	9.33E-32

ID-building	Failure criteria	Curve fitting method	*IM*	η	β	*LFM*
	UPD	LSF	Sa(0.15s)	0.180	0.200	1.20E-11
URM-E2-2-MI-C	GC	LSF	Sa(0.15s)	0.296	0.124	5.24E-18
	UPD	LSF	Sa(0.15s)	0.062	0.165	1.49E-05
URM-E2-3-AQ-A	GC	LSF	Sa(0.15s)	0.424	0.535	0.88
	UPD	LSF	Sa(0.15s)	-0.243	0.421	1
URM-E2-3-MI-A	GC	LSF	Sa(0.15s)	-0.523	0.082	2.00E-09
	UPD	LSF	Sa(0.15s)	-0.725	0.106	0.0066
URM-E2-3-MI-C	GC	LSF	Sa(0.15s)	-0.415	0.081	7.47E-09
	UPD	LSF	Sa(0.15s)	-0.380	0.196	0.015
URM-E2-3-NA-C	GC	LSF	Sa(0.15s)	0.877	0.245	0.29
	UPD	LSF	Sa(0.15s)	-0.065	0.571	0.91
URM-E5-2-AQ-C	GC	LSF	Sa(0.15s)	0.557	0.427	0.95

ID-building	Failure criteria	Curve fitting method	*IM*	η	β	*LFM*
	UPD	LSF	Sa(0.15s)	-0.324	0.261	1
URM-E5-2-MI-A	GC	LSF	Sa(0.15s)	1.216	0.206	6.66E-29
	UPD	LSF	Sa(0.15s)	-0.162	0.211	8.47E-08
URM-E5-3-MI-A	GC	LSF	Sa(0.15s)	-0.652	0.096	1.67E-10
	UPD	LSF	Sa(0.15s)	-1.286	0.243	0.91
URM-E5-3-NA-A	GC	LSF	Sa(0.15s)	0.658	0.622	0.44
	UPD	LSF	Sa(0.15s)	-1.282	0.323	1
URM-E8-2-AQ-C	GC	LSF	Sa(0.15s)	0.611	0.321	1
	UPD	LSF	Sa(0.15s)	-0.249	0.199	1
URM-E8-2-NA-A	GC	LSF	Sa(0.15s)	0.842	0.408	0.27
	UPD	LSF	Sa(0.15s)	-0.173	0.266	0.88
URM-E8-3-AQ-A	GC	LSF	Sa(0.15s)	0.468	0.514	0.90

ID-building	Failure criteria	Curve fitting method	*IM*	η	β	*LFM*
	UPD	LSF	Sa(0.15s)	-0.258	0.382	1
URM-E8-3-MI-C	GC	LSF	Sa(0.15s)	-0.389	0.131	0.00059
	UPD	LSF	Sa(0.15s)	-0.641	0.147	0.13
URM-E8-3-NA-C	GC	LSF	Sa(0.15s)	0.865	0.323	0.35
	UPD	LSF	Sa(0.15s)	-0.115	0.508	0.95
URM-E9-2-AQ-C	GC	LSF	Sa(0.15s)	0.279	0.262	0.95
	UPD	LSF	Sa(0.15s)	-0.111	0.178	1
URM-E9-3-MI-C	GC	LSF	Sa(0.15s)	-0.634	0.094	0.032
	UPD	LSF	Sa(0.15s)	-0.763	0.098	0.32

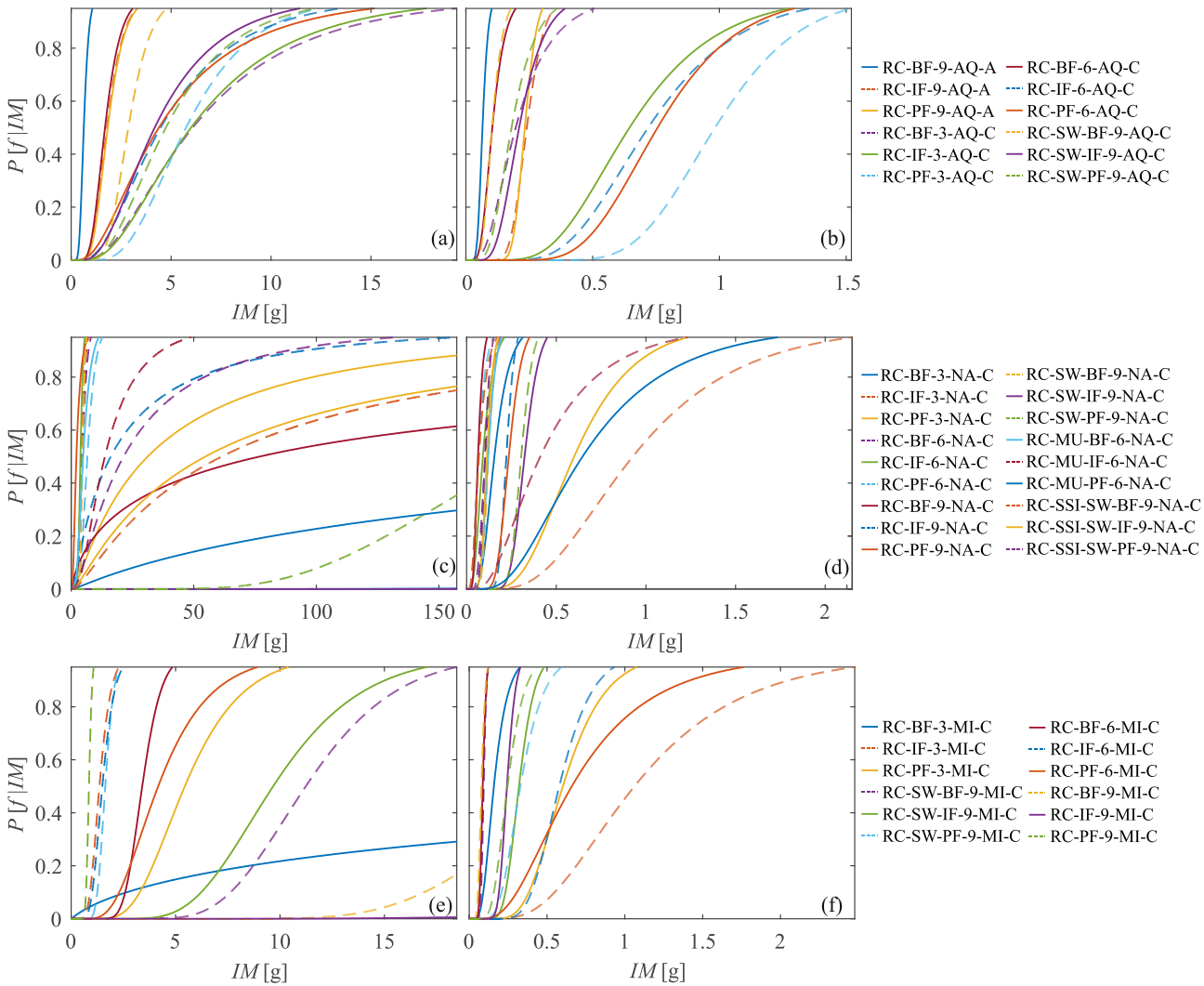
P [f |IM]
IM [g]
(a)
(b)
(c)
(d)
(e)
(f)
RC-BF-9-AQ-A
RC-IF-9-AQ-A
RC-PF-9-AQ-A
RC-BF-3-AQ-C
RC-IF-3-AQ-C
RC-PF-3-AQ-C
RC-BF-6-AQ-C
RC-IF-6-AQ-C
RC-PF-6-AQ-C
RC-SW-BF-9-AQ-C
RC-SW-IF-9-AQ-C
RC-SW-PF-9-AQ-C
RC-BF-3-NA-C
RC-IF-3-NA-C
RC-PF-3-NA-C
RC-BF-6-NA-C
RC-IF-6-NA-C
RC-PF-6-NA-C
RC-BF-9-NA-C
RC-IF-9-NA-C
RC-PF-9-NA-C
RC-SW-BF-9-NA-C
RC-SW-IF-9-NA-C
RC-SW-PF-9-NA-C
RC-MU-BF-6-NA-C
RC-MU-IF-6-NA-C
RC-MU-PF-6-NA-C
RC-SSI-SW-BF-9-NA-C
RC-SSI-SW-IF-9-NA-C
RC-SSI-SW-PF-9-NA-C
RC-BF-3-MI-C
RC-IF-3-MI-C
RC-PF-3-MI-C
RC-SW-BF-9-MI-C
RC-SW-IF-9-MI-C
RC-SW-PF-9-MI-C
RC-BF-6-MI-C
RC-IF-6-MI-C
RC-PF-6-MI-C
RC-BF-9-MI-C
RC-IF-9-MI-C
RC-PF-9-MI-C

Figure 65. Fragility curves for RC buildings. Figures show curves for L'Aquila (a,b), Naples (c,d) and Milan (e,f) at GC (left) and UPD (right) respectively.

Table 18. RC buildings.

ID-building	**Failure criteria**	**Curve fitting method**	***IM***	η	β	***LFM***
RC-BF-9-AQ-A	GC	LSF	Sa(2.0s)	-0.461	0.317	0.68
	UPD	LSF	Sa(2.0s)	-2.725	0.271	1
RC-IF-9-AQ-A	GC	LSF	Sa(1.0s)	0.582	0.367	0.68
	UPD	ML	Sa(1.0s)	-1.426	0.225	1
RC-PF-9-AQ-A	GC	ML	Sa(1.0s)	0.604	0.362	0.65
	UPD	LSF	Sa(1.0s)	-1.460	0.162	1
RC-BF-3-AQ-C	GC	LSF	Sa(1.0s)	1.805	0.702	0.22
	UPD	LSF	Sa(1.0s)	-1.627	0.576	1
RC-IF-3-AQ-C	GC	LSF	Sa(0.15s)	1.791	0.661	0.32
	UPD	LSF	Sa(0.15s)	-0.438	0.414	1

ID-building	Failure criteria	Curve fitting method	*IM*	η	β	*LFM*
RC-PF-3-AQ-C	GC	LSF	Sa(0.5s)	1.748	0.465	0.73
	UPD	LSF	Sa(0.5s)	-0.017	0.265	1
RC-BF-6-AQ-C	GC	LSF	Sa(1.5s)	0.526	0.365	0.71
	UPD	NPP	Sa(1.5s)	-2.261	0.388	1
RC-IF-6-AQ-C	GC	ML	Sa(0.5s)	1.498	0.670	0.75
	UPD	ML	Sa(0.5s)	-0.330	0.388	1
RC-PF-6-AQ-C	GC	LSF	Sa(0.5s)	1.479	0.754	0.75
	UPD	ML	Sa(0.5s)	-0.280	0.327	1
RC-SW-BF-9-AQ-C	GC	LSF	Sa(1.5s)	1.051	0.312	0.15
	UPD	LSF	Sa(1.5s)	-2.270	0.332	1
RC-SW-IF-9-AQ-C	GC	LSF	Sa(1.0s)	1.430	0.613	0.39
	UPD	LSF	Sa(1.0s)	-1.560	0.379	1

ID-building	Failure criteria	Curve fitting method	*IM*	η	β	*LFM*
RC-SW-PF-9-AQ-C	GC	LSF	Sa(1.0s)	1.555	0.577	0.30
	UPD	LSF	Sa(1.0s)	-1.714	0.423	1
RC-BF-3-MI-C	GC	ML	Sa(1.0s)	4.373	2.649	0.05
	UPD	LSF	Sa(1.0s)	-1.841	0.439	0.85
RC-IF-3-MI-C	GC	LSF	Sa(0.15s)	0.303	0.318	3.56E-05
	UPD	LSF	Sa(0.15s)	0.060	0.515	0.05
RC-PF-3-MI-C	GC	NPP	Sa(0.5s)	1.694	0.394	7.07E-09
	UPD	LSF	Sa(0.5s)	-0.508	0.354	0.34
RC-SW-BF-9-MI-C	GC	NPP	Sa(2.0s)	2.419	0.302	4.87E-48
	UPD	LSF	Sa(2.0s)	-2.373	0.160	0.90
RC-SW-IF-9-MI-C	GC	NPP	Sa(1.0s)	2.269	0.344	2.09E-13
	UPD	LSF	Sa(1.0s)	-1.140	0.249	0.25

ID-building	Failure criteria	Curve fitting method	*IM*	η	β	*LFM*
RC-SW-PF-9-MI-C	GC	NPP	Sa(1.0s)	0.490	0.208	3.62E-20
	UPD	LSF	Sa(1.0s)	-1.111	0.358	0.29
RC-BF-6-MI-C	GC	NPP	Sa(1.5s)	1.225	0.215	3.36E-44
	UPD	LSF	Sa(1.5s)	-2.442	0.207	1
RC-IF-6-MI-C	GC	LSF	Sa(0.5s)	0.400	0.309	1.09E-05
	UPD	LSF	Sa(0.5s)	-0.547	0.290	0.36
RC-PF-6-MI-C	GC	NPP	Sa(0.5s)	1.427	0.464	1.68E-05
	UPD	ML	Sa(0.5s)	-0.417	0.599	0.40
RC-BF-9-MI-C	GC	NPP	Sa(2.0s)	3.183	0.277	9.84E-42
	UPD	ML	Sa(2.0s)	-2.539	0.257	0.95
RC-IF-9-MI-C	GC	NPP	Sa(1.0s)	4.732	0.721	4.05E-13
	UPD	LSF	Sa(1.0s)	-1.417	0.186	0.73

ID-building	Failure criteria	Curve fitting method	*IM*	η	β	*LFM*
RC-PF-9-MI-C	GC	NPP	Sa(1.0s)	-0.162	0.143	1.06E-17
	UPD	LSF	Sa(1.0s)	-1.402	0.344	0.61
RC-BF-3-NA-C	GC	NPP	Sa(1.0s)	7.020	0.687	1.27E-11
	UPD	ML	Sa(1.0s)	-1.866	0.430	1
RC-IF-3-NA-C	GC	LSF	Sa(0.15s)	1.411	0.322	0.02
	UPD	NPP	Sa(0.15s)	-0.076	0.512	0.84
RC-PF-3-NA-C	GC	ML	Sa(0.5s)	3.441	1.367	0.05
	UPD	LSF	Sa(0.5s)	-0.511	0.437	0.99
RC-BF-6-NA-C	GC	NPP	Sa(1.5s)	1.498	0.357	9.94E-10
	UPD	ML	Sa(1.5s)	-2.262	0.362	1
RC-IF-6-NA-C	GC	LSF	Sa(0.5s)	1.329	0.235	0.01
	UPD	LSF	Sa(0.5s)	-1.108	0.494	1

ID-building	Failure criteria	Curve fitting method	*IM*	η	β	*LFM*
RC-PF-6-NA-C	GC	LSF	Sa(0.5s)	1.887	0.397	2.07E-03
	UPD	ML	Sa(0.5s)	-1.420	0.480	1
RC-BF-9-NA-C	GC	ML	Sa(2.0s)	4.343	2.462	0.05
	UPD	LSF	Sa(2.0s)	-2.757	0.355	1
RC-IF-9-NA-C	GC	ML	Sa(1.0s)	2.782	1.384	0.05
	UPD	ML	Sa(1.0s)	-1.507	0.160	1
RC-PF-9-NA-C	GC	ML	Sa(1.0s)	0.756	0.702	0.15
	UPD	LSF	Sa(1.0s)	-1.447	0.243	1
RC-SW-BF-9-NA-C	GC	NPP	Sa(1.5s)	1.530	0.185	1.11E-11
	UPD	LSF	Sa(1.5s)	-2.110	0.239	1
RC-SW-IF-9-NA-C	GC	NPP	Sa(1.0s)	8.298	0.653	1.51E-14
	UPD	LSF	Sa(1.0s)	-1.130	0.202	1

ID-building	Failure criteria	Curve fitting method	*IM*	η	β	*LFM*
RC-SW-PF-9-NA-C	GC	NPP	Sa(1.0s)	5.220	0.433	1.35E-16
	UPD	ML	Sa(1.0s)	-1.190	0.168	1
RC-MU-BF-6-NA-C	GC	NPP	Sa(1.5s)	1.585	0.509	4.03E-04
	UPD	NPP	Sa(1.5s)	-2.122	0.298	1
RC-MU-IF-6-NA-C	GC	NPP	Sa(0.5s)	2.621	0.770	4.25E-03
	UPD	LSF	Sa(0.5s)	-0.890	0.667	0.98
RC-MU-PF-6-NA-C	GC	LSF	Sa(0.5s)	6.187	2.115	4.67E-03
	UPD	NPP	Sa(0.5s)	-0.436	0.600	0.98
RC-SSI-SW-BF-9-NA-C	GC	LSF	Sa(1.0s)	4.117	1.394	2.22E-04
	UPD	ML	Sa(1.0s)	-2.679	0.549	1
RC-SSI-SW-IF-9-NA-C	GC	LSF	Sa(1.0s)	4.003	1.459	9.25E-04
	UPD	ML	Sa(1.0s)	-2.180	0.270	1

ID-building	Failure criteria	Curve fitting method	*IM*	η	β	*LFM*
RC-SSI-SW-PF-9-NA-C	GC	LSF	Sa(1.0s)	3.062	1.108	4.13E-04
	UPD	ML	Sa(1.0s)	-2.283	0.241	1

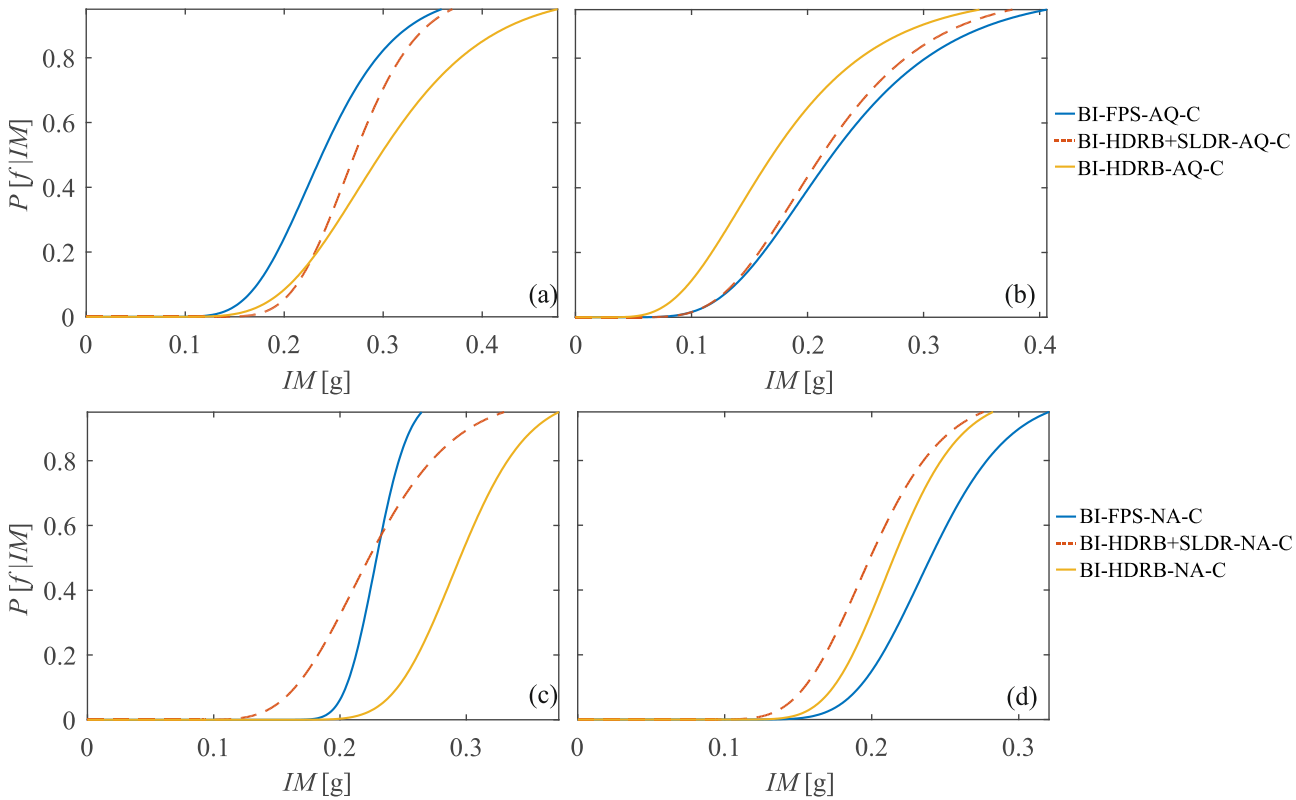

Figure 66. Fragility curves for BI buildings. Figures show curves for L'Aquila (a,b) and Naples (c,d) at GC (left) and UPD (right), respectively.

*Table 19. BI buildings. *D= means that fragility parameters are been manually evaluated, without numerical procedure. For uncertainty estimation, fragility function for each sample has been evaluated by means LSF method*

ID-building	Failure criteria	Curve fitting method	*IM*	η	β	*LFM*
BI-FPS-AQ-C	GC	ML	Sa(3.0s)	-1.435	0.250	1
	UPD	ML	Sa(3.0s)	-1.510	0.370	1
BI-FPS- NA-C	GC	LSF	Sa(3.0s)	-1.474	0.088	1
	UPD	LSF	Sa(3.0s)	-1.427	0.176	0.98
BI-HDRB+SLDR-AQ-C	GC	ML	Sa(3.0s)	-1.306	0.189	1
	UPD	ML	Sa(3.0s)	-1.551	0.349	1
BI-HDRB+SLDR-NA-C	GC	ML	Sa(3.0s)	-1.501	0.238	1
	UPD	ML	Sa(3.0s)	-1.614	0.199	1
BI-HDRB-AQ-C	GC	ML	Sa(3.0s)	-1.214	0.287	1
	UPD	ML	Sa(3.0s)	-1.774	0.437	1

ID-building	Failure criteria	Curve fitting method	*IM*	η	β	*LFM*
BI-HDRB-NA-C	GC	D*	Sa(3.0s)	-1.221	0.143	0.90
	UPD	ML	Sa(3.0s)	-1.537	0.166	1

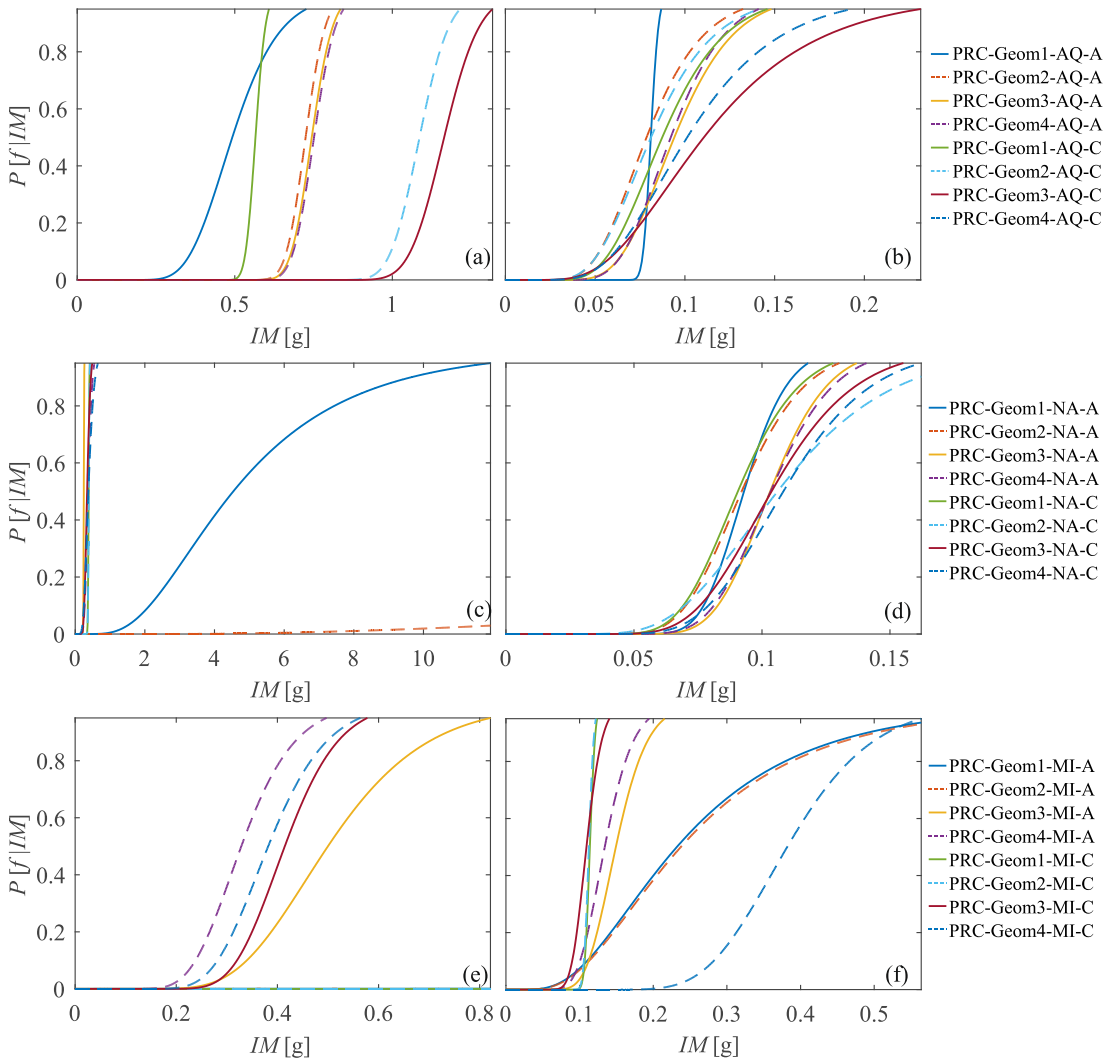
P [f |IM]
IM [g]
(a)
(b)
(c)
(d)
(e)
(f)
PRC-Geom1-AQ-A
PRC-Geom2-AQ-A
PRC-Geom3-AQ-A
PRC-Geom4-AQ-A
PRC-Geom1-AQ-C
PRC-Geom2-AQ-C
PRC-Geom3-AQ-C
PRC-Geom4-AQ-C
PRC-Geom1-NA-A
PRC-Geom2-NA-A
PRC-Geom3-NA-A
PRC-Geom4-NA-A
PRC-Geom1-NA-C
PRC-Geom2-NA-C
PRC-Geom3-NA-C
PRC-Geom4-NA-C
PRC-Geom1-MI-A
PRC-Geom2-MI-A
PRC-Geom3-MI-A
PRC-Geom4-MI-A
PRC-Geom1-MI-C
PRC-Geom2-MI-C
PRC-Geom3-MI-C
PRC-Geom4-MI-C

Figure 67. Fragility curves for PRC buildings. Figures show curves for L'Aquila (a,b), Naples (c,d) and Milan (e,f) at GC and UPD respectively.

Table 20. PRC building. CoV_{λ_f} = NaN means that resampling procedure does not provide results. This may happen when collapses/failures occur only for few records in a single stripe.

ID-building	**Failure criteria**	**Curve fitting method**	***IM***	η	β	***LFM***
PRC-Geom1-AQ-A	GC	ML	Sa(2.0s)	-0.709	0.237	0.95
	UPD	ML	Sa(2.0s)	-2.513	0.042	1
PRC-Geom2-AQ-A	GC	ML	Sa(2.0s)	-0.322	0.068	0.55
	UPD	ML	Sa(2.0s)	-2.543	0.317	1
PRC-Geom3-AQ-A	GC	ML	Sa(2.0s)	-0.295	0.071	0.40
	UPD	ML	Sa(2.0s)	-2.363	0.276	1
PRC-Geom4-AQ-A	GC	ML	Sa(2.0s)	-0.286	0.072	0.35
	UPD	ML	Sa(2.0s)	-2.385	0.259	1
PRC-Geom1-AQ-C	GC	ML	Sa(2.0s)	-0.570	0.044	1

ID-building	Failure criteria	Curve fitting method	*IM*	η	β	*LFM*
	UPD	ML	Sa(2.0s)	-2.438	0.312	1
PRC-Geom2-AQ-C	GC	ML	Sa(2.0s)	0.083	0.068	0.45
	UPD	ML	Sa(2.0s)	-2.512	0.338	1
PRC-Geom3-AQ-C	GC	ML	Sa(2.0s)	0.152	0.075	0.15
	UPD	ML	Sa(2.0s)	-2.202	0.449	1
PRC-Geom4-AQ-C	GC	ML	Sa(2.0s)	0.083	0.068	0.45
	UPD	ML	Sa(2.0s)	-2.290	0.392	1
PRC-Geom1-MI-A	GC	LSF	Sa(2.0s)	22.780	7.167	1.69E-14
	UPD	LSF	Sa(2.0s)	-1.461	0.582	0.02
PRC-Geom2-MI-A	GC	LSF	Sa(2.0s)	22.780	7.167	3.30E-14
	UPD	LSF	Sa(2.0s)	-1.438	0.582	0.02
PRC-Geom3-MI-A	GC	NPP	Sa(2.0s)	-0.195	0.265	4.02E-19

ID-building	Failure criteria	Curve fitting method	*IM*	η	β	*LFM*
	UPD	LSF	Sa(2.0s)	-1.902	0.223	6.44E-04
PRC-Geom4-MI-A	GC	NPP	Sa(2.0s)	-1.113	0.251	7.94E-09
	UPD	LSF	Sa(2.0s)	-2.009	0.225	3.45E-03
PRC-Geom1-MI-C	GC	NPP	Sa(2.0s)	13.283	1.749	3.95E-10
	UPD	ML	Sa(2.0s)	-2.172	0.050	0.50
PRC-Geom2-MI-C	GC	NPP	Sa(2.0s)	3.544	0.705	7.11E-12
	UPD	ML	Sa(2.0s)	-2.184	0.049	0.60
PRC-Geom3-MI-C	GC	NPP	Sa(2.0s)	-0.880	0.202	4.41E-06
	UPD	NPP	Sa(2.0s)	-2.213	0.152	0.69
PRC-Geom4-MI-C	GC	NPP	Sa(2.0s)	-0.963	0.237	2.54E-05
	UPD	LSF	Sa(2.0s)	-0.963	0.237	2.56E-05
PRC-Geom1-NA-A	GC	NPP	Sa(2.0s)	1.513	0.587	0.04

ID-building	Failure criteria	Curve fitting method	*IM*	η	β	*LFM*
	UPD	ML	Sa(2.0s)	-2.375	0.145	1
PRC-Geom2-NA-A	GC	NPP	Sa(2.0s)	4.296	0.962	7.96E-08
	UPD	ML	Sa(2.0s)	-2.385	0.211	1
PRC-Geom3-NA-A	GC	ML	Sa(2.0s)	-1.401	0.042	0.90
	UPD	ML	Sa(2.0s)	-2.271	0.172	1
PRC-Geom4-NA-A	GC	NPP	Sa(2.0s)	-0.994	0.241	1.03E-04
	UPD	ML	Sa(2.0s)	-2.269	0.188	1
PRC-Geom1-NA-C	GC	ML	Sa(2.0s)	-0.951	0.046	0.45
	UPD	ML	Sa(2.0s)	-2.402	0.209	1
PRC-Geom2-NA-C	GC	ML	Sa(2.0s)	-0.939	0.047	0.35
	UPD	ML	Sa(2.0s)	-2.244	0.327	1
PRC-Geom3-NA-C	GC	NPP	Sa(2.0s)	-1.071	0.216	0.04

ID-building	Failure criteria	Curve fitting method	*IM*	η	β	*LFM*
PRC-Geom4-NA-C	UPD	ML	Sa(2.0s)	-2.266	0.245	1
	GC	NPP	Sa(2.0s)	-0.970	0.328	0.09
	UPD	ML	Sa(2.0s)	-2.222	0.245	1

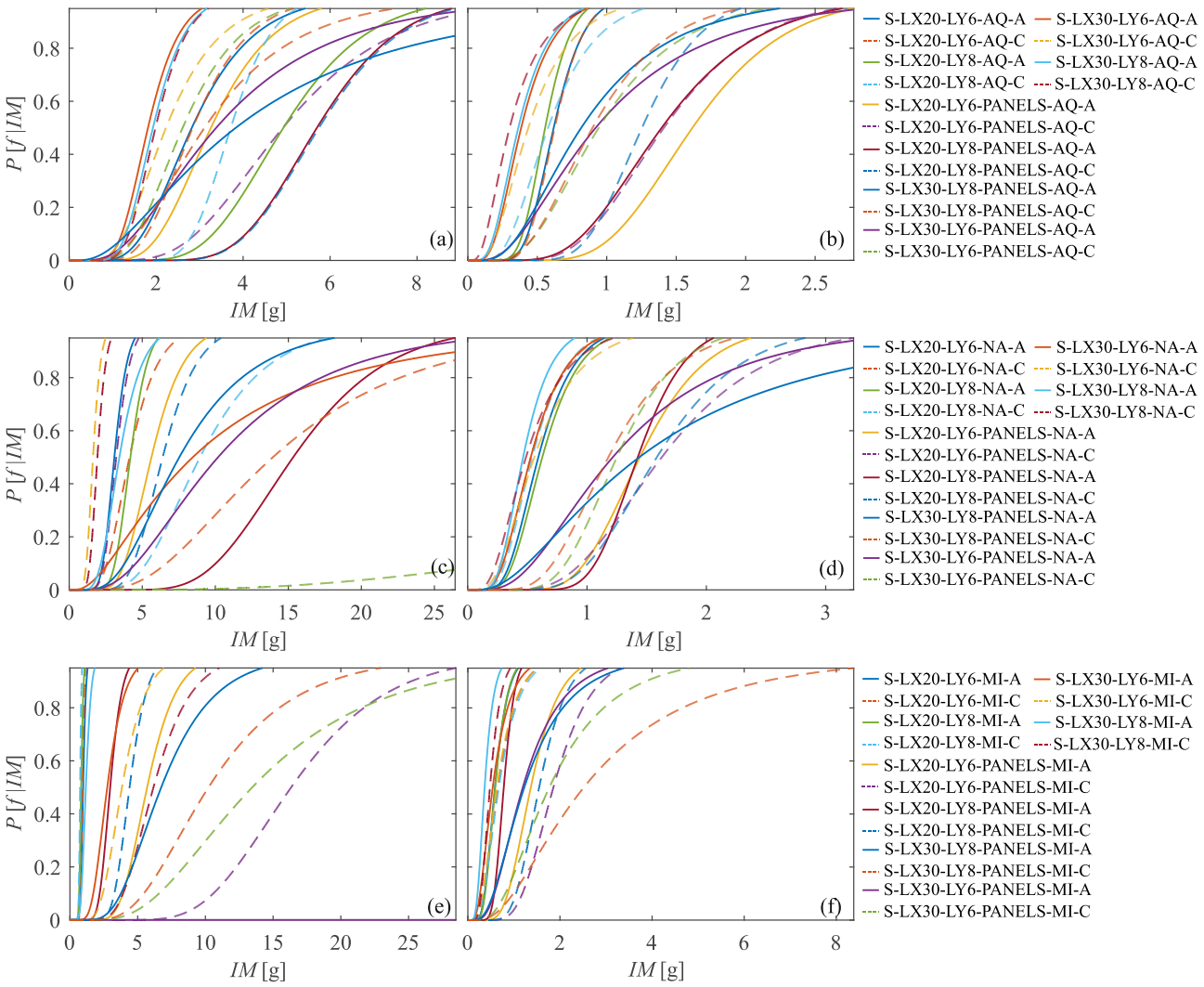
P [f |IM]
IM [g]
(a)
(b)
(c)
(d)
(e)
(f)
S-LX20-LY6-AQ-A
S-LX30-LY6-AQ-A
S-LX20-LY6-AQ-C
S-LX30-LY6-AQ-C
S-LX20-LY8-AQ-A
S-LX30-LY8-AQ-A
S-LX20-LY8-AQ-C
S-LX30-LY8-AQ-C
S-LX20-LY6-PANELS-AQ-A
S-LX20-LY6-PANELS-AQ-C
S-LX20-LY8-PANELS-AQ-A
S-LX20-LY8-PANELS-AQ-C
S-LX30-LY8-PANELS-AQ-A
S-LX30-LY8-PANELS-AQ-C
S-LX30-LY6-PANELS-AQ-A
S-LX30-LY6-PANELS-AQ-C
S-LX20-LY6-NA-A
S-LX30-LY6-NA-A
S-LX20-LY6-NA-C
S-LX30-LY6-NA-C
S-LX20-LY8-NA-A
S-LX30-LY8-NA-A
S-LX20-LY8-NA-C
S-LX30-LY8-NA-C
S-LX20-LY6-PANELS-NA-A
S-LX20-LY6-PANELS-NA-C
S-LX20-LY8-PANELS-NA-A
S-LX20-LY8-PANELS-NA-C
S-LX30-LY8-PANELS-NA-A
S-LX30-LY8-PANELS-NA-C
S-LX30-LY6-PANELS-NA-A
S-LX30-LY6-PANELS-NA-C
S-LX20-LY6-MI-A
S-LX30-LY6-MI-A
S-LX20-LY6-MI-C
S-LX30-LY6-MI-C
S-LX20-LY8-MI-A
S-LX30-LY8-MI-A
S-LX20-LY8-MI-C
S-LX30-LY8-MI-C
S-LX20-LY6-PANELS-MI-A
S-LX20-LY6-PANELS-MI-C
S-LX20-LY8-PANELS-MI-A
S-LX20-LY8-PANELS-MI-C
S-LX30-LY8-PANELS-MI-A
S-LX30-LY8-PANELS-MI-C
S-LX30-LY6-PANELS-MI-A
S-LX30-LY6-PANELS-MI-C

Figure 68. Fragility curves for steel buildings. Figures show curves for L'Aquila (a,b), Naples (c,d) and Milan (e,f) at GC and UPD respectively.

Table 21. S buildings.

ID-building	Failure criteria	Curve fitting method	*IM*	η	β	*LFM*
S-LX20-LY6-AQ-A	GC	LSF	Sa(0.5s)	1.037	0.398	0.88
	UPD	LSF	Sa(0.5s)	-0.481	0.280	1
S-LX20-LY6-AQ-C	GC	LSF	Sa(0.5s)	1.043	0.362	0.96
	UPD	LSF	Sa(0.5s)	-0.470	0.269	1
S-LX20-LY6-MI-A	GC	LSF	Sa(0.5s)	-0.027	0.179	8.20E-16
	UPD	LSF	Sa(0.5s)	-0.530	0.375	0.06
S-LX20-LY6-MI-C	GC	LSF	Sa(0.5s)	-0.081	0.131	1.24E-14
	UPD	LSF	Sa(0.5s)	-0.431	0.514	0.33
S-LX20-LY6-NA-A	GC	LSF	Sa(0.5s)	1.129	0.231	3.35E-04

	UPD	LSF	Sa(0.5s)	-0.524	0.401	0.96
S-LX20-LY6-NA-C	GC	LSF	Sa(0.5s)	1.418	0.368	0.03
	UPD	LSF	Sa(0.5s)	-0.634	0.456	1
S-LX20-LY6-PANELS-AQ-A	GC	LSF	Sa(0.5s)	1.181	0.351	0.87
	UPD	LSF	Sa(0.5s)	0.480	0.329	1
S-LX20-LY6-PANELS-AQ-C	GC	LSF	Sa(0.5s)	1.592	0.408	0.86
	UPD	LSF	Sa(0.5s)	0.344	0.385	1
S-LX20-LY6-PANELS-MI-A	GC	LSF	Sa(0.5s)	1.741	0.296	3.59E-23
	UPD	LSF	Sa(0.5s)	0.313	0.356	3.91E-06
S-LX20-LY6-PANELS-MI-C	GC	LSF	Sa(0.5s)	2.793	0.338	5.46E-27
	UPD	LSF	Sa(0.5s)	0.619	0.351	1.01E-04
S-LX20-LY6-PANELS-NA-A	GC	LSF	Sa(0.5s)	1.728	0.311	5.28E-05
	UPD	LSF	Sa(0.5s)	0.367	0.302	0.47
	GC	LSF	Sa(0.5s)	1.169	0.239	0.04

S-LX20-LY6-PANELS-NA-C	UPD	LSF	Sa(0.5s)	0.486	0.418	0.76
S-LX20-LY8-AQ-A	GC	LSF	Sa(0.5s)	1.594	0.310	0.47
	UPD	LSF	Sa(0.5s)	-0.587	0.270	1
S-LX20-LY8-AQ-C	GC	LSF	Sa(0.5s)	1.312	0.209	0.98
	UPD	LSF	Sa(0.5s)	-0.549	0.479	1
S-LX20-LY8-MI-A	GC	LSF	Sa(0.5s)	-0.184	0.160	4.09E-16
	UPD	LSF	Sa(0.5s)	-0.522	0.360	0.05
S-LX20-LY8-MI-C	GC	LSF	Sa(0.5s)	-0.285	0.108	2.72E-13
	UPD	LSF	Sa(0.5s)	-0.398	0.520	0.31
S-LX20-LY8-NA-A	GC	LSF	Sa(0.5s)	1.433	0.229	7.33E-08
	UPD	LSF	Sa(0.5s)	-0.469	0.393	1
S-LX20-LY8-NA-C	GC	LSF	Sa(0.5s)	2.192	0.413	1.42E-05
	UPD	LSF	Sa(0.5s)	-0.614	0.427	1

S-LX20-LY8-PANELS-AQ-A	GC	LSF	Sa(0.5s)	1.740	0.264	0.27
	UPD	LSF	Sa(0.5s)	0.333	0.400	1
S-LX20-LY8-PANELS-AQ-C	GC	LSF	Sa(0.5s)	1.748	0.265	0.86
	UPD	LSF	Sa(0.5s)	0.226	0.273	1
S-LX20-LY8-PANELS-MI-A	GC	LSF	Sa(0.5s)	1.089	0.236	2.03E-21
	UPD	LSF	Sa(0.5s)	-0.248	0.244	2.86E-05
S-LX20-LY8-PANELS-MI-C	GC	LSF	Sa(0.5s)	1.482	0.230	1.20E-29
	UPD	LSF	Sa(0.5s)	0.437	0.306	1.84E-05
S-LX20-LY8-PANELS-NA-A	GC	LSF	Sa(0.5s)	2.730	0.331	6.66E-07
	UPD	LSF	Sa(0.5s)	0.354	0.224	0.48
S-LX20-LY8-PANELS-NA-C	GC	LSF	Sa(0.5s)	1.856	0.295	1.51E-05
	UPD	LSF	Sa(0.5s)	0.461	0.352	0.82
S-LX30-LY6-AQ-A	GC	LSF	Sa(1.0s)	0.594	0.317	0.69
	UPD	LSF	Sa(1.0s)	-0.958	0.487	1

S-LX30-LY6-AQ-C	GC	LSF	Sa(1.0s)	0.800	0.439	0.85
	UPD	LSF	Sa(1.0s)	-0.831	0.569	1
S-LX30-LY6-MI-A	GC	LSF	Sa(1.0s)	1.013	0.366	1.60E-15
	UPD	LSF	Sa(1.0s)	-0.615	0.556	0.02
S-LX30-LY6-MI-C	GC	LSF	Sa(1.0s)	1.346	0.359	1.70E-12
	UPD	LSF	Sa(1.0s)	-0.460	0.533	0.06
S-LX30-LY6-NA-A	GC	LSF	Sa(1.0s)	2.135	0.902	2.24E-03
	UPD	LSF	Sa(1.0s)	-0.637	0.452	0.70
S-LX30-LY6-NA-C	GC	LSF	Sa(1.0s)	0.489	0.258	0.05
	UPD	LSF	Sa(1.0s)	-0.583	0.551	0.93
S-LX30-LY6-PANELS-AQ-A	GC	LSF	Sa(1.0s)	1.218	0.628	0.23
	UPD	LSF	Sa(1.0s)	-0.083	0.690	0.90
S-LX30-LY6-PANELS-AQ-C	GC	LSF	Sa(1.0s)	0.959	0.404	0.77
	UPD	LSF	Sa(1.0s)	-0.060	0.504	1

S-LX30-LY6-PANELS-MI-A	GC	LSF	Sa(1.0s)	8.573	1.176	7.62E-17
	UPD	LSF	Sa(1.0s)	0.176	0.569	1.81E-04
S-LX30-LY6-PANELS-MI-C	GC	LSF	Sa(1.0s)	2.600	0.558	2.65E-12
	UPD	LSF	Sa(1.0s)	0.570	0.608	9.99E-04
S-LX30-LY6-PANELS-NA-A	GC	LSF	Sa(1.0s)	2.321	0.625	1.92E-03
	UPD	LSF	Sa(1.0s)	0.195	0.630	0.17
S-LX30-LY6-PANELS-NA-C	GC	LSF	Sa(1.0s)	4.400	0.785	4.86E-03
	UPD	LSF	Sa(1.0s)	0.223	0.328	0.30
S-LX30-LY8-AQ-A	GC	LSF	Sa(1.0s)	0.656	0.304	0.62
	UPD	LSF	Sa(1.0s)	-1.013	0.505	1
S-LX30-LY8-AQ-C	GC	LSF	Sa(1.0s)	0.686	0.291	0.99
	UPD	LSF	Sa(1.0s)	-1.201	0.646	1
S-LX30-LY8-MI-A	GC	LSF	Sa(1.0s)	0.162	0.268	1.45E-12
	UPD	LSF	Sa(1.0s)	-19	0.428	0.03

S-LX30-LY8-MI-C	GC	LSF	Sa(1.0s)	1.819	0.353	6.20E-15
	UPD	LSF	Sa(1.0s)	-0.733	0.397	0.07
S-LX30-LY8-NA-A	GC	LSF	Sa(1.0s)	1.234	0.360	3.08E-04
	UPD	LSF	Sa(1.0s)	-0.766	0.400	0.82
S-LX30-LY8-NA-C	GC	LSF	Sa(1.0s)	0.659	0.246	0.01
	UPD	LSF	Sa(1.0s)	-0.716	0.560	0.95
S-LX30-LY8-PANELS-AQ-A	GC	LSF	Sa(1.0s)	1.343	0.821	0.23
	UPD	LSF	Sa(1.0s)	-0.203	0.615	0.98
S-LX30-LY8-PANELS-AQ-C	GC	LSF	Sa(1.0s)	1.135	0.534	0.59
	UPD	LSF	Sa(1.0s)	-0.108	0.475	1
S-LX30-LY8-PANELS-MI-A	GC	LSF	Sa(1.0s)	1.908	0.454	5.63E-18
	UPD	LSF	Sa(1.0s)	0.203	0.619	4.30E-04
S-LX30-LY8-PANELS-MI-C	GC	LSF	Sa(1.0s)	2.325	0.491	4.22E-14
	UPD	LSF	Sa(1.0s)	0.923	0.731	1.12E-03

S-LX30-LY8-PANELS-NA-A	GC	LSF	Sa(1.0s)	2.020	0.534	1.44E-04
	UPD	LSF	Sa(1.0s)	0.363	0.821	0.16
S-LX30-LY8-PANELS-NA-C	GC	LSF	Sa(1.0s)	2.635	0.577	1.96E-03
	UPD	LSF	Sa(1.0s)	0.165	0.392	0.39

Fitted lognormal fragility curves show a large parameter variability for structures belonging to the same structural typology at the same site (e.g., RC). This partly depends on the fact that these curves are poorly constrained by non-linear dynamic analysis results (in turn, a question may arise about the curves' usability in seismic risk evaluation, which is discussed in the following section). More specifically, defining the lumped fragility values as $P\left[f \left| IM = im_i \right. \right] = N_{f,IM=im_i} / N_{tot}$ (i.e., *empirical percentiles* according to the terminology used in Chapter 3), past research (e.g., [55]) has shown that some issue may occur when the *IM* levels at which $P\left[f \left| IM = im \right. \right]$ are evaluated, discretize in some manner the *IM* domain. Intuitively, the fragility curve is best constrained when the *IM* discretization at which dynamic analysis is performed gives a large and densely populated range of $P\left[f \left| IM = im \right. \right]$ from 0% to 100%. The fixed *IM* levels adopted in the RINTC project lead to a series of situations that can be summarized by those sketched in Figure 69, where the lumped fragility values are plotted against the result of the fitting procedure obtained via ML method (black solid line) for four among all the buildings examined so far, chosen as paradigm to deepen different situations in which fragility fitting has been performed.

The level of constraint to the fragility can be quantified by the estimation uncertainty of the fragility parameters. To this end, given the lumped fragility values from dynamic analysis, procedure above described, performed $k = 500$ times, has been applied (grey solid line in Figure 69 represents the *k* parametric resampling) and the root mean square error of the sample standard deviation of the fragility curves, given that β_i^* is the lognormal standard deviation from *i-th* simulation, evaluated as:

$$RMSE = \sqrt{\frac{\sum_{i=1}^{k} \left(\frac{\beta_i^* - \beta}{\beta} \right)^2}{k}}, i = 1,2,...,500 . \quad (51)$$

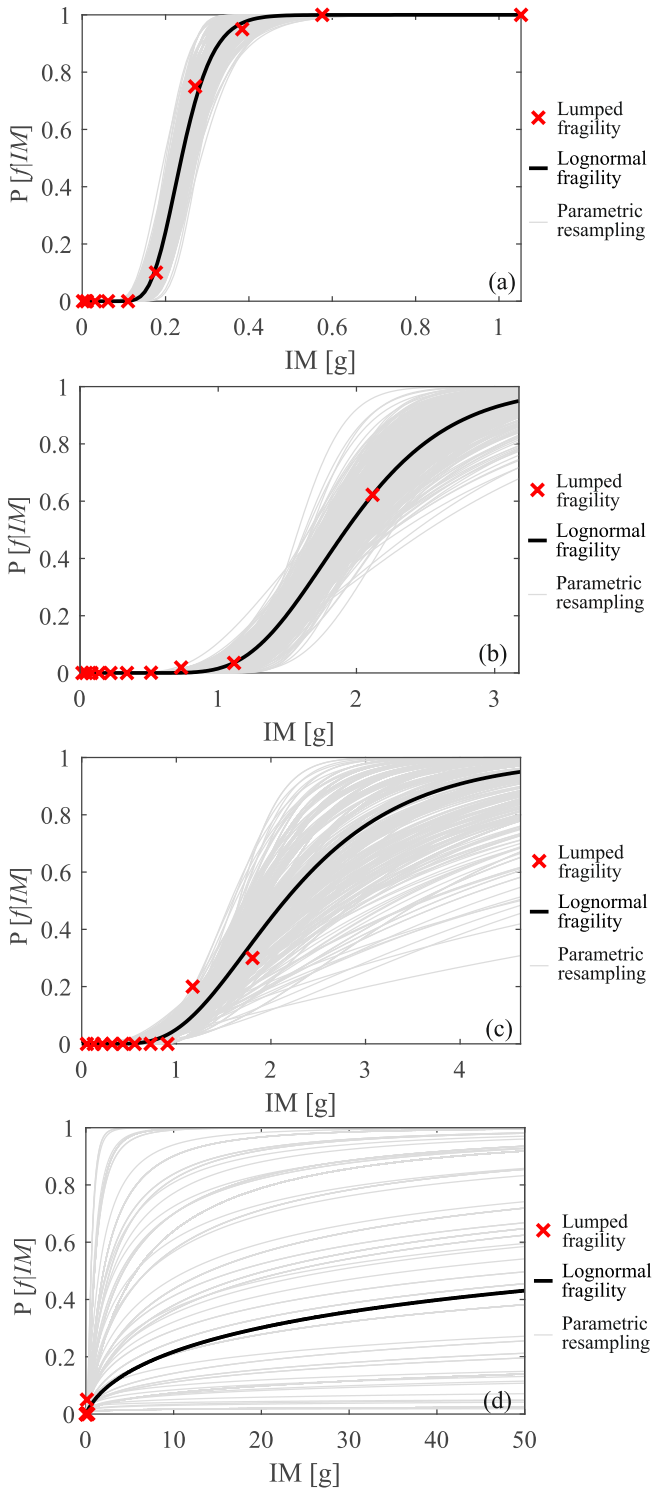
P [f|IM]
IM [g]
(a)
(b)
(c)
(d)
Lumped fragility
Lognormal fragility
Parametric resampling

Figure 69. Fragility curves and parametric resampling for four different buildings exhibiting different LFM: 1 (a), 0.60 (b), 0.30 (c) and 0.05 (d).

Defining the maximum values of the lumped fragility (from now on *LFM*) as: $LFM = \max\left(P\left[\, f \,|IM = im_i \,\right]\right), i = 1,2,...,10$, where im_i is the intensity corresponding to an exceedance return period of 10^5 years at the site of interest, allows to identify different situations/issues:

- $LFM \approx 1$ means that in one of the ten stripes at least, all the records applied to the structure lead to failure and/or collapse. Capacity of the fragility fitting is considered well constrained, being that the black curve is well anchored to the empirical data (i.e., MSA results). As a reference, *RMSE* is equal to 0.18 (Figure 69a).
- $LFM = 0.60$ means that the data from dynamic analysis are available up to *IM* levels slightly above the median. Fragility fitting continues to well represent the trend of the empirical data, but the estimation uncertainty increases with *RMSE* equal to 0.21, three times greater than the previous case (Figure 69b).
- $LFM = 0.30$ means that empirical data are available up to *IM* level lower than the median. Curve fitting is somewhat getting worse and estimation uncertainty greatly increases with a *RMSE* equal to 0.32 which means that heterogeneity of the parametric resampling around the black solid line significantly increases (Figure 69c).
- $LFM = 0.05$ means that no failures and/or collapses occur in nine over ten stripes and only one failure occurs in the remaining stripe. Fragility curve is extrapolated for $P\left[\, f \,|IM = im\right]$ values greater than 0.05, therefore uncertainty in parameters estimation is very high with *RMSE* equal to 1.30 (Figure 69d).

Summarizing what observed, when *LFM* decreases, the heterogeneity of the parametric resampling around the black solid line increases, meaning that the uncertainty in lognormal parameters estimation rises. For this reason, *RMSE* increases when *LFM* decreases, showing that, as expected, the estimation of the lognormal parameters gets worse when *LFM* is not high enough to warrant that the fitted curve is well constrained by lumped fragility values. Analogous considerations could be made even if the others curve fitting methods (LSF and NPP) were used to estimate fragility parameters and parametric resampling,

taking care to evaluate, in that case, $P\left[f \left| IM = im \right. \right]$ according to the second Equation (44) and not as $N_{f,IM=im_i} / N_{tot}$. *LFM*, for all the structures, is listed from Table 17 to Table 21.

As it could be expected from the conclusion obtained within RINTC project, fragility curves for structures designed in the low-seismicity area are most likely to exhibit results affected by high estimation uncertainty because of the low number of failure cases for each *IM*-stripe. Conversely, this issue more rarely occurs for the structures designed on high-seismicity area (see also [154]). These fitting issues could be possibly addressed by using a larger number of records for each stripe (instead of the twenty here used) and/or increasing the number of return periods at which the *IM* stripes are evaluated, but this is not the focus of the study herein presented, which is based on the results of the RINTC project.

In all the figures, where fragility curves show large parameters variability, in particular large values of the parameter β , the case is similar to those described in Figure 69c and d. Lower is LFM, more fragility curves are unsuitable to well represent structural behavior, being results with $LFM < 0.50$ to be handled carefully. Some detailed observation can be worth discussing.

- At GC, fragility curves for the structures designed in the low-hazard site show relatively large estimation uncertainty of parameters linked to the low number of structural failures. This happens for all the structural typology (BI buildings have not been designed in Milan). Among the others, this occurs for the three-storey, bare frame, RC building sites in Milan on soil C (*RC-BF-3-MI-C*), the S building sited in Milan on soil A identified as *S-LX30-LY6-PANELS-MI-A*, the PRC building having ID *PRC-Geom4-MI-C* and the URM building *URM-C1-2-MI-A*. In these cases, fragility fitting issues are the same as those shown in Figure 69c,d.
- At GC, fragility curves for the structures designed in the mid-hazard site show similar fitting issues except for most of URM buildings and BI buildings (with few structures). This happens, that is, for the RC building *RC-SW-PF-9-NA-C*, for the S building *S-LX30-LY6-PANELS-NA-C* and for the PRC building *PRC-Geom2-NA-A*. The global trend of the results is not clearly defined, this means that all the possible cases described in Figure 69 are encountered. All the RC buildings, except

the case *RC-9-PF-NA-C* having $LFM = 0.15$, and S buildings have $LFM \leq 0.05$, falling into the case described in Figure 69d. All the BI buildings have $LFM = 1$, reflecting the situation described in Figure 69a. URM buildings spread within a range from $LFM = 0.27$ and $LFM = 1$.

- At GC, fragility curves for structures designed in the high-hazard site seem to provide more constrained results for all the typologies except for PRC buildings, where five over eight cases show $LFM < 0.50$. Most of the buildings fall into the situation depicted in Figure 69a and b, that is, RC building *RC-6-PF-AQ-C*, PRC-building *PRC-Geom1-AQ-A*, URM building *URM-I1-2-AQ-C*, S building *S-LX30-LY8-AQ-C*, and BI building *BI-FPS-NTC08-AQ-C*.
- Such considerations can be extended to the results at UPD, with a global reduction of the estimation uncertainty due to the increasing of failure cases which leads to the increasing of *LFM* (see from Table 17 to Table 21 for details).

The estimation uncertainty produced by the lognormal distribution fitting procedure of the empirical data, is not necessarily propagated to the failure rate (see the next section). This can be explained because the *IM* levels more relevant for estimating failure rate are located toward the left tail of the fragility function and this is due to typical shape of hazard curves. For this reason, when quantifying the rate of collapse is the goal, it is more relevant the accurate estimation of the left side of the fragility function than the right side.

5.4.2 Curves' validation and applicability

In fact, to validate the obtained fragility curves with respect to the failure rates computed in the RINTC project, the rates were also computed using the fitted curves, that is via the following equation:

$$\lambda_f(\eta,\beta) = \int_{IM} \Phi\left[\frac{\log(im)-\eta}{\beta}\right] \cdot \left|d\lambda_{im}\right|. \tag{52}$$

To integrate hazard curves in a *IM* range larger than those considered in the RINTC project (i.e., return period up to 10,000 years) probabilistic seismic hazard analysis was performed again via REASSESS software [103] for the sites in terms the spectral accelerations at the periods at which the curves have been developed (0.15s, 0.50s, 1s, 1.5s, 2s and 3s) on soil conditions A and C. The seismic zone source model, magnitude distribution and rates and ground

motion prediction equations are the same described before and the resulting curves are shown in Figure 70.

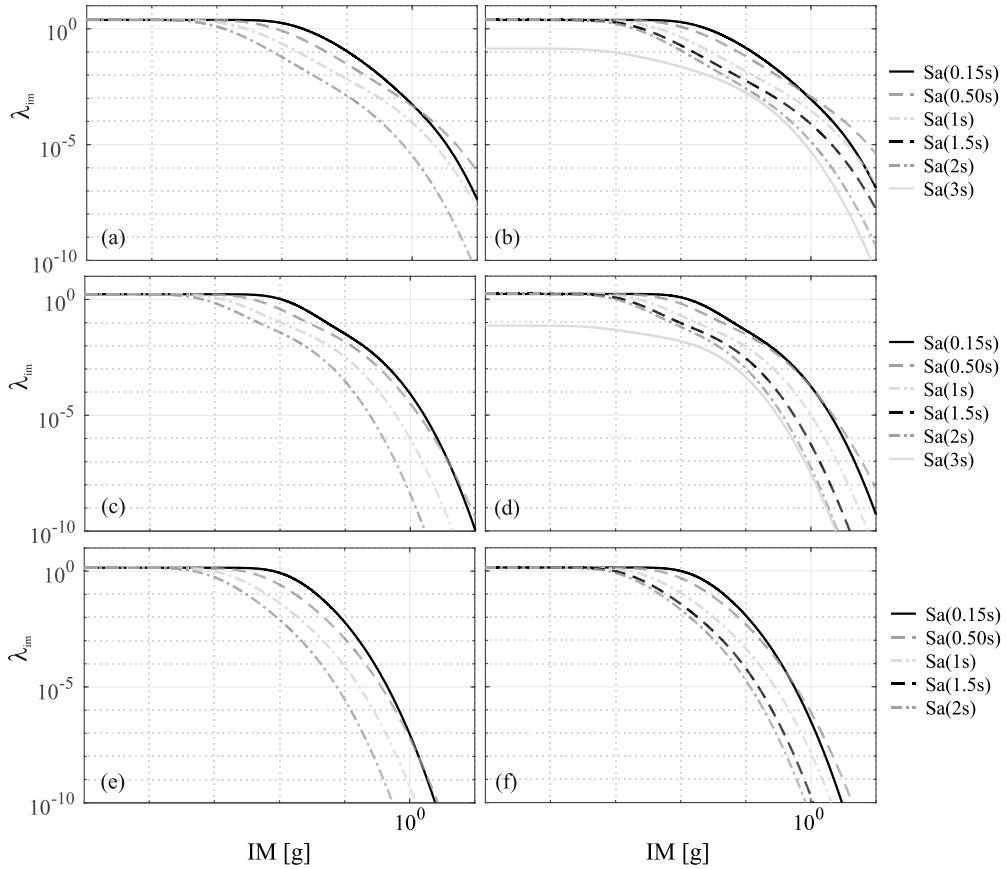

Figure 70. Hazard curves for soil condition A and C respectively for L'Aquila (a,b), Naples (c,d) and Milan (e,f).

Combining the fragility curves shown from Figure 64 to Figure 68 with the relevant hazard curves among those shown in Figure 70, Equation (52) provides the failure rates shown in Figure 71a,c for GC and UPD. Apparently, looking at Figure 71, where colors identify different buildings within the same structural typology, there is a general coherency with the results of the RINTC project (Figure 71b,d) and the rates computed via the fitted fragility. Differences among the procedures occur when no or quite few failure cases from dynamic analysis are observed (e.g., for structures designed at low-to-mid seismicity) up to the largest *IM*s, this impels that the fragility fitting issues, already discussed, arise: estimates of the lognormal fragility parameters could be particularly

uncertain. As an example, evaluation of the rate of failure at GC for a RC structure site in Milan, identified with the ID *RC-BF-3-MI-C* (gray circle in Figure 71a,b), is deepened: it is equal to 1.19×10^{-4} when lognormal fragility is considered while it is equal to 1.00×10^{-5} using RINTC procedure; i.e., Equation (44). Structural responses do not exhibit any failure cases and only one collapse case at eighth stripe with a probability of failure $P\left[f \left| IM = im \right. \right]$ equal to zero for each *IM* value except for $IM = 0.123g$ where it is equal to 0.05 (one over twenty). Figure 72a shows lumped fragility values $P\left[f \left| IM = im \right. \right]$, lognormal fragility and hazard curve (right vertical axis). The difference of one order of magnitude of the failure between two procedures is caused by the lognormal fragility fit which gives values of probability of failure different from zero at low levels of *IM* where the hazard magnitude is more relevant. Figure 72b shows the impact of the specific *IM*-level contribution to the failure rate evaluation.[10]

[10] Differences among failure rates of BI buildings designed in L'Aquila are not strictly related to fragility fitting, yet by the hazard curves used for the validation, which are not exactly those of the RINTC original study.

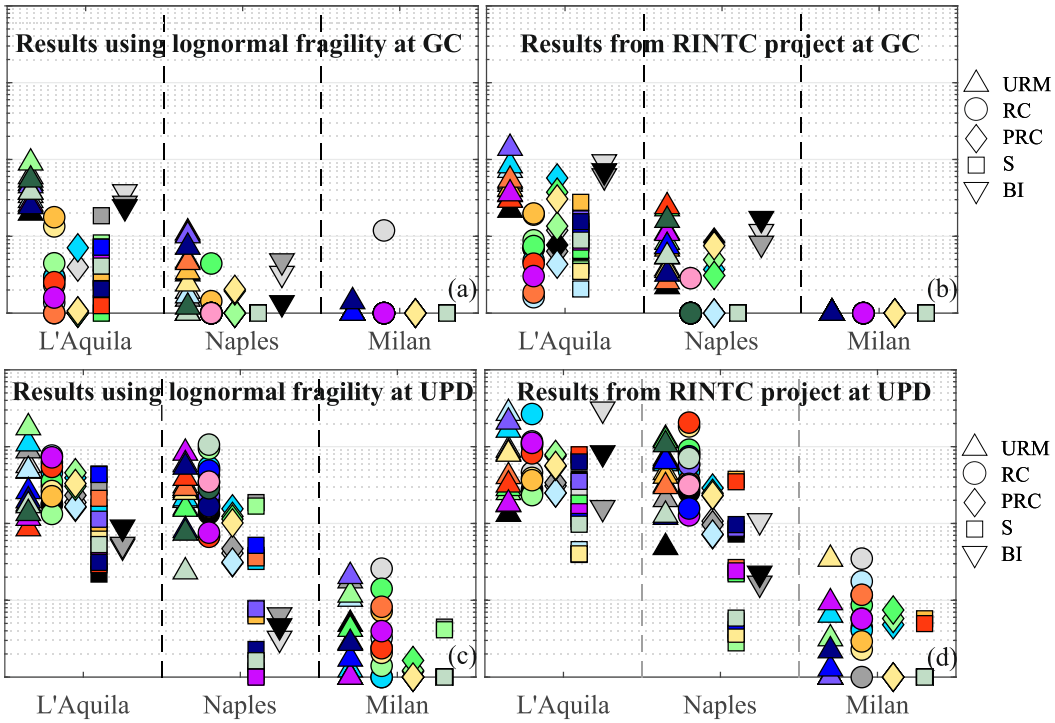

Figure 71. Failure rates evaluated by means of lognormal fragility curves for GC (a) and UPD (c) and using the procedure implemented in RINTC project for GC (b) and UPD (d). Colors represent different buildings in each typology.

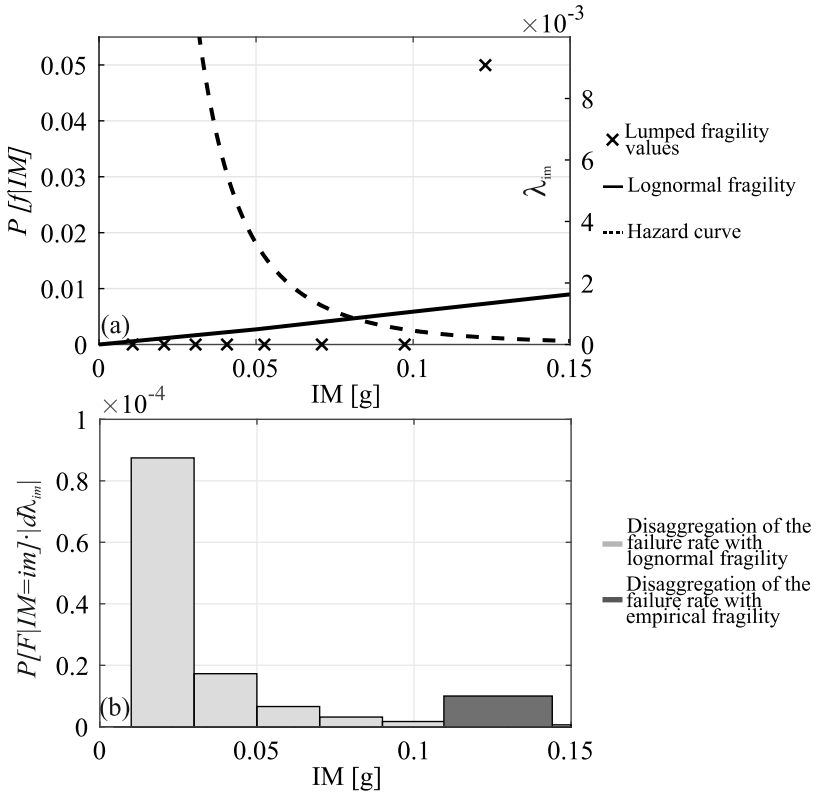

Figure 72. Empirical percentiles, lognormal fragility and hazard curve for the structure identified by the ID RC-MI-C-3-BF (a); disaggregation of the failure rate (b).

With the purpose of a quantification of how much the estimation uncertainty involved in the fragility fitting procedure impacts on the seismic rate evaluation and to investigate about curves' usability, parametric resampling, evaluated in the previous section for four structures, are now calculated for all the structures under investigation.[11] Given the couple of parameters defining lognormal fragility from the *i*-th simulation, indicated as $\left\{\eta_i^*, \beta_i^*\right\}$, the corresponding rate, $\lambda_{f,i}^*\left(\eta_i^*, \beta_i^*\right)$, can be evaluated via Equation (52) to finally obtain a distribution of the failure rates varying $i = 1, 2, ...k$. The coefficient of variation of such a failure rate distribution can be evaluated as:

[11] For all the structures, fragility fitting method to evaluate $\left\{\eta^*, \beta^*\right\}$, shown from Table 17 to Table 21, is the same as that used to get $\left\{\eta, \beta\right\}$.

$$CoV_{\lambda_f} = \frac{\sqrt{VAR\left[\lambda_f\right]}}{E\left[\lambda_f\right]} = \frac{\sqrt{\frac{1}{k-1}\cdot\sum_{i=1}^{k}\left(\lambda_{f,i}^{*} - E\left[\lambda_f\right]\right)^2}}{\frac{1}{k}\cdot\sum_{i=1}^{k}\lambda_{f,i}^{*}}, i = 1,2,...,k \quad (53)$$

where $STD\left[\lambda_f\right]$ and $E\left[\lambda_f\right]$ are the variance and the mean of the estimator of the failure rate. In Figure 73 CoV_{λ_f} has been related to the *LFM* for all the structures involved in RINTC project, grouped by typology and site (red, cyan and green markers identify buildings located in L'Aquila, Naples and Milan respectively).

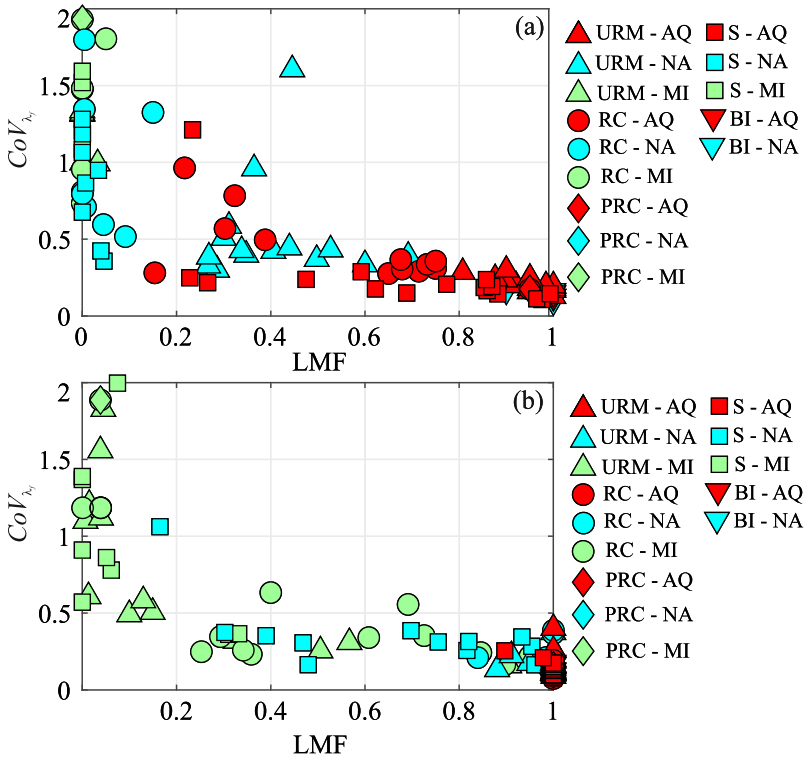

Figure 73. Coefficient of variation of failure rate versus LFM for each structure designed within RINTC project for GC(a) and UPD(b).

Analysis of results at GC (Figure 73a) suggests the following.

- When *LFM* is lower than 20%, CoV_{λ_f} reaches high levels, sometimes greater than unit. This happens for all the buildings, belonging to all the typologies, designed in Milan where the minimum CoV_{λ_f} is about

equal to 0.8 and the *LFM* is lower than 5%. Conclusion is the same for buildings designed in Naples (60% out of the total for this site) while for L'Aquila the number of buildings in this range is not significant (two structures out of fifty-two).

- When *LFM* lies within the range of 20% and 50%, which includes 22% of the buildings designed in Naples and 23% of the buildings designed in L'Aquila, CoV_{λ_f} decreases with a high intra-site varying from 0.32 and 1.60 for the mid-hazard site 0.24 and 1.21 for the high-hazard site.
- When *LFM* is greater than 50%, CoV_{λ_f} drops considerably up to values under 20%. In this range lies the 18% of the buildings designed in Naples and more than 75% of the buildings designed in L'Aquila.

For GC, results referring to buildings designed in low-hazard site (Milan) suggest that fragility fitting provides particularly uncertain parameters estimates; therefore, these curves must be used with caution, at least considering estimation uncertainty in the risk analysis. Results for code-conforming structures in high-hazard site (L'Aquila) suggests that fragility fitting appears to be well constrained, therefore they can be of reference for other similar structures; for the mid-hazard site (Naples) the trend of results is ambiguous, it is however suggested to account for estimation uncertainty in risk analysis carried out employing these curves.

Analysis of results at UPD (Figure 73b) suggests differentiating some conclusion for structural typology. For the low-hazard site:

- about 90% of the steel structures (14 over 16) have *LFM* lower than 7% (minimum CoV_{λ_f} about 0.80). Remaining two structures show *LFM* about 35% and CoV_{λ_f} about 0.36;
- 75% (11 over 15) of the URM structures have *LFM* lower than 15% and show minimum CoV_{λ_f} equal to 0.50. 2 out of 15 structures do not exceed 60% *LFM* while only one structure shows CoV_{λ_f} lower than 0.20;
- any PRC structure shows CoV_{λ_f} greater than 0.50, independently from *LFM* value;
- 50% (6 over 12) of the RC structures show *LFM* greater than 60% with CoV_{λ_f} ranging from 0.16 and 0.35; for 5 over 6 structures remaining,

LFM varies from 0.25 and 0.40 with CoV_{λ_f} within a range from 0.24 and 0.6; only one structure shows a CoV_{λ_f} equal to 2 (*LFM* lower than 5%);

- all the BI structures in mid- and high- hazard sites show CoV_{λ_f} lower than 0.20.

At UPD fragility curves for structures designed in Milan may be poorly explanatory of the structural behavior for all the typologies except, apparently, for RC buildings. For mid- and high- hazard sites conclusions are essentially equivalent: CoV_{λ_f} ranges from 7% to 40% for all the structures belonging to all the investigated typologies except for two (over sixteen) steel structures exhibiting CoV_{λ_f} greater than one, so parameters of fragility function seem to be explanatory of structural behavior at UPD more than at GC.

5.5. Conclusions

In the presented study parametric fragility curves referred to global collapse failure and usability preventing damage for the buildings analyzed within RINTC project are derived. It is recalled that structures, belonging to a variety of structural types, were designed for damage-limitation and life safety for two soil conditions at three sites characterized by seismic hazard ranging from low-to-high in the country (Milan, Naples and L'Aquila). Starting with results of the multi-stripe analysis performed within the project to *IM* levels corresponding to 10,000 years exceedance return period at the construction site, *EDP*-based lognormal fragility was assessed, for all the code-designed structures, by means of one fitting method among maximum likelihood, normal probability paper and least square regression. The fitting methods include quantification of estimation uncertainty that can be carried over the evaluation of the seismic structural reliability expressed in terms of failure fatality rates.

The results show significant heterogeneity of fragility parameters within each typology and among typologies. This mainly derives from the number of failures observed in the structural dynamic analysis in the range of *IM*s at which they are performed in the project. This has been investigated looking at the estimation uncertainty in the fragility parameters and the consequent variability of the failure rates when these curves are integrated with the site's hazard. The main conclusions to be drawn from this study are listed here.

- At GC, fragility fitting for all the typologies of structures designed at low-site hazard provides results relatively weakly constrained, in general. This could be motivated by conservative requirements that the Italian code imposes regardless of the design seismic actions leading to structures which under strong seismic actions do not exhibit any (or exhibit very few) failure cases. Conversely, results for structures designed at the high-hazard site suggest that estimated fragility parameters well represent structural behaviour of all the buildings belonging to all the typologies. For the mid-hazard site, the trend in the results is not particularly clear, as for the low- and high-hazard sites.
- At UPD, steel, URM, and PRC structures designed at low-hazard site have fragility parameters which are also relatively poorly constrained. Only for RC structures designed at Milan, fragilities give results, which may indicate the possibility to use the curves with some confidence.
- At UPD, for mid- and high- hazard sites conclusions are essentially equivalent for almost all the buildings belonging to all the typologies: parameters of fragility functions seem to be somewhat explanatory of structural seismic vulnerability.

With these considerations in mind, these curves are made available for further risk assessment studies involving code-conforming buildings.

Chapter 6 – SUMMARY AND CONCLUSIONS

In the framework of PBEE the evaluation of the fragility function is a fundamental step for estimating the rate of earthquakes leading the structure to fail in meeting a performance objective.

In the state-of-the-art approach, fragility assessment is based on procedures that require non-linear dynamic analysis of a detailed (e.g., modelling highly non-linear structural behaviour) structural model subjected to many ground motions selected consistently with the seismic hazard of the site. The main disadvantage of these procedures is the computational load needed for modelling, performing analysis and for post-processing results; for these reasons, engineers are strongly driven to look for simpler alternatives. Providing tools and methodologies in order to reduce time spent in analysis was the first target in the thesis.

In this perspective, Chapter 2 introduces two MATLAB-based tools developed: SPO2FRAG and DYANAS. SPO2FRAG tool eschews the need for computationally demanding dynamic analyses by simulating the results of incremental dynamic analysis via the SPO2IDA algorithm and an equivalent single-degree-of-freedom approximation of the structure. The software is characterized by versatility, accepting as input static pushover results obtained from the structural analysis software package of the user's choice and allowing the user to control the IDA simulation and fragility estimation procedure at its various steps and intervene where one deems necessary.

DYANAS uses the OpenSees finite element platform to perform non-linear dynamic analysis of the SDOF oscillators. The scope of this open-source, freely distributed software is to serve as a tool for earthquake engineering research. The main advantages offered by the DYANAS interface are ease in the definition of the required analysis parameters and corresponding seismic input, efficient execution of the analyses themselves and availability of a suite of convenient, in-built post-processing tools for the management and organization of the structural responses. The types of dynamic analysis frameworks supported are incremental, B2B-incremental (needed for the evaluation of the state-dependent fragility) and multiple-stripe and cloud.

As introduced, the assessment of the fragility term, when simplified methods cannot be used, is based on the results of non-linear dynamic analysis of a numerical model, which is subjected to a sample of ground motions, in order to capture the record-to-record variability of structural response. The

simulations aim at the generation of samples of structural response given samples of ground motions, following that only an estimate of the fragility (and of the failure rate consequently) is obtained; this implies that the failure rate changes with the sample of structural responses so an uncertainty in its estimation may arise. Providing operational tools for the quantification of estimation uncertainty behind seismic risk estimates due to record-to-record variability of structural response was herein the second task.

Chapter 3 presents R2R-EU which is a PBEE software tool (developed in MATLAB) that numerically implements various schemes for estimating structure-specific seismic fragility and for the quantification of the estimation uncertainty behind seismic risk estimates, emanating from record-to-record variability in structural response. The software accepts as input the results of structural dynamic analysis to a set of accelerograms and seismic hazard curves. Estimation uncertainty is quantified by providing statistics, such as mean and variance, of the estimators of the failure rate and the fragility parameters (where applicable) and possibly an approximation of their distribution. The user can choose the analysis method among some resampling and/or simulation schemes belonging to the bootstrap family, the delta method and other solutions from probability and statistics theory.

According to what introduced, uncertainty in seismic rate estimation strictly depends on the number of records used to perform dynamic non-linear analysis. Intuitively, increasing the number of records may lead to get results least affected by estimation uncertainty but the need to limit the computation time forces to investigate the choice of the number of records to use for dynamic analysis to achieve quantifiable levels of mean relative estimation error on seismic risk metrics The sample size of the ground-motion record set is nowadays usually governed by computation-demand constraints, yet it directly affects the uncertainty in estimation of seismic response.

Chapter 4 uses analytical and numerical means to investigate the record sample size, n, required to achieve quantifiable levels of mean relative estimation error on seismic risk metrics. Regression-based cloud analysis in the context of Cornell's reliability method and incremental dynamic analysis using various intensity measures were employed to derive a relation of the form $\Delta/\sqrt{n}$, where Δ is a parameter that depends on both the dispersion of structural responses and the shape of the hazard curve at the site. For the cases examined, n can be kept in the forty to one-hundred range and achieve 10%

mean relative error. The study can contribute to guide engineers towards an informed a-priori assessment of the number of records needed to achieve a desired value for the coefficient of variation of the estimator of structural seismic risk.

In the second part of the chapter, question of the number of records is faced off from the code-provisions point of view: while structural seismic reliability studies use a few tens of records, codes often require no more than seven to eleven records for obtaining an estimate of mean response, mandating that these records be selected based on criteria of compatibility with the design spectrum. This issue is addressed by investigating the effect of spectrum-compatible acceleration records' sample size on estimating average single-stripe inelastic structural response. Examination of the results reveals that the spectral compatibility condition leads to response statistics that do not exhibit the trends expected in the case of simple random samples of various sizes. In fact, the responses obtained by using the selected spectrum-compatible records cannot be considered neither independent nor identically distributed. Thus, such statistics do not provide estimates of the intended characteristics of the underlying distribution. In other words, looking at the estimation uncertainty in the response distribution's parameters, by using statistics only suitable for cases of simple random sampling, is an ill-posed problem, since the sampled distribution may be very different from the one implicitly assumed by this approach. In conclusion, when code-based record selection is of concern, using tools of statistical inference such as the assessment of estimation uncertainty, suitable in cases of simple random sampling, to determine the necessary number of spectrum-compatible records, may be conceptually inappropriate.

Coming back to fragility assessment, often, a probability model is assigned to define structural fragility. There is no need to describe it with an equation that has parameters, but it is often convenient. There are many such distributions for this purpose but only one is used in the present work, the lognormal, being the most frequently used in applications. Basically, each time a parametric model is used to fit empirical data, it accounts for some limitation in its use which needs to become known by the user. In Chapter 5 fragility curves referred to two different performance levels, global collapse failure and usability preventing damage, for the different structural types analysed within RINTC project are derived. Buildings are designed in three different Italian sites (characterized by different seismic hazard) for two different soil

conditions. *EDP*-based lognormal fragility was assessed by means of one fitting method among maximum likelihood, normal probability paper and least square regression. Estimation uncertainty that can be carried over the evaluation of the seismic structural reliability expressed in terms of failure fatality rates, has been quantified. The results show significant heterogeneity of fragility parameters within each typology and among typologies. Estimation uncertainty grows when the number of failures observed analytically, within the range of *IM*s considered for the dynamic runs, decreases. Due to this consideration, parametric (lognormal) representations of fragility should be used with caution in risk assessment and the standard error in estimation of the fragility parameters should not be neglected.

REFERENCES

[1] Cornell CA, Krawinkler H. Progress and challenges in seismic performance assessment. PEER Cent News 2000;3:1–3.

[2] Cornell CA. Hazard, ground motions and probabilistic assessment for PBSD. vol. 23. 2004.

[3] Krawinkler H, Seneviratna GDPK. Pros and cons analysis of seismic evaluation. Eng Struct 1998;20:452–64. https://doi.org/10.1016/S0141-0296(97)00092-8.

[4] Fragiadakis M, Vamvatsikos D, Aschheim M. Application of non-linear static procedures for the seismic assessment of regular RC moment frame buildings. Earthq Spectra 2014;30:767–94. https://doi.org/10.1193/111511EQS281M.

[5] Fajfar P. A Non-linear Analysis Method for Performance-Based Seismic Design. Earthq Spectra 2000;16:573–92. https://doi.org/10.1193/1.1586128.

[6] Shome N, Cornell CA, Bazzurro P, Carballo JE. Earthquakes, records, and non-linear responses. Earthq Spectra 1998;14:469–500. https://doi.org/10.1193/1.1586011.

[7] Shome N, Cornell CA. Probabilistic seismic demand analysis of non-linear structures. Reliability of marine structures program technical report RMS-35. Stanford University 1999.

[8] Iervolino I. Assessing uncertainty in estimation of seismic response for PBEE. Earthq Eng Struct Dyn 2017;46:1711–23. https://doi.org/10.1002/eqe.2883.

[9] Gehl P, Douglas J, Seyedi DM. Influence of the number of dynamic analyses on the accuracy of structural response estimates. Earthq Spectra 2015;31. https://doi.org/10.1193/102912EQS320M.

[10] Eads L, Miranda E, Krawinkler H, Lignos DG. An efficient method for estimating the collapse risk of structures in seismic regions. Earthq Eng Struct Dyn 2013;42:25–41. https://doi.org/10.1002/eqe.2191.

[11] Iervolino I, Spillatura A, Bazzurro P. Seismic Reliability of Code-Conforming Italian Buildings. J Earthq Eng 2018. https://doi.org/10.1080/13632469.2018.1540372.

[12] Calvi GM, Pinho R. Development of seismic vulnerability assessment methodologies over the past 30 years. ISET J {…} 2006;43:75–104.

[13] Vamvatsikos D, Cornell CA. Incremental dynamic analysis. Earthq Eng

Struct Dyn 2002;31:491–514. https://doi.org/10.1002/eqe.141.

[14] Dolsek M. Incremental dynamic analysis with consideration of modeling uncertainties. Earthq Eng Struct Dyn 2009;38:805–25. https://doi.org/10.1002/eqe.869.

[15] Vamvatsikos D, Fragiadakis M. Performance, Incremental dynamic analysis for estimating seismic Uncertainty, sensitivity and. Earthq Eng Struct Dyn 2010;39:141–63.

[16] Vamvatsikos D. Seismic Performance Uncertainty Estimation via IDA with Progressive Accelerogram-Wise Latin Hypercube Sampling. J Struct Eng 2014;140. https://doi.org/10.1061/(asce)st.1943-541x.0001030.

[17] Bazzurro P, Cornell CA, Shome N, Carballo JE. Three proposals for characterizing MDOF non-linear seismic response. J Struct Eng 1998. https://doi.org/10.1061/(ASCE)0733-9445(1998)124:11(1281).

[18] Jalayer F, Cornell CA. A Technical Framework for Probability-Based Demand and Capacity Factor Design (DCFD) Seismic Formats. PEER Rep 2003/8 2003:122.

[19] Jalayer F, Cornell CA. Alternative non-linear demand estimation methods for probability-based seismic assessments. Earthq Eng Struct Dyn 2009;38:951–72. https://doi.org/10.1002/eqe.876.

[20] Jalayer F, De Risi R, Manfredi G. Bayesian Cloud Analysis: Efficient structural fragility assessment using linear regression. Bull Earthq Eng 2015;13:1183–203. https://doi.org/10.1007/s10518-014-9692-z.

[21] Luco N, Bazzurro P, Cornell CA. Dynamic Versus Static Computation Of The Residual Capacity Of A Mainshock-damaged Building To Withstand An Aftershock. Proc 13th World Conf Earthq Eng Vancouver, Canada 2004.

[22] Vidic T, Fajfar P, Fischinger M. Consistent inelastic design spectra: Hysteretic and input energy. Earthq Eng Struct Dyn 1994;23:523–37. https://doi.org/10.1002/eqe.4290230505.

[23] Vamvatsikos D, Cornell CA. Direct estimation of the seismic demand and capacity of oscillators with multi-linear static pushovers through IDA. Earthq Eng Struct Dyn 2006;35:1097–117. https://doi.org/10.1002/eqe.573.

[24] Iervolino I, Baltzopoulos G, Vamvatsikos D, Baraschino R. SPO2FRAG V1.0: Software for pushover-based derivation of seismic

fragility curves. ECCOMAS Congr. 2016 - Proc. 7th Eur. Congr. Comput. Methods Appl. Sci. Eng. Crete Island, Greece, 5–10 June, vol. 3, 2016, p. 5962–76. https://doi.org/10.7712/100016.2233.11553.

[25] Pinto PE, Giannini R, Franchin P. Seismic Reliability Analysis of Structures. 2004.

[26] Veletsos AS, Newmark NM, Chelapati C V. Deformation Spectra for Elastic and Elastoplastic Systems Subjected to Ground Shock and Earthquake Motions. Proc 3rdWorld Conf Earthq Eng 1965:663–82.

[27] Fajfar P, Gašperšič P. the N2 Method for the Seismic Damage Analysis of Rc Buildings. Earthq Eng Struct Dyn 1996;25:31–46. https://doi.org/10.1002/(SICI)1096-9845(199601)25:1<31::AID-EQE534>3.0.CO;2-V.

[28] Chopra AK, Goel RK. Capacity-demand-diagram methods based on inelastic design spectrum. Earthq Spectra 1999;15:637–55. https://doi.org/10.1193/1.1586065.

[29] Miranda E. Estimation of Inelastic Deformation Demands of SDOF Systems. J Struct Eng 2001;127:1005–12. https://doi.org/10.1061/(asce)0733-9445(2001)127:9(1005).

[30] FEMA. FEMA-440: improvement of non-linear static seismic analysis procedures. Prep by ATC FEMA, Washington, DC 2005.

[31] Priestley MJN, Calvi GM, Kowalsky MJ. Displacement-based seismic design of structures. Building 2007;23:1453–60. https://doi.org/10.1016/S0141-0296(01)00048-7.

[32] Guerrini G, Graziotti F, Penna A, Magenes G. Improved evaluation of inelastic displacement demands for short-period masonry structures. Earthq Eng Struct Dyn 2017;46:1411–30. https://doi.org/https://doi.org/10.1002/eqe.2862.

[33] Fragiadakis M, Vamvatsikos D. Fast performance uncertainty estimation via pushover and approximate IDA. Earthq Eng Struct Dyn 2010;39:683–703. https://doi.org/10.1002/eqe.965.

[34] Tothong P, Cornell CA. An empirical ground-motion attenuation relation for inelastic spectral displacement. Bull Seismol Soc Am 2006;96:2146–64. https://doi.org/10.1785/0120060018.

[35] Iervolino I, Cornell CA. Record selection for non-linear seismic analysis of structures. Earthq Spectra 2005;21:685–713. https://doi.org/10.1193/1.1990199.

[36] Kwong NS, Chopra AK, Mcguire RK. A framework for the evaluation of ground motion selection and modification procedures. Earthq Eng Struct Dyn 2015;44:795–815. https://doi.org/10.1002/eqe.2502.

[37] Ibarra LF, Krawinkler H. Global collapse of frame structures under seismic excitations. 2005.

[38] Adam C, Jäger C. Seismic collapse capacity of basic inelastic structures vulnerable to the P-delta effect. Earthq Eng Struct Dyn 2012;41:775–93. https://doi.org/10.1002/eqe.1157.

[39] Ibarra LF, Medina RA, Krawinkler H. Hysteretic models that incorporate strength and stiffness deterioration. Earthq Eng Struct Dyn 2005;34:1489–511. https://doi.org/10.1002/eqe.495.

[40] Takeda T, Sozen MA, Nielsen NN. Reinforced Concrete Response to Simulated Earthquakes. J Struct Div 1970;96:2557–73. https://doi.org/10.1061/jsdeag.0002765.

[41] Graziotti F, Penna A, Magenes G. A non-linear SDOF model for the simplified evaluation of the displacement demand of low-rise URM buildings. Bull Earthq Eng 2016;14:1589–612. https://doi.org/10.1007/s10518-016-9896-5.

[42] Lignos DG, Krawinkler H. Deterioration Modeling of Steel Components in Support of Collapse Prediction of Steel Moment Frames under Earthquake Loading. J Struct Eng 2011;137:1291–302. https://doi.org/10.1061/(ASCE)ST.1943-541X.0000376.

[43] Kampenhuber D, Adam C. Degradation parameter for equivalent SDOF systems obtained from cyclic pushover analysis and parameter optimisation. Proc. Second Eur. Conf. Earthq. Eng. Seismol. (2ECEES), Istanbul, Turkey, Aug, 2014, p. 24–9.

[44] McKenna F. OpenSees: A framework for earthquake engineering simulation. Comput Sci Eng 2011;13:58–66. https://doi.org/10.1109/MCSE.2011.66.

[45] Ousterhout JK, Jones K. Tcl and the Tk Toolkit. 2nd editio. Addison Wesley; 2009.

[46] Scott MH, Haukaas T. Modules in OpenSees for the next generation of performance-based engineering. 17th Anal Comput Spec Conf 2006;2006:26. https://doi.org/10.1061/40878(202)33.

[47] Psyrras NK, Sextos AG. Build-X: Expert system for seismic analysis and assessment of 3D buildings using OpenSees. Adv Eng Softw

2018;116:23–35. https://doi.org/10.1016/j.advengsoft.2017.11.007.

[48] Papanikolaou VK, Kartalis-Kaounis T, Protopapadakis VK, Papadopoulos T. GiD+ OpenSees interface: an integrated finite element analysis platform. Greece Lab R/C Mason Struct Aristotle Univ Thessaloniki 2017.

[49] Dolšek M, Šebenik Ž, Klinc R, Dolenc M, Brozovič M. Web Application for the Selection of Characteristic Ground Motions. 6th Int. Conf. Earthq. Geotech. Eng. Christcurch, New Zealand, 1-4 Novemb., 2015.

[50] Elkady A, Lignos DG. Interactive Interface for Dynamic Analysis Procedures (II-DAP): Version 1.0 Manual and Examples. 2018.

[51] Vamvatsikos D, Cornell CA. Applied incremental dynamic analysis. Earthq Spectra 2004;20:523–53. https://doi.org/10.1193/1.1737737.

[52] FEMA P695. Quantification of building seismic performance factors. Washington, DC: 2009.

[53] Lin T, Haselton CB, Baker JW. Conditional spectrum-based ground motion selection. Part I: Hazard consistency for risk-based assessments. Earthq Eng Struct Dyn 2013;42:1847–65. https://doi.org/10.1002/eqe.2301.

[54] Cornell CA, Jalayer F, Hamburger RO, Foutch DA. Probabilistic Basis for 2000 SAC Federal Emergency Management Agency Steel Moment Frame Guidelines. J Struct Eng 2002;128:526–33. https://doi.org/10.1061/(ASCE)0733-9445(2002)128:4(526).

[55] Baker JW. Efficient analytical fragility function fitting using dynamic structural analysis. Earthq Spectra 2015;31:579–99. https://doi.org/10.1193/021113EQS025M.

[56] Shome N, Cornell CA. Structural seismic demand analysis: Consideration of collapse. 8th ACSE Spec. Conf. Probabilistic Mech. Struct. Reliab., 2000, p. PMC2000-119. https://doi.org/10.1016/j.bjoms.2014.08.001.

[57] Agresti A. Categorical data analysis. Wiley, New York; 2012.

[58] Cornell AC, Benjamin JR. Probability, Statistics and Decision for Civil Engineers. McGraw-Hill, New York; 1970.

[59] Draper NR, Smith H. Applied Regression Analysis. 3rd ed. New York: John Wiley & Sons; 1998.

[60] Luco N, Cornell CA. Structure-specific scalar intensity measures for near-source and ordinary earthquake ground motions. Earthq Spectra 2007;23:357–92. https://doi.org/10.1193/1.2723158.

[61] Adam C, Ibarra LF. Seismic Collapse Assessment. vol. 3. Berlin: Springer; 2015. https://doi.org/10.1007/978-3-642-35344-4_248.

[62] Vamvatsikos D, Cornell CA. Direct Estimation of Seismic Demand and Capacity of Multidegree-of-Freedom Systems through Incremental Dynamic Analysis of Single Degree of Freedom Approximation. J Struct Eng 2005;131:589–99. https://doi.org/10.1061/(asce)0733-9445(2005)131:4(589).

[63] CEN. EN 1998-1: Eurocode 8 - Design of structures for earthquake resistance. Part 1: General rules, seismic actions and rules for buildings. European Committee for Standardization; 2004.

[64] ASCE. FEMA-356: prestandard and commentary for the seismic rehabilitation of building. Dev by ASCE FEMA, Washington, DC 2000.

[65] BSSC. FEMA-273: NEHRP guidelines for the seismic rehabilitation of buildings. Dev by ATC FEMA, Washington, DC n.d.;1997.

[66] FEMA 440. Improvement of Non-linear Static Seismic Analysis Procedures. FEMA 440, Fed Emerg Manag Agency, Washingt DC 2005;440:392.

[67] ASCE. Seismic rehabilitation of existing buildings. ASCE/SEI 41-06, Rest 2007:1–428. https://doi.org/10.1061/9780784408841.

[68] Han SW, Moon KH, Chopra AK. Application of MPA to estimate probability of collapse of structures. Earthq Eng Struct Dyn 2010;39:1259–78. https://doi.org/10.1002/eqe.992.

[69] De Luca F, Vamvatsikos D, Iervolino I. Near-optimal piecewise linear fits of static pushover capacity curves for equivalent SDOF analysis. Earthq Eng Struct Dyn 2013;42:523–43. https://doi.org/10.1002/eqe.2225.

[70] Moehle JP. Displacement-Based Design of RC Structures Subjected to Earthquakes. Earthq Spectra 1992;8:403–28. https://doi.org/10.1193/1.1585688.

[71] Katsanos EI, Vamvatsikos D. Yield frequency spectra and seismic design of code-compatible RC structures: an illustrative example. Earthq Eng Struct Dyn 2017;46:1727–45. https://doi.org/10.1002/eqe.2877.

[72] FEMA 58-1. Seismic Performance Assessment of Buildings - methodology. vol. 1. Washington, DC: 2012.

[73] SEAOC. Performance based seismic engineering of buildings, Vision 2000 committee. Struct Eng Assoc California, Sacramento, California; 1995 1995.

[74] Haselton CB, Liel AB, Deierlein GG, Dean BS, Chou JH. Seismic Collapse Safety of Reinforced Concrete Buildings. I: Assessment of Ductile Moment Frames. J Struct Eng 2011;137:481–91. https://doi.org/10.1061/(asce)st.1943-541x.0000318.

[75] Mood AM, Graybill FA, Boes DC. Introduction to the Theory of Statistics. 3rd ed. 1974.

[76] Efron B. The jackknife, the bootstrap, and other resampling plans 1982.

[77] NIST. Evaluation of the FEMA P-695 Methodology for Quantification of Building Seismic Performance Factors. 2010.

[78] Baltzopoulos G, Chioccarelli E, Iervolino I. The displacement coefficient method in near-source conditions. Earthq Eng Struct Dyn 2015;44. https://doi.org/10.1002/eqe.2497.

[79] McKenna F, Fenves GL, Scott MH, Jeremic B. Open System for Earthquake Engineering Simulation (OpenSees) 2000.

[80] Haselton CB, Deierlein GG. Assessing Seismic Collapse Safety of Modern Reinforced Concrete Moment-Frame Buildings. 2007.

[81] Zareian F, Medina RA. A practical method for proper modeling of structural damping in inelastic plane structural systems. Comput Struct 2010;88:45–53. https://doi.org/10.1016/j.compstruc.2009.08.001.

[82] Akkar S, Bommer JJ. Empirical Equations for the Prediction of PGA, PGV, and Spectral Accelerations in Europe, the Mediterranean Region, and the Middle East. Seismol Res Lett 2010;81:195–206. https://doi.org/10.1785/gssrl.81.2.195.

[83] Iervolino I, Chioccarelli E, Cito P. Reassess V1.0: A computationally-efficient software for probabilistic seismic hazard analysis. ECCOMAS Congr. 2016 - Proc. 7th Eur. Congr. Comput. Methods Appl. Sci. Eng. Crete Island, Greece, 5–10 June, vol. 3, 2016, p. 5999–6012. https://doi.org/10.7712/100016.2236.12116.

[84] Meletti C, Galadini F, Valensise G, Stucchi M, Basili R, Barba S, et al. A seismic source zone model for the seismic hazard assessment of the Italian territory. Tectonophysics 2008;450:85–108.

https://doi.org/10.1016/j.tecto.2008.01.003.

[85] Barani S, Spallarossa D, Bazzurro P. Disaggregation of probabilistic ground-motion Hazard in Italy. Bull Seismol Soc Am 2009;99:2638–61. https://doi.org/10.1785/0120080348.

[86] Barani S, Spallarossa D, Bazzurro P. Erratum to disaggregation of probabilistic ground-motion hazard in Italy. Bullettin Seismol Soc Am 2010;100:3335–6.

[87] Seneviratna GDPK, Krawinkler H. Evaluation of inelastic MDOF effects for seismic design. 1997.

[88] Altoontash A, Deierlein G. Simulation and damage models for performance assessment of reinforced concrete beam-column joints. Stanford University, 2004.

[89] Lowes LN, Mitra N, Altoontash A. A Beam-Column Joint Model for Simulating the Earthquake Response of Reinforced Concrete Frames Nilanjan Mitra University of Washington Arash Altoontash. PEER Rep 2003/10 2004.

[90] Perzyna P. Thermodynamic Theory of Viscoplasticity. Adv Appl Mech 1971;11:313–54. https://doi.org/10.1016/S0065-2156(08)70345-4.

[91] FEMA P440A. Effects of Strength and Stiffness Degradation on Seismic Response. Washingt Fed Emerg Manag Agency 2009.

[92] Kazantzi AK, Vamvatsikos D. Intensity measure selection for vulnerability studies of building classes. Earthq Eng Struct Dyn 2015;44:2677–94. https://doi.org/10.1002/eqe.2603.

[93] Kohrangi M, Vamvatsikos D, Bazzurro P. Implications of intensity measure selection for seismic loss assessment of 3-D buildings. Earthq Spectra 2016;32:2167–89. https://doi.org/10.1193/112215EQS177M.

[94] Ancheta TD, Darragh RB, Stewart JP, Seyhan E, Silva WJ, Chiou BSJ, et al. NGA-West2 Database. Earthq Spectra 2014;30:989–1005. https://doi.org/https://doi.org/10.1193/070913EQS197M.

[95] Luzi L, Puglia R, Russo E. ORFEUS WG5. Engineering strong motion database, version 1.0. Istituto Nazionale di Geofisica e Vulcanologia, Observatories & Research Facilities for European Seismology 2016. https://doi.org/https://doi.org/10.13127/ESM.

[96] Camata G, Celano F, De Risi MT, Franchin P, Magliulo G, Manfredi V, et al. Rintc project: Non-linear dynamic analyses of Italian code-conforming reinforced concrete buildings for risk of collapse

assessment. COMPDYN 2017 - Proc 6th Int Conf Comput Methods Struct Dyn Earthq Eng Rhodes Island, Greece, 2017;1:1474–85. https://doi.org/10.7712/120117.5507.17050.

[97] Iervolino I, Spillatura A, Bazzurro P. RINTC Project - Assessing the (Implicit) Seismic Risk of Code-Conforming Structures in Italy. In: Papadrakakis M, Fragiadakis M, editors. Proc. 6th Int. Conf. Comput. Methods Struct. Dyn. Earthq. Eng. (COMPDYN 2015), 2017, p. 1545–57. https://doi.org/10.7712/120117.5512.17282.

[98] Suzuki A, Baltzopoulos G, Iervolino I, RINTC-Workgroup. A look at the seismic risk of Italian code-conforming RC buildings. Proc. 16th Eur. Conf. Earthq. Eng. Thessaloniki, Greece, 2018, p. 18–21.

[99] Kappos AJ, Gkatzogias KI, Gidaris IG. Extension of direct displacement-based design methodology for bridges to account for higher mode effects. Earthq Eng Struct Dyn 2013;42:581–602. https://doi.org/10.1002/eqe.2229.

[100] Iervolino I, Giorgio M, Chioccarelli E. Markovian modeling of seismic damage accumulation. Earthq Eng Struct Dyn 2016;45:441–61. https://doi.org/10.1002/eqe.2668.

[101] Raghunandan M, Liel AB, Luco N. Aftershock collapse vulnerability assessment of reinforced concrete frame structures. Earthq Eng Struct Dyn 2015;44:419–39. https://doi.org/10.1002/eqe.2478.

[102] Oehlert GW. A Note on the Delta Method. Am Stat 1992;46:27–9. https://doi.org/10.1671/0272-4634(2007)27[763:EOODIF]2.0.CO;2.

[103] Chioccarelli E, Cito P, Iervolino I, Giorgio M. REASSESS V2.0: software for single- and multi-site probabilistic seismic hazard analysis. Bull Earthq Eng 2019;17:1769–93. https://doi.org/10.1007/s10518-018-00531-x.

[104] Pacor F, Felicetta C, Lanzano G, Sgobba S, Puglia R, D'Amico M, et al. NESS v1.0: A worldwide collection of strong-motion data to investigate near source effects. Seismol Res Lett 2018. https://doi.org/10.1785/0220180149.

[105] Iervolino I, Dolce M. Foreword to the Special Issue for the RINTC (The Implicit Seismic Risk of Code-Conforming Structures) Project. J Earthq Eng 2018. https://doi.org/10.1080/13632469.2018.1543697.

[106] CEN. EN 1998-2: Eurocode 8 - design of structures for earthquake resistance. Part 2: bridges 2005.

[107] RINTC-Workgroup. Results of the 2015-2017 implicit seismic risk of code-conforming structures in Italy (RINTC) project. ReLUIS Report, Rete Dei Lab Univ Di Ing Sismica (ReLUIS), Naples, Italy 2018.

[108] Scozzese F, Terracciano G, Zona A, Della Corte G, Dall'Asta A, Landolfo R. Modeling and Seismic Response Analysis of Italian Code-Conforming Single-Storey Steel Buildings. J Earthq Eng 2018;22:2104–33. https://doi.org/10.1080/13632469.2018.1528913.

[109] Ricci P, Manfredi V, Noto F, Terrenzi M, Petrone C, Celano F, et al. Modeling and Seismic Response Analysis of Italian Code-Conforming Reinforced Concrete Buildings. J Earthq Eng 2018;22:105–39. https://doi.org/10.1080/13632469.2018.1527733.

[110] Manzini CF, Magenes G, Penna A, da Porto F, Camilletti D, Cattari S, et al. Masonry Italian Code-Conforming Buildings. Part 1: Case Studies and Design Methods. J Earthq Eng 2018;22:54–73. https://doi.org/10.1080/13632469.2018.1532358.

[111] McGuire RK. Probabilistic Seismic Hazard Analysis and Design Earthquakes: Closing the Loop. Bull Seismol Soc Am 1995;85:1275–84. https://doi.org/10.1016/0148-9062(96)83355-9.

[112] Campbell KW, Bozorgnia Y. NGA-West2 ground motion model for the average horizontal components of PGA, PGV, and 5% damped linear acceleration response spectra. Earthq Spectra 2014;30:1087–114. https://doi.org/10.1193/062913EQS175M.

[113] Jalayer F, Cornell CA. Direct probabilistic seismic analysis: implementing non-linear dynamic assessments. Stanford University, 2003.

[114] Hancock J, Bommer JJ, Stafford PJ. Numbers of scaled and matched accelerograms required for inelastic dynamic analyses. Earthq Eng Struct Dyn 2008;37:1585–607. https://doi.org/10.1002/eqe.827.

[115] Reyes JC, Kalkan E. How many records should be used in an ASCE/SEI-7 ground motion scaling procedure? Earthq Spectra 2012;28:1223–42. https://doi.org/10.1193/1.4000066.

[116] FEMA. FEMA-350: Recommended Seismic Design Criteria for New Steel Moment-Frame Buildings. SAC Joint Venture: 2000.

[117] Stucchi M, Meletti C, Montaldo V, Crowley H, Calvi GM, Boschi E. Seismic hazard assessment (2003-2009) for the Italian building code. Bull Seismol Soc Am 2011;101:1885–911. https://doi.org/10.1785/0120100130.

[118] Luzi L, Puglia R, Russo E, D'Amico M, Felicetta C, Pacor F, et al. The Engineering Strong-Motion Database: A Platform to Access Pan-European Accelerometric Data. Seismol Res Lett 2016;87:987–97. https://doi.org/10.1785/0220150278.

[119] Vamvatsikos D. Accurate Application and Second-Order Improvement of SAC/FEMA Probabilistic Formats for Seismic Performance Assessment. J Struct Eng 2014;140:4013058. https://doi.org/10.1061/(ASCE)ST.1943-541X.0000774.

[120] Bozorgnia Y, Abrahamson NA, Al Atik L, Ancheta TD, Atkinson GM, Baker JW, et al. NGA-West2 research project. Earthq Spectra 2014;30:973–87. https://doi.org/10.1193/072113EQS209M.

[121] Eads L, Miranda E, Lignos DG. Average spectral acceleration as an intensity measure for collapse risk assessment. Earthq Eng Struct Dyn 2015;44:2057–73. https://doi.org/10.1002/eqe.2575.

[122] Bojórquez E, Iervolino I. Spectral shape proxies and non-linear structural response. Soil Dyn Earthq Eng 2011;31:996–1008. https://doi.org/10.1016/j.soildyn.2011.03.006.

[123] Kazantzi AK, Vamvatsikos D. Intensity measure selection for vulnerability studies of building classes. Earthq Eng Struct Dyn 2015;44:2677–94. https://doi.org/10.1002/eqe.2603.

[124] Tsantaki S, Adam C, Ibarra LF. Intensity measures that reduce collapse capacity dispersion of P-delta vulnerable simple systems. Bull Earthq Eng 2017;15:1085–109. https://doi.org/10.1007/s10518-016-9994-4.

[125] Iervolino I, Galasso C, Cosenza E. REXEL: Computer aided record selection for code-based seismic structural analysis. Bull Earthq Eng 2010;8:339–62. https://doi.org/10.1007/s10518-009-9146-1.

[126] Jayaram N, Lin T, Baker JW. A Computationally efficient ground-motion selection algorithm for matching a target response spectrum mean and variance. Earthq Spectra 2011;27:797–815. https://doi.org/10.1193/1.3608002.

[127] Baker JW, Lee C. An Improved Algorithm for Selecting Ground Motions to Match a Conditional Spectrum. J Earthq Eng 2017. https://doi.org/10.1080/13632469.2016.1264334.

[128] Katsanos EI, Sextos AG. ISSARS: An integrated software environment for structure-specific earthquake ground motion selection. Adv Eng Softw 2013;58:70–85. https://doi.org/10.1016/J.ADVENGSOFT.2013.01.003.

[129] Eads L. Seismic Collapse Risk Assessment Of Buildings: Effects Of Intensity Measure Selection and Computational Approach,Report No. 184. John A. Blume Earthquake Engineering Center, Stanford University, Stanford, CA., 2013.

[130] Lin T, Haselton CB, Baker JW. Conditional spectrum-based ground motion selection. Part II: Intensity-based assessments and evaluation of alternative target spectra. Earthq Eng Struct Dyn 2013;42:1867–84. https://doi.org/10.1002/eqe.2303.

[131] Goulet CA, Watson-Lamprey J, Baker JW, Haselton CB, Luco N. Assessment of ground motion selection and modification (GMSM) methods for non-linear dynamic analyses of structures. 4th Decenn. Geotech. Earthq. Eng. Soil Dyn. Conf. (GEESD IV), ASCE, May 18-22 2007, Sacramento, CA. ASCE Geotech. Spec. Publ. No. 181., 2008, p. 1–10. https://doi.org/10.1061/40975(318)3.

[132] Baker JW, Cornell CA. A vector-valued ground motion intensity measure consisting of spectral acceleration and epsilon. Earthq Eng Struct Dyn 2005;34:1193–217. https://doi.org/10.1002/eqe.474.

[133] CS.LL.PP. Norme tecniche per le costruzioni. Gazz Uff Della Repubb Ital GU 2008;29:(in Italian).

[134] CS.LL.PP. Aggiornamento delle norme tecniche per le costruzioni. Gazz Uff Della Repubb Ital GU 2018;42:1-198 (in Italian).

[135] CEN. Eurocode 8: Design Provisions for Earthquake Resistance of Structures, Part 1.1: General rules, seismic actions and rules for buildings, EN1998-1 2004.

[136] Cornell CA. Engineering seismic risk analysis. Bull Seism Soc Am 1968;58:1583–606.

[137] Cattari S, Camilletti D, Lagomarsino S, Bracchi S, Rota M, Penna A. Masonry Italian Code-Conforming Buildings. Part 2: Non-linear Modelling and Time-History Analysis. J Earthq Eng 2018;22:2010–40. https://doi.org/10.1080/13632469.2018.1541030.

[138] Franchin P, Ragni L, Rota M, Zona A. Modelling Uncertainties of Italian Code-Conforming Structures for the Purpose of Seismic Response Analysis. J Earthq Eng 2018;22:1964–89. https://doi.org/10.1080/13632469.2018.1527262.

[139] Ragni L, Cardone D, Conte N, Dall'Asta A, Di Cesare A, Flora A, et al. Modelling and Seismic Response Analysis of Italian Code-Conforming Base-Isolated Buildings. J Earthq Eng 2018;22:198–230.

https://doi.org/10.1080/13632469.2018.1527263.

[140] Micozzi F, Flora A, Viggiani LR., Cardone D, Ragni L, Dall'Asta A. Risk assessment of Reinforced Concrete buildings with Rubber Isolation Systems designed by the Italian Seismic Code. J Earthq Eng 2021.

[141] Ponzo FC, Di Cesare A, Telesca A, Pavese A, Furinghetti M. Advanced modelling and risk analysis of rc buildings with sliding isolation systems designed by the italian seismic code. Appl Sci 2021;11:1–16. https://doi.org/10.3390/app11041938.

[142] Magliulo G, Bellotti D, Cimmino M, Nascimbene R. Modeling and Seismic Response Analysis of RC Precast Italian Code-Conforming Buildings. J Earthq Eng 2018;22:140–67. https://doi.org/10.1080/13632469.2018.1531093.

[143] Magliulo G, Di Salvatore C, Ercolino M. Modeling of the Beam-To-Column Dowel Connection for a Single-Story RC Precast Building. Front Built Environ 2021;7:1–10. https://doi.org/10.3389/fbuil.2021.627546.

[144] Gajera K, Dal Lago B, Capacci L, Biondini F. Multi-Stripe Seismic Assessment of Precast Industrial Buildings With Cladding Panels. Front Built Environ 2021;7:1–15. https://doi.org/10.3389/fbuil.2021.631360.

[145] Hsiao P, Lehman DE, Roeder CW. Evaluation of the response modification coefficient and collapse potential of special concentrically braced frames. Earthq Eng Struct Dyn 2013;42:1547–64. https://doi.org/10.1002/eqe.2286.

[146] FEMA. Recommended Seismic Design Criteria for New Steel Moment-Frame Buildings: FEMA 350. Washington, DC, USA: FEMA; 2013.

[147] Ambraseys NN, Simpson KA, Bommer JJ. Prediction of horizontal response spectra in Europe. Earthq Eng Struct Dyn 1996;25:371–400. https://doi.org/10.1002/(SICI)1096-9845(199604)25.

[148] Monelli D, Pagani M, Weatherill G, Silva V, Crowley H. The hazard component of OpenQuake: The calculation engine of the Global Earthquake Model. 15th World Conf Earthq Eng 2012:8.

[149] Luzi L, Hailemikael S, Bindi D, Pacor F, Mele F, Sabetta F. ITACA (ITalian ACcelerometric Archive): a web portal for the dissemination of Italian strong-motion data. Seism Res Lett 2008;79:716–22.

[150] Dobry R, Idriss IM, Ng E. Duration characteristics of horizontal

components of strongmotion earthquake records. B Seism Soc Am 1978;68:1487–520.

[151] Lagomarsino S, Penna A, Galasco A, Cattari S. TREMURI program: An equivalent frame model for the non-linear seismic analysis of masonry buildings. Eng Struct 2013;56:1787–99. https://doi.org/10.1016/j.engstruct.2013.08.002.

[152] Cito P, Iervolino I. Peak-over-threshold: Quantifying ground motion beyond design. Earthq Eng Struct Dyn 2020;49:458–78. https://doi.org/10.1002/eqe.3248.

[153] Vamvatsikos D, Cornell CA. Developing efficient scalar and vector intensity measures for IDA capacity estimation by incorporating elastic spectral shape information. Earthq Eng Struct Dyn 2005;34:1573–600. https://doi.org/10.1002/eqe.496.

[154] Suzuki A, Iervolino I. Seismic fragility of code-conforming Italian buildings based on SDoF approximation. J Earthq Eng 2019.

[155] Lignos DG, Krawinkler H. Development and Utilization of Structural Component Databases for Performance-Based Earthquake Engineering. J Struct Eng 2013;139:1382–94. https://doi.org/10.1061/(ASCE)ST.1943-541X.0000646.

[156] Panagiotakos TB, Fardis MN. Deformation of reinforced concrete at yielding and untimate. ACI Struct J 2001;98:135–47. https://doi.org/10.14359/10181.

[157] Porter K, Kennedy R, Bachman R. Creating Fragility Functions for Performance-Based Earthquake Engineering. Earthq Spectra 2007;23:471–89. https://doi.org/10.1193/1.2720892.

LINKS TO DEVELOPED SOFTWARE TOOLS

Tools developed during the Ph.D. are freely available for non-commercial purposes.

SPO2FRAG is a MATLAB®-coded software tool for estimating structure-specific seismic fragility curves of buildings, using the results of static pushover analysis, introduced in Chapter 2 and available at:
http://wpage.unina.it/iuniervo/doc_en/SPO2FRAG.htm

DYANAS is a MATLAB®-based graphical user interface that uses the OpenSees finite element platform to perform nonlinear dynamic analysis of

single-degree-of-freedom (SDOF) oscillators, introduced in Chapter 2 and available at:
http://wpage.unina.it/georgios.baltzopoulos/software/software_page.html

R2R is a MATLAB®-coded PBEE software tool that numerically implements various schemes for estimating structure-specific seismic fragility and for the quantification of the estimation uncertainty behind seismic risk estimates, emanating from record-to-record variability in structural response. It is described in Chapter 3 and available at:
https://www.reluis.it/it/progettazione/software/r2r-eu.html